

Simulation of
steady-state and ultrafast transport of
charge, spin, and orbital angular
momenta

Dissertation

zur Erlangung des Doktorgrades der Naturwissenschaften
(Dr. rer. nat.)

der

Naturwissenschaftlichen Fakultät II
Chemie, Physik und Mathematik

der Martin-Luther-Universität
Halle-Wittenberg

vorgelegt von

Herrn Oliver Busch

Erstgutachterin: Prof. Dr. Ingrid Mertig
Zweitgutachter: Prof. Dr. Steffen Trimper
Drittgutachter: Prof. Dr. Mathias Kläui

Datum der Abgabe: 13.12.2023

Tag der öffentlichen Verteidigung: 16.05.2024

Vorsitzender der Promotionskommission: Prof. Dr. Thomas Thurn-Albrecht

"The wise speak only of what they know."

GANDALF in *"The Lord of the Rings"* by J. R. R. Tolkien

Abstract

This cumulative thesis reports on the simulation of transport properties in two different regimes: steady-state and ultrafast processes. The considered quantities are in particular, the electron's charge, spin, and orbital angular momenta, which are carried by respective currents.

One part of the thesis deals with the steady-state transverse transport, where an applied homogeneous electric field causes responding charge, spin and orbital currents. The resulting currents are transverse, since they flow perpendicular to the applied electric field; this phenomenon is denoted as 'Hall effect'. In this theoretical work, I investigate the anomalous, spin and orbital Hall effect in the two-dimensional kagome lattice. Model calculations based on the tight-binding approach and the Berry curvature formalism, contribute to an understanding of the effects in the kagome systems on a microscopic level. Thereby, the role of the lattice structure, spin-orbit coupling, and a noncollinear magnetic texture, which is localized on the atomic sites, is discussed.

In the other part of the thesis, the focus is on ultrafast transport, where electron dynamics is induced by excitation of thin films with femtosecond laser pulses. By utilizing an effective one-electron density matrix approach combined with real space tight-binding calculations, the time evolution during laser excitation is simulated with atomic resolution. I performed the simulations with the computational framework *EVOLVE*, a computer code which is being developed in our group. The investigated materials are thin films, in particular homogeneous Cu or Co samples and a Co/Cu heterostructure, which are illuminated with laser pulses of different light polarization. I analyze how spin and orbital angular momenta are generated, manipulated and transferred by laser excitation. Thereby, the role of surfaces and interfaces as well as the light polarization of the laser pulse is discussed.

Kurzzusammenfassung

In dieser kumulativen Arbeit wird über die Simulation von Transporteigenschaften in zwei verschiedenen Regimen berichtet: zeitunabhängige und ultraschnellen Prozesse. Bei den betrachteten Größen handelt es sich insbesondere um die Ladung, den Spin und den Bahndrehimpuls des Elektrons, die durch entsprechende Ströme transportiert werden.

Ein Teil der Arbeit befasst sich mit dem zeitunabhängigen transversalen Transport, bei dem ein angelegtes homogenes elektrisches Feld zu entsprechenden Ladungs-, Spin- und Orbitalströmen führt. Die resultierenden Ströme sind transversal, da sie senkrecht zum angelegten elektrischen Feld fließen; dieses Phänomen wird als „Hall-Effekt“ bezeichnet. In dieser theoretischen Arbeit untersuche ich den anomalen, spin und orbitalen Hall-Effekt im zweidimensionalen Kagome-Gitter. Modellrechnungen, die auf dem Tight-Binding-Ansatz und dem Berry-curvature-Formalismus basieren, tragen zum Verständnis der Effekte in den Kagome-Systemen auf mikroskopischer Ebene bei. Dabei wird die Rolle der Gitterstruktur, der Spin-Bahn-Kopplung und einer nicht-kollinearen magnetischen Textur, die auf den atomaren Plätzen lokalisiert ist, diskutiert.

Im anderen Teil der Arbeit liegt der Schwerpunkt auf dem ultraschnellen Transport, bei dem die Elektronendynamik durch die Anregung dünner Filme mit Femtosekunden-Laserpulsen induziert wird. Durch die Verwendung eines effektiven Ein-Elektronen-Dichtematrix-Ansatzes in Kombination mit Realraum-Tight-Binding-Berechnungen wird die zeitliche Entwicklung während der Laseranregung mit atomarer Auflösung simuliert. Ich habe die Simulationen mit *EVOLVE* durchgeführt, einem Computercode, der in unserer Gruppe entwickelt wird. Bei den untersuchten Materialien handelt es sich um dünne Filme, insbesondere homogene Cu- oder Co-Proben und eine Co/Cu-Heterostruktur, die mit Laserpulsen unterschiedlicher Lichtpolarisation beleuchtet werden. Ich analysiere, wie Spin- und Bahndrehimpuls durch Laseranregung erzeugt, manipuliert und transportiert werden. Dabei wird die Rolle von Oberflächen und Grenzflächen sowie der Lichtpolarisation des Laserpulses diskutiert.

Contents

1	Introduction	1
2	Electronic properties and intrinsic steady-state transport	5
2.1	Tight-binding method	5
2.2	Topological properties of the electronic structure: Berry theory in solid-state physics	11
2.3	Transverse transport: anomalous, spin and orbital Hall effect	16
2.4	Properties of the investigated kagome magnets	23
2.5	Experimental aspects	27
3	Simulation of ultrafast laser-induced electron dynamics	31
3.1	Real-space tight-binding approach for finite systems	31
3.2	Density matrix and equation of motion	33
3.3	Theoretical description of laser excitation	36
3.4	Observables: spin and orbital angular momenta and their currents	42
3.5	Advantages and limitations of the approach	47
4	Publications: transverse charge, spin, and orbital transport in the steady state	49
4.1	Anomalous Hall effect as an effective topological Hall effect	49
4.2	Sources of the spin Hall effect in noncollinear kagome magnets	62
4.3	Unconventional orbital Hall effect arising in <i>s</i> -orbital systems	72
5	Publications: Laser-induced ultrafast electron dynamics	82
5.1	Photo-induced spin angular momentum and (spin-polarized) currents	83
5.2	Ultrafast dynamics of laser-induced orbital angular momentum	93
6	Conclusion and outlook	99
	List of own publications	103
	References	104

1 Introduction

Spin- and orbitronics. The world has changed: a field alternative to conventional electronics is emerging, namely ‘spintronics’, which could make smaller devices with lower power consumption possible [1–3]. Traditional electronic devices, such as solar cells, transistors, sensors, and LCD/LED displays, have conventionally relied solely on the charge of electrons for operation. However, in spintronics, as the name implies, the electron’s spin degree of freedom and the associated angular momentum are also harnessed. This shows great potential for designing more compact and energy-efficient nanoelectronic devices with increased memory and processing capabilities [4, 5].

One class of materials has gained great interest in this field: antiferromagnets that build on their versatility since they can be (semi)metallic, insulating or semiconducting [2]. A conventional (collinear) antiferromagnet is a magnetically ordered state that has a vanishing net magnetization [3, 6]. Although this property challenges the detection or manipulation of antiferromagnets in experiments, it also offers intriguing possibilities, since these materials allow for ultrafast spin dynamics and particular transport quantities. Besides, antiferromagnets are more ‘robust’ against perturbation by (external) magnetic fields and create no stray fields [2, 3].

Since spin (angular momentum) is used for efficient storage and transfer of information, one important aspect of spintronics is the generation of spin(-polarized) currents and their injection into other materials. Spintronics can be roughly divided into two subfields: spin-transfer electronics and spin-orbitronics [2]. The former focuses on effects arising from strong exchange interactions between itinerant and highly localized magnetic moments, such as spin-transfer torque [7, 8], which allows for electrical control of magnetic textures, and the ‘inverse’ effect of spin pumping, where spin currents are created by precessing magnetic moments [9]. In contrast, the latter subfield typically relies on spin-orbit coupling (SOC), leading to phenomena like anisotropic magnetoresistance [10] as well as the ‘famous’ anomalous and spin Hall effects [11, 12]. The latter two effects are used to generate transverse charge and spin(-polarized) currents. For a long time, it was believed that the anomalous Hall effect (AHE) is a signature of ferromagnetism, since the generated charge current could be related to the net magnetization. In contrast, the spin Hall effect (SHE) exists in nonmagnetic materials (where the AHE is absent), but typically large SOC is essential for the generation of large spin currents.

Both effects have become very significant for antiferromagnetic spintronics since both theoretical [13–17] and experimental [18–20] works during the last 10 years showed large AHE and SHE in the noncollinear antiferromagnetic material class Mn_3X ($X=Rh, Ir, Pt, Ga, Ge, Sn$). Most interestingly, the AHE exists despite a vanishing net magnetization, and the SHE is allowed even without SOC in these systems. The two effects have been predicted mainly based on symmetry arguments for the noncollinear magnetic texture formed by the Mn magnetic moments on the two-dimensional kagome lattice (cf. Fig. 1): in these materials, specific symmetries are broken which allows for non-vanishing Berry curvatures – which are topological properties of the electronic structure – that give rise to the ‘intrinsic’ contributions to the AHE [13, 14] and the SHE [15–17]. In the first section in the cumulative part of this thesis, I am going beyond this symmetry analysis and discuss the unconventional transport properties in these noncollinear kagome magnets on a microscopic level.

The aforementioned aspects of *spintronics* have focused only on the manipulation and transfer of angular momentum arising from the intrinsic spin degree of freedom of electrons. Yet, the total magnetic moment also has contributions from the orbital counterpart, which even dominates in some materials [21]. Nevertheless, the orbital degree of freedom was given less consideration because of the so-called ‘orbital quenching’, a phenomenon where the crystal field suppresses orbital angular momentum in *equilibrium* [22]. However, recent studies showed that the generation and transport of orbital angular momentum in *non-equilibrium* is possible despite orbital

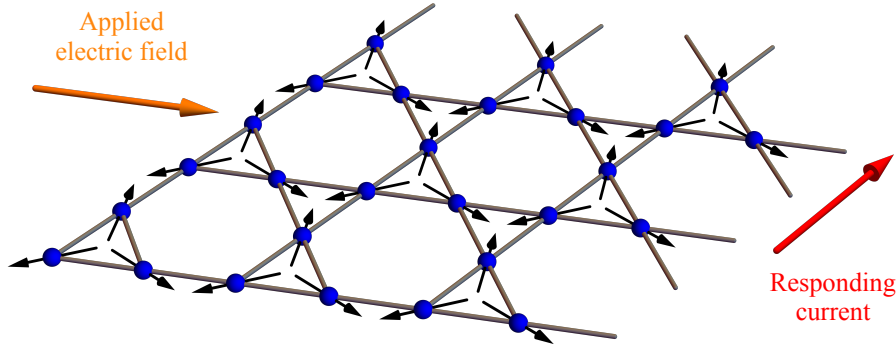


Figure 1: **Illustration of steady-state transport in a kagome lattice.** The atoms (blue spheres) are arranged in a two-dimensional kagome lattice and carry a magnetic moment (black arrows). The latter form a noncollinear magnetic texture, as it is observed in Mn_3Ir [13]. The application of an homogeneous electric field (orange arrow) yields as a response a current (red arrow) that may carry charge, spin or orbital angular momentum.

quenching [21, 23, 24].

Thus, a field alternative to conventional electronics that relies on the orbital degree of freedom is denoted as ‘orbitronics’ [21, 25–27], which builds on ‘new’ effects like the orbital Rashba effect, orbital torque, and the orbital Hall effect (OHE). The latter phenomenon is used to generate transverse orbital currents, and is also investigated in this work. Akin to the intrinsic AHE and SHE, a non-vanishing ‘orbital Berry curvature’ leads to an intrinsic contribution to the OHE which is closely related to the SHE. However, it has been demonstrated that the OHE does *not* require SOC. Consequently, (transverse) orbital currents may exist in materials where the SHE is small or forbidden due to weak SOC [23]. Furthermore, orbital currents can be converted to spin currents via SOC, which makes their distinction challenging in experiments. At the current state, it has been revealed that the generation of orbital currents are facilitated by two contributions. Typically, the atomic center approximation with a restriction to *intra*-atomic contributions is considered, in which the OHE requires hybridization of specific orbitals [21, 23]. However very recently, *inter*-atomic contributions, that have been disregarded for a long time, are also included if the OHE is computed according to the modern formulation of orbital magnetization [28]. In the first section in the cumulative part of the thesis, the modern formulation of orbital magnetization is exploited, and as we demonstrate, the kagome lattice plays also an interesting role in orbital transport.

Light-induced ultrafast magnetization dynamics. On top of exploiting the spin and orbital degree of freedom, in addition to the charge of electrons, another approach to expanding conventional electronics is to focus on light-matter interaction [3]. Exciting materials with laser pulses is advantageous, since one can achieve high temporal resolution ranging from ns down to a few fs and also a spatial resolution of less than a μm , even though combining both aspects is very challenging in experiments [29]. Nevertheless, utilizing laser pulses gained interest for designing new devices that have high performance, while being compact and low-energy consuming, since lasers have the potential to operate very efficiently on ultrafast timescales with high spatial accuracy [29–33].

During the last three decades, many ultrafast phenomena have been intensely investigated in condensed matter physics. A pioneering experimental work, in which ferromagnetic Nickel became demagnetized in the sub-ps regime by excitation with a femtosecond laser pulse [34] laid the foundation for the field of ‘light-induced ultrafast magnetization dynamics’. A decade later,

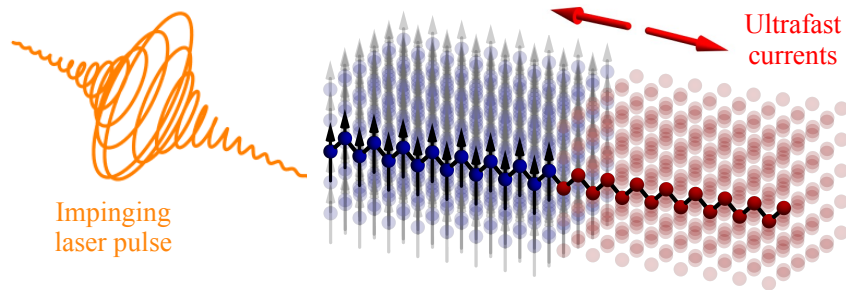


Figure 2: **Illustration of laser-induced electron dynamics.** A heterostructure is illuminated with an ultrafast laser pulse (orange), which induces electron dynamics. For example, ultrafast currents (red arrows) are initiated at the interface and propagate into the magnetic (blue) and nonmagnetic (dark red) layers.

it was shown in experiments with a ferrimagnetic GdFeCo alloy that the magnetization can be entirely reversed by using circularly polarized laser pulses without applying external magnetic fields [35, 36]. Since the final magnetization state depended on the helicity of the laser pulse, it was denoted as ‘helicity-dependent all-optical switching’ [33]. A few years later, all-optical switching of the same alloy (with a different composition) was also realized by excitation with linearly-polarized light [37]. Nevertheless, the polarization of the laser pulse plays an important role for the manipulation of magnetic moments, since the polarization lowers the symmetry of the irradiated system [38–40].

In the literature, one often focuses on the demagnetization and manipulation of the component of the angular momentum associated with the ground state magnetization. Thus, the other components are often neglected. As I will address in this thesis, the polarization of the laser pulse plays a crucial role, since it determines which (other) components are allowed or forbidden by symmetry. Moreover, it is also known that spin polarization can be induced by laser excitation of *nonmagnetic* materials through the inverse Faraday effect [41–43]. Thereby, the transfer of the angular momentum of light to the atoms offers new possibilities to control ultrafast magnetization dynamics.

Besides focusing on demagnetization of ferromagnets [34, 44] and optical manipulation of magnetic moments [30, 40], other works followed that studied the laser-induced transfer of magnetic moments in form of spin(-polarized) currents. Thus, multilayer structures (cf. Fig. 2) gained interest in magnetization dynamics, since it has been shown that (spin) angular momentum of electrons can be transported between different layers, for example via optical inter-site spin transfer (OISTR) [45]. This laser-induced transfer of spin angular momentum has been observed across interfaces between ferromagnetic [46, 47], and between ferromagnetic/nonmagnetic heterostructures [48, 49].

Finally, it is worth noting that, akin to steady-state phenomena, the early works of the ultrafast community mainly focused on the optical manipulation of the *spin* degree of freedom of the magnetic moments. However, the investigation of the laser-induced ultrafast dynamics of the orbital angular momentum has also started during the last decade [50–53]. Therefore, the time evolution of the orbital degree of freedom is also taken into account in this thesis.

In the second section in the cumulative part of this thesis, Co/Cu heterostructures are investigated to address the role of interfaces and surfaces for the generation and transfer of spin and orbital angular momenta by excitation with ultrafast laser pulses. The simulations have been performed with the computational framework *EVOLVE* [54], which is being developed in our group. The obtained results provide detailed insight into the electron dynamics, since observables can be accessed with both femtosecond and atomic resolution.

Goals of the thesis. Based on the above motivation, the following main goals for this work are:

1. Establishing a microscopic understanding of the unconventional transverse, steady-state transport of charge, spin, and orbital angular momenta in kagome systems that goes beyond symmetry arguments. Thereby, the interplay of the kagome lattice, the noncollinear magnetic texture, and the spin-orbit interaction is revealed.
2. Tuning the ultrafast laser-induced generation, manipulation and transfer of spin and orbital angular momenta and the respective currents in finite systems with atomic and femtosecond resolution.

Outline of the thesis. In the next two sections, the necessary background for understanding the results presented in the cumulative part of the thesis is explained. Sec. 2 contains the reciprocal-space tight-binding method that was used to compute the electronic structure and the transverse transport properties based on the Berry-curvature formalism. Furthermore, the magnetic properties of the investigated kagome systems and experimental aspects are summarized at the end of the section. Sec. 3 briefly introduces the real-space tight-binding model and the effective one-electron density matrix approach for describing the time evolution of a system. Afterward, the theory of laser excitation of the electron system, which triggers ultrafast electron dynamics in the simulated clusters, is described in dipole approximation. Finally, it is explained how the time evolution of observables, in particular, spin and orbital angular momenta and their currents, are computed with spatio-temporal resolution. The section concludes with the discussion of advantages and limitations of the computational framework `EVOLVE`.

In the first section in the cumulative part of the thesis (Sec. 4), three publications considering transverse transport of charge, spin and orbital angular momenta in kagome systems in the steady state address goal 1 (cf. Fig. 1). In publication [OB1], the microscopic origin of the anomalous Hall effect in several noncollinear kagome magnets is established, which allows to interpret the effect as an effective topological Hall effect. In publication [OB2], two sources of the spin Hall effect in these systems are revealed: the main signal originates from the magnetic texture and can be reduced by spin-orbit coupling. In publication [OB3], a nonmagnetic *s*-orbital kagome lattice is introduced as a minimal model for the orbital Hall effect and a cycloid motion of the electrons in the edge states, thereby carrying orbital angular momentum, is predicted.

Sec. 5 is the second section in the cumulative part of the thesis, in which two publications are presented. They are attributed to goal 2: the ultrafast photo-induced generation, manipulation and transfer of angular momentum in thin films (cf. Fig. 2) simulated with the `EVOLVE` computer code. In publication [OB4], a systematic investigation of the laser-induced spin angular momentum and the respective currents is presented. Results for Co/Cu heterostructures and homogeneous Cu or Co samples are compared. Thereby, the role of inhomogeneities (surfaces and interfaces) and the polarization of the impinging laser pulse is addressed. In publication [OB5], the orbital companion is analyzed in the same material combinations, thereby comparing the findings of spin and orbital angular momenta. However, the focus is on excitation with circularly polarized laser pulses, which turns out to be useful in order to induce an orbital angular momentum of sizable magnitude in a normal metal.

Finally, the concluding Sec. 6 provides a summary of the established results and an outlook to possible future investigations motivated by the findings in this thesis.

2 Electronic properties and intrinsic steady-state transport

In this chapter, the theoretical background of electronic properties is introduced. First, the tight-binding approach is explained in Sec. 2.1, which is used to compute the electronic band structure of periodic crystals. In Sec. 2.2, the topological properties of the electronic structure are motivated and described via the Berry theory. Thereafter, the obtained Berry curvature and related quantities are used in Sec. 2.3 to compute the intrinsic contributions to the anomalous, spin, and orbital Hall effects in a semiclassical approach. Afterward, the kagome lattice with different possible magnetic configurations is introduced in Sec. 2.4, since it is the model system investigated in publications [OB1], [OB2] and [OB3]. The results are presented in the first section in the cumulative part (Sec. 4), in which the three Hall effects are discussed. Finally, a few aspects of experimental techniques to study the Hall effects are summarized in Sec. 2.5.

2.1 Tight-binding method

Bloch theorem. A real solid is a many-body system consisting of at least 10^{23} particles. The exact description of such a system would be a Hamiltonian H_{tot} as a sum of terms describing the kinetic energy as well as repulsive and attractive Coulomb interactions of *all* electrons and nuclei, respectively [6, 55]. Diagonalization of H_{tot} would yield both the exact many-particle wave function Ψ and the exact energy spectrum, but the computations would be very demanding. Besides, finding the exact solution is not necessary in practice and therefore the problem can be mapped to an effective one-particle problem by exploiting the Born-Oppenheimer and the Hartree-Fock approximation [55–58]. The obtained single-particle Hamiltonian

$$H(\mathbf{r}) \equiv H_{\text{eff}}(\mathbf{r}) = \frac{\mathbf{p}^2}{2m} + V_{\text{eff}}(\mathbf{r}) = -\frac{\hbar^2}{2m} \nabla_{\mathbf{r}}^2 + V_{\text{eff}}(\mathbf{r}) \quad (2.1)$$

describes one electron at \mathbf{r} moving in an effective potential $V_{\text{eff}}(\mathbf{r})$ that is formed by all other particles, in particular all other electrons and nuclei in the solid. Thus, the electron motion is already decoupled from the motion of the nuclei.

In periodic ideal crystals, that satisfy $V_{\text{eff}}(\mathbf{r}) = V_{\text{eff}}(\mathbf{r} + \mathbf{R})$, the Hamiltonian is translational invariant, i.e. $H_{\text{eff}}(\mathbf{r}) = H_{\text{eff}}(\mathbf{r} + \mathbf{R})$, where $\mathbf{R} = \sum_i n_i \mathbf{a}_i$ is a lattice vector. This lattice periodicity of the Hamiltonian can be exploited to prove Bloch's theorem [59] which describes the translational properties of electrons in ideal crystals. Bloch showed that the eigenstates of the one-electron Hamiltonian are a product of plane waves $\exp(i\mathbf{k} \cdot \mathbf{r})$ modulated with a lattice periodic function $u_{\nu, \mathbf{k}}(\mathbf{r}) = u_{\nu, \mathbf{k}}(\mathbf{r} + \mathbf{R})$, where ν is the band index. These Bloch functions

$$\varphi_{\nu, \mathbf{k}}(\mathbf{r}) = \exp(i\mathbf{k} \cdot \mathbf{r}) u_{\nu, \mathbf{k}}(\mathbf{r}) \quad (2.2)$$

fulfill

$$\varphi_{\nu, \mathbf{k}}(\mathbf{r} + \mathbf{R}) = \exp(i\mathbf{k} \cdot \mathbf{R}) \varphi_{\nu, \mathbf{k}}(\mathbf{r}) \quad (2.3)$$

and solve the effective one-electron Schrödinger equation

$$H(\mathbf{r}) \varphi_{\nu, \mathbf{k}}(\mathbf{r}) = \varepsilon_{\nu, \mathbf{k}} \varphi_{\nu, \mathbf{k}}(\mathbf{r}). \quad (2.4)$$

Now, the goal is to find a method to compute the eigenstates $\varphi_{\nu, \mathbf{k}}(\mathbf{r})$ and the eigenenergies $\varepsilon_{\nu, \mathbf{k}}$ of $H(\mathbf{r})$ as will be presented in the following.

The tight-binding model. The above Hamiltonian is already an enormous simplification of the original many-body problem. However, computations can still be very demanding if one is using ab initio methods like density functional theory, in particular if the unit cells contain many atoms. A beneficial approach yielding the electronic structure and the Bloch states is the tight-binding method [59] which simplifies the computational effort enormously, as will be shown in the following. Another advantage of this approach is that tight-binding models are useful as toy models, in which contributions like spin-orbit coupling or the effect of coupling to a magnetic texture can be discussed separately (cf. publications [OB1] and [OB2]).

Within the tight-binding approach [6, 59–67], one assumes that electrons do not move freely in the crystal, but they are bound tightly to the nucleus and are thus (strongly) localized in the vicinity of the atomic sites. Thus, the starting point are atomic orbitals $\phi_{\mathcal{M}}(\mathbf{r} - \mathbf{R})$ located at $\mathbf{R} \equiv \mathbf{R}_n + \mathbf{R}^b$ which is the position of basis atom b within the n -th unit cell. Here, a multi index \mathcal{M} is introduced that is composed of the needed quantum numbers, i.e. basis atom b , spin σ and orbital type α [66]. If N is the number of atomic sites, one can construct wave functions from those atomic orbitals

$$\psi_{\mathcal{M},\mathbf{k}}(\mathbf{r}) = \frac{1}{\sqrt{N}} \sum_{\mathbf{R}} \exp(i\mathbf{k} \cdot \mathbf{R}) \phi_{\mathcal{M}}(\mathbf{r} - \mathbf{R}), \quad (2.5)$$

which satisfy Eq. (2.3). Thus, they are Bloch functions, but they do not fulfill the Schrödinger equation (2.4) in general. However, one can expand the solutions of Eq. (2.4) in terms of the Bloch waves

$$\varphi_{\nu,\mathbf{k}}(\mathbf{r}) = \sum_{\mathcal{M}} c_{\nu,\mathbf{k}}^{\mathcal{M}} \psi_{\mathcal{M},\mathbf{k}}(\mathbf{r}) = \frac{1}{\sqrt{N}} \sum_{\mathcal{M}} c_{\nu,\mathbf{k}}^{\mathcal{M}} \sum_{\mathbf{R}} \exp(i\mathbf{k} \cdot \mathbf{R}) \phi_{\mathcal{M}}(\mathbf{r} - \mathbf{R}). \quad (2.6)$$

This equation is also known as linear combination of atomic orbitals (LCAO) [60, 61] and is used in the following to compute the eigenenergies and the eigenstates of the Hamiltonian in terms of the expansion coefficients $c_{\nu,\mathbf{k}}^{\mathcal{M}}$.

Rewriting the Schrödinger equation with the above ansatz and integrating after multiplication with $\psi_{\mathcal{M}',\mathbf{k}}^*(\mathbf{r})$ from the left yields

$$\sum_{\mathcal{M}} c_{\nu,\mathbf{k}}^{\mathcal{M}} \int \psi_{\mathcal{M}',\mathbf{k}}^*(\mathbf{r}) H(\mathbf{r}) \psi_{\mathcal{M},\mathbf{k}}(\mathbf{r}) d^3r = \varepsilon_{\nu,\mathbf{k}} \sum_{\mathcal{M}} c_{\nu,\mathbf{k}}^{\mathcal{M}} \int \psi_{\mathcal{M}',\mathbf{k}}^*(\mathbf{r}) \psi_{\mathcal{M},\mathbf{k}}(\mathbf{r}) d^3r. \quad (2.7)$$

Herein, the overlap $\int \psi_{\mathcal{M}',\mathbf{k}}^*(\mathbf{r}) \psi_{\mathcal{M},\mathbf{k}}(\mathbf{r}) d^3r$ between two Bloch waves is given by

$$S_{\mathcal{M}',\mathcal{M}}(\mathbf{k}) = \frac{1}{N} \sum_{\mathbf{R}'} \sum_{\mathbf{R}} \exp(i\mathbf{k} \cdot (\mathbf{R} - \mathbf{R}')) \int \phi_{\mathcal{M}'}^*(\mathbf{r} - \mathbf{R}') \phi_{\mathcal{M}}(\mathbf{r} - \mathbf{R}) d^3r, \quad (2.8)$$

which defines the overlap matrix. Exploiting the translational invariance of the periodic lattice allows setting $\mathbf{R}' \equiv \mathbf{0}$ and thus rewriting this expression in terms of atomic overlap integrals

$$S_{\mathcal{M}',\mathcal{M}}(\mathbf{R}) \equiv \int \phi_{\mathcal{M}'}^*(\mathbf{r}) \phi_{\mathcal{M}}(\mathbf{r} - \mathbf{R}) d^3r. \quad (2.9)$$

Thereby, the overlap-matrix elements (in reciprocal space) read

$$S_{\mathcal{M}',\mathcal{M}}(\mathbf{k}) = \sum_{\mathbf{R}} \exp(i\mathbf{k} \cdot \mathbf{R}) S_{\mathcal{M}',\mathcal{M}}(\mathbf{R}). \quad (2.10)$$

They are a Fourier transform of the atomic overlap from real to reciprocal space. The Hamilton

matrix in reciprocal space is defined by the matrix elements on the left-hand side of Eq. (2.7)

$$H_{\mathcal{M}',\mathcal{M}}(\mathbf{k}) \equiv \int \psi_{\mathcal{M}',\mathbf{k}}^*(\mathbf{r}) H(\mathbf{r}) \psi_{\mathcal{M},\mathbf{k}}(\mathbf{r}) d^3r. \quad (2.11)$$

These matrix elements are written in analogy to the overlap matrix as

$$\begin{aligned} H_{\mathcal{M}',\mathcal{M}}(\mathbf{k}) &= \sum_{\mathbf{R}} \exp(i\mathbf{k} \cdot \mathbf{R}) H_{\mathcal{M}',\mathcal{M}}(\mathbf{R}) \\ &= \sum_{\mathbf{R}} \exp(i\mathbf{k} \cdot \mathbf{R}) \int \phi_{\mathcal{M}'}^*(\mathbf{r}) H(\mathbf{r}) \phi_{\mathcal{M}}(\mathbf{r} - \mathbf{R}) d^3r. \end{aligned} \quad (2.12)$$

According to Eq. (2.1), this term can be split into $H_{\mathcal{M}',\mathcal{M}}(\mathbf{k}) = T_{\mathcal{M}',\mathcal{M}}(\mathbf{k}) + V_{\mathcal{M}',\mathcal{M}}(\mathbf{k})$ where the potential-energy term

$$\begin{aligned} V_{\mathcal{M}',\mathcal{M}}(\mathbf{k}) &= \frac{1}{N} \sum_{\mathbf{R}''} \sum_{\mathbf{R}'} \sum_{\mathbf{R}} \exp(i\mathbf{k} \cdot (\mathbf{R} - \mathbf{R}')) \\ &\quad \times \int \phi_{\mathcal{M}'}^*(\mathbf{r} - \mathbf{R}') V_{(A)}(\mathbf{r} - \mathbf{R}'') \phi_{\mathcal{M}}(\mathbf{r} - \mathbf{R}) d^3r \end{aligned} \quad (2.13)$$

has to be discussed in more detail. While evaluating the matrix elements three types of integrals occur [62, 67–69]:

- First, on-site integrals appear for $\mathbf{R} = \mathbf{R}' = \mathbf{R}''$, i.e. both wavefunctions and the atomic potential $V_{(A)}$ are located at the same atomic site. They do not depend on the wave vector \mathbf{k} , since $\mathbf{R} - \mathbf{R}' \equiv \mathbf{0}$.
- If the wavefunctions are located at different atomic sites, but the atomic potential is located at one of those two sites, they are called two-center integrals or hopping integrals. They describe the transition of (valence) electrons between atomic sites at distance $|\mathbf{R} - \mathbf{R}'|$.
- Finally, if $\mathbf{R} \neq \mathbf{R}' \neq \mathbf{R}''$, the terms are called three-center integrals which are typically neglected within the tight-binding approach due to the assumption of strong localization of the wave functions.

Summarizing up to this point, one has to solve a generalized eigenvalue problem

$$\sum_{\mathcal{M}} [H_{\mathcal{M}',\mathcal{M}}(\mathbf{k}) - \varepsilon_{\nu,\mathbf{k}} S_{\mathcal{M}',\mathcal{M}}(\mathbf{k})] c_{\nu,\mathbf{k}}^{\mathcal{M}} = 0. \quad (2.14)$$

With the matrices $\mathbf{H}(\mathbf{k}) \equiv (H_{\mathcal{M}',\mathcal{M}}(\mathbf{k}))$ and $\mathbf{S}(\mathbf{k}) \equiv (S_{\mathcal{M}',\mathcal{M}}(\mathbf{k}))$, and the vector $\mathbf{c}_{\nu,\mathbf{k}} \equiv (c_{\nu,\mathbf{k}}^{\mathcal{M}})$, that contains all expansion coefficients, the above expression is given as a matrix equation

$$[\mathbf{H}(\mathbf{k}) - \varepsilon_{\nu,\mathbf{k}} \mathbf{S}(\mathbf{k})] \mathbf{c}_{\nu,\mathbf{k}} = 0. \quad (2.15)$$

This equation can be transformed to a conventional eigenvalue problem by Löwdin orthogonalization [70], as explained subsequently. Although the basis set $\{\phi_{\mathcal{M}}\}$ of all atoms in the unit cell is orthogonal, two wave functions located at different atomic sites do not have to be in general. In other words, the overlap of atomic orbitals defined in Eq. (2.9) does not always fulfill $S_{\mathcal{M}',\mathcal{M}}(\mathbf{R}) = \delta_{\mathcal{M}',\mathcal{M}}$. This is achieved by decomposing the overlap matrix in reciprocal space as

$S(\mathbf{k}) = S^{1/2}(\mathbf{k}) S^{1/2}(\mathbf{k})$.¹ With

$$\tilde{H}(\mathbf{k}) = S^{-1/2}(\mathbf{k}) H(\mathbf{k}) S^{-1/2}(\mathbf{k}) \quad (2.16)$$

$$\tilde{c}_{\nu,\mathbf{k}} = S^{1/2}(\mathbf{k}) c_{\nu,\mathbf{k}} \quad (2.17)$$

one obtains the conventional eigenvalue problem in matrix form

$$\left[\tilde{H}(\mathbf{k}) - \varepsilon_{\nu,\mathbf{k}} \mathbf{1} \right] \tilde{c}_{\nu,\mathbf{k}} = 0. \quad (2.18)$$

Slater-Koster parameters. In the previous part, the Schrödinger equation for solids has been mapped to a conventional eigenvalue problem that can be solved for each \mathbf{k} -point by straight-on diagonalization. In the derivation of the tight-binding matrix, the matrix elements $H_{\mathcal{M}',\mathcal{M}}(\mathbf{R}) \equiv \int \phi_{\mathcal{M}'}^*(\mathbf{r}) H(\mathbf{r}) \phi_{\mathcal{M}}(\mathbf{r} - \mathbf{R}) d^3r$ [cf. Eq. (2.12)], which are also called hopping integrals, need to be evaluated. Since their direct computation may be very demanding, it is possible to fit them to reference data obtained from ab-initio calculations (e.g. via QUANTUM ESPRESSO [71]) or fit them to experimental data obtained from spectroscopy measurements like angle-resolved photoemission spectroscopy (ARPES) [72, 73].

A common approach in tight-binding is the use of the Slater-Koster formalism [60]. This method allows to reduce the numbers of fitting parameters enormously by exploiting the crystal symmetry once again [65, 66, 74, 75]. Slater and Koster demonstrated that several matrix elements are linearly dependent on each other and can thus be parameterized by only ten different Slater-Koster parameters $V_{\alpha\alpha'\beta}$ for s , p and d orbitals. The used notation describes a hopping of electrons between two atomic orbitals α and α' ($\alpha, \alpha' = s, p, d$) with bond type $\beta = \sigma, \pi, \delta$. Within the Slater-Koster scheme, the hopping integrals are written as a linear combination of those parameters, where the direction cosine l_k of the hopping vector \mathbf{R}_{ij} from atom i and j with respect to the cartesian k -axis ($k = x, y, z$) is utilized. For example, the hopping integrals between s and p_x orbitals, are approximated by $l_x \cdot V_{sp\sigma}$, and between two p_y orbitals by $l_y^2 \cdot V_{pp\sigma} + (1 - l_y^2) \cdot V_{pp\pi}$. All relations are tabulated in literature, see Ref. [63] for example. Computed values for the Slater-Koster parameters of a variety of materials can be found for example in Ref. [67].

Spin and Hund's coupling. In the above derivation, the spin of the valence electron has already been included in the multi index as well because it is needed for simulating magnetic systems and spin-orbit interaction (see next paragraph). Akin to charge, spin is an intrinsic property of electrons, but in the form of an angular momentum. Hence, electrons carry the spin magnetic moment $\boldsymbol{\mu} = -\frac{\mu_B g_s}{\hbar} \mathbf{S}$, where μ_B and $g_s \approx 2.0023$ are the Bohr magneton and the gyromagnetic ratio, respectively [76]. Thus, the spin of the electron can couple either to an external magnetic field \mathbf{B}_{ext} or to a magnetic texture $\mathbf{m} \equiv \{\mathbf{m}_i\}$ which is formed by magnetic moments \mathbf{m}_i localized at the atomic sites i of the lattice. The total magnetic moment (of the electron) originates not only from the spin, but also from an orbital contribution [76]. The spin and orbital degree of freedom will be discussed in more detail within the context of their transport mechanisms in Secs. 2.3 and 3.4.

The spin operator is expressed in terms of the vector of the three Pauli matrices $\boldsymbol{\sigma} \equiv (\sigma^x, \sigma^y, \sigma^z)$ as $\mathbf{S} = \hbar/2 \boldsymbol{\sigma}$ [77]. Within the tight-binding approach, the coupling of spin to a magnetic field or atomic magnetic moments can be incorporated by adding a term $H_{\text{EX}}^{(i)}$, arising from mean-field

¹Another method is the Cholesky decomposition of the overlap matrix into a lower and an upper triangular matrix, i.e. $S = LL^\dagger$.

theory, to the Hamiltonian [65]. This so-called ‘exchange interaction’ (EX) [78] lifts Kramer’s degeneracy [6] and causes an effective magnetic field \mathbf{B}_{eff} to which $\boldsymbol{\mu}$ aligns parallel $\boldsymbol{\mu} \uparrow \uparrow \mathbf{B}_{\text{eff}}$ or antiparallel $\boldsymbol{\mu} \downarrow \uparrow \mathbf{B}_{\text{eff}}$. Thus, the electronic states split according to their spin orientation with respect to the external field or the local magnetic moments. Hence, one obtains twice the number of bands in the electronic structure compared to the spinless case. One can assume an on-site approximation such that a (strongly) localized electron interacts only with magnetic moments located at atom i . This is also known as Hund’s coupling [79] (coupling constant m) and is expressed as [65, 66, 80]

$$H_{\text{EX}}^{(i)} = m \boldsymbol{\sigma} \cdot \mathbf{m}_i \equiv m \begin{pmatrix} m_z^{(i)} & m_x^{(i)} - i \cdot m_y^{(i)} \\ m_x^{(i)} + i \cdot m_y^{(i)} & -m_z^{(i)} \end{pmatrix}, \quad (2.19)$$

which is added to the diagonal elements $H_{\mathcal{M}', \mathcal{M}}$ of the Hamiltonian. Thereby, one is able to include the coupling to a ferromagnetic texture, where the magnetic moments \mathbf{m}_i of all atoms i point in the same direction. Coupling to antiferromagnetic textures, which may be either collinear or even noncollinear, can thus be simulated as well. Noncollinear magnetic textures will be discussed in more detail in Sec. 2.4.

Spin-orbit coupling and orbital angular momentum. Up to this point, a very important phenomenon has not been considered: spin-orbit coupling (SOC). This relativistic effect plays an important role in various fields of solid-state physics like Rashba splitting [81], Dzyaloshinskii-Moriya interaction (DMI) [82, 83] in noncollinear magnetic textures or transport properties like anomalous or spin Hall effect, as demonstrated in publications [OB1] and [OB2].

The above Schrödinger equation does not include relativistic effects, but one may add SOC as a correction to the above tight-binding matrix, as derived in [84]. From basic quantum mechanics [76] an expression for SOC is known as

$$H_{\text{SOC}} = \frac{\hbar}{4(mc)^2} \frac{\partial V}{\partial r} \frac{1}{r} (\mathbf{r} \times \mathbf{p}) \cdot \boldsymbol{\sigma} \equiv \lambda \mathbf{L} \cdot \boldsymbol{\sigma}, \quad (2.20)$$

which is denoted as ‘ $\mathbf{L} \cdot \mathbf{S}$ coupling’. It is valid in the vicinity of the nucleus, where the electrostatic potential is approximately spherically symmetric, i.e. $V \equiv V(|\mathbf{r}|)$. The factor λ is the coupling strength between orbital angular momentum $\mathbf{L} = \mathbf{r} \times \mathbf{p}$ and spin angular momentum $\mathbf{S} = \hbar/2 \boldsymbol{\sigma}$ of the electron. Within the tight-binding approach, the used basis set are atomic orbitals and a common treatment is to express them in terms of real cubic harmonics that are a superposition of the complex spherical harmonics [85–88]. In the following, the explicit form will be derived only for p orbitals for the sake of simplicity; expressions for d orbitals follow straightforwardly.

In order to compute the components L_i of the orbital angular momentum operator \mathbf{L} in the basis of the complex spherical harmonics $|l, m\rangle$ (in real-space representation $Y_l^m(\theta, \phi)$; l is the orbital angular momentum quantum number and m is the magnetic quantum number), one introduces ladder operators $L_{\pm} = L_x \pm i L_y$.

By exploiting the relation $L_{\pm} |l, m\rangle = \hbar \sqrt{(l(l+1) - m(m \pm 1))} |l, m \pm 1\rangle$ one finds [76, 80]

$$L_x |l, m\rangle = \frac{L_+ + L_-}{2} |l, m\rangle; \quad L_y |l, m\rangle = \frac{L_+ - L_-}{2i} |l, m\rangle; \quad L_z |l, m\rangle = \hbar m |l, m\rangle. \quad (2.21)$$

The quantum numbers for p orbitals read $l = 1$ and $m = -1, 0, 1$, which yields the matrix representation $L_i^s \equiv \langle l', m' | L_i | l, m \rangle$ of the components of the orbital angular momentum operator in

the basis of the spherical harmonics $\mathbf{b}^s = (|1, -1\rangle, |1, 0\rangle, |1, 1\rangle)^T$

$$\mathbf{L}_x^s = \frac{\sqrt{2}}{2}\hbar \begin{pmatrix} 0 & 1 & 0 \\ 1 & 0 & 1 \\ 0 & 1 & 0 \end{pmatrix}; \quad \mathbf{L}_y^s = -i\frac{\sqrt{2}}{2}\hbar \begin{pmatrix} 0 & -1 & 0 \\ 1 & 0 & -1 \\ 0 & 1 & 0 \end{pmatrix}; \quad \mathbf{L}_z^s = \hbar \begin{pmatrix} -1 & 0 & 0 \\ 0 & 0 & 0 \\ 0 & 0 & 1 \end{pmatrix}. \quad (2.22)$$

The cubic harmonics $|p_i\rangle$ are superpositions of the complex spherical harmonics

$$|p_x\rangle = \frac{1}{\sqrt{2}}(|1, -1\rangle - |1, 1\rangle); \quad |p_y\rangle = \frac{i}{\sqrt{2}}(|1, -1\rangle + |1, 1\rangle); \quad |p_z\rangle = |1, 0\rangle \quad (2.23)$$

and form a new basis $\mathbf{b}^a = (|p_x\rangle, |p_y\rangle, |p_z\rangle)^T$. The transformation between these two basis sets according to $\mathbf{b}^a = \mathbf{T} \mathbf{b}^s$ is mediated via the unitary transformation matrix

$$\mathbf{T} = \frac{1}{\sqrt{2}} \begin{pmatrix} 1 & 0 & -1 \\ i & 0 & i \\ 0 & \sqrt{2} & 0 \end{pmatrix} \quad \text{and} \quad \mathbf{T}^\dagger = \mathbf{T}^{-1} = \frac{1}{\sqrt{2}} \begin{pmatrix} 1 & -i & 0 \\ 0 & 0 & \sqrt{2} \\ -1 & -i & 0 \end{pmatrix}. \quad (2.24)$$

Finally, one obtains the matrix representation of the orbital angular momentum in atomic orbitals $\mathbf{L}_i^a \equiv \langle p_i | L_i | p_i \rangle$, as needed within the tight-binding approach, by transforming \mathbf{L}_i^s according to $\mathbf{L}_i^a = \mathbf{T} \mathbf{L}_i^s \mathbf{T}^\dagger$:

$$\mathbf{L}_x^a = i\hbar \begin{pmatrix} 0 & 0 & 0 \\ 0 & 0 & -1 \\ 0 & 1 & 0 \end{pmatrix}; \quad \mathbf{L}_y^a = i\hbar \begin{pmatrix} 0 & 0 & 1 \\ 0 & 0 & 0 \\ -1 & 0 & 0 \end{pmatrix}; \quad \mathbf{L}_z^a = i\hbar \begin{pmatrix} 0 & -1 & 0 \\ 1 & 0 & 0 \\ 0 & 0 & 0 \end{pmatrix}. \quad (2.25)$$

Hence, one finds a matrix representation of the SOC term 2.20 for p orbitals as

$$\mathbf{H}_{\text{SOC}}^p = \lambda \mathbf{L} \cdot \boldsymbol{\sigma} = \lambda \sum_i \mathbf{L}_i^a \sigma^i = i \begin{pmatrix} 0 & -\sigma^z & \sigma^y \\ \sigma^z & 0 & -\sigma^x \\ -\sigma^y & \sigma^x & 0 \end{pmatrix}. \quad (2.26)$$

The matrix elements derived here are tabulated e.g. in Refs. [89, 90], together with analog expressions for d orbitals. Thus, the matrix representation $\mathbf{H}_{\text{SOC}}^p$ shows that SOC is an on-site interaction that couples orbitals with different spin, and consequently, leads to spin-mixing effects.

2.2 Topological properties of the electronic structure: Berry theory in solid-state physics

This subsection introduces the concept of the Berry phase and related quantities that have become very important and helpful in the field of solid-state physics during the last decades. Intrinsic topological properties of the electronic structure are linked to transport phenomena like anomalous, spin or orbital Hall effect, as explained in the next subsection. First, three quantities are introduced in a general way: Berry phase, Berry connection, and Berry curvature. Afterward, it will be shown how these quantities are evaluated from the electronic states and energies within the tight-binding framework. The derivation follows mainly the original publication of M. Berry [91], complemented with Refs. [92–94].

Motivation and derivation of the Berry phase. An illustrative example where a phase is accumulated geometrically is the Levi-Civita or parallel transport [6]: a vector $\mathbf{R}(\mathbf{r})$ is moved along a closed path Γ on a surface that is characterized by a local normal vector $\mathbf{n}(\mathbf{r})$. During this motion, $\mathbf{R}(\mathbf{r})$ must always be parallel to the surface and it shall not be twisted around $\mathbf{n}(\mathbf{r})$.

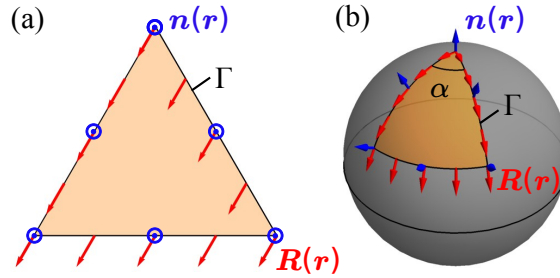


Figure 3: **Illustration of parallel transport.** (a) Parallel transport on a 2D plane. (b) Same as (a), but on a 3D sphere (this figure is reproduced from Ref. [6]).

Fig. 3 shows two examples of the parallel transport: in one case, the surface is planar, and in the other case it is curved. By comparing the direction of $\mathbf{R}(\mathbf{r})$ after a closed loop along Γ , one notices different results. If the surface is a 2D plane [panel (a)], $\mathbf{R}(\mathbf{r})$ is always pointing in the same direction, whereas, if the surface is a sphere, $\mathbf{R}(\mathbf{r})$ changes its orientation about an angle α with respect to the beginning [panel (b)].² This phenomenon is explained by the different geometries of the surfaces. The topic that deals with such phenomena is called ‘topology’. Motivated by this example, the Berry phase will be introduced in a more general way, subsequently.

In Ref. [91], Berry considers a Hamiltonian $H = H(\mathbf{R}(t))$ which depends on a set of external time-dependent parameters $\mathbf{R}(t) = \{R_i(t)\}$ spanning a parameter space. Within the framework of this thesis, it is assumed that $\mathbf{R}(t) \in \mathbb{R}^3$ which allows for exploiting 3D vector analysis. As demonstrated later, \mathbf{R} is not necessarily the position vector in real space. The quantum system described by H evolves in time according to the time-dependent Schrödinger equation

$$H(\mathbf{R}(t)) |\psi(\mathbf{R}(t))\rangle = -\frac{\hbar}{i} \frac{\partial}{\partial t} |\psi(\mathbf{R}(t))\rangle. \quad (2.27)$$

During the time evolution, the Hamiltonian describes a path in the parameter space due to the time dependence of the parameters $\{R_i(t)\}$. This path is considered as a closed loop Γ , such that $\mathbf{R}(T) \stackrel{\text{!}}{=} \mathbf{R}(0)$ implying that the Hamiltonian is in its original form after time T has passed. However, the system will not return to its initial state. At the beginning ($t = 0$), the system is in an eigenstate $|\psi(0)\rangle = |\varphi_\nu(\mathbf{R}(0))\rangle$, where the eigenstates of H satisfy the stationary Schrödinger

²It can be shown that $\alpha = \Omega$ where Ω is the solid angle defined by the curve Γ [6].

equation

$$H(\mathbf{R}) |\varphi_\nu(\mathbf{R})\rangle = \varepsilon_\nu(\mathbf{R}) |\varphi_\nu(\mathbf{R})\rangle. \quad (2.28)$$

For a large time interval $T \gg 0$, one can apply the adiabatic approximation [92]. Thereby, the quantum system will be in an eigenstate for all times

$$|\psi(\mathbf{R}(t))\rangle = \alpha(t) |\varphi_\nu(\mathbf{R}(t))\rangle, \quad (2.29)$$

where α is a time-dependent phase factor. The ansatz for the phase factor is a product of two exponential functions

$$\alpha(t) \equiv \alpha_d(t) \alpha_g(t) = \exp\left\{-\frac{i}{\hbar} \int_0^t \varepsilon_\nu(\mathbf{R}(\tau)) d\tau\right\} \exp\{i\gamma_\nu(t)\}. \quad (2.30)$$

Herein, the conventional dynamical phase factor α_d [80] is multiplied with a geometrical phase factor α_g containing the ‘new’ Berry phase $\gamma_\nu(t)$ introduced by Berry [91]. The explicit time dependence will be omitted from now on, i.e. $\mathbf{R} \equiv \mathbf{R}(t)$ [93]. An expression for the Berry phase is found by plugging the ansatz $|\psi\rangle \equiv |\psi(\mathbf{R}(t))\rangle = \alpha(t) |\nu(\mathbf{R})\rangle$ (with $|\nu(\mathbf{R})\rangle \equiv |\varphi_\nu(\mathbf{R}(t))\rangle$) into the time-dependent Schrödinger equation (2.27)

$$\alpha_d(t) \alpha_g(t) \varepsilon_\nu |\nu(\mathbf{R})\rangle = -\frac{\hbar}{i} \alpha_d(t) \alpha_g(t) \left[\left(-\frac{i}{\hbar} \varepsilon_\nu + i \dot{\gamma}_\nu \right) |\nu(\mathbf{R})\rangle + |\nabla_{\mathbf{R}} \nu(\mathbf{R})\rangle \cdot \dot{\mathbf{R}} \right].$$

Multiplying with $\langle \nu(\mathbf{R}) | \equiv \langle \varphi_\nu(\mathbf{R}(t)) |$ from the left yields

$$\dot{\gamma}_\nu \langle \nu(\mathbf{R}) | \nu(\mathbf{R}) \rangle = i \langle \nu(\mathbf{R}) | \nabla_{\mathbf{R}} \nu(\mathbf{R}) \rangle \cdot \dot{\mathbf{R}}. \quad (2.31)$$

By integrating along the loop Γ , one obtains γ_ν which determines the (geometrical) phase change of $|\psi(T)\rangle$ after one loop Γ with respect to the initial state $|\psi(0)\rangle$. Note that one can show that the term $\langle \nu(\mathbf{R}) | \nabla_{\mathbf{R}} \nu(\mathbf{R}) \rangle$ is purely imaginary. Thus, a first expression for the accumulated Berry phase reads

$$\gamma_\nu(\Gamma) = i \oint_{\Gamma} \langle \nu(\mathbf{R}) | \nabla_{\mathbf{R}} \nu(\mathbf{R}) \rangle \cdot d\mathbf{R} = \oint_{\Gamma} -\text{Im} \langle \nu(\mathbf{R}) | \nabla_{\mathbf{R}} \nu(\mathbf{R}) \rangle \cdot d\mathbf{R}. \quad (2.32)$$

This is a real number and thus may be interpreted as an intrinsic (and physical) quantity originating from the topological properties of the quantum system. The integrand in Eq. (2.32) is defined as the ‘Berry connection’ of band ν

$$\mathcal{A}_\nu(\mathbf{R}) \equiv -\text{Im} \langle \nu(\mathbf{R}) | \nabla_{\mathbf{R}} \nu(\mathbf{R}) \rangle \quad (2.33)$$

and will be discussed in more detail in the next paragraph.

Berry connection and Berry curvature. The eigenstates $|\nu\rangle \equiv |\nu(\mathbf{R})\rangle$ are not gauge invariant and one can chose their phase $\beta \equiv \beta(\mathbf{R})$ arbitrarily

$$|\nu\rangle \mapsto |\nu'\rangle = \exp\{i\beta\} |\nu\rangle. \quad (2.34)$$

It follows that the Berry connection $\mathcal{A}_\nu \equiv \mathcal{A}_\nu(\mathbf{R})$ is not gauge invariant since it transforms under such a gauge transformation as $\mathcal{A}_\nu \mapsto \mathcal{A}'_\nu = -\text{Im} \langle \nu' | \nabla_{\mathbf{R}} \nu' \rangle = \mathcal{A}_\nu - \nabla_{\mathbf{R}} \beta$. However, the Berry

phase itself is invariant which is easily shown with the above equation and Stokes' theorem:

$$\gamma_\nu(\Gamma) \mapsto \gamma'_\nu(\Gamma) = \oint_{\Gamma} \mathcal{A}'_\nu \cdot d\mathbf{R} = - \oint_{\Gamma=\partial S} \nabla_{\mathbf{R}}\beta \cdot d\mathbf{R} + \oint_{\Gamma} \mathcal{A}_\nu \cdot d\mathbf{R} \quad (2.35)$$

$$= - \int_S (\nabla_{\mathbf{R}} \times \nabla_{\mathbf{R}}\beta) \cdot d\mathbf{S} + \oint_{\Gamma} \mathcal{A}_\nu \cdot d\mathbf{R} = \gamma_\nu(\Gamma). \quad (2.36)$$

Here, $\nabla_{\mathbf{R}} \times \nabla_{\mathbf{R}}\beta = 0$ has been used which motivates to define the curl of the Berry connection as the gauge invariant Berry curvature of band ν [91]

$$\mathbf{\Omega}_\nu(\mathbf{R}) \equiv \nabla_{\mathbf{R}} \times \mathcal{A}_\nu(\mathbf{R}). \quad (2.37)$$

This allows to rewrite the Berry phase as

$$\gamma_\nu(\Gamma) = \oint_{\Gamma=\partial S} \mathcal{A}_\nu(\mathbf{R}) \cdot d\mathbf{R} = \int_S \mathbf{\Omega}_\nu(\mathbf{R}) \cdot d\mathbf{S}. \quad (2.38)$$

The Berry connection \mathcal{A}_ν is sometimes called Berry potential because of the analogy to electrodynamics where the magnetic field $\mathbf{B}(\mathbf{r}) = \nabla_{\mathbf{r}} \times \mathbf{A}(\mathbf{r})$ is the curl of the electromagnetic vector potential. Thus, the Berry curvature $\mathbf{\Omega}_\nu \equiv \mathbf{\Omega}_\nu(\mathbf{R}) = \nabla_{\mathbf{R}} \times \mathcal{A}_\nu$ can be interpreted as an abstract magnetic field acting in the parameter space. The next paragraph deals with the calculation of the Berry curvature in practice.

Evaluation of the Berry curvature. In the following derivation, the parameter \mathbf{R} will be omitted. Inserting the definition of the Berry connection (2.33) into the Berry curvature [Eq. (2.37)] yields

$$\mathbf{\Omega}_\nu = - \text{Im} \langle \nabla\nu | \times | \nabla\nu \rangle. \quad (2.39)$$

This expression might be problematic in practical calculations, since evaluating the derivative of the eigenstates $\nabla\nu$ directly may be difficult or requires high computational effort with numerical methods [91]. However, the derivative of the Hamiltonian ∇H can be calculated analytically if the Hamiltonian is given in analytical form, for example in tight-binding or toy models [13, 95–97]. This motivates to find a reformulation of the Berry curvature, where terms with $\nabla\nu$ are eliminated. By inserting the completeness relation $\mathbb{1} = \sum_\mu |\mu\rangle \langle\mu|$ in the above equation one finds

$$\mathbf{\Omega}_\nu = - \sum_{\mu \neq \nu} \text{Im} \langle \nabla\nu | \mu \rangle \times \langle \mu | \nabla\nu \rangle, \quad (2.40)$$

where integrals of the form $\langle \nu | \nabla\mu \rangle$ need to be replaced. This is achieved by considering the derivative of the matrix elements $\nabla \langle \mu | H | \nu \rangle$. Exploiting the product rule for derivatives first and the stationary Schrödinger equation $H | \nu \rangle = \varepsilon_\nu | \nu \rangle$ afterward yields

$$\nabla \langle \mu | H | \nu \rangle = \varepsilon_\nu \langle \nabla\mu | \nu \rangle + \langle \mu | \nabla H | \nu \rangle + \varepsilon_\mu \langle \mu | \nabla\nu \rangle. \quad (2.41)$$

On the other hand, one can apply the derivative *after* H has acted on the eigenstates to find

$$\nabla \langle \mu | H | \nu \rangle = \nabla \langle \mu | \varepsilon_\nu | \nu \rangle = \varepsilon_\nu \langle \nabla\mu | \nu \rangle + \varepsilon_\nu \langle \mu | \nabla\nu \rangle \quad (2.42)$$

if $\mu \neq \nu$. Combining both equations leads to the relation

$$\langle \mu | \nabla \nu \rangle = \frac{\langle \mu | \nabla H | \nu \rangle}{\varepsilon_\mu - \varepsilon_\nu} \quad (2.43)$$

and similarly, one can find an analog expression for the integral $\langle \nabla \nu | \mu \rangle$ that is independent of $\nabla \nu$ but can be calculated via ∇H . Finally, the Berry curvature, which can be applied directly in numerical calculations, reads

$$\Omega_\nu(\mathbf{R}) = -\text{Im} \sum_{\mu \neq \nu} \frac{\langle \nu(\mathbf{R}) | \nabla_{\mathbf{R}} H(\mathbf{R}) | \mu(\mathbf{R}) \rangle \times \langle \mu(\mathbf{R}) | \nabla_{\mathbf{R}} H(\mathbf{R}) | \nu(\mathbf{R}) \rangle}{[\varepsilon_\nu(\mathbf{R}) - \varepsilon_\mu(\mathbf{R})]^2}. \quad (2.44)$$

The Berry theory within the tight-binding model. The above derivation considered a general abstract parameter space. At the end of this subsection, following Ref. [98], it will be demonstrated how Berry's quantities can be computed in solid-state physics and in particular within the tight-binding approach, as shown in [65]. First, one inserts the Bloch functions $\varphi_{\nu, \mathbf{k}}(\mathbf{r}) = \exp(i \mathbf{k} \cdot \mathbf{r}) u_{\nu, \mathbf{k}}(\mathbf{r})$ [cf. Eq. (2.2)] into the stationary Schrödinger equation (2.4) $H(\mathbf{r}) \varphi_{\nu, \mathbf{k}}(\mathbf{r}) = \varepsilon_{\nu, \mathbf{k}} \varphi_{\nu, \mathbf{k}}(\mathbf{r})$. Since the action of $\nabla_{\mathbf{r}}$ on the Bloch function is

$$\nabla_{\mathbf{r}} \exp(i \mathbf{k} \cdot \mathbf{r}) u_{\nu, \mathbf{k}}(\mathbf{r}) = \exp(i \mathbf{k} \cdot \mathbf{r}) (i \mathbf{k} + \nabla_{\mathbf{r}}) u_{\nu, \mathbf{k}}(\mathbf{r}), \quad (2.45)$$

one obtains with $H(\mathbf{r}) = -\frac{\hbar^2}{2m} \nabla_{\mathbf{r}}^2 + V(\mathbf{r})$ from Eq. (2.1)

$$\exp(i \mathbf{k} \cdot \mathbf{r}) \left[\frac{1}{2m} \left(\frac{\hbar}{i} \nabla_{\mathbf{r}} + \hbar \mathbf{k} \right)^2 + V(\mathbf{r}) \right] u_{\nu, \mathbf{k}}(\mathbf{r}) = \exp(i \mathbf{k} \cdot \mathbf{r}) \varepsilon_{\nu, \mathbf{k}} \varphi_{\nu, \mathbf{k}}(\mathbf{r}). \quad (2.46)$$

Multiplying with $\exp(-i \mathbf{k} \cdot \mathbf{r})$ yields a new stationary Schrödinger equation

$$H'(\mathbf{k}) u_{\nu}(\mathbf{k}) = \varepsilon_{\nu}(\mathbf{k}) u_{\nu}(\mathbf{k}), \quad (2.47)$$

where the new Hamiltonian is parameterized by the wave vector \mathbf{k}

$$H(\mathbf{k}) = \exp(-i \mathbf{k} \cdot \mathbf{r}) H(\mathbf{r}) \exp(i \mathbf{k} \cdot \mathbf{r}) = \left[\frac{1}{2m} \left(\frac{\hbar}{i} \nabla_{\mathbf{r}} + \hbar \mathbf{k} \right)^2 + V(\mathbf{r}) \right]. \quad (2.48)$$

Herein, $H(\mathbf{k}) \equiv H'(\mathbf{k})$ is lattice periodic and corresponds to the tight-binding Hamiltonian derived previously which acts on the lattice periodic part $u_{\nu}(\mathbf{k})$ of the Bloch function. Formally, Eq. (2.47) corresponds to Eq. (2.28) which allows to compute the Berry curvature in solid-state physics from the eigenenergies $\varepsilon_{\nu}(\mathbf{k})$ and the lattice-periodic part of the eigenvectors $u_{\nu}(\mathbf{k})$ that are the result of the solution of Eq. (2.18). From now on, the parameter space is spanned by the reciprocal space vector (i.e. $\mathbf{R} = \mathbf{k}$). Hence, the Berry curvature of Eq. (2.44) is now given as

$$\Omega_\nu(\mathbf{k}) = -\text{Im} \sum_{\mu \neq \nu} \frac{\langle u_{\nu}(\mathbf{k}) | \nabla_{\mathbf{k}} H(\mathbf{k}) | u_{\mu}(\mathbf{k}) \rangle \times \langle u_{\mu}(\mathbf{k}) | \nabla_{\mathbf{k}} H(\mathbf{k}) | u_{\nu}(\mathbf{k}) \rangle}{[\varepsilon_{\nu}(\mathbf{k}) - \varepsilon_{\mu}(\mathbf{k})]^2}. \quad (2.49)$$

The general definition of the Berry curvature $\Omega^k(\mathbf{k}) = \epsilon_{ijk} \frac{\partial}{\partial k_i} \mathcal{A}_j(\mathbf{k})$ [cf. Eq. (2.37)], implies that it is also possible to interpret the Berry curvature as the antisymmetric part of a tensor [93, 99]

$$\Omega_{ij}(\mathbf{k}) = \frac{\partial A_j(\mathbf{k})}{\partial k_i} - \frac{\partial A_i(\mathbf{k})}{\partial k_j}. \quad (2.50)$$

Thus, in matrix form, diagonal elements vanish and off-diagonal elements are antisymmetric

$$\Omega(\mathbf{k}) = (\Omega_{ij}(\mathbf{k})) = \begin{pmatrix} 0 & \Omega_{xy}(\mathbf{k}) & \Omega_{xz}(\mathbf{k}) \\ -\Omega_{xy}(\mathbf{k}) & 0 & \Omega_{yz}(\mathbf{k}) \\ -\Omega_{xz}(\mathbf{k}) & -\Omega_{yz}(\mathbf{k}) & 0 \end{pmatrix}. \quad (2.51)$$

The three linearly independent components are connected to the vector $\Omega_\nu(\mathbf{k})$ via

$$\Omega_\nu(\mathbf{k}) = (\Omega_\nu^x(\mathbf{k}), \Omega_\nu^y(\mathbf{k}), \Omega_\nu^z(\mathbf{k})) = (\Omega_{\nu,yz}(\mathbf{k}), \Omega_{\nu,zx}(\mathbf{k}), \Omega_{\nu,xy}(\mathbf{k})). \quad (2.52)$$

Taking the z component of Eq. (2.49), which will be investigated in publications [OB1] and [OB2], and considering the antisymmetry of the Berry curvature, yields

$$\Omega_{\nu,xy}(\mathbf{k}) = -2 \operatorname{Im} \sum_{\mu \neq \nu} \frac{\langle u_\nu(\mathbf{k}) | \partial_{k_x} H(\mathbf{k}) | u_\mu(\mathbf{k}) \rangle \langle u_\mu(\mathbf{k}) | \partial_{k_y} H(\mathbf{k}) | u_\nu(\mathbf{k}) \rangle}{[\varepsilon_\nu(\mathbf{k}) - \varepsilon_\mu(\mathbf{k})]^2}. \quad (2.53)$$

Subsequently, transport properties will be related to the topological properties of the electronic structure. As will be explained, the intrinsic contribution to Hall effects can be computed by integrating the respective Berry curvature over the whole Brillouin zone (BZ).

2.3 Transverse transport: anomalous, spin and orbital Hall effect

The application of an external electric field \mathbf{E} leads to a response of the electron system. In the most simple case, the responding charge current density can be described by Ohm's law $\mathbf{j}_c = \sigma \mathbf{E}$ [6], in which the conductivity σ is in general a matrix. Herein, off-diagonal elements describe transverse transport effects, where \mathbf{j}_c is not aligned with the applied field \mathbf{E} . The transport phenomena of electrons by means of transverse currents are known as 'Hall effects'.

In 1879, E. Hall discovered the well-known ('normal') Hall effect (NHE): in nonmagnetic conductors, charge carriers are deflected transversely to an applied electric current in the presence of an external magnetic field B_z^{ext} due to the Lorentz force [100]. Two years later, he measured a transverse signal that was even stronger and occurred in ferromagnets at temperatures below the Curie temperature even without an applied magnetic field [101]. This contribution to the Hall effect was proportional to the spontaneous magnetization M_z^S and is nowadays called the 'anomalous Hall effect' (AHE) [11]. The AHE could not be understood until Karplus and Luttinger considered spin-orbit coupling (SOC) as the mechanism that breaks time-reversal symmetry [102]. Much later, a third contribution, which is denoted as the 'topological Hall effect' (THE), has been discovered in systems with a noncoplanar magnetic texture even if SOC is not taken into account [103–108]. Here, the contribution to the Hall effect arises from the real-space topology of the magnetic textures and is proportional to the scalar spin chirality χ_S . These three contributions to the Hall effect can be described empirically for the specific resistivity $\rho \equiv \sigma^{-1}$ [11, 109]

$$\rho_{xy} = R^{\text{NHE}} B_z^{\text{ext}} + R^{\text{AHE}} M_z^S + R^{\text{THE}} \chi_S, \quad (2.54)$$

and is valid for many materials like iron or cobalt. In general, extrinsic and intrinsic mechanisms are responsible for the Hall effect [11]. The former comprise the skew-scattering [110] and side jump mechanisms [111] which are both related to the SOC of impurities. Consequently, extrinsic mechanisms are negligible in perfect samples (without any defects), whereas intrinsic ones are always present. Throughout this work, only the intrinsic contribution to the Hall effect is considered. Although the three contributions in Eq. (2.54) can be distinguished phenomenologically, the driving mechanism is the Berry curvature which gives rise to the intrinsic Hall conductivity.

As already mentioned in the introduction, most interestingly, another class of materials gained interest for spin-orbitronics, namely coplanar noncollinear magnetic textures which have been observed in the famous kagome antiferromagnets Mn_3X ($X=\text{Rh, Ir, Pt, Ga, Ge, Sn}$). These materials will be introduced in Sec. 2.4 in more detail. Among many other interesting features, these *coplanar* systems with *compensated* net magnetization exhibit an unconventional AHE: it has been predicted nearly a decade ago [13, 14] and has been experimentally confirmed shortly after in Mn_3Sn [18] and Mn_3Ge [19]. Based on this motivation, transverse transport properties of these kagome systems are investigated in the first section in the cumulative part of this thesis (Sec. 4). In the following, a semiclassical approach is used to derive an expression for the Hall conductivity, which links electron transport to the Berry theory introduced in the previous subsection. Finally, the essential ideas of two closely related transport phenomena, that are also considered in Sec. 4, will be presented: the spin and orbital Hall effect, where transverse currents carrying spin and orbital angular momentum are generated, respectively.

Semiclassical approach. A semiclassical treatment in the context of this work means that the electronic structure is computed from the quantum-mechanical tight-binding approach, whereas external fields are treated classically [112]. Although it is a more simplified picture than a full quantum-mechanical treatment, phenomena like the anomalous Hall effect may be understood intuitively. Furthermore, one can show that an alternative treatment via Kubo formalism [113] yields the same results for the Hall conductivity as obtained by the approach shown below

(cf. [65, 114, 115]). The subsequent derivation follows Refs. [6, 112, 116, 117].

Within the semiclassical approach, the electron wave function is constructed as a wave packet of Bloch waves. The width of that wave packet in reciprocal space is assumed to be much smaller than the extent of the first Brillouin zone (BZ) [6]. The semiclassical equations of motion under the influence of external electric and magnetic fields \mathbf{E} and \mathbf{B} are derived in Ref. [112]:

$$\dot{\mathbf{r}} = \frac{1}{\hbar} \nabla_{\mathbf{k}} \varepsilon(\mathbf{k}) - \dot{\mathbf{k}} \times \boldsymbol{\Omega}(\mathbf{k}) \quad \text{and} \quad \dot{\mathbf{k}} = \frac{q}{\hbar} (\mathbf{E} + \dot{\mathbf{r}} \times \mathbf{B}). \quad (2.55)$$

Herein, $\mathbf{r} \equiv \langle \mathbf{r} \rangle$ and \mathbf{k} denote the center of mass and the momentum of the wave packet. Without external magnetic fields, the above equations (2.55) decouple and read

$$\dot{\mathbf{r}} = \frac{1}{\hbar} \nabla_{\mathbf{k}} \varepsilon(\mathbf{k}) - \frac{q}{\hbar} \mathbf{E} \times \boldsymbol{\Omega}(\mathbf{k}) \quad \text{and} \quad \dot{\mathbf{k}} = \frac{q}{\hbar} \mathbf{E}. \quad (2.56)$$

The electron velocity $\dot{\mathbf{r}}$ is not only determined by the dispersion $\varepsilon(\mathbf{k})$, but there is a ‘new’ additional term, denoted as ‘anomalous velocity’ [102, 116], that arises from the Berry curvature $\boldsymbol{\Omega}(\mathbf{k})$. The transport of electrons due to an electric field can be investigated by combining these equations with the Boltzmann equation [6, 118, 119]:

$$\frac{df}{dt} = \dot{f} + \dot{\mathbf{r}} \cdot \nabla_{\mathbf{r}} f + \dot{\mathbf{k}} \cdot \nabla_{\mathbf{k}} f = \dot{f}_{\text{scatt.}}. \quad (2.57)$$

In general, this equation describes the total variation of the non-equilibrium distribution function $f = f(\mathbf{r}, \mathbf{k}, t)$ of electrons in solids if external fields and scattering processes are considered. This equation is simplified by the following approximations [6, 118, 119]. First, the terms \dot{f} and $\nabla_{\mathbf{r}} f$ are negligible, since we restrict ourselves to time-independent processes and translational invariant systems. Next, one assumes $f = f_0 + g$ and considers only small deviations $g \ll f_0$ from the Fermi-Dirac distribution function f_0 that describes the occupation of electrons. Besides, the relaxation-time approximation states that, after external fields have vanished, scattering processes within a relaxation-time interval τ yield a relaxation of the system back to equilibrium. Thus, one can replace the scattering term

$$\dot{f}_{\text{scatt.}} \approx -\frac{f - f_0}{\tau} = -\frac{g}{\tau}. \quad (2.58)$$

Combining the approximations with the semiclassical equations of motion (2.56) yields the simplified linearized Boltzmann equation

$$\frac{q}{\hbar} \mathbf{E} \cdot \nabla_{\mathbf{k}} (f_0 + g) = -\frac{g}{\tau}. \quad (2.59)$$

Since $f_0 = f_0(\varepsilon(\mathbf{k}), \mu, T)$ is the Fermi-Dirac distribution, one can substitute

$$\nabla_{\mathbf{k}} f_0 = \frac{\partial f_0}{\partial \varepsilon} \nabla_{\mathbf{k}} \varepsilon(\mathbf{k}) = \hbar \frac{\partial f_0}{\partial \varepsilon} \mathbf{v}, \quad (2.60)$$

where $\mathbf{v} = \frac{1}{\hbar} \nabla_{\mathbf{k}} \varepsilon(\mathbf{k})$ is the group velocity of an electron. As a last assumption only small electric fields are considered in linear response theory, which means the difference g from equilibrium is linear in \mathbf{E} and terms of order \mathbf{E}^2 are neglected. Consequently, one finds

$$g = -\tau \frac{q}{\hbar} \mathbf{E} \cdot \nabla_{\mathbf{k}} f_0 = -\tau q \frac{\partial f_0}{\partial \varepsilon} \mathbf{E} \cdot \mathbf{v}. \quad (2.61)$$

The anomalous Hall effect. Based on the previous results, an expression for the intrinsic Hall conductivity will be derived following Refs. [6, 112, 116, 117]. As mentioned before, Ohm's law reads $\mathbf{j}_c = \sigma \mathbf{E}$, which allows for defining the electric conductivity as a second-order tensor

$$\sigma_{ij} \equiv \frac{\partial j_{c,i}}{\partial E_j} \quad (i, j = x, y, z). \quad (2.62)$$

The contribution of band ν to the electric current density reads [6, 112]

$$\mathbf{j}_{c,\nu} = q \int_{\text{BZ}} \frac{f_\nu}{(2\pi)^d} \dot{\mathbf{r}}_\nu d^d k, \quad (2.63)$$

where d is the dimension of the system. Inserting the decoupled equations of motion [Eq. (2.56)] and $f_\nu = f_{0,\nu} + g_\nu$ with Eq. (2.61) yields the total current density $\mathbf{j}_c = \sum_\nu \mathbf{j}_{c,\nu}$ [117]

$$\mathbf{j}_c = q \sum_\nu \int_{\text{BZ}} \frac{1}{(2\pi)^d} \left(f_{0,\nu} - \tau q \frac{\partial f_{0,\nu}}{\partial \varepsilon} \mathbf{E} \cdot \mathbf{v}_\nu \right) \left(\mathbf{v}_\nu - \frac{q}{\hbar} \mathbf{E} \times \boldsymbol{\Omega}_\nu(\mathbf{k}) \right) d^d k. \quad (2.64)$$

The occurring term $\int_{\text{BZ}} f_{0,\nu} \mathbf{v}_\nu d^d k$ vanishes identically, since $f_{0,\nu}$ is even and \mathbf{v}_ν is odd in \mathbf{k} , and the integration is performed over the symmetric BZ. Besides, a term $\propto \mathbf{E}^2$ occurs which is neglected as well due to the assumption of linear response and a small applied field. The responding current can be separated into longitudinal and transverse contributions $\mathbf{j}_c = \mathbf{j}_c^{\text{long.}} + \mathbf{j}_c^{\text{transv.}}$

$$\mathbf{j}_c^{\text{long.}} = q^2 \tau \sum_\nu \int_{\text{BZ}} \frac{1}{(2\pi)^d} \left(-\frac{\partial f_{0,\nu}}{\partial \varepsilon} \right) (\mathbf{v}_\nu \otimes \mathbf{v}_\nu) \mathbf{E} d^d k + \mathcal{O}(\mathbf{E}^2) \quad \text{and} \quad (2.65)$$

$$\mathbf{j}_c^{\text{transv.}} = -\frac{q^2}{\hbar} \sum_\nu \int_{\text{BZ}} \frac{f_{0,\nu}}{(2\pi)^d} \boldsymbol{\Omega}_\nu(\mathbf{k}) d^d k \times \mathbf{E}. \quad (2.66)$$

A comparison with Ohm's law $\mathbf{j}_c = \sigma \mathbf{E}$ allows for identifying the longitudinal and the transverse electric conductivity, where the latter arises from a non-vanishing Berry curvature. Within Sec. 4, only two-dimensional systems located in the xy plane are considered at zero temperature. Thereby, the Fermi-Dirac distribution function $f_{0,\nu}$ reduces to a step function (1 for energies below the Fermi energy E_F and vanishes for higher energies). Thus, the transverse conductivity, which is denoted as (intrinsic) 'Hall conductivity', is computed from the Berry curvature $\Omega_{\nu,xy}(\mathbf{k}) = \Omega_\nu^z(\mathbf{k})$ [cf. Eqs. (2.49) and (2.53)] as [116, 120]

$$\sigma_{xy}(E_F) = -\frac{e^2}{\hbar} \sum_\nu \frac{1}{(2\pi)^2} \int_{\varepsilon_\nu(\mathbf{k}) \leq E_F} \Omega_{\nu,xy}(\mathbf{k}) d^2 k \quad (2.67)$$

if $\mathbf{E} \parallel \mathbf{e}_y$ and $\mathbf{j} \parallel \mathbf{e}_x$ are assumed as in publications [OB1] and [OB2]. Note that this equation can be used to calculate all contributions to the Hall effect, i.e. NHE, AHE and THE. One can also derive an expression for the Hall conductivity via Kubo formalism [93, 113]. In this case, the expression reads [11, 121]

$$\sigma_{xy}^{\text{intr.}} = e^2 \hbar \int_{\text{BZ}} \sum_\nu \sum_{\mu \neq \nu} \frac{f_{0,\nu}}{(2\pi)^d} \text{Im} \frac{[\langle \varphi_\nu(\mathbf{k}) | \mathbf{v} | \varphi_\mu(\mathbf{k}) \rangle \times \langle \varphi_\mu(\mathbf{k}) | \mathbf{v} | \varphi_\nu(\mathbf{k}) \rangle]_z}{[\varepsilon_\nu(\mathbf{k}) - \varepsilon_\mu(\mathbf{k})]^2} d^d k \quad (2.68)$$

with $|\varphi_\nu(\mathbf{k})\rangle = \exp(i\mathbf{k} \cdot \mathbf{r}) |u_\nu(\mathbf{k})\rangle$ and the velocity operator \mathbf{v} . The equivalence of Eqs. (2.68) and (2.67) is proven in Ref. [65]. The Berry curvature in Eq. (2.67) has been derived in the previous

subsection [cf. Eq. (2.49)]:

$$\Omega_{\nu,xy}(\mathbf{k}) = \Omega_{\nu}^z(\mathbf{k}) = -\text{Im} \sum_{\mu \neq \nu} \frac{[\langle u_{\nu}(\mathbf{k}) | \nabla_{\mathbf{k}} H(\mathbf{k}) | u_{\mu}(\mathbf{k}) \rangle \times \langle u_{\mu}(\mathbf{k}) | \nabla_{\mathbf{k}} H(\mathbf{k}) | u_{\nu}(\mathbf{k}) \rangle]_z}{[\varepsilon_{\nu}(\mathbf{k}) - \varepsilon_{\mu}(\mathbf{k})]^2}.$$

Herein, one can replace the lattice-periodic part $|u_{\nu}(\mathbf{k})\rangle = \exp(-i\mathbf{k} \cdot \mathbf{r}) |\varphi_{\nu}(\mathbf{k})\rangle$ and perform the reciprocal-space derivative of the Hamiltonian $H(\mathbf{k})$ [cf. Eq. (2.48)]

$$\nabla_{\mathbf{k}} H(\mathbf{k}) = \nabla_{\mathbf{k}} (\exp(-i\mathbf{k} \cdot \mathbf{r}) H(\mathbf{r}) \exp(i\mathbf{k} \cdot \mathbf{r})) = \exp(-i\mathbf{k} \cdot \mathbf{r}) i [H, \mathbf{r}]_{-} \exp(i\mathbf{k} \cdot \mathbf{r}). \quad (2.69)$$

The commutator $[H, \mathbf{r}]_{-}$ can be substituted by exploiting the Heisenberg equations of motion for the position operator [76]

$$\mathbf{v} = \frac{d\mathbf{r}}{dt} = \frac{i}{\hbar} [H, \mathbf{r}]_{-} + \dot{\mathbf{r}}. \quad (2.70)$$

Assuming that \mathbf{r} is *not* explicitly time-dependent, one finds

$$\nabla_{\mathbf{k}} H(\mathbf{k}) = \exp(-i\mathbf{k} \cdot \mathbf{r}) \hbar \mathbf{v} \exp(i\mathbf{k} \cdot \mathbf{r}), \quad (2.71)$$

which proves the equivalence of Eqs. (2.67) and (2.68).

The spin Hall effect. In the previous paragraph about the AHE, the spin degree of freedom has not been taken into account. However, in a simple picture, the electric current as response to an external applied electric field is a superposed current $\mathbf{j}_c = \mathbf{j}_c^{\uparrow} + \mathbf{j}_c^{\downarrow}$ of two independent charge currents for electrons that carry either spin up (\uparrow) or down (\downarrow). This is known as the two-current model [122] that is used to explain charge transport in ferromagnets below the Curie temperature, when spin-mixing effects are negligible [123]. Herein, one expresses the contributions of each band [cf. Eq. (2.63)] as spin-resolved currents with $m_S = \uparrow, \downarrow$

$$\mathbf{j}_c^{m_S} = \sum_{\nu} \mathbf{j}_{c,\nu}^{m_S} = q \sum_{\nu} \int_{\text{BZ}} \frac{f_{\nu}^{m_S}}{(2\pi)^d} \dot{\mathbf{r}}_{\nu}^{m_S} d^d k. \quad (2.72)$$

SOC causes a deflection of electrons with opposite spin orientation in opposite directions, as is visualized in Fig. 4. Thus, \mathbf{j}_c^{\uparrow} and $\mathbf{j}_c^{\downarrow}$ flow in opposite directions. In a ferromagnet (FM), an *imbalance* of spin \uparrow and \downarrow electrons leads to a nonzero magnetization in an equilibrium state, and to a non-vanishing transverse charge current \mathbf{j}_c in a non-equilibrium state [panel (a)]. In other words, an anomalous Hall current in a FM arises from the time-reversal breaking magnetization. In contrast, in a nonmagnetic metal, the *balance* of spin \uparrow and \downarrow electrons due to time-reversal symmetry renders the charge current zero, since $\mathbf{j}_c^{\uparrow} = -\mathbf{j}_c^{\downarrow}$. In this case, one can define the difference between spin \uparrow and \downarrow currents as the spin current $\mathbf{j}_S = \mathbf{j}_c^{\uparrow} - \mathbf{j}_c^{\downarrow}$ that is nonzero and leads to accumulation of spin angular momentum at the edges of the sample [panel (b)].

The generation of a transverse spin current as response to an applied electric field is denoted as ‘spin Hall effect’ (SHE) [124–128], which was predicted 50 years ago [129, 130] and is closely related to the AHE. The Hall conductivity σ_{xy} is already characterized by the directions of the applied electric field and the responding charge current (along y and x direction, respectively). However, one has to include the spin polarization of the resulting spin current in addition to classify a corresponding spin Hall conductivity. Hence, the latter is defined as a third-order tensor [12, 17, 65]

$$\sigma_{ij}^k \equiv \frac{\partial j_{S,i}^k}{\partial E_j} \quad (i, j, k = x, y, z), \quad (2.73)$$

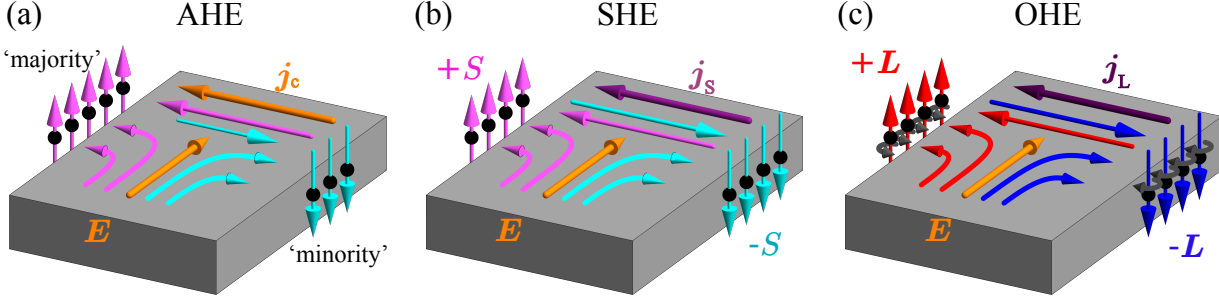


Figure 4: **Schematic illustration of the anomalous (AHE), spin (SHE) and orbital Hall effect (OHE).** When an electric field E is applied, electrons with opposite angular momenta are deflected into opposite directions. (a) AHE: A transverse charge current j_c can be measured due to the majority of electrons with one spin direction (here \uparrow). (b) SHE: In nonmagnetic metals, there is a balance of electrons with spin \uparrow and \downarrow which renders j_c zero. However, a net spin current j_s emerges that leads to the accumulation of electrons with opposite spin angular momentum $\pm S$ at the opposite edges of the sample. (c) OHE: A net transverse orbital current j_L leads to accumulation of orbital angular momentum $\pm L$ at opposite edges.

where $\sigma_{ij}^{S_k}$ describes a spin current $j_{S,i}^k$ with spin polarization along k , and flowing along i , if the electric field is applied in j direction. Like the AHE, the SHE originates from extrinsic and intrinsic mechanisms [12], and within this work, again only the latter are taken into account. An expression for the intrinsic spin Hall conductivity can be constructed in analogy to the Hall conductivity via Kubo formalism [15, 17, 23]. One has to replace the velocity operator, which is associated with the response of the system, in the expression for the Hall conductivity in Eq. (2.68) with the so-called ‘spin-current operator’ [127, 131]

$$\Sigma_i^k \equiv \frac{1}{2} [v_i, S_k]_+ . \quad (2.74)$$

Herein, $[\cdot, \cdot]_+$ is the anticommutator and $S_k = \frac{\hbar}{2} \sigma_k$ is the spin operator. The spin Hall conductivity for a 2D system (in the xy plane) at $T = 0$ K can then be computed as a function of E_F . In analogy to the Hall conductivity, the spin Hall conductivity

$$\sigma_{xy}^{S_z}(E_F) = \frac{e}{\hbar} \sum_{\nu} \frac{1}{(2\pi)^2} \int_{\varepsilon_{\nu}(\mathbf{k}) \leq E_F} \Omega_{\nu,xy}^{S_z}(\mathbf{k}) d^2k \quad (2.75)$$

is also given as the BZ integral of a quantity denoted as ‘spin Berry curvature’ [17, 23, 65, 132].

$$\Omega_{\nu,xy}^{S_z}(\mathbf{k}) = -2\hbar^2 \text{Im} \sum_{\mu \neq \nu} \frac{\langle u_{\nu}(\mathbf{k}) | \Sigma_x^z | u_{\mu}(\mathbf{k}) \rangle \langle u_{\mu}(\mathbf{k}) | v_y | u_{\nu}(\mathbf{k}) \rangle}{[\varepsilon_{\nu}(\mathbf{k}) - \varepsilon_{\mu}(\mathbf{k})]^2} . \quad (2.76)$$

For a long time, it was believed that the crucial condition for the existence of a SHE is SOC which is responsible for the above-presented transverse spin-dependent deflection of electrons [12, 65, 128, 133]. However, some studies showed that *noncoplanar* magnetic textures show a SHE in the absence of SOC, which arises from a non-vanishing spin Berry curvature [17, 134, 135]. And very recently, it was predicted that the *coplanar* kagome antiferromagnets Mn_3X exhibit a SHE as well even in the absence of SOC [16, 17]. The ‘unconventional’ SHE has already been measured in Mn_3Sn [20, 136].

Thus, as illustratively summarized in Fig. 1 in Ref. [17], SOC is only essential for the AHE

in ferromagnets or in coplanar (noncollinear) antiferromagnets, and for the SHE in nonmagnetic materials or in collinear (anti)ferromagnets. Publications [OB1] and [OB2] presented in Sec. 4 contribute to this topic by investigating the interplay of the noncollinearity of the magnetic texture with SOC and the consequences for the AHE and the SHE. As will be explained in the following, spin-orbit coupling is also not important for another effect that is closely related to the SHE, namely the orbital Hall effect, where the orbital degree of freedom is now taken into account as well.

Up to now, only the spin degree of freedom has been included on top of the electron's charge by means of (transverse) transport phenomena. In contrast to conventional electronics, spin-based devices, that rely on the manipulation of spin angular momentum and its currents, have the potential to operate at high speed while consuming low power [1, 2, 4, 5]. There, the SHE can be utilized for charge-to-spin conversion, i.e. conversion of an electric current into a transverse spin current. Subsequent injection into a ferromagnetic layer allows for domain wall motion [137, 138] or magnetization switching due to spin-transfer torque [139, 140]. However, only recently, the (conduction) electron's orbital degree of freedom and transport of orbital angular momentum (OAM) have gained enormous attention leading to the upcoming field of orbitronics, in which energy-efficient applications are promising, as well [21, 25–27].

The orbital Hall effect. Orbital transport has long been disregarded, since the crystal field typically suppresses the OAM in *equilibrium*, a phenomenon denoted as ‘orbital quenching’ that will be explained below in more detail [22]. However, it has been shown that the situation can be different in *non-equilibrium*: although the OAM is quenched in the ground state, it may be induced dynamically by the application of an electric field [23]. It has been demonstrated that the dynamically generated OAM gives rise to an intrinsic transverse current of OAM [cf. Fig. 4 (c)], which is denoted as (intrinsic) ‘orbital Hall effect’ (OHE) [25, 141–144].

For example, the cubic harmonic orbitals $|p_x\rangle$ and $|p_y\rangle$ on their own do not carry OAM (orbital quenching) if they are ‘isolated’. However, once they hybridize, such that $(|p_x\rangle \pm i|p_y\rangle)/\sqrt{2}$, their superposition forms a spherical harmonic orbital with magnetic quantum number $m = \pm 1$ giving rise to the OAM $\langle L_z \rangle = \pm \hbar$ [23]. Recall that according to Eq. (2.25), the diagonal elements of L_z vanish in the basis of cubic harmonics, i.e. $\langle p_i | L_z | p_i \rangle = 0$, but can be nonzero in the basis of spherical harmonics $\langle l, m | L_z | l, m \rangle = \langle 1, \pm 1 | L_z | 1, \pm 1 \rangle = \pm \hbar$ [cf. Eq. (2.22)]. Similarly, d orbitals need to hybridize, such as $(|d_{zx}\rangle \pm i|d_{yz}\rangle)/\sqrt{2}$ [24]. Thereby, the generated OAM can be transported as a (transverse) orbital current through the crystal.

As for the AHE and SHE, restricting the investigation of the OHE to 2D systems in the xy plane at zero temperature is suitable within the framework of this thesis. Hence, the intrinsic contribution to the orbital Hall conductivity, as computed in publication [OB3], is given by [21, 23, 24, 28]

$$\sigma_{xy}^{L_z}(E_F) = \frac{e}{\hbar} \sum_{\nu} \frac{1}{(2\pi)^2} \int_{\varepsilon_{\nu}(\mathbf{k}) \leq E_F} \Omega_{\nu,xy}^{L_z}(\mathbf{k}) d^2k. \quad (2.77)$$

In analogy to the spin Hall conductivity [cf. Eqs. (2.75) and (2.76)], it is obtained as a function of the Fermi level E_F by integrating the ‘orbital Berry curvature’ [28, 145]

$$\Omega_{\nu,xy}^{L_z}(\mathbf{k}) = -2\hbar^2 \operatorname{Im} \sum_{\mu \neq \nu} \frac{\langle u_{\nu}(\mathbf{k}) | \Lambda_x^z | u_{\mu}(\mathbf{k}) \rangle \langle u_{\mu}(\mathbf{k}) | v_y | u_{\nu}(\mathbf{k}) \rangle}{[\varepsilon_{\nu}(\mathbf{k}) - \varepsilon_{\mu}(\mathbf{k})]^2} \quad (2.78)$$

over all occupied states in the BZ. Instead of the spin-current operator, herein, the orbital-current

operator is used which is given by the anticommutator

$$\Lambda_x^z = \frac{1}{2} [v_x, L_z]_+ . \quad (2.79)$$

The origin and mechanisms of the OHE are still actively discussed. Most interestingly, it has been shown in Ref. [23] that SOC is *not* necessary for the OHE and that the OHE is allowed in nonmagnetic, centrosymmetric systems (e.g. a simple cubic lattice), where the SHE is forbidden without SOC [17]. In fact, therein it was demonstrated that the SHE is generated from the OHE through SOC. Thus, orbital currents are indeed more fundamental since they may be interpreted as a ‘new’ source for spin currents. This makes the OHE and orbital currents highly attractive for orbitronic devices [21]. In orbitronics one can thereby build on more materials, where strong SOC is not essential anymore, as it would be the case for the generation of large spin currents for spintronics devices.

In many studies, it was claimed that the existence of the OHE relies on hybridization of specific atomic orbitals [21, 23–27, 141–144]. The above description of the superposition of cubic harmonic orbitals to form spherical harmonics creates the OAM of a wave packet at a specific atomic site which can be transported as an orbital current. This is known as the atomic center approximation (ACA) which considers only *intra*-atomic contributions and has been used in the previously mentioned studies. In this case, the matrix elements of the OAM operator entering the orbital-current operator in Eq. (2.79) are constant and given by the expressions derived in Sec. 2.1 [Eq. (2.25) for p orbitals]. The ACA yields suitable results for systems with (partially) occupied, but strongly localized d or f orbitals like in magnetic transition metals. However, as already pointed out by Go *et al.* [23, 24, 146], the ACA is incomplete and the authors highly encouraged future investigations to apply the modern formulation of orbital magnetization [147–151]. Within the latter approach, one takes into account the fact that an OAM may also be carried by motion of the Bloch wave packet between atomic sites — regardless of the orbital composition [112].

Recently, these *inter*-atomic contributions to the OHE were included by Pezo *et al.* [28]. A detailed derivation of the following expressions can be found in their publication. Based on the modern formulation of orbital magnetization, they showed that the matrix elements of the orbital-current operator [Eq. (2.79)]

$$\begin{aligned} \langle u_\nu(\mathbf{k}) | \Lambda_x^z | u_\mu(\mathbf{k}) \rangle = & \frac{1}{2} \sum_\alpha [\langle u_\nu(\mathbf{k}) | v_x | u_\alpha(\mathbf{k}) \rangle \langle u_\alpha(\mathbf{k}) | L_z | u_\mu(\mathbf{k}) \rangle \\ & + \langle u_\nu(\mathbf{k}) | L_z | u_\alpha(\mathbf{k}) \rangle \langle u_\alpha(\mathbf{k}) | v_x | u_\mu(\mathbf{k}) \rangle], \end{aligned} \quad (2.80)$$

that enter the orbital Berry curvature [Eq. (2.78)], have to be computed from the eigenstates [28, 145]. Herein, the matrix elements of the orbital angular momentum are given by

$$\begin{aligned} \langle u_\nu(\mathbf{k}) | L_z | u_\alpha(\mathbf{k}) \rangle = & -i \frac{e\hbar^2}{4g_L\mu_B} \sum_{\beta \neq \nu, \alpha} \left(\frac{1}{\varepsilon_\beta(\mathbf{k}) - \varepsilon_\nu(\mathbf{k})} + \frac{1}{\varepsilon_\beta(\mathbf{k}) - \varepsilon_\alpha(\mathbf{k})} \right) \\ & \times (\langle u_\nu(\mathbf{k}) | v_x | u_\beta(\mathbf{k}) \rangle \langle u_\beta(\mathbf{k}) | v_y | u_\alpha(\mathbf{k}) \rangle - \langle u_\nu(\mathbf{k}) | v_y | u_\beta(\mathbf{k}) \rangle \langle u_\beta(\mathbf{k}) | v_x | u_\alpha(\mathbf{k}) \rangle) \end{aligned} \quad (2.81)$$

and do not only comprise the diagonal elements, but also the *off-diagonal* elements which are essential according to the modern formulation of orbital magnetization. In publication [OB3] (see Sec. 4.3), we introduce the nonmagnetic kagome lattice, where only s orbitals are assumed, as a minimal model for the OHE based on the approach derived by Pezo *et al.*. However, we corrected a small mistake in their derivation in Eq. (2.81), and replaced ‘ Im ’ (which determines the imaginary part of the following expression) by the factor ‘ $-i$ ’.

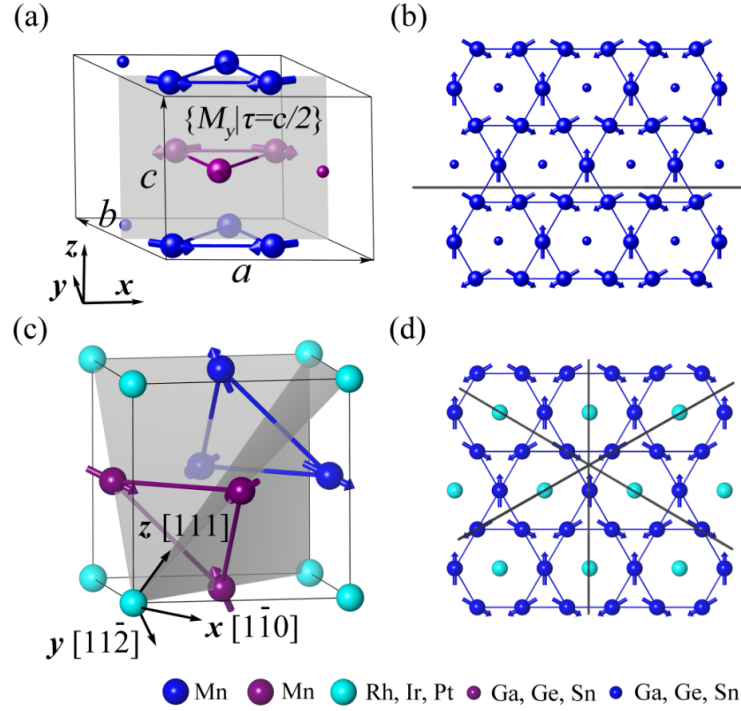


Figure 5: **Crystalline and magnetic structures of manganese compounds.** Arrows indicate the magnetic moments of Mn atoms and gray planes and lines represent respective mirror planes. (a) The lattice in the family of Mn_3Y ($Y=\text{Ga}, \text{Ge}, \text{Sn}$) is hexagonal where the Mn atoms arrange in kagome sublattices that are stacked along $[0001]$ which is the z axis. (b) One Mn_3Y kagome sublattice with a noncollinear antiferromagnetic order formed by the magnetic moments of Mn. (c) In contrast, Mn_3X ($X=\text{Rh}, \text{Ir}, \text{Pt}$) compounds are crystallizing in a face-centered cubic (fcc) lattice with X atoms located at the corners and Mn atoms at the face-center sites. Kagome sublattices are formed by Mn atoms as well, but in the (111) planes and stacked along $[111]$. (d) The antiferromagnetic order on the Mn_3X kagome sublattice has a different chirality than the one in (b), which is explained in more detail below (cf. Fig. 6 in Sec. 2.4). Whole figure: Reprinted (figure) with permission from Y. Zhang *et al.*, *Physical Review B* **95**, 075128 (2017); Ref. [15]; Strong anisotropic anomalous Hall effect and spin Hall effect in the chiral antiferromagnetic compounds Mn_3X ($X = \text{Ge}, \text{Sn}, \text{Ga}, \text{Ir}, \text{Rh}, \text{and Pt}$). Copyright (2017) by the American Physical Society.

2.4 Properties of the investigated kagome magnets

In the introduction, two materials have been mentioned in the context of theoretical prediction [13] and experimental confirmation [18] of the anomalous Hall effect in noncollinear antiferromagnets: Mn_3Ir and Mn_3Sn , respectively. These materials are both constituted of layered two-dimensional sublattices, namely ‘kagome’ lattices, that are subject to the first section in the cumulative part of this thesis (Sec. 4). This kagome lattice has been observed in several materials including Fe_3Sn_2 [152, 153] or $\text{Co}_3\text{Sn}_2\text{S}_2$ [154, 155], which are known as ferromagnetic ‘kagome magnets’, and the chiral antiferromagnets Mn_3Z [13, 15, 18, 19]. The latter can be separated into two classes — Mn_3X and Mn_3Y compounds — since they have different crystallographic structures *and* different magnetic textures (cf. Fig. 5). In the following, the kagome lattice and magnetic properties of its magnetic order are described. Besides, the model Hamiltonian utilized in publications [OB1, OB2] and [OB3], is introduced as well.

The kagome lattice. The space groups of Mn_3Y ($Y=\text{Ga, Ge, Sn}$) and Mn_3X ($X=\text{Rh, Ir, Pt}$) are $P6_3/mmc$ and $Pm\bar{3}m$, respectively [15]. These materials have in common that Mn atoms form the kagome sublattice [Fig. 5 (b) and (d)], but in different crystallographic planes. Thus, the kagome sublattices are stacked along different directions: Mn_3Y has a hexagonal lattice where the stacking of the kagome sublattices is an AB-AB sequence along [0001] [panel (a)]. In the case of the face-centered cubic (fcc) Mn_3X , the kagome sublattices are stacked along [111] according to ABC-ABC [panel (c)].

The kagome sublattice is a hexagonal lattice with three basis atoms per unit cell that form an equilateral triangle. Consequently, the reciprocal lattice is hexagonal as well, and the first BZ is a hexagon with high-symmetry points Γ , M and K. In Sec. 4, the focus is on the two-dimensional kagome lattice (located in the xy plane) and coupling to adjacent planes is neglected. Thus, a restriction to 2D systems reduces the computational effort enormously.

As visible in Fig. 5 (b) and (d), in both Mn_3Y and Mn_3X , the magnetic moments of the Mn atoms form a coplanar noncollinear antiferromagnetic order, but with a different vector spin chirality [cf. Eq. (2.89)] which will be explained in more detail below. All of these chiral antiferromagnets have high transition temperatures ranging from 365 K (Mn_3Ge) to 960 K (Mn_3Ir), which are all well above room temperature (cf. Tab. I in Ref. [15]). The stability of the magnetic order at room temperature originates from an interplay of strong magnetic anisotropy and coupling between the kagome planes [13]. Hence, they are interesting for antiferromagnetic spintronics applications [2, 156]. For example, Mn_3Ir is already used in spin-valve devices, i.e. for read heads in hard-disc drives and in magnetic sensors [2]. As described before, the AHE and SHE are widely exploited in spintronics and for both families Mn_3X and Mn_3Y large intrinsic anomalous and spin Hall effects have been predicted [13, 15, 17]. However, only in Mn_3Y the AHE ($Y=\text{Sn}$ [18], Ge [19]) and the SHE ($Y=\text{Sn}$ [20]) have been measured in experiments.

The model Hamiltonian. The model Hamiltonian used in publications [OB1, OB2] and [OB3] is adapted from Ref. [13], in which the AHE in a coplanar noncollinear kagome-antiferromagnet was predicted. It is denoted as double-exchange model or s - d model which simulates the interaction of the magnetic spin moment of the conduction electron (itinerant s electrons) with a magnetic texture (formed by d magnetic moments) localized at the atomic sites. Furthermore, spin-orbit interaction (SOC) is also taken into account. In second quantization, the full Hamiltonian reads

$$\mathcal{H} = \mathcal{H}_{\text{kin}} + \mathcal{H}_Z + \mathcal{H}_{\text{SOC}} \quad (2.82)$$

$$\mathcal{H}_{\text{kin}} = t \sum_{\langle i,j \rangle} \sum_{\sigma} a_{i,\sigma}^{\dagger} a_{j,\sigma} \quad (2.83)$$

$$\mathcal{H}_Z = m \sum_i \sum_{\sigma,\sigma'} a_{i,\sigma}^{\dagger} (\mathbf{m}_i \cdot \boldsymbol{\sigma})_{\sigma\sigma'} a_{i,\sigma'} \quad (2.84)$$

$$\mathcal{H}_{\text{SOC}} = i\lambda \sum_{\langle i,j \rangle} \sum_{\sigma,\sigma'} a_{i,\sigma}^{\dagger} (\mathbf{n}_{ij} \cdot \boldsymbol{\sigma})_{\sigma\sigma'} a_{i,\sigma'}. \quad (2.85)$$

The first term is the kinetic energy \mathcal{H}_{kin} , where $a_{i,\sigma}^{\dagger}$ and $a_{i,\sigma}$ are the creation and annihilation operators of an electron at site i with spin σ , respectively. $\sum_{\langle i,j \rangle}$ implies a restriction to nearest-neighbor hopping between sites i and j with hopping energy t . Besides, m in \mathcal{H}_Z is the strength of the onsite Hund's coupling between the spin moment of the conduction electron and the magnetic texture $\{\mathbf{m}_i\}$. As demonstrated in Refs. [13, 17, 99], the transport properties depend on the symmetry of the various magnetic textures; more details on the magnetic configurations entering \mathcal{H}_Z will be explained below.

Instead of using the conventional $\mathbf{L} \cdot \mathbf{S}$ form of SOC, as described in Sec. 2.1 [Eq. (2.26)], Eq. (2.85)

can be identified with SOC (strength λ) as well, and turns out to be advantageous for the investigation of kagome materials. The SOC term \mathcal{H}_{SOC} was first introduced in similar form in Ref. [96], in which the quantum spin Hall effect in graphene was predicted. Later, it was adapted in Ref. [13], in which the AHE in the coplanar noncollinear antiferromagnet Mn_3Ir was predicted. The vectors \mathbf{n}_{ij} are displayed in Fig. 1 of Ref. [OB1]. They are anticlockwise orthogonal to the hopping vectors \mathbf{R}_{ij} that connect sites i and j and were defined in Ref. [13]. Thus, in a kagome lattice, the set of vectors $\{\mathbf{n}_{ij}\}$ account for the different environments of nearest-neighbor hopping (left or right hand) [13].

Classification of the magnetic textures. In the publications [OB1] and [OB2] presented in Sec. 4, kagome lattices with several magnetic configurations are investigated. They have different properties, and thus are important for the Hamiltonian's symmetry. Therefore, it is helpful to introduce quantities that describe the kagome magnets.

Since the s - d model comprises a subset of a full Hamiltonian, only the relevant bands near the Fermi level are considered, instead of taking into account all energy bands. Besides, the magnetic texture $\{\mathbf{m}_i\}$ entering the Hamiltonian is assumed to be fixed and formed by energetically lower states. Thus, two magnetic textures have to be distinguished in this minimal model. First of all, a 'spin texture' is formed in reciprocal space by the spin magnetic moments of the itinerant s electrons. It depends on the band index ν and is given by the spin-expectation value

$$\langle \mathbf{S}_\nu(\mathbf{k}) \rangle = \langle u_\nu(\mathbf{k}) | \boldsymbol{\Sigma} | u_\nu(\mathbf{k}) \rangle. \quad (2.86)$$

The vector $\boldsymbol{\Sigma} \equiv (\Sigma^k)$ can be constructed from the vector of Pauli matrices $\boldsymbol{\sigma} = (\sigma^k)$ and consists of diagonal matrices $\Sigma^k = \text{diag}(\sigma^k, \dots, \sigma^k)$. Besides, the 'fixed magnetic texture' is a real-space texture which is described in more detail, subsequently. It is formed by the d -magnetic moments $\{\mathbf{m}_i\}$ at the Mn sites i and is characterized in spherical coordinates,

$$\mathbf{m}_i = (\cos(\phi_i) \sin(\theta), \sin(\phi_i) \sin(\theta), \cos(\theta)) \quad (i = 1, 2, 3). \quad (2.87)$$

Here, it is assumed that for every configuration all magnetic moments have the same magnitude $|\mathbf{m}_i| \stackrel{!}{=} 1$ and the same out-of-plane component $m_{i,z} = \cos(\theta)$, i.e. they have the same azimuthal angle $\theta \equiv \theta_1 = \theta_2 = \theta_3$ [cf. Fig. 6 (a)]. Consequently, coplanar magnetic textures are classified by $\theta = 90^\circ$.

Another important quantity, that has already been mentioned in Sec. 2.3 in the context of the topological Hall effect, is the scalar spin chirality [103–108]

$$\chi_S \equiv \mathbf{m}_i \cdot (\mathbf{m}_j \times \mathbf{m}_k), \quad (2.88)$$

where $\mathbf{m}_{i,j,k}$ denote three neighboring magnetic moments. Obviously, χ_S can be nonzero for noncoplanar magnetic textures (here $\theta \neq 90^\circ$), but vanishes for coplanar and collinear configurations. In the case of coplanar configurations, another quantity is defined as in Ref. [99], namely the vector spin chirality

$$\boldsymbol{\kappa} \equiv \frac{2\sqrt{3}}{9} \sum_{\langle ij \rangle} (\mathbf{m}_i \times \mathbf{m}_j) \cdot \mathbf{e}_z. \quad (2.89)$$

Herein, the sum is restricted to nearest neighbors.

Fig. 6 displays four coplanar magnetic textures, where the inplane-orientation of neighboring atoms differs by 120° and azimuthal angles are fixed at $\theta = 90^\circ$. However, the configurations have a different vector spin chirality: $\boldsymbol{\kappa}$ in Eq. (2.89) is normalized such that 'right-hand' and 'left-

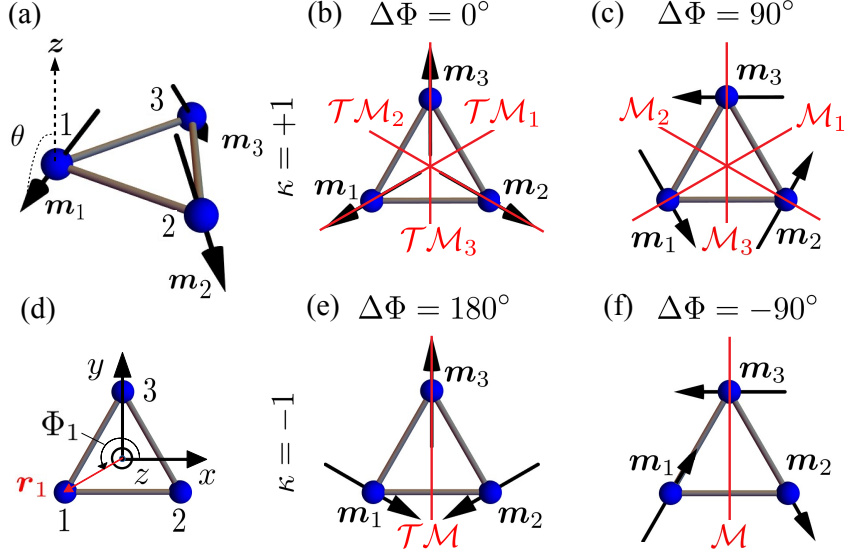


Figure 6: **Different magnetic textures on the kagome lattice.** Black arrows indicate the local magnetic moments m_i at the atomic sites i . (a) Noncoplanar texture with equal azimuthal angles θ of each magnetic moment. (b), (c) and (e), (f) coplanar configurations with a positive and a negative vector spin chirality [$\kappa = +1$ and $\kappa = -1$], respectively. These magnetic textures are characterized by an inplane offset angle $\Delta\Phi$ as indicated above the cartoons. (b) is denoted as ‘radial’ and (c) as ‘toroidal’ phase. Red lines indicate the symmetry planes (\mathcal{M} : mirror reflection or \mathcal{TM} : a combination of \mathcal{M} with time reversal \mathcal{T}). (d) illustrates the polar angle Φ_1 of the position vector r_1 (red) that is used in Eq. (2.90). Panels (a)-(c), (e) and (f) are taken from publication [OB1].

hand’ magnetic textures in Fig. 6 are characterized by $\kappa = +1$ and $\kappa = -1$, respectively. Thereby, the inplane-orientation (polar angles ϕ_i) of the local magnetic moments $\{m_i\}$ can be expressed as

$$\phi_i = \kappa\Phi_i + \Delta\Phi, \quad (2.90)$$

with Φ_i as the polar angle of the position vector r_i that is pointing from the center of the unit cell (i.e. from the center of the triangle) to atom i [cf. Fig. 6 (d)]. Hence, the inplane orientation of the noncollinear magnetic textures in Fig. 6 can be specified solely by one ‘inplane offset angle’ $\Delta\Phi$ and the vector spin chirality κ .

Panels (b) and (c) show two arrangements with a positive vector spin chirality, but different inplane orientations. In the antiperovskites Mn_3ZN ($Z=\text{Ni, Ga, Zn, Sn, Ag, Rh, Pt}$) [157, 158] and in Mn_3X materials ($X=\text{Rh, Ir, Pt}$) [159], two magnetic orders with $\kappa = +1$ have been found. In contrast, panels (e) and (f) show two configurations with a negative vector spin chirality ($\kappa = -1$) that have been observed in Mn_3Y ($Y=\text{Ga, Ge, Sn}$) compounds for which the AHE in a noncollinear antiferromagnet has been confirmed experimentally [18, 19, 160]. The arrangement in which all magnetic moments are pointing away from the center of the unit cell [panel (b)] is denoted here as ‘radial’ ($\Delta\Phi = 0^\circ$). A simultaneous anti-clockwise rotation of all magnetic moments by 90° around the z axis yields a configuration that is called ‘toroidal’ ($\Delta\Phi = 90^\circ$). In contrast to the radial texture, it has a nonzero toroidal moment $t = \frac{g\mu_B}{2} \sum_i r_i \times m_i$, where m_i is localized at r_i (position vector of atom i with respect to the center of the unit cell) [161].

As indicated by red lines, the toroidal arrangement has three mirror symmetry planes \mathcal{M} , whereas the radial texture has three symmetry planes \mathcal{TM} where mirror reflection \mathcal{M} is combined with time reversal \mathcal{T} [99]. The configurations with $\kappa = -1$ have only one symmetry plane

each ($\mathcal{T}\mathcal{M}$ and \mathcal{M}) and are briefly discussed in Ref. [OB1], but the focus in [OB1] and [OB2] is put on magnetic textures with $\kappa = +1$ (Sec. 4). SOC as considered in Eq. (2.85) breaks the $\mathcal{T}\mathcal{M}$ symmetry. This allows for non-vanishing values of the Berry curvature and thus an AHE which is the integral over the Berry curvature [13, 14]. In contrast, the \mathcal{M} symmetry cannot be broken by SOC, which renders the AHE zero due to a vanishing Berry curvature [99]. However, a non-vanishing spin Berry curvature, which gives rise to the SHE for these coplanar noncollinear configurations, can be obtained, even though SOC is neglected [17].

In publications [OB1] and [OB2], we go beyond symmetry arguments and reveal microscopic mechanisms for the predicted AHE and SHE in these noncollinear kagome antiferromagnets. Furthermore, in publication [OB3], we restrict the discussion to the nonmagnetic kagome lattice: we investigate the OHE and establish an alternative mechanism for orbital transport.

2.5 Experimental aspects

At the end of this section, some remarks about experimental techniques that can be used for studying the presented (Hall) effects are summarized.

Measurement of the AHE. An experimental technique to measure the ordinary Hall effect as well as the anomalous and topological companions, will be briefly described mainly following Ref. [162]. Since the AHE has been known for more than 100 years, experiments have been performed for a wide range of materials (for a review see e.g. Refs. [11, 163]). These comprise works on $3d$ transition metals and respective oxides, complex oxide ferromagnets, and ferromagnetic semiconductors. And very recently, the AHE has also been measured in Mn_3X compounds [18, 19, 162, 164, OB6].

Typically, the resistivity $\rho = \sigma^{-1}$ is used to characterize the electric transport [cf. (2.54)]. In experiments with a so-called ‘Hall-bar geometry’, one can determine a longitudinal ρ_{xx} and a transverse resistivity ρ_{xy} by measuring the voltage parallel and perpendicular to a constant electric current I_x (applied along the x direction) as a function of an external magnetic field [162]. In a conventional Hall-bar geometry (located in the xy plane), the transverse Hall voltage U_y is measured as a response to I_x in dependence of B_z (perpendicular to the Hall bar). For the ordinary Hall effect, the Hall signal depends linearly on the magnetic field, whereas the dependence for the AHE is nonlinear and shows a hysteresis. The Hall conductivity can then be calculated as $\sigma_{xy} = \rho_{xy}/(\rho_{xx})^2$, which is typically much larger for the anomalous than for the conventional Hall signal.

Measurement of the SHE. For the AHE, one is able to measure the voltage drop due an imbalance of spin \uparrow and \downarrow electrons that accumulate at opposite edges of the Hall bar. However, in a normal metal, an equal number of \uparrow and \downarrow electrons are deflected to opposite edges of the sample [cf. Sec. 2.3]. Thus, a voltage drop is absent and the above setup cannot be used for measuring the SHE. Since the SHE has become a widely explored phenomenon, many techniques have been used for the detection of the SHE in different materials. A broad review of experimental techniques and results can be found for example in Refs. [1, 12] and a few aspects are listed, below.

The first concepts to measure the SHE, which was predicted five decades ago [129, 130], were introduced more than 20 years ago, and followed two ‘strategies’ that relied on extrinsic scattering events and electric detection. First, it was suggested to probe the SHE via its inverse effect: the SHE-generated spin current is injected into an attached layer, in which it is converted back to a charge current that can be detected electrically [124]. The experimental realization of this method took ten years and was performed in a nonmagnetic HgTe nanostructure [165]. Another approach was proposed in Ref. [125], where the idea is to detect the spin accumulation at the

edge by attaching a ferromagnetic sample to the nonmagnetic material. This method requires a measurement of the electrochemical potential (at the ferromagnetic electrode) that depends on the relative orientation of the spins (accumulating in the nonmagnet) and the magnetization direction of the ferromagnet [1]. The first experimental observation was achieved in a metallic junction composed of ferromagnetic permalloy (Py) and nonmagnetic Pt [166].

The study of the intrinsic contribution to the SHE started also 20 years ago. Early theoretical studies [126, 127] predicted experiments with a focus on semiconductors and suggested to take advantage of the optical activity. Shortly afterward, the magneto-optical Kerr effect and circularly polarized electroluminescence were used to measure the SHE in the semiconductors GaAs and InGaAs [167], and in p-n diodes composed of (Al,Ga)As/GaAs heterostructures doped with Si and Be [168].

The interaction of electromagnetic radiation with magnetic materials gives rise to magneto-optical effects that have their origin in Faraday. In 1845, he measured a rotation of the polarization of linearly polarized light while it was propagating through a medium parallel to an applied magnetic field. In contrast to this magneto-optical Faraday effect (MOFE), where radiation is transmitted, the polarization can also be rotated when radiation is reflected. The latter phenomenon has been observed by Kerr in 1877, and nowadays it is denoted as ‘magneto-optical Kerr effect’ (MOKE) [99, 169]. These effects can be explained by considering linearly polarized light as a superposition of two circularly polarized (partial) waves with opposite helicities: the applied magnetic field leads to a difference in the refractive indices ($n_{L/R}$) for left- and right-circularly polarized waves, $\Delta n = n_L - n_R$ [169]. Both partial waves (frequency ω) propagate through the medium over a distance L . The result is a phase difference $\Delta\theta = \Delta n \omega L/c$ of the two circularly polarized waves, which manifests itself in a rotation of the linearly polarized light by an angle $\Delta\theta/2$. In short, a time-reversal breaking magnetic field or a magnetization is the cause for the phase shift between the circularly polarized waves which results in a rotation of the linearly polarized light’s polarization from the initial direction. Thus, MOKE is a useful tool to detect the accumulation of angular momentum at edges or surfaces. However, spin *and* orbital angular momenta sum up to the total angular momentum which would be detected via MOKE measurements. Hence, the disentanglement of spin and orbital contributions is complicated, since the SHE stems from the OHE which is partially converted into the SHE via SOC, as explained before [23].

Measurement of the OHE - the problem of separating spin and orbital contributions. Since the OHE is predicted to be large in systems with negligible SOC, MOKE spectroscopy could be used to detect the OHE via the accumulation of orbital angular momentum at the edges, which was achieved recently in Ti [170]. In order to separate spin and orbital signals in materials with stronger SOC, where the OHE is accompanied by the SHE, one could perform X-ray magnetic circular dichroism (XMCD) measurements after MOKE has been done.

Magnetic dichroism effects, that arise from X-ray spectroscopy, can be used to measure magnetic properties such as the magnetic moment [38, 39, 162, 171]. The X-ray radiation excites electrons from the ground state (occupied orbitals) into unoccupied states, which is described by transition matrix elements, as will be described in detail in Sec. 3.3. Thereby, characteristic energies are absorbed by the electrons which allows for identifying different magnetic states of the atoms in the sample. The probability for dipole transitions depends on the occupation of the final state, on selection rules ($\Delta L = \pm 1$; $\Delta m_L = 0, \pm 1$; $\Delta S = 0$) due to the dipole approximation, and on the energy difference (between the initial and the final state), which has to match the X-ray photon energy [162]. The intensity of the energy absorption depends strongly on the chosen polarization of the radiation leading to dichroic effects, as is measured by X-ray absorption spectroscopy (XAS). The contrast in absorption can be very pronounced if magnetic samples are illuminated with either left- or right-circularly polarized X-rays, which is denoted as X-ray

magnetic circular dichroism (XMCD). Besides, linearly polarized X-ray excitation by radiation with polarization perpendicular to each other yields dichroic effects as well. Hence, one speaks of X-ray magnetic linear dichroism (XMLD), which can be utilized to detect domain structures in collinear AFMs. The observed contrast arises from a magnetization reversal of the sample while the polarization is fixed or vice versa [39]. The obtained XAS and XMCD signals allow to determine values for both spin and orbital angular momenta by exploiting so-called ‘XMCD sum rules’ (for details see Ref. [171]).

Another proposal suggests detecting the orbital current by injection into an adjacent ferromagnetic material, in which an orbital torque on the magnetic moments is created, similar to the situation where a spin-transfer torque arises from spin injection [24]. Yet, the detection of orbital currents and the separation from spin currents remains challenging; some experimental methods are reviewed in Ref. [21].

Time-resolved measurements. Up to now, only steady-state phenomena have been taken into account. However, as motivated in the introduction, the field of ultrafast magnetization dynamics gained great interest during the last three decades. In order to detect the laser-induced effects with subpicosecond resolution, so-called ‘pump-probe’ techniques have been developed [40, 172].

A short optical ‘pump’ pulse with high intensity induces the magnetization dynamics by generating photoelectrons in the excited material. This changes the reflection or transmission properties of another, less intense, ‘probe’ pulse that also illuminates the sample and has a controllable time delay with respect to the pump pulse. Measuring this change as a function of the delay between the two pulses allows for reconstructing the change in magnetization and thus the magnetization dynamics. Temporal resolution and sensitivity to spin and orbital degree of freedom of such experiments are governed by the duration and the energy spectrum of the probe pulse, respectively. One can distinguish different spectral regimes with particular sensitivities – optical, ultraviolet (UV) and X-ray – that are briefly summarized below; for a review see Ref. [40] and references therein.

- Interaction with optical pulses leads to the linear magneto-optical effects, such as the above-described MOKE and MOFE, which allow for indirectly probing spin ordering [173, 174]. Also nonlinear effects like second-harmonic generation (SHG), where light with a doubled optical frequency is emitted from the excited material, can be used to probe magnetization. However, the SHG is only allowed in systems without inversion symmetry, and thus this method is widely used for the detection of surface and interface magnetization [40].
- Excitation with UV probe pulses is used for photoelectron emission microscopy (PEEM) or spectroscopy: if the photon energy is larger than the difference of vacuum and Fermi energy, electrons are emitted. With angle-resolved photoemission spectroscopy (ARPES) one has access to energy and momentum, allowing for mapping the electronic structure [175]. With some experimental ARPES setups one can also detect the spin polarization of photoelectrons [176]. Consequently, one can directly measure the spin distribution [40].
- Finally, X-ray radiation allows for the detection of time-resolved magnetic dichroism effects (XMCD and XMLD) [177, 178] which can be utilized for probing magnetization similar to the magneto-optical effects. However, XMCD and XMLD are more challenging in experiments, but provide elemental and chemical specificity as well as selective access to spin and orbital angular momentum.

In this section, a theoretical description of steady-state transverse transport based on tight-binding calculations has been presented. The different Hall effects are described by respective conductivity tensors σ that relate the responding currents $\mathbf{j} = \sigma \mathbf{E}$ with the applied homogeneous electric

field [11, 12, 23]. Although there have been approaches where such response tensors are described in the time domain, access to spatial resolution is hardly possible. Besides, the approach of Sec. 2 is only valid for bulk systems. Thus, the method is not appropriate for a description of ultrafast magnetization dynamics in finite systems (like heterostructures), where surface and interface effects play an important role. In the next chapter, the theoretical aspects of the computational framework `EVOLVE` [54], are presented. This effective one-electron density-matrix approach allows for simulating the laser-induced ultrafast electron dynamics of such systems, and it provides access to a number of observables, such as spin and orbital angular momenta and their currents with both atomic and femtosecond resolution.

3 Simulation of ultrafast laser-induced electron dynamics

In the previous section, the necessary background for understanding different types of transverse currents has been presented; the results will be discussed in the first section in the cumulative part of the thesis (Sec. 4). However, that approach deals with linear responses to an applied homogeneous electric field, and it is limited to bulk systems without defects. Furthermore, the spatial and temporal distribution of observables is lacking.

This section lays the foundation for the second section in the cumulative part of this thesis (Sec. 5), in which the focus is on the investigation of electron dynamics triggered by ultrafast laser pulses. Of interest are finite systems, such as heterostructures, allowing to address the effect of inhomogeneities, like surfaces and interfaces. Therefore, the tight-binding approach has to be considered in real space, as is presented briefly in Sec. 3.1. In Sec. 3.2, the time evolution of the system in an effective one-electron density matrix approach is introduced. Sec. 3.3 presents an elegant way to describe the perturbation due to excitation with femtosecond laser pulses: optical transition matrix elements enter a unitary transformation of the unperturbed (real-space) tight-binding Hamiltonian. Afterward, expressions for the computation of observables with atomic and femtosecond resolution, in particular spin and orbital angular momenta and their respective currents, are derived in Sec. 3.4. The section concludes (Sec. 3.5) with a discussion of the limitations and advantages of the computational framework `EVOLVE` [54]. It is used for the simulations published in the publications [OB4] and [OB5] (cf. Sec. 5).

3.1 Real-space tight-binding approach for finite systems

In Sec. 2.1, the ‘conventional’ tight-binding model has been derived. It is in reciprocal space because one assumes periodicity, i.e. periodic boundary conditions in all directions (in real space), and thus, the Bloch theorem is fulfilled. However, this approach cannot be used to investigate finite systems with defects or other inhomogeneities, like surfaces or interfaces, which play an important role for the electron dynamics, as will be presented in publications [OB4] and [OB5]. An inhomogeneity breaks the translation invariance – at least in one direction along which one *cannot* apply periodic boundary conditions anymore [6]. Thus, the Bloch theorem is not valid and eigenenergies and eigenfunctions of the Hamiltonian do *not* depend on the crystal momentum \mathbf{k} . Therefore, the effective one-electron Schrödinger equation (2.1) of the previous section now reads $H(\mathbf{r})\varphi_n(\mathbf{r}) = \varepsilon_n\varphi_n(\mathbf{r})$, and one can derive a real-space tight-binding model in analogy to the reciprocal-space approach presented in Sec. 2.1. The main results are briefly summarized, below. In order to stress the difference to the reciprocal-space approach, which has the goal to compute the *band* structure $\varepsilon_\nu(\mathbf{k})$ with band index ν , in the real-space approach the index labeling different states of the Hamiltonian will be denoted with n instead of ν . The calculated eigenenergies ε_n form the *electronic* structure with discrete energy levels and without dispersion.

In this approach, one considers a finite cluster of atomic sites as a supercell that is composed of (small) unit cells [54]. The latter form (separate) blocks in real space and one can apply individual boundary conditions along different directions. One is confronted with either a ‘closed’ circuit with periodic boundary conditions or an ‘open’ circuit geometry without periodicity along the respective direction. This allows to simulate heterostructures, chains or thin films as it has been done in some works of our group [54, OB4, OB5, OB7, OB8] with the computational framework `EVOLVE`, which is briefly explained later in this section.

Due to the broken translation invariance, the electron wave functions do not fulfill the Bloch theorem. Thus, the LCAO ansatz for the solution of the Schrödinger equation is then given by

$$\varphi_n(\mathbf{r}) = \frac{1}{\sqrt{N}} \sum_{\mathcal{M}, \mathbf{R}} c_{n, \mathbf{R}}^{\mathcal{M}} \phi_{\mathcal{M}}(\mathbf{r} - \mathbf{R}). \quad (3.1)$$

Inserting the ansatz into the Schrödinger equation, multiplying with $\phi_{\mathcal{M}'}^*(\mathbf{r} - \mathbf{R}')$ from the left and integrating afterward yields

$$\sum_{\mathcal{M}, \mathbf{R}} c_{n, \mathbf{R}}^{\mathcal{M}} \int \phi_{\mathcal{M}'}^*(\mathbf{r} - \mathbf{R}') H(\mathbf{r}) \phi_{\mathcal{M}}(\mathbf{r} - \mathbf{R}) d^3r = \varepsilon_n \sum_{\mathcal{M}, \mathbf{R}} c_{n, \mathbf{R}}^{\mathcal{M}} \int \phi_{\mathcal{M}'}^*(\mathbf{r} - \mathbf{R}') \phi_{\mathcal{M}}(\mathbf{r} - \mathbf{R}) d^3r. \quad (3.2)$$

Introducing another multi index $\alpha \equiv (\mathcal{M}, \mathbf{R})$ allows to define real-space overlap matrix elements

$$S_{\alpha', \alpha} \equiv S_{\mathcal{M}', \mathbf{R}'; \mathcal{M}, \mathbf{R}} = \int \phi_{\mathcal{M}'}^*(\mathbf{r} - \mathbf{R}') \phi_{\mathcal{M}}(\mathbf{r} - \mathbf{R}) d^3r \quad (3.3)$$

as well as real-space Hamilton matrix elements

$$H_{\alpha', \alpha} \equiv H_{\mathcal{M}', \mathbf{R}'; \mathcal{M}, \mathbf{R}} = \int \phi_{\mathcal{M}'}^*(\mathbf{r} - \mathbf{R}') H(\mathbf{r}) \phi_{\mathcal{M}}(\mathbf{r} - \mathbf{R}) d^3r. \quad (3.4)$$

With this, Eq. (3.2) becomes

$$\sum_{\alpha} H_{\alpha', \alpha} c_{n, \alpha} = \varepsilon_n \sum_{\alpha} S_{\alpha', \alpha} c_{n, \alpha}. \quad (3.5)$$

As before in Sec. 2.1, herein three-center integrals are neglected due to the assumption of strongly localized electrons and one is confronted again with a generalized eigenvalue problem. In matrix form, it reads $[\mathbf{H} - \varepsilon_n \mathbf{S}] \mathbf{c}_n = 0$, and in analogy, the matrices are $\mathbf{H} \equiv (H_{\alpha', \alpha})$ and $\mathbf{S} \equiv (S_{\alpha', \alpha})$, and the vector is given by $\mathbf{c}_n \equiv (c_{n, \alpha})$.

This equation can again be transformed to a conventional eigenvalue problem by Löwdin orthogonalization [70], where a diagonalization of H_0 , the unperturbed ground state Hamiltonian, yields the electronic structure and the eigenstates

$$[\mathbf{H}_0 - \varepsilon_n \mathbf{1}] \tilde{\mathbf{c}}_n = 0, \quad (3.6)$$

with $\mathbf{H}_0 \equiv \mathbf{S}^{-1/2} \mathbf{H} \mathbf{S}^{-1/2}$ and $\tilde{\mathbf{c}}_n \equiv \mathbf{S}^{1/2} \mathbf{c}_n$. In the results presented in Sec. 5 different setups are simulated.

In publications [OB4] and [OB5], face-centered cubic (fcc) films with a thickness of 40 atomic layers are investigated. These films are homogenous samples composed of Cu or Co, and a Co/Cu heterostructure (two blocks with 20 layers each). The primitive cell of an fcc lattice contains two basis atoms, such that each layer of a (100) film would contain one atom in its (2D) unit cell. Thus, in each simulated case, one fcc(100) sample has a depth of 40 layers. Consequently, one large supercell contains 40 atoms that form a zigzag chain in x -direction (open boundary conditions; cf. Fig. 1 in [OB4] and Fig. 1 [OB5]). Periodic boundary conditions are applied along the other two directions. For the chosen materials one can find lattice constants that slightly differ (0.36 nm for Cu [179] and 0.34 nm for fcc Co [180]). Consequently in practice, epitaxial growth of fcc Co on Cu(100) results in a slightly distorted geometry, where Co adopts the inplane fcc lattice of the Cu substrate, so that the Co films form a face-centered tetragonal lattice [181]. However, in the simulations with *EVOLVE*, only one lattice constant can be used; i.e. we assume identical lattice constants.

In order to describe the electronic structure of these samples s , p and d orbitals of Cu and Co enter H_0 according to the Slater-Koster formalism presented in Sec. 2.1. Numerical values for both materials are based on parameters that have been obtained by a fit to ab-initio calculations in Ref. [67]. Collinear magnetism is considered by an exchange splitting of the Slater-Koster parameters. For the Co atoms, this results in a ground state intrinsic spin and orbital angular

momentum pointing along z -direction for the chosen setups [182, 183]. Spin-orbit coupling, as derived in Ref. [90], is included in H_0 (cf. Eq. (2.26) for p -orbitals).

A simulation in `EVOLVE` starts with the determination of the chemical potential μ for the given number of electrons and the given temperature T . Each atom in the supercell provides a certain number of valence electrons (11 for Cu and 9 for Co [183]), and the chosen temperature is $T = 300$ K. These values, together with the eigenenergies ε_n of H_0 , determine the chemical potential. The eigenstates $|n\rangle$ of H_0 are then occupied according to the respective Fermi-Dirac distribution $f_D(\varepsilon_n, \mu, T)$. The occupation probabilities enter the diagonal elements of the density matrix (in the eigenstate basis), which is subject of the following subsection.

3.2 Density matrix and equation of motion

The diagonalization of the tight-binding Hamiltonian of the previous section yields a set of eigenenergies and eigenstates from which expectation values of observables can be computed. However, one can also use the density operator³ instead of the eigenstates, which is advantageous as will be explained below following Refs. [57, 58, 76, 184–186].

Pure and mixed states. In general, a quantum system which is described by an abstract Hilbert vector $|\psi\rangle$ can be in two different states: pure or mixed states. Let now \mathcal{O} be an operator with eigenvalues o_n and eigenstates $|n\rangle \equiv |\phi_n\rangle$ forming a normalized basis set; i.e. $\mathcal{O}|n\rangle = o_n|n\rangle$. By choosing this basis, one may express the state $|\psi\rangle = \sum_n c_n |n\rangle$ as a superposition of these eigenstates $|n\rangle$, where $|c_n|^2 = |\langle n|\psi\rangle|^2 \in [0, 1]$ is the probability of obtaining the value o_n while measuring \mathcal{O} . Only, if the system is prepared in a so-called ‘*pure*’ quantum state, one knows the *complete (quantum) information* about the system. Hence, it can be described by a *single* state; this could be for example the above superposition $|\psi\rangle = \sum_n c_n |n\rangle$ or a certain eigenstate $|\psi\rangle = |n\rangle$. This motivates to introduce the expectation value of \mathcal{O} as an averaged value obtained from a large number of measurements under identical conditions in order to account for the quantum mechanical uncertainty during the measuring process [184]

$$\langle \mathcal{O} \rangle = \sum_n o_n |c_n|^2 = \sum_n o_n \langle \psi | n \rangle \langle n | \psi \rangle = \sum_n \langle \psi | \mathcal{O} | n \rangle \langle n | \psi \rangle = \langle \psi | \mathcal{O} | \psi \rangle. \quad (3.7)$$

In the last step, the completeness relation $\mathbb{1} = \sum_n |n\rangle \langle n|$ has been exploited. If one is confronted with a *statistical ensemble* of such pure states, the system is in a so-called ‘*mixed*’ state. That means the information about the quantum system is incomplete due to a ‘*mixture*’ of pure states [185, 186]. In practice, where one deals with macroscopic objects of 10^{23} particles, it is impossible (and mostly unnecessary) to know everything about the entire system and only information about a subsystem is sufficient. In this case, the mixed state cannot be represented by one single state, but one may assume that each possible (pure) state $|\psi_i\rangle$ is realized with a probability p_i which requires $\sum_i p_i \stackrel{!}{=} 1$. Consequently, the expectation value above has to be averaged again statistically, which yields the following expression:

$$\langle \mathcal{O} \rangle = \sum_i p_i \langle \psi_i | \mathcal{O} | \psi_i \rangle = \sum_i p_i \left(\sum_n o_n |c_{n,i}|^2 \right) = \sum_n o_n \sum_i p_i w_{n,i} = \sum_n o_n w_n. \quad (3.8)$$

Herein, $w_n \equiv \sum_i p_i w_{n,i}$ is defined as the probability of finding the eigenvalue o_n when measuring \mathcal{O} at the *mixed* system state. $w_{n,i} \equiv |c_{n,i}|^2 = |\langle n | \psi_i \rangle|^2$ is the corresponding probability that the

³Sometimes the density operator is also called density matrix, although the latter is strictly speaking a matrix representation of the density operator in a specific set of eigenstates. Since the many-body problem for non-interacting electrons has been mapped to an effective single-particle problem, the density operator is an effective one-particle density operator.

system is in the *pure* system state $|\psi_i\rangle$ (and o_n is measured) [184–186]. Thereby, one finds

$$\langle \mathcal{O} \rangle = \sum_i p_i \sum_n o_n \langle \psi_i | n \rangle \langle n | \psi_i \rangle = \sum_n \sum_i p_i \langle \psi_i | \mathcal{O} | n \rangle \langle n | \psi_i \rangle = \sum_n \sum_i p_i \langle n | \psi_i \rangle \langle \psi_i | \mathcal{O} | n \rangle, \quad (3.9)$$

which allows us to define the density operator

$$\rho = \sum_i p_i |\psi_i\rangle \langle \psi_i|. \quad (3.10)$$

Properties of the density matrix. As explained above, in contrast to a pure state, a mixed quantum state *cannot* be represented by a single state due to missing information, and one has to use the density operator to cover both cases. A density operator approach is a very general description of a quantum system since ρ is composed of both Hilbert vectors $|\psi_i\rangle$, which encode the information about the quantum system, and probabilities p_i for the system being in state $|\psi_i\rangle$. This approach is very advantageous for several reasons; some important properties are summarized in the following [184–186].

First of all, instead of directly utilizing the eigenstates to compute the expectation value of an observable \mathcal{O} , one can use Eq. (3.9) and the definition of ρ , to obtain

$$\langle \mathcal{O} \rangle = \text{tr } \rho \mathcal{O}, \quad (3.11)$$

which has the advantage that the trace is invariant under basis transformations. From the definition of ρ it is clear that $\rho^\dagger = \rho$ since the $p_i \in [0, 1]$ are real numbers and the projection operator $|\psi_i\rangle \langle \psi_i|$ is hermitian. Consequently, ρ can be interpreted as a physical observable itself: for an arbitrary quantum state $|\phi\rangle$ it is

$$\langle \phi | \rho | \phi \rangle = \sum_i p_i \langle \phi | \psi_i \rangle \langle \psi_i | \phi \rangle = \sum_i p_i |\langle \phi | \psi_i \rangle|^2 \geq 0. \quad (3.12)$$

Thus, ρ is positive definite which ensures that the expectation value of ρ , which is the probability of finding the system in the state $|\phi\rangle$, can never be less than zero. If ρ is represented in the (normalized) eigenstate basis $\{|n\rangle\}$ of the observable \mathcal{O} the diagonal element p_i of ρ can be interpreted as the probability of measuring o_n in the mixed state. Furthermore, with $\mathcal{O} = 1$ it follows directly from Eq. (3.11) that $\text{tr } \rho = 1$, which is in agreement with the interpretation as probabilities (cf. $\text{tr } \rho = 1 \Leftrightarrow \sum_i p_i = 1$). As mentioned above, the density operator is also able to describe a pure state $|\psi\rangle = |\psi_i\rangle$ that is characterized by $p_i = 1$ for this *one* state $|\psi_i\rangle$ and $p_j = 0$ for all other states $|\psi_j\rangle$ due to complete knowledge about the system. In this case, the density operator reduces to $\rho = |\psi\rangle \langle \psi|$, and one finds for the squared density matrix ρ^2 that $\rho^2 = \rho$ and $\text{tr } \rho^2 = 1$, whereas for mixed states one finds $\rho^2 \neq \rho$ and $\text{tr } \rho^2 < 1$. Finally, in order to investigate the time evolution of observables, one has to propagate the density operator in time. Therefore, one can use the time-dependent Schrödinger equation $i\hbar |\dot{i}\rangle = H |i\rangle$ and express ρ in terms of the eigenstates $|i\rangle$ of H to derive the time evolution of ρ , which is described by the von Neumann equation [184, 185]

$$\dot{\rho} \equiv \frac{\partial \rho}{\partial t} = \frac{i}{\hbar} (\rho H - H \rho) = \frac{i}{\hbar} [\rho, H]_-. \quad (3.13)$$

Time evolution of a perturbed system. From now on, the density operator is time dependent:

$$\rho(t) = \sum_{n,m} |n\rangle p_{nm}(t) \langle m|. \quad (3.14)$$

Herein, in contrast to a diagonal element p_{nn} which is interpreted as occupation number of state $|n\rangle$, an off-diagonal element p_{nm} describes an interference or a coherent superposition of states $|n\rangle$ and $|m\rangle$ which can be generated by a perturbation, for example by excitation with a laser pulse. This will be explained in more detail in the next subsection and will be motivated briefly in the following.

As explained above, the time evolution of the density operator is governed by the von Neumann equation (3.13) which is also valid for the dynamics of time-dependent Hamiltonians $H(t)$ as considered in this work [184, 185]. Therefore, now H is decomposed into a constant part H_0 , the real-space tight-binding Hamiltonian of the previous subsection, and a time-dependent term $V(t)$ mimicking a weak perturbation. In Eq. (3.14), $\{|n\rangle\}$ is the set of eigenstates of H_0 (i.e. $H_0 |n\rangle = \varepsilon_n |n\rangle$) which are atomic orbitals of the atomic sites in the cluster in real space. Throughout this work, it is assumed that the Hilbert space is spanned by the eigenstates of H_0 . Thus, the (time-independent) eigenstates and eigenvalues of H_0 are taken into account throughout the time evolution. In this case, for the equation of motion $\dot{\rho}(t) = \frac{i}{\hbar}[\rho(t), H(t)]$ follows

$$\sum_{n,m} |n\rangle \dot{p}_{nm}(t) \langle m| = \frac{i}{\hbar} \sum_{n,m} [|n\rangle p_{nm}(t) \langle m|, H_0 + V(t)] \quad (3.15)$$

$$= \frac{i}{\hbar} \sum_{n,m} (\varepsilon_m - \varepsilon_n) |n\rangle p_{nm}(t) \langle m| + [|n\rangle p_{nm}(t) \langle m|, V(t)]. \quad (3.16)$$

Multiplication with $\langle k|$ from the left and with $|l\rangle$ from the right as well as introducing matrix elements $V_{ij}(t) \equiv \langle i|V(t)|j\rangle$ results in the equation of motion

$$\dot{p}_{kl}(t) = \frac{i}{\hbar}(\varepsilon_l - \varepsilon_k) p_{kl}(t) + \frac{i}{\hbar} \sum_m p_{km}(t) V_{ml}(t) - \frac{i}{\hbar} \sum_n V_{kn}(t) p_{nl}(t). \quad (3.17)$$

From this, one can see that the last two terms arising from the perturbation induce transitions between eigenstates which are also called coherences. In the next subsection expressions for these transition matrix elements will be derived.

3.3 Theoretical description of laser excitation

In the introduction, it was already explained that light-matter interaction offers new perspectives for modern spin-orbitronics. Ultrafast laser pulses allow for both high spatial and temporal resolution which has great potential for designing small devices with fast processing times [3, 29, 31–33, 40]. Laser excitation can lead to phenomena like ultrafast demagnetization [34, 44], all-optical switching [35–37] or ultrafast spin transport across interfaces of heterostructures [46–49].

Based on this motivation, this subsection explains how the laser-induced perturbation is modeled within the `EVOLVE` computer code. First, the electric dipole approximation is introduced. Afterward, it is demonstrated how the (minimal) coupling of the electron to electromagnetic radiation is used to derive the time-dependent Hamiltonian. Finally, explicit expressions for the dipole-transition matrix elements are derived.

Electric dipole approximation. This paragraph introduces the electric dipole approximation mainly following Ref. [6]. This approach is a simplification that accounts for the coupling of a particle with charge q to an electromagnetic field, which is defined via the electric scalar potential Φ and the magnetic vector potential \mathbf{A} , as $\mathbf{E} = -\nabla\Phi - \dot{\mathbf{A}}$ and $\mathbf{B} = \nabla \times \mathbf{A}$. Choosing the Coulomb gauge, $\nabla \cdot \mathbf{A} = 0$ and $\Phi = 0$, yields $\mathbf{E} = -\dot{\mathbf{A}}$. The interaction of an electron (charge $q = -e$) with the electric field enters the Hamiltonian via Peierls substitution [76, 80, 187]

$$\mathbf{p} \rightarrow \mathbf{p} - \frac{q}{c} \mathbf{A}, \quad (3.18)$$

which is also known as ‘minimal coupling’ [188]. If \mathbf{A} is time dependent, as in laser-excitation processes, and terms of order \mathbf{A}^2 are neglected, one can show that a time-dependent perturbation term $V(t) = -\frac{q}{m} \mathbf{A}(t) \cdot \mathbf{p}$ arises in Coulomb gauge [6]. Fermi’s golden rule tells that the probability for a transition from an initial state $|i\rangle$ to a final state $|f\rangle$ reads $p_{i \rightarrow f} \propto |\langle f|V(t)|i\rangle|^2$ with transition matrix elements $V_{if} = \langle f|V(t)|i\rangle$ of the perturbation term [cf. Eq. (3.17)]. An ansatz for the vector potential of a monochromatic laser is given by [189]

$$\mathbf{A}(\mathbf{r}, t) = \frac{A_0}{2} \mathbf{e} \exp \{i(\mathbf{k} \cdot \mathbf{r} - \omega t)\} + \text{c.c.}, \quad (3.19)$$

where A_0 is the amplitude of the laser’s vector potential, and \mathbf{e} , \mathbf{k} , and ω are the (unit vector of) polarization, propagation direction, and the carrier frequency of the laser, respectively. The spatial term in the above exponential is approximately given by $|\mathbf{k} \cdot \mathbf{r}| \approx \frac{2\pi}{\lambda} a_0 \ll 1$, since the Bohr radius $a_0 = 0.5$ nm is much smaller than typical wavelengths $\lambda \approx 10^3 \dots 10^4$ nm; note that the simulated finite samples (cf. Sec. 3.1 and publications [OB4] and [OB5]) have a size of a few nm. Consequently, one can expand the electromagnetic radiation in terms of multipoles (like it is known from classical electrodynamics) [189] and take into account only the dipole terms. This is achieved by expanding the exponentials in the above equation and considering the lowest order, i.e. $\exp \{\pm i(\mathbf{k} \cdot \mathbf{r})\} = 1 \pm i(\mathbf{k} \cdot \mathbf{r}) + \dots \approx 1$, which allows treating the vector potential as spatially constant. With this, the matrix elements above read

$$V_{if} = -\frac{A_0}{m} \cos(\omega t) \langle f|qe \cdot \mathbf{p}|i\rangle = i \frac{A_0}{\hbar} \cos(\omega t) (\varepsilon_i - \varepsilon_f) \langle f|qe \cdot \mathbf{r}|i\rangle, \quad (3.20)$$

where the momentum operator $\mathbf{p} = m\dot{\mathbf{r}}$ has been replaced by the commutator $\mathbf{p} = -m\frac{i}{\hbar}[\mathbf{r}, H_0]$ of the position operator \mathbf{r} and the unperturbed Hamiltonian H_0 [6, 186]. In summary, the dipole approximation allows for treating the vector potential as spatially constant and expressing the perturbation term as $V = q\mathbf{E} \cdot \mathbf{r}$ [6, 39, 190].

Minimal coupling in dipole approximation by unitary transformation. In the following, an elegant way to replace Peierls substitution [187] by a unitary transformation of the ground state Hamiltonian is explained following the derivation in Ref. [190], and references therein [191–194]. The starting point of the derivation is the equation [190, 194]

$$\exp(i f(\mathbf{r}, t)) g(\mathbf{r}, \tilde{\mathbf{p}}) \exp(-i f(\mathbf{r}, t)) = g(\mathbf{r}, \tilde{\mathbf{p}} - \nabla f(\mathbf{r}, t)). \quad (3.21)$$

One can define a scalar function χ via $\nabla \chi(\mathbf{r}, t) = \mathbf{A}(\mathbf{r}, t)$ which fulfills the Coulomb gauge $\nabla \cdot \mathbf{A} = \nabla \cdot (\nabla \chi) = 0$. As pointed out above, the spatial dependence of the vector potential is neglected. Furthermore, if the interaction between the electron and the laser's magnetic field are neglected (as will be discussed later in this section), one chooses

$$\chi(\mathbf{r}, t) \equiv \mathbf{A}(\mathbf{r} = \mathbf{0}, t) \cdot \mathbf{r} = \mathbf{A}_0(t) \cdot \mathbf{r}, \quad (3.22)$$

which is the dipole operator in length form [191]. With this, a choice for the function f entering Eq. (3.21) is given by

$$f(\mathbf{r}, t) = \frac{q}{c\hbar} \chi(\mathbf{r}, t) \quad \Rightarrow \quad \nabla f(\mathbf{r}, t) = \frac{q}{c\hbar} \mathbf{A}_0(t). \quad (3.23)$$

Consequently, one can define a unitary operator

$$U = U(\mathbf{r}, t) = \exp\left(i \frac{q}{c\hbar} \chi(\mathbf{r}, t)\right) = \exp(i f(\mathbf{r}, t)) \approx 1 + i f(\mathbf{r}, t) \quad (3.24)$$

[and $U^\dagger(\mathbf{r}, t) = \exp(-i f^*(\mathbf{r}, t))$] which allows for applying a unitary transformation to the unperturbed ground state Hamiltonian $H_0(\mathbf{r}, \tilde{\mathbf{p}})$ (with $\tilde{\mathbf{p}} = \frac{1}{\hbar} \mathbf{p} = -i\nabla$)

$$H_0(\mathbf{r}, \tilde{\mathbf{p}}) \rightarrow U(\mathbf{r}, t) H_0(\mathbf{r}, \tilde{\mathbf{p}}) U^\dagger(\mathbf{r}, t) = H(\mathbf{r}, \tilde{\mathbf{p}}, t). \quad (3.25)$$

In doing so, the time-independent Hamiltonian has been transformed to the time-dependent Hamiltonian $H(\mathbf{r}, \tilde{\mathbf{p}}) = H(\mathbf{r}, \tilde{\mathbf{p}} - \nabla f(\mathbf{r}, t)) = H(\mathbf{r}, \tilde{\mathbf{p}} - \frac{q}{c\hbar} \mathbf{A}_0(t))$ according to Eq. (3.21). This method is more general than the Peierls substitution, since it applies to nonlocal potentials as well [190].

The unperturbed tight-binding Hamiltonian can be written as [190]

$$H_0 = \sum_{n,m} |n\rangle h_{nm}^{(0)} \langle m| \quad \text{with} \quad h_{nm}^{(0)} = (\mathbf{H}_0)_{nm} = \langle n|H_0|m\rangle. \quad (3.26)$$

Applying the above unitary transformation $H_0 \rightarrow H = U H_0 U^\dagger$ yields

$$H = \sum_{n,m} \sum_{k,l} |k\rangle \langle k|U|n\rangle h_{nm}^{(0)} \langle m|U^\dagger|l\rangle \langle l| \quad (3.27)$$

$$\approx \sum_{n,m} \sum_{k,l} |k\rangle \langle k| \left[1 + i \frac{q}{c\hbar} \chi|n\rangle h_{nm}^{(0)} \langle m| \left[1 - i \frac{q}{c\hbar} \chi|l\rangle \langle l|\right], \quad (3.28)$$

where the approximation for U in Eq. (3.24) has been used, and the completeness relations have been inserted. Defining the matrix elements of the dipole transitions operator in length form

$$\chi_{nm} = (\mathbf{X})_{nm} = \langle n|\chi|m\rangle = \langle n|\mathbf{A}_0(t) \cdot \mathbf{r}|m\rangle, \quad (3.29)$$

and exploiting the orthogonality $\langle n|m\rangle = \delta_{nm}$ of the basis functions yields

$$H \approx \sum_{n,m} \sum_{k,l} |k\rangle \left(\delta_{kn} + i \frac{q}{c\hbar} \chi_{kn} \right) h_{nm}^{(0)} \left(\delta_{ml} - i \frac{q}{c\hbar} \chi_{ml}^* \right) \langle l| \quad (3.30)$$

$$= \sum_{n,m} |n\rangle h_{nm}^{(0)} \langle m| + i \frac{q}{c\hbar} \left(\sum_k |k\rangle \chi_{kn} h_{nm}^{(0)} \langle m| - \sum_l |n\rangle h_{nm}^{(0)} \chi_{ml}^* \langle l| \right) + \mathcal{O}\left(\frac{1}{c^2}\right). \quad (3.31)$$

Herein, only paramagnetic terms of order $\frac{1}{c}$ (arising from terms that are linear in the vector potential \mathbf{A}) are taken into account. Terms of order $\frac{1}{c^2} \ll 1$, the so-called ‘diamagnetic contributions’, are neglected, since $c \approx 137$ in atomic units [76, 195]. In other words, only the interaction of electrons with the electric field is considered, whereas the interaction with the magnetic field of the laser is neglected. Finally, the obtained result in matrix form reads

$$H(t) \approx H_0 + i \frac{q}{c\hbar} \left(X(t)H_0 - H_0X^\dagger(t) \right). \quad (3.32)$$

In the context of simulations in *EVOLVE*, the chosen basis set $\{|n\rangle\}$ is either a set of atomic orbitals or of the eigenstates of the tight-binding Hamiltonian H_0 that are obtained by a unitary transformation. It is worth noting that in contrast to the unperturbed Hamiltonian H_0 , the transition matrix $X(t)$ is not hermitian, but the combinations $X(t)H_0$ and $H_0X^\dagger(t)$ are. Subsequently, the matrix elements $X(t)$ which enter the perturbation term in the above equation are evaluated. Therefore, it is helpful to separate the transition matrix elements into a time-dependent and a time-independent part, as will be demonstrated in the next paragraph.

Derivation of the transition matrix elements. The subsequent derivation follows mainly Ref. [39] and references therein. The plane of incidence of a laser pulse impinging under angles θ_{ph} and ϕ_{ph} is defined by the surface normal \mathbf{n}_s , which is assumed to be the cartesian z -axis in this subsection, and by the incidence direction [cf. Fig. 7]

$$\mathbf{n}_{\text{ph}} = - \begin{pmatrix} \cos(\phi_{\text{ph}}) \sin(\theta_{\text{ph}}) \\ \sin(\phi_{\text{ph}}) \sin(\theta_{\text{ph}}) \\ \cos(\theta_{\text{ph}}) \end{pmatrix}. \quad (3.33)$$

The electric field $\mathbf{E} = \mathbf{E}_s + \mathbf{E}_p$ of the laser pulse is decomposed into components perpendicular (s; originating from the German word ‘senkrecht’) and parallel (p) to the plane of incidence. For example, with a coordinate system as chosen in Fig. 7, \mathbf{E}_s has only a y component, whereas \mathbf{E}_p has x and z components. Thus, the time-dependent field is expressed as a coherent superposition of two partial fields that are modulated with an envelope function $\text{env}(t)$, e.g. a Gaussian or a Lorentzian distribution function,

$$\mathbf{E}(t) = \text{env}(t) \sum_{l=s,p} \mathbf{E}_l \cos(\omega t + \Delta_l). \quad (3.34)$$

Herein, the partial fields may be shifted in phase with respect to each other by Δ_s and Δ_p , which allows for simulating not only linearly but also circularly polarized laser pulses. Since the amplitudes \mathbf{E}_l are constant in time, one can derive time-independent transition matrix elements that are combined into dipole-transition matrices $\mathbf{V} = \text{env}(t) \sum_{l=s,p} \mathbf{V}_l \cos(\omega t + \Delta_l)$. The derivation follows Ref. [39] and references therein.

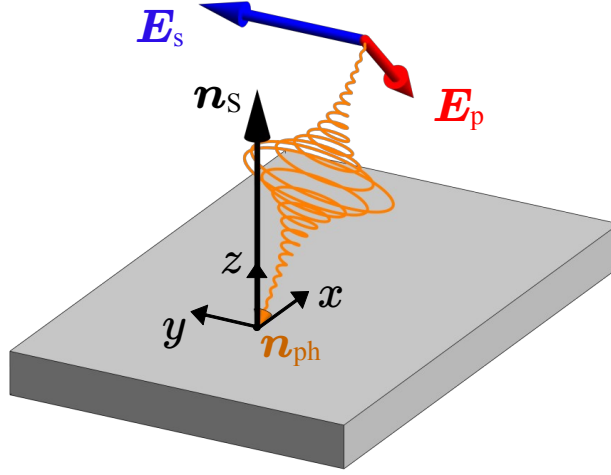


Figure 7: **Illustration of an impinging laser pulse.** The incidence direction \mathbf{n}_{ph} defines the plane of incidence together with the surface normal \mathbf{n}_s . In this sketch, the coordinate system is chosen such that \mathbf{n}_s points along z direction and the plane of incidence is the xz plane. The blue and red arrows visualize the electric field components \mathbf{E}_s and \mathbf{E}_p perpendicular and parallel to the plane of incidence, respectively.

The partial fields are expressed in terms of the angles of incidence,

$$\mathbf{E}_s = E_s \begin{pmatrix} -\sin(\phi_{\text{ph}}) \\ \cos(\phi_{\text{ph}}) \\ 0 \end{pmatrix} \quad \text{and} \quad \mathbf{E}_p = E_p \begin{pmatrix} \cos(\phi_{\text{ph}}) \cos(\theta_{\text{ph}}) \\ \sin(\phi_{\text{ph}}) \cos(\theta_{\text{ph}}) \\ -\sin(\theta_{\text{ph}}) \end{pmatrix}. \quad (3.35)$$

With the unit-vector $\mathbf{e}_r = \frac{1}{r}\mathbf{r}$ in spherical coordinates (r, θ, ϕ) , the dipole operator in length form reads [6, 39, 190]

$$\mathbf{E} \cdot \mathbf{r} = r (\mathbf{E}_s \cdot \mathbf{e}_r + \mathbf{E}_p \cdot \mathbf{e}_r), \quad (3.36)$$

which describes electron-photon interaction in dipole approximation. The two terms are discussed, subsequently. First of all, the perpendicular part is taken into account. Inserting the expression for \mathbf{E}_s yields

$$\mathbf{E}_s \cdot \mathbf{e}_r = -E_s [\sin(\phi_{\text{ph}}) \cos(\phi) - \cos(\phi_{\text{ph}}) \sin(\phi)] \sin(\theta) \quad (3.37)$$

$$= +E_s \frac{i}{\sqrt{2}} \left[\frac{1}{\sqrt{2}} e^{i\phi_{\text{ph}}} e^{-i\phi} - \frac{1}{\sqrt{2}} e^{-i\phi_{\text{ph}}} e^{i\phi} \right] \sin(\theta), \quad (3.38)$$

which can be further rewritten by inserting the complex spherical harmonics $Y_l^m \equiv Y_l^m(\theta, \phi)$ for $l = 1$. The latter read [186]

$$Y_1^{\pm 1} = \mp \frac{C}{\sqrt{2}} e^{\pm i\phi} \sin(\theta), \quad Y_1^0 = C \cos(\theta) \quad \text{with} \quad C \equiv \sqrt{\frac{3}{4\pi}}. \quad (3.39)$$

With this follows

$$\mathbf{E}_s \cdot \mathbf{e}_r = \frac{E_s}{C} \frac{i}{\sqrt{2}} \left[e^{i\phi_{\text{ph}}} Y_1^{-1}(\theta, \phi) + e^{-i\phi_{\text{ph}}} Y_1^1(\theta, \phi) \right] \quad \left(C = \sqrt{\frac{3}{4\pi}} \right). \quad (3.40)$$

Similarly one finds for the parallel part of the dipole operator

$$\mathbf{E}_p \cdot \mathbf{e}_r = E_p \frac{1}{\sqrt{2}} \left[\frac{1}{\sqrt{2}} e^{i\phi_{ph}} e^{-i\phi} + \frac{1}{\sqrt{2}} e^{-i\phi_{ph}} e^{i\phi} \right] \cos(\theta_{ph}) \sin(\theta) - E_p \sin(\theta_{ph}) \cos(\theta). \quad (3.41)$$

Analogously to the treatment of the perpendicular part before, one can also replace terms with complex spherical harmonics which allows for defining [39]

$$H_s = \frac{i}{\sqrt{2}} \left[e^{i\phi_{ph}} Y_1^{-1}(\theta, \phi) + e^{-i\phi_{ph}} Y_1^1(\theta, \phi) \right] \quad (3.42)$$

$$H_p = \frac{1}{\sqrt{2}} \left[e^{i\phi_{ph}} Y_1^{-1}(\theta, \phi) - e^{-i\phi_{ph}} Y_1^1(\theta, \phi) \right] \quad (3.43)$$

$$H_z = Y_1^0(\theta, \phi). \quad (3.44)$$

Consequently, the dipole operator in a compact form reads

$$\mathbf{E} \cdot \mathbf{r} = \frac{r}{C} [E_s H_s + E_p (H_p \cos(\phi_{ph}) - H_z \sin(\theta_{ph}))] \quad \left(C = \sqrt{\frac{3}{4\pi}} \right). \quad (3.45)$$

Based on this, one can evaluate matrix elements $\langle f | \mathbf{E} \cdot \mathbf{r} | i \rangle$ that describe the transitions [6, 76]

$$\Psi_i = \psi_i(r) Y_l^m(\theta, \phi) \quad \rightarrow \quad \Psi_f = \psi_f(r) Y_{l'}^{m'}(\theta, \phi) \quad (3.46)$$

from the initial orbital $|i\rangle \equiv |\Psi_i\rangle$ to the final orbital $|f\rangle \equiv |\Psi_f\rangle$. These matrix elements decompose into three contributions $\langle f | \mathbf{E} \cdot \mathbf{r} | i \rangle_{(\cdot)}$ with $(\cdot) = s, p, z$. It is

$$\langle f | \mathbf{E} \cdot \mathbf{r} | i \rangle_{(\cdot)} = \int \psi_f^*(r) Y_{l'}^{m'*} r (\mathbf{E} \cdot \mathbf{e}_r)_{(\cdot)} \psi_i(r) Y_l^m d^3r \quad (3.47)$$

$$= \frac{1}{C} \int \psi_f^*(r) r^3 \psi_i(r) dr \int Y_{l'}^{m'*} C (\mathbf{E} \cdot \mathbf{e}_r)_{(\cdot)} Y_l^m d\Omega, \quad (3.48)$$

where one can separate the radial part R_{fi} and evaluate the three contributions separately:

$$\langle f | \mathbf{E} \cdot \mathbf{r} | i \rangle_{(\cdot)} = R_{fi} C \int Y_{l'}^{m'*} (\mathbf{E} \cdot \mathbf{e}_r)_{(\cdot)} Y_l^m d\Omega \quad \text{with} \quad (3.49)$$

$$R_{fi} \equiv \frac{1}{C} \int \psi_f^*(r) r^3 \psi_i(r) dr \quad \left(C = \sqrt{\frac{3}{4\pi}} \right). \quad (3.50)$$

For the perpendicular part $(\cdot) = s$, Eq. (3.49) yields

$$\langle f | \mathbf{E} \cdot \mathbf{r} | i \rangle_s = \frac{i}{\sqrt{2}} R_{fi} E_s \int Y_{l'}^{m'*} \left[e^{i\phi_{ph}} Y_1^{-1} + e^{-i\phi_{ph}} Y_1^1 \right] Y_l^m d\Omega \quad (3.51)$$

$$= -\frac{i}{\sqrt{2}} R_{fi} E_s \left[e^{i\phi_{ph}} \mathcal{G}_{l'l}^{m'1m} + e^{-i\phi_{ph}} \mathcal{G}_{l'l}^{m'-1m} \right], \quad (3.52)$$

where $Y_l^m = (-1)^m Y_l^{-m*}$ has been used and the integrals have been replaced by Gaunt coefficients in the Gordon-Shortley convention [196]

$$\mathcal{G}_{l''l'l}^{m''m'm} \equiv \int Y_{l''}^{m''*} Y_{l'}^{m'*} Y_l^m d\Omega. \quad (3.53)$$

With an analog treatment of the parallel part one finds

$$\langle f | \mathbf{E} \cdot \mathbf{r} | i \rangle_{\text{p}} = \frac{1}{\sqrt{2}} R_{fi} E_{\text{p}} \cos(\phi_{\text{ph}}) \int Y_{l'}^{m'*} \left[e^{i\phi_{\text{ph}}} Y_1^{-1} - e^{-i\phi_{\text{ph}}} Y_1^1 \right] Y_l^m d\Omega \quad (3.54)$$

$$= -\frac{1}{\sqrt{2}} R_{fi} E_{\text{p}} \cos(\phi_{\text{ph}}) \left[e^{i\phi_{\text{ph}}} \mathcal{G}_{l'1l}^{m'1m} - e^{-i\phi_{\text{ph}}} \mathcal{G}_{l'1l}^{m'-1m} \right], \quad (3.55)$$

and

$$\langle f | \mathbf{E} \cdot \mathbf{r} | i \rangle_{\text{z}} = -R_{fi} E_{\text{p}} \sin(\theta_{\text{ph}}) \int Y_{l'}^{m'*} Y_1^0 Y_l^m d\Omega \quad (3.56)$$

$$= -R_{fi} E_{\text{p}} \sin(\theta_{\text{ph}}) \mathcal{G}_{l'1l}^{m'0m}. \quad (3.57)$$

In summary it is

$$\langle f | \mathbf{E} \cdot \mathbf{r} | i \rangle = \langle f | \mathbf{E} \cdot \mathbf{r} | i \rangle_{\text{s}} + \langle f | \mathbf{E} \cdot \mathbf{r} | i \rangle_{\text{p}} + \langle f | \mathbf{E} \cdot \mathbf{r} | i \rangle_{\text{z}} \quad \text{with} \quad (3.58)$$

$$\langle f | \mathbf{E} \cdot \mathbf{r} | i \rangle_{\text{s}} = -\frac{i}{\sqrt{2}} R_{fi} E_{\text{s}} \left[e^{i\phi_{\text{ph}}} \mathcal{G}_{l'1l}^{m'1m} + e^{-i\phi_{\text{ph}}} \mathcal{G}_{l'1l}^{m'-1m} \right] \quad (3.59)$$

$$\langle f | \mathbf{E} \cdot \mathbf{r} | i \rangle_{\text{p}} = -\frac{1}{\sqrt{2}} R_{fi} E_{\text{p}} \cos(\phi_{\text{ph}}) \left[e^{i\phi_{\text{ph}}} \mathcal{G}_{l'1l}^{m'1m} - e^{-i\phi_{\text{ph}}} \mathcal{G}_{l'1l}^{m'-1m} \right] \quad (3.60)$$

$$\langle f | \mathbf{E} \cdot \mathbf{r} | i \rangle_{\text{z}} = -R_{fi} E_{\text{p}} \sin(\theta_{\text{ph}}) \mathcal{G}_{l'1l}^{m'0m}, \quad (3.61)$$

which imply the optical selection rules [197, 198] $l' = l \pm 1$, $m' = \pm 1$ [cf. $(\cdot) = \text{s, p}$] and $l' = l \pm 1$, $m' = m$ [cf. $(\cdot) = \text{z}$]. In the computational framework `EVOLVE`, the orbitals are expressed in terms of cubic harmonics that are a superposition of complex spherical harmonics, as described before [cf. Eq. (2.23)]. Thus, the selection rules allow for transitions between s and p orbitals or between p and d orbitals with $l' - l = \pm 1$. These transitions comprise coherent excitations and deexcitations of states that get populated or depopulated, respectively.

In the publications presented in the second section in the cumulative part (Sec. 5), it is assumed that the thickness of the sample is much smaller than the spatial extent of the impinging laser pulse. Consequently, in the simulations, all atomic sites of the cluster are illuminated simultaneously with the same laser intensity. However, in a real experiment with a thick sample, an inhomogeneous distribution of occupation and observables across the film would be observed due to the decay of the laser intensity towards the interior of the slab. Consequently, interpreting the outcome of our simulations is easier than for experimental results.

3.4 Observables: spin and orbital angular momenta and their currents

Up to now, the time evolution of a laser-excited system has been described using a density matrix approach. In Sec. 3.2, the one-electron density matrix has been introduced which is propagated in time according to the von Neumann equation (3.13). Therein, the time-dependent Hamiltonian comprises the time-independent real-space Hamiltonian H_0 of the ground state [cf. Sec. 3.1] and the time-dependent electric field of the laser pulse entering via minimal coupling [cf. Sec. 3.3].

In the following, expressions for expectation values of specific observables that are relevant for the publications presented in Sec. 5 will be derived. In particular, the time evolution of spin and orbital angular momenta and respective currents are addressed. In addition to having time-resolved access to those observables with femtosecond resolution, the utilized computational framework `EVOLVE` allows for investigating the spatial distribution of observables with atomic resolution.

Approaches to describe ultrafast spin currents. In literature, ultrafast electron motion in the form of (spin-polarized) currents has been studied for the last two decades using various approaches. In order to model femtosecond electron motion, diffusive and ballistic transport can be considered as the two limits of transport processes. They are characterized by a diffusion exponent γ describing the time dependence of a particle's displacement distribution $\sigma_d^2(t) \propto t^\gamma$ [199, 200]. Brownian motion leads to standard diffusion ($\gamma = 1$), but one assumes large velocities and a vanishing electron mean-free path, whereas ballistic transport ($\gamma = 2$) neglects scattering events. Thus, both approaches are not suitable for describing electronic motion with finite lifetimes and mean-free paths. A combination with an assumed time-dependent $\gamma(t)$, which starts in the ballistic regime and goes to standard diffusion for long times results in 'superdiffusive' electron transport. In the latter scenario, electrons move with constant velocities and undergo a finite number of elastic scattering events [199–202].

Ultrafast superdiffusive spin currents are calculated in a semiclassical two-current model by considering spin-dependent relaxation times, scattering rates and transition probabilities. Besides, laser-excitation is taken into account as a source term. As a result 'hot majority-spin electrons' have a higher mobility than 'minority-spin electrons'. This enables the laser-induced transfer of spin-angular momentum from a ferromagnet across an interface into a nonmagnetic layer [199, 201, 203, 204]. Consequently, the spin-polarized currents carry spin angular momentum and lead to demagnetization of the ferromagnet and a magnetization of the nonmagnetic region. This phenomenon has been observed experimentally, for example in Fe/Au [48, 203] or in Co/Cu heterostructures [181]. Later, it has been demonstrated that in such a Co/Cu heterostructure, this scenario is accompanied by a 'backflow mechanism': minority-spin Cu electrons flow from the nonmagnetic region back to the ferromagnetic Co region, in which unoccupied orbitals get populated [49]. This reflow mechanism is very similar to optically induced inter-site spin transfer (OISTR), where spin polarization is redistributed in the vicinity of an interface, leading to laser-induced switching of the magnetic order in a ferromagnetic/antiferromagnetic heterostructure [45].

Besides, it is worth noting that other semiclassical theories to describe the laser-induced dynamics of hot carriers exist. These are based on an extended wave-diffusion equation [205] or on the Boltzmann equation [203, 206]. In the following, the one-electron density matrix approach used in the `EVOLVE` computer code will be described in detail [54]. At the current stage, scattering of electrons with other (quasi-)particles, such as phonons or other electrons, is not included. However, the method used here enables spatio-temporal access to observables with atomic and femtosecond resolution, and goes beyond the two-current model. Limitations and advantages of this approach are summarized at the end of this section (Sec. 3.5).

Computation of observables with spatio-temporal resolution. As explained before, the time evolution of an observable's expectation value $\langle \mathcal{O} \rangle$ is calculated from Eq. (3.11) using the time-dependent density matrix

$$\langle \mathcal{O} \rangle(t) = \text{tr} \rho(t) \mathcal{O} = \text{tr} P(t) \mathcal{O}. \quad (3.62)$$

Herein, the right-hand side of the equation is given in matrix form. Spatio-temporal properties of this observable are computed by taking partial traces [207–209] with the density matrix P represented in a suitable basis. Within the computational framework `EVOLVE`, the electron dynamics is analyzed either in the eigenstate basis $\{|n\rangle\}$ of H_0 or after a unitary transformation in site-orbital-spin basis $\{|k\alpha\sigma\rangle\}$ [54]. Thus, one can express $|n\rangle = \sum_{k\alpha\sigma} c_{k\alpha\sigma,n} |k\alpha\sigma\rangle$. Hence, a resolution with respect to orbital type α (β) and spin orientation σ (σ') of site k (l) is achieved by defining submatrices

$$p_{kl}^{\sigma\sigma'} \equiv \left(p_{kl}^{\sigma\sigma'} \right)_{\alpha\beta} = p_{k\alpha\sigma,l\beta\sigma'} \quad \text{and} \quad h_{kl}^{\sigma\sigma'} \equiv \left(h_{kl}^{\sigma\sigma'} \right)_{\alpha\beta} = h_{k\alpha\sigma,l\beta\sigma'}, \quad (3.63)$$

which are combined into site-resolved block matrices, i.e. submatrices of the complete density matrix P and the Hamilton matrix H

$$P_{kl} = \begin{pmatrix} p_{kl}^{\uparrow\uparrow} & p_{kl}^{\uparrow\downarrow} \\ p_{kl}^{\downarrow\uparrow} & p_{kl}^{\downarrow\downarrow} \end{pmatrix} \quad \text{and} \quad H_{kl} = \begin{pmatrix} h_{kl}^{\uparrow\uparrow} & h_{kl}^{\uparrow\downarrow} \\ h_{kl}^{\downarrow\uparrow} & h_{kl}^{\downarrow\downarrow} \end{pmatrix}. \quad (3.64)$$

In publications [OB4] and [OB5], the addressed observables are the spin angular momentum (SAM) and orbital angular momentum (OAM) which are analyzed during the laser excitation with atomic and femtosecond resolution. Thus, the time-dependent i components of the local SAM $\langle s_l \rangle$ and OAM $\langle l_l \rangle$ at a specific atomic site l read

$$\langle s_l^i \rangle(t) = \text{tr} P_{ll}(t) \Sigma^i \quad \text{and} \quad \langle l_l^i \rangle(t) = \text{tr} P_{ll}(t) L_l^i \quad (i = x, y, z). \quad (3.65)$$

Herein, Σ^i and L_l^i are block matrices that comprise the Pauli matrices and the matrices of the OAM operator in the basis of cubic harmonic orbitals, respectively [cf. Eq. (2.25) for p orbitals], where the latter depends on the atomic species and orbitals at site l . If the number of sites in a sample's (large) unit cell N is considered, one can then compute the time evolution of the site-averaged (global) SAM $\langle S \rangle$ and OAM $\langle L \rangle$ according to

$$\langle S \rangle(t) = \frac{1}{N} \sum_l \langle s_l \rangle(t) \quad \text{and} \quad \langle L \rangle(t) = \frac{1}{N} \sum_l \langle l_l \rangle(t). \quad (3.66)$$

The site-resolved block matrix H_{kl} , that is also defined in Eq. (3.64), is needed to compute currents which will be discussed in detail, subsequently; the explicit time dependence in the expressions will be omitted in the derivation for clarity.

Charge currents. The existence of currents can be motivated by taking the equation of motion for the density matrix of a specific site l into account. The equation of motion (3.13) (in atomic units, $\hbar = 1$) implies that the change of occupation dp_{ll} within dt is given by

$$\frac{dp_{ll}}{dt} = i \sum_k (p_{lk} h_{kl} - p_{kl} h_{lk}) = i \sum_k p_{lk} h_{kl} - \langle l \leftrightarrow k \rangle, \quad (3.67)$$

where ' $\langle l \leftrightarrow k \rangle$ ' means that the expression before the brackets is subtracted with interchanged indices l and k . Comparing the above result with the continuity equation $\dot{p} = -\nabla \cdot j$ motivates

defining currents j_{kl} flowing from site l to site k as

$$j_{kl} = -i p_{lk} h_{kl} - \langle l \leftrightarrow k \rangle. \quad (3.68)$$

Consequently, all currents j_{kl} starting from site l yield the change of occupation of site l as

$$\dot{p}_{ll} = - \sum_k j_{kl}. \quad (3.69)$$

The finite hopping range of the tight-binding Hamiltonian restricts the sum to first- or second-nearest neighbors k of site l . It is easy to show that the currents are antisymmetric, i.e. $j_{kl} = -j_{lk}$ by exploiting the hermiticity of the density matrix and the Hamiltonian.

Subsequently, expressions for the computation of currents are derived following Mahan, where the current operator is defined as [58]

$$\mathbf{j} = -i \sum_{kl} \mathbf{r}_{kl} |k\rangle h_{kl} \langle l| \equiv \sum_{kl} \mathbf{r}_{kl} j_{kl}. \quad (3.70)$$

Herein, the direction of the current from site l to k is given by the vector $\mathbf{r}_{kl} \equiv \mathbf{r}_k - \mathbf{r}_l$, and the magnitude of the current operator is defined by

$$j_{kl} = -i |k\rangle h_{kl} \langle l| = -\frac{i}{2} (|k\rangle h_{kl} \langle l| - |l\rangle h_{lk} \langle k|) = -\frac{i}{2} |k\rangle h_{kl} \langle l| - \langle l \leftrightarrow k \rangle. \quad (3.71)$$

By using the site-orbital-spin resolved basis one can extend the indices $k \rightarrow k\alpha\sigma$ and $l \rightarrow l\beta\sigma'$ to compute the magnitude of the current operator with $(h_{kl}^{\sigma\sigma'})_{\alpha\beta}$ from Eq. (3.63)

$$j_{kl} = -\frac{i}{2} \sum_{\alpha\sigma} \sum_{\beta\sigma'} |k\alpha\sigma\rangle (h_{kl}^{\sigma\sigma'})_{\alpha\beta} \langle l\beta\sigma'| - \langle l\beta\sigma' \leftrightarrow k\alpha\sigma \rangle. \quad (3.72)$$

The expectation value of the current operator \mathbf{j} reads

$$\langle \mathbf{j} \rangle = \text{tr} \rho \mathbf{j} = \mathbf{r}_{kl} \sum_{kl} \text{tr} \rho j_{kl} = \mathbf{r}_{kl} \sum_{kl} \langle j_{kl} \rangle. \quad (3.73)$$

Therein, the expectation value of the magnitude is then given by

$$\langle j_{kl} \rangle = -\frac{i}{2} \sum_{n\delta\mu'} \sum_{m\gamma\mu} \sum_{\alpha\sigma} \sum_{\beta\sigma'} (p_{nm}^{\mu'\mu})_{\delta\gamma} \langle m\gamma\mu | k\alpha\sigma \rangle (h_{kl}^{\sigma\sigma'})_{\alpha\beta} \langle l\beta\sigma' | n\delta\mu' \rangle - \langle l\beta\sigma' \leftrightarrow k\alpha\sigma \rangle \quad (3.74)$$

$$= -\frac{i}{2} \sum_{\alpha\sigma} \sum_{\beta\sigma'} (p_{lk}^{\sigma'\sigma})_{\beta\alpha} (h_{kl}^{\sigma\sigma'})_{\alpha\beta} - \langle l\beta\sigma' \leftrightarrow k\alpha\sigma \rangle. \quad (3.75)$$

Utilizing the submatrices defined in Eq. (3.63) yields $\langle j_{kl} \rangle = -\frac{i}{2} \text{tr} \sum_{\sigma\sigma'} p_{lk}^{\sigma'\sigma} h_{kl}^{\sigma\sigma'} - \langle l \leftrightarrow k \rangle$. Writing the spins explicitly results in

$$\langle j_{kl} \rangle = -\frac{i}{2} \text{tr} \left(p_{lk}^{\uparrow\uparrow} h_{kl}^{\uparrow\uparrow} + p_{lk}^{\uparrow\downarrow} h_{kl}^{\downarrow\uparrow} + p_{lk}^{\downarrow\uparrow} h_{kl}^{\uparrow\downarrow} + p_{lk}^{\downarrow\downarrow} h_{kl}^{\downarrow\downarrow} \right) - \langle l \leftrightarrow k \rangle. \quad (3.76)$$

This expression can be interpreted as a sum of \uparrow - and \downarrow -spin resolved currents in the case of collinear magnetic textures, where inter-site hopping with spin flip do not occur in the Hamiltonian, i.e. $h_{kl}^{\uparrow\downarrow} = 0$ resp. $h_{kl}^{\downarrow\uparrow} = 0$. However, spin-orbit coupling and noncollinear magnetic textures allow for nonvanishing spin-flip hoppings, and thus open additional transport channels.

Spin-resolved currents. Now, one can take into account currents $j_{kl}^{S^i}$ that are resolved with respect to the component $i = x, y, z$ of the spin S . These spin-resolved currents carry SAM and their expectation values can be expressed in a symmetrized form as [54, 58]

$$\langle j_{kl}^{S^i} \rangle = \frac{1}{2} (\langle \Sigma^i j_{kl} \rangle + \langle j_{kl} \Sigma^i \rangle), \quad (3.77)$$

where Σ^i is again the block Pauli matrix. The two expressions on the right can be evaluated separately. It is

$$\begin{aligned} \langle \Sigma^i j_{kl} \rangle &= -\frac{i}{2} \sum_{n\delta\mu'} \sum_{m\gamma\mu} \sum_{\alpha\sigma} \sum_{\beta\sigma'} \left(p_{nm}^{\mu'\mu} \right)_{\delta\gamma} \langle m\gamma\mu | \Sigma^i | k\alpha\sigma \rangle \left(h_{kl}^{\sigma\sigma'} \right)_{\alpha\beta} \langle l\beta\sigma' | n\delta\mu' \rangle - \langle l\beta\sigma' \leftrightarrow k\alpha\sigma \rangle \\ &= -\frac{i}{2} \sum_{\mu} \sum_{\alpha\sigma} \sum_{\beta\sigma'} \left(p_{lk}^{\sigma'\mu} \right)_{\beta\alpha} \langle \mu | \Sigma^i | \sigma \rangle \left(h_{kl}^{\sigma\sigma'} \right)_{\alpha\beta} - \langle l\beta\sigma' \leftrightarrow k\alpha\sigma \rangle. \end{aligned} \quad (3.78)$$

In the last step, one uses the fact that the Pauli matrix is diagonal in site and orbitals. Analogously, one can find

$$\langle j_{kl} \Sigma^i \rangle = -\frac{i}{2} \sum_{\mu'} \sum_{\alpha\sigma} \sum_{\beta\sigma'} \left(p_{lk}^{\mu'\sigma} \right)_{\beta\alpha} \left(h_{kl}^{\sigma\sigma'} \right)_{\alpha\beta} \langle \sigma' | \Sigma^i | \mu' \rangle - \langle l\beta\sigma' \leftrightarrow k\alpha\sigma \rangle. \quad (3.79)$$

From these results, it is obvious that the non-vanishing matrix elements of the Pauli matrices have to be considered in order to find explicit expressions for the spin-resolved currents. For the z component only the diagonal elements $\langle \uparrow | \Sigma^z | \uparrow \rangle = 1$ and $\langle \downarrow | \Sigma^z | \downarrow \rangle = -1$ are nonzero. Considering this and writing the spins explicitly in the previous equations yields

$$\begin{aligned} \langle \Sigma^z j_{kl} \rangle &= -\frac{i}{2} \text{tr} \left[\mathbf{p}_{lk}^{\uparrow\uparrow} \mathbf{h}_{kl}^{\uparrow\uparrow} - \mathbf{p}_{kl}^{\uparrow\uparrow} \mathbf{h}_{lk}^{\uparrow\uparrow} \right] + \left[\mathbf{p}_{lk}^{\downarrow\uparrow} \mathbf{h}_{kl}^{\uparrow\downarrow} - \mathbf{p}_{kl}^{\downarrow\uparrow} \mathbf{h}_{lk}^{\uparrow\downarrow} \right] \\ &\quad - \left[\mathbf{p}_{lk}^{\uparrow\downarrow} \mathbf{h}_{kl}^{\downarrow\uparrow} - \mathbf{p}_{kl}^{\uparrow\downarrow} \mathbf{h}_{lk}^{\downarrow\uparrow} \right] - \left[\mathbf{p}_{lk}^{\downarrow\downarrow} \mathbf{h}_{kl}^{\downarrow\downarrow} - \mathbf{p}_{kl}^{\downarrow\downarrow} \mathbf{h}_{lk}^{\downarrow\downarrow} \right] - \langle l \leftrightarrow k \rangle \end{aligned} \quad (3.80)$$

$$= -\frac{i}{2} \text{tr} \begin{pmatrix} \mathbf{p}_{lk}^{\uparrow\uparrow} & \mathbf{p}_{lk}^{\uparrow\downarrow} \\ \mathbf{p}_{lk}^{\downarrow\uparrow} & \mathbf{p}_{lk}^{\downarrow\downarrow} \end{pmatrix} \begin{pmatrix} 1 & 0 \\ 0 & -1 \end{pmatrix} \begin{pmatrix} \mathbf{h}_{kl}^{\uparrow\uparrow} & \mathbf{h}_{kl}^{\uparrow\downarrow} \\ \mathbf{h}_{kl}^{\downarrow\uparrow} & \mathbf{h}_{kl}^{\downarrow\downarrow} \end{pmatrix} - \langle l \leftrightarrow k \rangle, \quad (3.81)$$

and analogously one finds

$$\langle j_{kl} \Sigma^z \rangle = -\frac{i}{2} \text{tr} \begin{pmatrix} \mathbf{p}_{lk}^{\uparrow\uparrow} & \mathbf{p}_{lk}^{\uparrow\downarrow} \\ \mathbf{p}_{lk}^{\downarrow\uparrow} & \mathbf{p}_{lk}^{\downarrow\downarrow} \end{pmatrix} \begin{pmatrix} \mathbf{h}_{kl}^{\uparrow\uparrow} & \mathbf{h}_{kl}^{\uparrow\downarrow} \\ \mathbf{h}_{kl}^{\downarrow\uparrow} & \mathbf{h}_{kl}^{\downarrow\downarrow} \end{pmatrix} \begin{pmatrix} 1 & 0 \\ 0 & -1 \end{pmatrix} - \langle l \leftrightarrow k \rangle. \quad (3.82)$$

Furthermore, it is easy to show that the anticommutator $[\Sigma^z, \mathbf{H}_{kl}]_+$ reads

$$\left[\begin{pmatrix} 1 & 0 \\ 0 & -1 \end{pmatrix}, \begin{pmatrix} \mathbf{h}_{kl}^{\uparrow\uparrow} & \mathbf{h}_{kl}^{\uparrow\downarrow} \\ \mathbf{h}_{kl}^{\downarrow\uparrow} & \mathbf{h}_{kl}^{\downarrow\downarrow} \end{pmatrix} \right]_+ = 2 \begin{pmatrix} \mathbf{h}_{kl}^{\uparrow\uparrow} & 0 \\ 0 & -\mathbf{h}_{kl}^{\downarrow\downarrow} \end{pmatrix}. \quad (3.83)$$

With this, the symmetrized form for the spin- z polarized current can be calculated as follows:

$$\langle j_{kl}^{S^z} \rangle = -\frac{i}{4} \text{tr} \begin{pmatrix} \mathbf{p}_{lk}^{\uparrow\uparrow} & \mathbf{p}_{lk}^{\uparrow\downarrow} \\ \mathbf{p}_{lk}^{\downarrow\uparrow} & \mathbf{p}_{lk}^{\downarrow\downarrow} \end{pmatrix} \left[\begin{pmatrix} 1 & 0 \\ 0 & -1 \end{pmatrix}, \begin{pmatrix} \mathbf{h}_{kl}^{\uparrow\uparrow} & \mathbf{h}_{kl}^{\uparrow\downarrow} \\ \mathbf{h}_{kl}^{\downarrow\uparrow} & \mathbf{h}_{kl}^{\downarrow\downarrow} \end{pmatrix} \right]_+ - \langle l \leftrightarrow k \rangle \quad (3.84)$$

$$= -\frac{i}{2} \text{tr} \left(\mathbf{p}_{lk}^{\uparrow\uparrow} \mathbf{t}_{kl}^{\uparrow\uparrow} - \mathbf{p}_{lk}^{\downarrow\downarrow} \mathbf{h}_{kl}^{\downarrow\downarrow} \right) - \langle l \leftrightarrow k \rangle. \quad (3.85)$$

Herein, the spin-mixing terms cancel each other and similar to the current j_{kl} , this expression can be interpreted as the difference of \uparrow and \downarrow -polarized currents, as is known from the two-current model (cf. Sec. 2.3). Expressions for the x - and y -spin polarized currents are obtained analogously:

$$\langle j_{kl}^{S^x} \rangle = -\frac{i}{4} \text{tr} \left(\mathbf{p}_{lk}^{\uparrow\uparrow} + \mathbf{p}_{lk}^{\downarrow\downarrow} \right) \left(\mathbf{h}_{kl}^{\uparrow\downarrow} + \mathbf{h}_{kl}^{\downarrow\uparrow} \right) + \left(\mathbf{p}_{lk}^{\uparrow\downarrow} + \mathbf{p}_{lk}^{\downarrow\uparrow} \right) \left(\mathbf{h}_{kl}^{\uparrow\uparrow} + \mathbf{h}_{kl}^{\downarrow\downarrow} \right) - \langle l \leftrightarrow k \rangle, \quad (3.86)$$

$$\langle j_{kl}^{S^y} \rangle = \frac{1}{4} \text{tr} \left(\mathbf{p}_{lk}^{\uparrow\uparrow} + \mathbf{p}_{lk}^{\downarrow\downarrow} \right) \left(\mathbf{h}_{kl}^{\uparrow\downarrow} - \mathbf{h}_{kl}^{\downarrow\uparrow} \right) + \left(\mathbf{p}_{lk}^{\uparrow\downarrow} - \mathbf{p}_{lk}^{\downarrow\uparrow} \right) \left(\mathbf{h}_{kl}^{\uparrow\uparrow} + \mathbf{h}_{kl}^{\downarrow\downarrow} \right) - \langle l \leftrightarrow k \rangle. \quad (3.87)$$

In contrast to the z -spin resolved current, here the non-vanishing off-diagonal matrix elements of the Pauli matrices Σ^x and Σ^y yield contributions to the spin-polarized currents arising from spin-mixing terms. One is again able to express the spin-resolved currents with the respective anticommutators $[\Sigma^x, \mathbf{H}_{kl}]_+$ and $[\Sigma^y, \mathbf{H}_{kl}]_+$, which allows for writing the (spin-polarized) currents in a compact form

$$\langle j_{kl} \rangle = -\frac{i}{2} \text{tr} \mathbf{P}_{lk} \mathbf{H}_{kl} - \langle l \leftrightarrow k \rangle \quad \text{and} \quad (3.88)$$

$$\langle j_{kl}^{S^i} \rangle = -\frac{i}{4} \text{tr} \mathbf{P}_{lk} [\Sigma^i, \mathbf{H}_{kl}]_+ - \langle l \leftrightarrow k \rangle \quad (i = x, y, z). \quad (3.89)$$

Orbital currents. In analogy to the spin-polarized currents above, orbital currents, i.e. currents carrying OAM from site l to k can be computed. In the following, expressions as utilized in publication [OB5] are derived. Starting from a symmetrized form $\langle j_{kl}^{L^i} \rangle = \frac{1}{2} (\langle L_k^i j_{kl} \rangle + \langle j_{kl} L_l^i \rangle)$, similarly to the currents of SAM, one finds with the above compact form for the currents

$$\langle j_{kl}^{L^i} \rangle = -\frac{i}{4} \text{tr} \left(\mathbf{P}_{lk} \mathbf{L}_k^i \mathbf{H}_{kl} + \mathbf{P}_{lk} \mathbf{H}_{kl} \mathbf{L}_l^i \right) - \langle l \leftrightarrow k \rangle \quad (i = x, y, z). \quad (3.90)$$

Herein, the i -th component of the OAM operator depends on the atomic species and orbitals at site $j = k$ or $j = l$ and in the basis of the cubic harmonic orbitals they read in block form

$$\mathbf{L}_j^i = \begin{pmatrix} l_j^i & 0 \\ 0 & l_j^i \end{pmatrix}. \quad (3.91)$$

Using the previously defined submatrices yields

$$\langle j_{kl}^{L^i} \rangle = -\frac{i}{4} \text{tr} \begin{pmatrix} \mathbf{p}_{lk}^{\uparrow\uparrow} & \mathbf{p}_{lk}^{\uparrow\downarrow} \\ \mathbf{p}_{lk}^{\downarrow\uparrow} & \mathbf{p}_{lk}^{\downarrow\downarrow} \end{pmatrix} \left[l_k^i \begin{pmatrix} \mathbf{h}_{kl}^{\uparrow\uparrow} & \mathbf{h}_{kl}^{\uparrow\downarrow} \\ \mathbf{h}_{kl}^{\downarrow\uparrow} & \mathbf{h}_{kl}^{\downarrow\downarrow} \end{pmatrix} + \begin{pmatrix} \mathbf{h}_{kl}^{\uparrow\uparrow} & \mathbf{h}_{kl}^{\uparrow\downarrow} \\ \mathbf{h}_{kl}^{\downarrow\uparrow} & \mathbf{h}_{kl}^{\downarrow\downarrow} \end{pmatrix} l_l^i \right] - \langle l \leftrightarrow k \rangle.$$

This expression can be split into ‘spin-conserving’ ($\uparrow\uparrow$ or $\downarrow\downarrow$) and ‘spin-mixing’ ($\uparrow\downarrow$ or $\downarrow\uparrow$) contributions, i.e. $\langle j_{kl}^{L^i} \rangle = \langle j_{kl}^{L^i} \rangle^{\sigma\sigma} + \langle j_{kl}^{L^i} \rangle^{\sigma\sigma'}$ with $\sigma' = -\sigma$. First of all, the spin-conserving terms, that occur after performing the matrix multiplication, read

$$\langle j_{kl}^{L^i} \rangle^{\sigma\sigma} = -\frac{i}{4} \text{tr} \left(\mathbf{p}_{lk}^{\uparrow\uparrow} \left[l_k^i \mathbf{h}_{kl}^{\uparrow\uparrow} + \mathbf{h}_{kl}^{\uparrow\uparrow} l_l^i \right] + \mathbf{p}_{lk}^{\downarrow\downarrow} \left[l_k^i \mathbf{h}_{kl}^{\downarrow\downarrow} + \mathbf{h}_{kl}^{\downarrow\downarrow} l_l^i \right] \right) - \langle l \leftrightarrow k \rangle \quad (3.92)$$

$$\begin{aligned} &= -\frac{i}{4} \text{tr} \left(\mathbf{p}_{lk}^{\uparrow\uparrow} \left[l_k^i \mathbf{h}_{kl}^{\uparrow\uparrow} + \mathbf{h}_{kl}^{\uparrow\uparrow} l_l^i \right] + \mathbf{p}_{lk}^{\downarrow\downarrow} \left[l_k^i \mathbf{h}_{kl}^{\downarrow\downarrow} + \mathbf{h}_{kl}^{\downarrow\downarrow} l_l^i \right] \right) \\ &\quad + \frac{i}{4} \text{tr} \left(\mathbf{p}_{lk}^{\uparrow\downarrow*} \left[l_l^{i*} \mathbf{h}_{kl}^{\uparrow\uparrow*} + \mathbf{h}_{kl}^{\uparrow\uparrow*} l_k^{i*} \right] + \mathbf{p}_{lk}^{\downarrow\uparrow*} \left[l_l^{i*} \mathbf{h}_{kl}^{\downarrow\downarrow*} + \mathbf{h}_{kl}^{\downarrow\downarrow*} l_k^{i*} \right] \right), \end{aligned} \quad (3.93)$$

where the hermiticity of the operators has been exploited ($\mathbf{p}_{lk}^{\sigma\sigma'*} = \mathbf{p}_{kl}^{\sigma'\sigma}$, $\mathbf{h}_{kl}^{\sigma\sigma'*} = \mathbf{h}_{kl}^{\sigma'\sigma}$ and $l_k^i* = l_k^i$). In an analog treatment, one finds for the occurring spin-mixing terms ($\sigma' = -\sigma$)

$$\langle j_{kl}^{L^i} \rangle^{\sigma\sigma'} = -\frac{i}{4} \text{tr} \left(\mathbf{p}_{lk}^{\uparrow\downarrow} \left[l_k^i \mathbf{h}_{kl}^{\downarrow\uparrow} + \mathbf{h}_{kl}^{\downarrow\uparrow} l_l^i \right] + \mathbf{p}_{lk}^{\downarrow\uparrow} \left[l_k^i \mathbf{h}_{kl}^{\uparrow\downarrow} + \mathbf{h}_{kl}^{\uparrow\downarrow} l_l^i \right] \right) - \langle l \leftrightarrow k \rangle \quad (3.94)$$

$$\begin{aligned} &= -\frac{i}{4} \text{tr} \left(\mathbf{p}_{lk}^{\uparrow\downarrow} \left[l_k^i \mathbf{h}_{kl}^{\downarrow\uparrow} + \mathbf{h}_{kl}^{\downarrow\uparrow} l_l^i \right] + \mathbf{p}_{lk}^{\downarrow\uparrow} \left[l_k^i \mathbf{h}_{kl}^{\uparrow\downarrow} + \mathbf{h}_{kl}^{\uparrow\downarrow} l_l^i \right] \right) \\ &\quad + \frac{i}{4} \text{tr} \left(\mathbf{p}_{lk}^{\downarrow\uparrow*} \left[l_l^i* \mathbf{h}_{kl}^{\uparrow\downarrow*} + \mathbf{h}_{kl}^{\uparrow\downarrow*} l_k^i* \right] + \mathbf{p}_{lk}^{\uparrow\downarrow*} \left[l_l^i* \mathbf{h}_{kl}^{\downarrow\uparrow*} + \mathbf{h}_{kl}^{\downarrow\uparrow*} l_k^i* \right] \right). \end{aligned} \quad (3.95)$$

In both expressions, terms of the form $\text{tr} (ABC - A^\dagger C^\dagger B^\dagger)$ occur with $A = \mathbf{p}_{lk}^{\sigma\sigma'}$, $B = l_k^i$ and $C = \mathbf{h}_{kl}^{\sigma'\sigma}$ (and $A^\dagger = \mathbf{p}_{lk}^{\sigma\sigma'*}$, $B^\dagger = l_k^i*$ and $C^\dagger = \mathbf{h}_{kl}^{\sigma'\sigma*}$). These expressions can be evaluated as $\text{tr} (ABC - A^\dagger C^\dagger B^\dagger) = 2i \text{Im} (\text{tr} (ABC))$ [184, 186], which allows to condense the spin-conserving and -mixing terms into

$$\langle j_{kl}^{L^i} \rangle^{\sigma\sigma} = \frac{1}{2} \text{Im} \left(\text{tr} \left(\mathbf{p}_{lk}^{\uparrow\uparrow} \left[l_k^i \mathbf{h}_{kl}^{\uparrow\uparrow} + \mathbf{h}_{kl}^{\uparrow\uparrow} l_l^i \right] + \mathbf{p}_{lk}^{\downarrow\downarrow} \left[l_k^i \mathbf{h}_{kl}^{\downarrow\downarrow} + \mathbf{h}_{kl}^{\downarrow\downarrow} l_l^i \right] \right) \right) \quad (3.96)$$

$$\langle j_{kl}^{L^i} \rangle^{\sigma\sigma'} = \frac{1}{2} \text{Im} \left(\text{tr} \left(\mathbf{p}_{lk}^{\uparrow\downarrow} \left[l_k^i \mathbf{h}_{kl}^{\downarrow\uparrow} + \mathbf{h}_{kl}^{\downarrow\uparrow} l_l^i \right] + \mathbf{p}_{lk}^{\downarrow\uparrow} \left[l_k^i \mathbf{h}_{kl}^{\uparrow\downarrow} + \mathbf{h}_{kl}^{\uparrow\downarrow} l_l^i \right] \right) \right). \quad (3.97)$$

In summary, one obtains for the expectation value of the orbital current by adding both contributions

$$\langle j_{kl}^{L^i} \rangle = \frac{1}{2} \text{Im} \sum_{\sigma, \sigma'} \left(\text{tr} \left(\mathbf{p}_{lk}^{\sigma\sigma'} \left[l_k^i \mathbf{h}_{kl}^{\sigma'\sigma} + \mathbf{h}_{kl}^{\sigma'\sigma} l_l^i \right] \right) \right). \quad (3.98)$$

3.5 Advantages and limitations of the approach

At the end of this section, a few aspects on the presented one-electron approach will be discussed, and some advantages and limits will be briefly summarized. The focus in the publications [OB4] and [OB5] presented in Sec. 5 is the simulation and investigation of ‘pure’ laser-induced electron dynamics, in particular on the relations of laser details and photo-induced spin and orbital angular momentum and their transport.

Advantages. The real-space tight-binding approach offers some advantages (cf. Sec. 3.1): although a simulation of ultrafast spin dynamics with time-dependent density functional theory (TDDFT) is very accurate [45, 210, 211], it has the disadvantage of very high computational cost. Thus, this approach is limited to simulations of a few 10 fs and only small samples consisting of a few unit atoms.

However, tight-binding approaches allow for very efficient calculations offering the opportunity for the simulation of large systems and long time intervals (cf. e.g. 20 atoms and simulation of 100 fs or more in Refs. [54, OB7]). With the real-space tight binding approach, individual boundary conditions (open or closed) along specific directions are possible and thus, the impact of inhomogeneities like surfaces and interfaces on electron dynamics can be investigated. Besides, exchange and spin-orbit interaction may be switched on or off, tuned for didactical purposes, and serve as ‘toy’ models to investigate their influence on the electron dynamics.

Finally, results are relatively easy to interpret (e.g. hybridization of atomic orbitals), and the real-space approach allows for the study of spatio-temporal distribution of observables with both atomic resolution on fs timescales (e.g. spin and orbital angular momenta or their currents, as presented in publications [OB4] and [OB5]; cf. Sec. 3.4).

Limitations. The approach has restrictions, since this effective one-particle model neglects interactions with other particles. Although the `EVOLVE` computer code has the feature of coupling the electron system to a bosonic heat bath (cf. Refs. [54, OB7]), electron-phonon interaction is not addressed in this work. The focus of this thesis (Sec. 5) is the study of ‘pure’ laser-induced electron dynamics on timescales of a few 10 fs after the laser pulse, whereas thermalization is relevant on the timescales of picoseconds. Consequently, the heat bath is not turned on in publications [OB4] and [OB5].⁴

Furthermore, electron-electron scattering is partially included in the Slater-Koster parameters that enter the ground-state Hamiltonian. As briefly explained before, these parameters are based on a fit to ab-initio band structures, where exchange-correlation functionals indirectly account for electron-electron interaction [67].

A full account of the electron-electron interaction would require a two-particle reduced density matrix approach, which is computationally very demanding [57, 58, 76] and thus typically restricted to small systems and time spans, similar to TDDFT methods. However, within the utilized one-electron approach, it is possible to explicitly account for electron-electron interaction by applying the Hartree-Fock approximation (for details see e.g. Refs. [57, 58, 76]). This feature is not implemented in `EVOLVE` at the present stage, but one can expect attraction and repulsion within the laser-induced spatio-temporal charge distribution. Attractive interactions may result in currents with reduced propagation length, whereas repulsive interactions may increase or decrease the occupation locally.

⁴One could account for thermalization which is implemented via so-called Lindblad superoperators that allow for energy transfer between the electron and the bosonic system (for details see [54] and references therein).

4 Publications: transverse charge, spin, and orbital transport in the steady state

In the previous two sections, the theoretical aspects for simulating transport phenomena have been introduced. In the following, the cumulative part of this thesis, five publication will be presented and placed into context of this work. In the present section, three publications concerning the transverse steady-state transport of charge, spin, and orbital angular momenta in kagome systems are discussed, respectively. Based on tight-binding calculations and the Berry-curvature formalism (as presented in Sec. 2), the results contribute to a microscopic understanding of the Hall effects in kagome systems (goal number one in the introduction).

Anomalous Hall effect (AHE) as an effective topological Hall effect (THE). The first publication [OB1] establishes the microscopic origin of the AHE in several noncollinear kagome magnets. Despite a vanishing net magnetization, a symmetry analysis shows that the effect is allowed by the magnetic point group of certain coplanar systems. In the publication, the system is analyzed on the Hamiltonian level by applying a set of unitary transformations to the Hamiltonian. Thereby, the equivalence of spin-orbit coupling (SOC) and a (virtual) tilting of the magnetic moments out of the kagome plane is revealed. This allows to interpret the unconventional AHE in compensated kagome magnets as an effective THE arising from the virtually noncoplanar magnetic texture.

Sources of the spin Hall effect (SHE) in noncollinear kagome magnets. In publication [OB2], the SHE has been computed for various noncollinear kagome magnets. Conventionally, SOC is considered to be essential for the SHE, but recently it has been demonstrated that the effect is allowed in these kagome systems, even though SOC is neglected. In this work, two sources which determine the spin Hall signal are revealed by relating the results to the findings of publication [OB1]. The dominant contribution arises from the coplanar noncollinear magnetic texture and exists without SOC. The second contribution mainly reduces the spin Hall signal and emerges from SOC or the equivalent out-of-plane tilting of the magnetic moments.

Unconventional orbital Hall effect (OHE) arising in s -orbital systems. In the third publication [OB3], an alternative mechanism for the generation of transverse orbital currents is established. Early studies on the OHE claimed hybridization of specific atomic orbitals [only *intra*-atomic contributions in atomic center approximation (ACA)] as the origin of the effect. However, in this publication, we go beyond the ACA and compute the OHE according to the modern formulation of orbital magnetization which includes *inter*-atomic contributions as well. In doing so, the *nonmagnetic* kagome lattice with only s orbitals is introduced as a minimal model for the OHE. By considering a slab geometry, it is demonstrated that orbital angular momentum is transported by a cycloid motion of a wave packet.

4.1 Anomalous Hall effect as an effective topological Hall effect

Anomalous Hall effect in noncollinear compensated kagome magnets. As presented in Sec. 2.3, the generation of transverse electric currents as a response to an applied homogeneous electric field is called Hall effect. It is described by off-diagonal elements $\sigma_{ij} = \frac{\partial j_i}{\partial E_j}$ of the electric conductivity tensor σ . In an experiment, one measures the Hall resistivity $\rho = \sigma^{-1}$ which allows to identify three contributions to the Hall signal [identical to Eq. (2.54)]

$$\rho_{xy} = R^{\text{NHE}} B_z^{\text{ext}} + R^{\text{AHE}} M_z^{\text{S}} + R^{\text{THE}} \chi_{\text{S}}. \quad (4.1)$$

Herein, the normal Hall effect (NHE) exists in nonmagnetic metals in the presence of an applied magnetic field B_z^{ext} . The second contribution is the anomalous Hall effect (AHE) which is typically related to a *net magnetization* M_z^S . Thus, the AHE has become a signature of ferromagnetism, but requires spin-orbit coupling (SOC). Finally, the topological Hall effect (THE) denotes the third contribution to the Hall signal. It exists in *noncoplanar* magnetic textures with a nonzero scalar spin chirality χ_S even without SOC.

Consequently, one would not expect that materials with a *coplanar* magnetic texture and *vanishing* net magnetization exhibit a Hall effect. However, a few years ago, it was demonstrated that the AHE exists in various Mn_3X compounds ($X=\text{Rh, Ir, Pt, Ga, Ge, Sn}$; cf. Fig. 5): the AHE was predicted in Mn_3Ir [13] and also reported experimentally shortly afterwards in Mn_3Sn [18] and Mn_3Ge [19]. These materials consist of layered kagome sublattices with a coplanar noncollinear antiferromagnetic texture formed by the Mn atoms and their magnetic moments, respectively (cf. Figs. 5 and 6). The three contributions in the above equation can be distinguished phenomenologically, but the origin to the intrinsic contribution to the Hall signal is a nonzero Berry curvature. Recall that the intrinsic Hall conductivity σ_{xy} is given by the k -space integral of the Berry curvature over all occupied states in the Brillouin zone (BZ) [cf. Eq. (2.67)]. The AHE in Mn_3X is allowed by the magnetic point group of the materials: a combination of the noncollinear magnetic texture in combination with SOC breaks certain symmetries [13, 14]. This leads to a nonzero Berry curvature which gives rise to the Hall conductivity. However, the microscopic mechanism of the unconventional Hall effect remains to be revealed.

This publication. In the following publication “Microscopic origin of the anomalous Hall effect in noncollinear kagome magnets” [OB1], an intuitive understanding of the AHE in several kagome magnets is established. The intrinsic Hall conductivity is computed according to the Berry curvature formalism based on tight-binding calculations, as presented in Sec. 2. Moreover, the system is analyzed on the Hamiltonian level by applying a set of unitary transformations to the model Hamiltonian [cf. Eq. (2.82)]. Each transformation rotates the local coordinate system at each lattice site i such that the z axis is tilted by an angle α towards the magnetic moment \mathbf{m}_i at this site (cf. Fig. 6 in [OB1]). In the new local coordinate system, each magnetic moment is virtually tilted by α out of the kagome plane. By applying the transformation to all terms of the Hamiltonian, we reveal that parameter-dependent effective hopping and SOC terms arise. The main result of the transformation is that this ‘virtual’ magnetic texture $\{\tilde{\mathbf{m}}_i\}$ arises in several noncollinear kagome magnets from SOC which is equivalent to an out-of-plane tilting of the magnetic moments $\{\mathbf{m}_i\}$.

In particular, a critical tilting angle exists for which SOC is effectively compensated. In this case, we interpret the unconventional AHE of the *coplanar* kagome antiferromagnets as an effective THE arising from a net scalar spin chirality of the *noncoplanar* virtual texture. Consequently the coplanar system with SOC behaves like a noncoplanar system without SOC. Furthermore, we demonstrate that a *noncoplanar* system with SOC can be transformed into a system with a virtual *coplanar* texture for which SOC is effectively compensated. Consequently, the Hall effect is absent for this configuration, although a conventional symmetry analysis would allow the effect.

The following publication: Reprinted (whole article) with permission from O. Busch, B. Göbel and I. Mertig, Physical Review Research **2**, 033112 (2020); Ref. [OB1]; Microscopic origin of the anomalous Hall effect in noncollinear kagome magnets. Published by the American Physical Society under the terms of the Creative Commons Attribution 4.0 International license.

Microscopic origin of the anomalous Hall effect in noncollinear kagome magnets

Oliver Busch , Borge Göbel ,* and Ingrid Mertig

Institut für Physik, Martin-Luther-Universität Halle-Wittenberg, D-06099 Halle (Saale), Germany



(Received 28 May 2020; accepted 1 July 2020; published 21 July 2020)

The anomalous Hall effect is commonly considered a signature of ferromagnetism. However, recently, an enormous anomalous Hall conductivity was measured in the compensated kagome magnets Mn_3Sn and Mn_3Ge . The occurrence of this effect is allowed by the magnetic point group of these materials; however, its emergence is still lacking a microscopic explanation. Herein we show that the spin-orbit coupling and an out-of-plane tilting of the texture are equivalent for several kagome magnets. Consequently, a coplanar system with spin-orbit coupling behaves as if it were virtually noncoplanar. We show via tight-binding model calculations that the Hall effect can mainly be interpreted as a topological Hall effect generated by the opening angle of the virtually tilted texture. Furthermore, upon tilting the fixed texture out of the kagome plane, we find a critical tilting angle for which the Hall conductivity vanishes for all energies. In this case, the Hamiltonian is invariant under a combined time-reversal and mirror symmetry, because the virtual texture is coplanar.

DOI: [10.1103/PhysRevResearch.2.033112](https://doi.org/10.1103/PhysRevResearch.2.033112)

I. INTRODUCTION

The Hall effect of electrons is one of the most intensely investigated effects in solid-state physics. It describes the transverse deflection of moving conduction electrons in a Hall bar when time-reversal symmetry is broken. Besides the conventional Hall effect which is caused by an externally applied magnetic field [1], the anomalous Hall effect [2] has become a signature of ferromagnets [3]. This effect can be caused by the skew-scattering [4,5] and side-jump [6] mechanisms. Both contributions are extrinsic; they are related to the spin-orbit coupling at defects [3]. Besides, even in a perfect sample, an anomalous Hall effect can arise intrinsically [7] due to the occurrence of a reciprocal-space Berry curvature [8,9]. Typically, all three contributions are related to a net magnetization; it breaks a set of time-reversal and spatial symmetries so that a reciprocal-space Berry curvature can arise. Furthermore, a Berry curvature can also be caused by noncollinear magnetic textures with a net scalar spin chirality [10], i.e., certain noncoplanar textures like magnetic skyrmions [11,12]. The canted magnetic moments effectively generate an emergent magnetic field (or real-space Berry curvature) that causes the so-called topological Hall effect [13].

Over the last years, a straightforward microscopic understanding has been established for all three of the above presented contributions to the Hall effect. However, recently it was found that also materials without a net magnetization can exhibit an anomalous Hall effect [14–18], whose microscopic origin must be different from the anomalous Hall effect mentioned above. In several layered kagome materials a coplanar

spin texture is observed with a vanishing net magnetization, and still tight-binding models and first-principle calculations predict finite anomalous Hall conductivities in agreement with magnetic point group analyses [18,19]. Recent experiments in Mn_3Sn [16] and Mn_3Ge [17], both members of the space group $P6_3/mmc$ (No. 194) [16,18], have reported large anomalous Hall conductivities of up to $500 \Omega^{-1} \text{cm}^{-1}$ confirming these predictions [20]. However, a straightforward microscopic understanding is still missing.

Herein we establish a microscopic explanation for the occurrence of a finite anomalous Hall effect in several kagome magnets. We show that the spin-orbit coupling for these systems is equivalent to a tilting of the magnetic moments out of the kagome plane. The Hall effect can then be explained by conventional means upon considering the net moment and the net scalar spin chirality of the virtually tilted texture instead of the actual texture. Using tight-binding calculations, we show that the topological Hall contribution (caused by the net scalar spin chirality) is dominant over the anomalous Hall contribution (caused by the net magnetic moment of the virtual texture). Furthermore, we show that the virtual tilting due to the spin-orbit coupling can be compensated by tilting the actual texture along the opposite out-of-plane direction. For a critical angle the virtual texture is coplanar, restoring the combined time-reversal and mirror symmetry of the Hamiltonian that forbids finite Hall conductivities.

II. MODEL AND METHODS

Throughout our study, we consider the tight-binding Hamiltonian as used in Ref. [14] in which the anomalous Hall effect in these kagome magnets has first been predicted,

$$H = t \sum_{(i,j)} c_i^\dagger c_j + m \sum_i c_i^\dagger (\mathbf{m}_i \cdot \boldsymbol{\sigma}) c_i + i\lambda \sum_{(i,j)} c_i^\dagger (\mathbf{n}_{ij} \cdot \boldsymbol{\sigma}) c_j. \quad (1)$$

*Corresponding author: boerge.goebel@physik.uni-halle.de

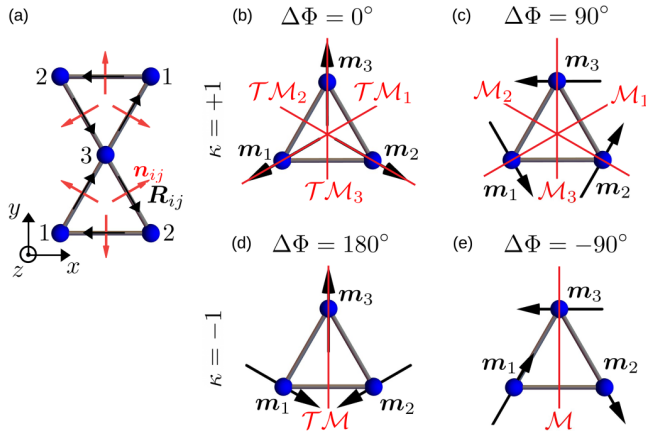


FIG. 1. Coplanar magnetic textures on a kagome lattice. (a) The three basis atoms have four nearest neighbors each. For each of these bonds the spin-orbit vector $\mathbf{n}_{ij} = -\mathbf{n}_{ji}$ is indicated (red); the black arrow indicates the direction ij versus ji). (b) The three basis atoms and magnetic moments \mathbf{m}_i (indicated by arrows) in the coplanar radial configuration. The unit cell has three symmetry planes indicating a combined time-reversal and mirror symmetry (red). The texture is characterized by a positive vector spin chirality $\kappa = +1$ and an in-plane offset $\Delta\Phi = 0^\circ$, as indicated. (c) The toroidal phase. All moments are locally rotated by 90° compared to (b) giving $\Delta\Phi = 90^\circ$. This magnetic texture has three mirror symmetry planes. (d), (e) Textures with a negative vector chirality are shown. They only have one symmetry plane each.

The first term represents the hopping of an electron from lattice site j to i with the amplitude t . The second term describes the Hund's coupling of electron spin and magnetic texture $\{\mathbf{m}_i\}$. The strength of this interaction is $m = 1.7t$ throughout this paper. The third term represents the spin-orbit coupling, as introduced in Ref. [14], similar to the spin-orbit coupling in graphene [21]. The term preserves the inversion symmetry, but accounts for the difference between left- and right-hand environments for electrons hopping along different paths in a kagome layer [14]. The vectors $\mathbf{n}_{ij} = -\mathbf{n}_{ji}$ are visualized in Fig. 1(a) (red arrows).

This minimal model comprises a subset of the full Hamiltonian. Only a few relevant bands near the Fermi energy are considered and the magnetic texture $\{\mathbf{m}_i\}$ is assumed to be constituted by energetically lower states and is fixed. Still, the model allows us to establish an understanding for the emerging Hall effect since it has the same symmetry as the complete system.

Diagonalizing this Hamiltonian gives the band structure as eigenvalues $E_n(\mathbf{k})$ and the eigenvectors $|n_{\mathbf{k}}\rangle \equiv |u_n(\mathbf{k})\rangle$ from which the intrinsic contribution to the Hall conductivity can be calculated [3],

$$\sigma_{xy}(E_F) = -\frac{e^2}{h} \frac{1}{2\pi} \sum_n \int_{E(\mathbf{k}) \leq E_F} \Omega_n^{(z)}(\mathbf{k}) d^2k. \quad (2)$$

We treat the Fermi energy E_F as a parameter that can be tuned by doping or application of a gate voltage. $\Omega_n^{(z)}(\mathbf{k})$ is the z

component of the reciprocal-space Berry curvature of band n ,

$$\Omega_n^{(z)}(\mathbf{k}) = -2 \operatorname{Im} \sum_{m \neq n} \frac{\langle n_{\mathbf{k}} | \partial_{k_x} H_{\mathbf{k}} | m_{\mathbf{k}} \rangle \langle m_{\mathbf{k}} | \partial_{k_y} H_{\mathbf{k}} | n_{\mathbf{k}} \rangle}{[E_n(\mathbf{k}) - E_m(\mathbf{k})]^2}.$$

Next, we introduce the different configurations of the considered magnetic texture. The unit cell of a kagome layer consists of three atoms. The three magnetic moments have an angle of 120° with respect to each other. The polar angle of their orientation Φ_i and the polar angle of their position vector ϕ_i (center of the coordinate system in the center of the plaquette) are related by

$$\Phi_i = \kappa \phi_i + \Delta\Phi \quad (3)$$

for all basis atoms $i = 1, 2, 3$. Here $\kappa = \pm 1$ is the vector spin chirality. We discuss the following experimentally observed kagome magnets: For a positive vector spin chirality $\kappa = +1$ there exist two different configurations of Mn_3ZN ($Z = \text{Ni}, \text{Ga}, \text{Zn}, \text{Sn}, \text{Ag}, \text{Rh}, \text{Pt}$) [22,23] or Mn_3X ($X = \text{Rh}, \text{Ir}, \text{Pt}$) [24] [radial order $\Delta\Phi = 0^\circ, 180^\circ$ and toroidal order $\Delta\Phi = \pm 90^\circ$ shown in Figs. 1(b) and 1(c)], and for a negative vector spin chirality $\kappa = -1$ there exist two different configuration of Mn_3Y ($Y = \text{Sn}, \text{Ge}, \text{Ga}$) [25] [$\Delta\Phi = 0^\circ, 180^\circ$ and $\Delta\Phi = \pm 90^\circ$ shown in Figs. 1(d) and 1(e)]. Additionally, the tight-binding model allows us to arbitrarily vary the in-plane offset angle $\Delta\Phi$, similarly to the study in Ref. [26], as well as the azimuthal angle θ [cf. Fig. 3(a); $\theta = 90^\circ$ for coplanar textures] like in Ref. [14] in order to analyze the canted magnetic textures later in this paper.

Before we present our results, we want to stress that we consider three fundamentally different types of textures throughout our paper: the fixed magnetic texture, the electron spin texture, and a virtual texture. The fixed magnetic texture $\{\mathbf{m}_i\}$ is a real-space texture that is formed by localized magnetic moments. This texture is predefined and directly enters the Hamiltonian (1). It is defined by the in-plane orientation given in Eq. (3) and the azimuthal angle θ . Besides, the itinerant spin magnetic moments of the conduction electrons form a texture in reciprocal space. We obtain this so called spin texture by calculating the spin expectation value

$$\langle s_n(\mathbf{k}) \rangle = \langle n_{\mathbf{k}} | \boldsymbol{\Sigma} | n_{\mathbf{k}} \rangle, \quad (4)$$

where $\boldsymbol{\Sigma} = \text{diag}(\boldsymbol{\sigma}, \dots, \boldsymbol{\sigma})$ is given by the vector of Pauli matrices $\boldsymbol{\sigma}$. For a deeper understanding we can also analyze the spin texture that originates from a single atom. In this case we use $\boldsymbol{\Sigma} = \text{diag}(\mathbf{0}, \dots, \boldsymbol{\sigma}, \dots, \mathbf{0})$. As we will present later in this paper, the transport properties are only loosely related to the fixed magnetic texture or the spin texture of electrons. Instead, the spin-orbit coupling gives rise to a virtual texture $\{\tilde{\mathbf{m}}_i\}$ which is effectively tilted with respect to the fixed texture out of the kagome plane. This virtual texture is not measurable but is determined by the symmetry of the system. Therefore, it determines the emerging Hall effects and can be utilized to explain whether and how certain symmetries are broken.

III. RESULTS AND DISCUSSION

In the following we present calculations of the band structure and the anomalous Hall conductivity within the

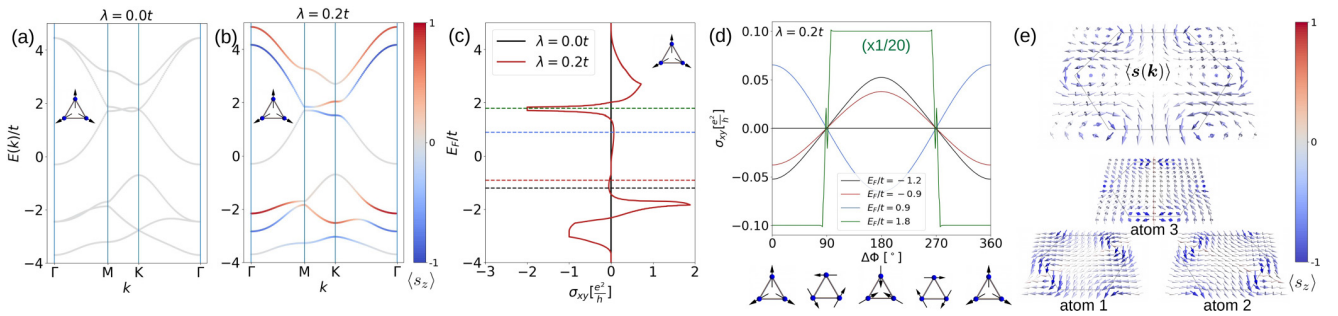


FIG. 2. Band structure and anomalous Hall conductivity for the coplanar configurations, $\theta = 90^\circ$. (a) The band structure of the radial configuration, $\Delta\Phi = 0$, when spin-orbit interaction is not taken into account. The out-of-plane spin expectation value $\langle s_z \rangle$ of all bands and k points vanishes (gray). (b) Similar to (a) but the spin-orbit interaction is now taken into account. Degeneracies are lifted and the spin expectation value now has a finite out-of-plane component (red, positive; blue, negative). (c) The anomalous Hall conductivity corresponding to the band structure in (b). (d) shows the anomalous Hall conductivity for various Fermi energies [colored lines indicated in (c)] upon locally rotating each moment around the local z axis. Cartoons of the texture for several angles $\Delta\Phi$ are shown below. (e) The spin expectation value for the energetically lowest band in (b). The color encodes the out-of-plane component. Below, the atom-resolved spin expectation value is shown.

framework of the presented tight-binding model. We focus here on the $\kappa = +1$ phase as for example Mn_3Pt . Later we will briefly refer to the $\kappa = -1$ phase as well, which shows similar results and for which the same arguments hold that we will establish in the following.

For the $\kappa = +1$ phase, we begin by discussing different coplanar configurations and with a review of the existing literature. To reveal the mechanism for the emergence of this effect—the main subject of our paper—we analyze the expectation value of the conduction electrons’ spin, establish the equivalence of the spin-orbit coupling and an out-of-plane tilting of the moments, and even consider fixed magnetic textures that have been tilted out of the kagome plane.

A. Band structure and anomalous Hall conductivity of the coplanar radial configuration

Before we consider magnetic systems, we start with a brief analysis of the structural kagome lattice. The three atoms in the unit cell of a nonmagnetic kagome layer without spin-orbit coupling give rise to three spin-degenerate bands (band structure shown in Fig. 1 of the Supplemental Material [27]). One of these bands is ideally flat and the other two bands exhibit a band structure similar to graphene: They touch linearly at the Brillouin zone’s K points exhibiting Dirac cones. Since a magnetic texture is not considered yet, time-reversal symmetry is conserved and an anomalous Hall conductivity is absent.

Next, we will review the results for coplanar configurations, similar to Refs. [14,18,26,28]. When we consider the magnetic texture like in the radial phase of Mn_3Pt , as shown in Fig. 1(b), the spin degeneracy of the bands is lifted due to the broken time-reversal symmetry and six individual bands are visible [Fig. 2(a)]. Reminiscent of the Dirac cones of the original band structure, bands touch linearly at the K points. Also, degeneracies are present at Γ . Here, in contrast to the Dirac points, the band structure is quadratic for all bands.

The mirror symmetry M is broken in the system which is essential for the emergence of a Hall conductivity. However, since spin-orbit coupling is still not taken into account, the system has a combined time-reversal and mirror symmetry

TM forbidding the occurrence of an anomalous Hall conductivity, since $\Omega_n^{(z)}(-\mathbf{k}) = -\Omega_n^{(z)}(\mathbf{k})$ [14] [cf. red lines representing TM symmetry planes in Fig. 1(b)]. The conduction electrons’ spins partially align with the spatially dependent fixed magnetic texture at each lattice site (see Fig. 2(a) of the Supplemental Material [27]). Both spin texture and fixed magnetic texture are oriented in the kagome plane.

When spin-orbit interaction is considered, TM symmetry is broken (we establish how this symmetry is broken microscopically later in this paper) and the degeneracies in the band structure are lifted [red in Fig. 2(b)]. Away from the high-symmetry points, the band structure stays mostly unchanged. The breaking of TM symmetry leads to the emergence of an anomalous Hall conductivity [red in Fig. 2(c)] that exhibits a pronounced energy dependence. In the global band gaps the conductivity is quantized in units of e^2/h ; i.e., a quantum anomalous Hall effect occurs [29]. The system becomes a Chern insulator.

B. In-plane rotation of the magnetic texture

A noncollinear coplanar magnetic texture does not always lead to the emergence of an anomalous Hall effect. When the magnetic moments $\{\mathbf{m}_i\}$ are collectively rotated around the local z axis by $\Delta\Phi = 90^\circ$, the alternative phase of materials like Mn_3Pt is established. This system has three mirror symmetry planes [red in Fig. 1(c)] which protect the Dirac points and render the anomalous Hall effect zero, even upon considering spin-orbit coupling.

In Ref. [26] Zhou *et al.* have investigated the anomalous Hall conductivity for phases between these two states. We find similar results and conclude the following: For Fermi energies that are close to the band edges [red and blue curves in Fig. 2(d)], the signal is proportional to $\cos(\Delta\Phi)$, where $\Delta\Phi$ is the in-plane rotation angle ($\Delta\Phi = 0^\circ, 180^\circ$ corresponds to the radial phase and $\Delta\Phi = \pm 90^\circ$ corresponds to the toroidal phase). This observation is reasonable, since the projection of each moment on the potential mirror plane breaks the mirror symmetry; it is given by $\cos(\Delta\Phi)$ as well. Loosely speaking, the broken mirror symmetry does not only allow for the anomalous Hall effect to arise, but the “degree by which

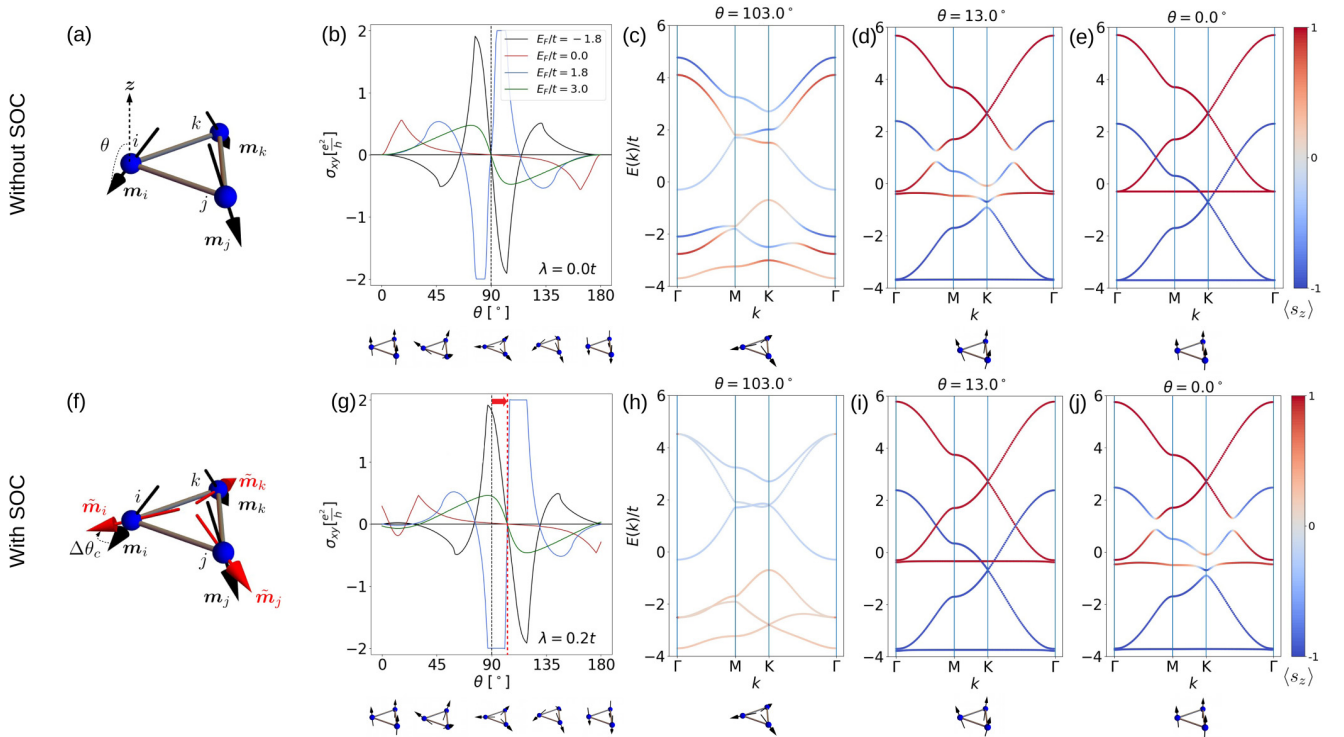


FIG. 3. Anomalous Hall conductivity under out-of-plane tilting of the fixed magnetic texture. In (a)–(e) spin-orbit coupling (SOC) has not been considered, whereas in (f)–(j) it is taken into account. (a) A noncollinear and noncoplanar configuration. Black arrows indicate the magnetic moments \mathbf{m}_i . (b) Hall conductivity versus azimuthal angle θ . All four curves (different colors correspond to different Fermi energies) are antisymmetric with respect to $\theta = 90^\circ$ which is the coplanar configuration as indicated by the cartoons below. (c)–(e) Band structures with out-of-plane components of the spin expectation value (red, positive; blue, negative) for different azimuthal angles θ as indicated. (f) The texture from (a) in black. Additionally, the virtual magnetic texture $\{\tilde{\mathbf{m}}_i\}$ is shown in red. This texture arises due to the spin-orbit coupling, as explained in the main text, and it is characterized by a reduced azimuthal angle $\theta - \Delta\theta_c$. (g) Same as (b), but spin-orbit interaction is taken into account. Here the curves are antisymmetric with respect to $\theta_c = 90^\circ + \Delta\theta_c \approx 103^\circ$. (h)–(j) Same as (c)–(e), but spin-orbit interaction is considered as in panel (g).

the symmetry is broken” even determines the magnitude of the effect. Furthermore, this projection also determines the size of the band gaps due to spin-orbit coupling. For the toroidal phase ($\Delta\Phi = \pm 90^\circ$), the band structure is unaffected by the spin-orbit coupling (band structures are shown in Fig. 3 of the Supplemental Material [27]).

The $\cos(\Delta\Phi)$ behavior does not hold for Fermi energies close to the band edge, let alone in the band gap: the black curve in Fig. 2(d) is not perfectly cosinusoidal and the green curve at $E_F = 1.8t$ is a step function, since the corresponding Fermi energy is located in a band gap (an opened Dirac point for $\Delta\Phi \neq \pm 90^\circ$) and the Hall conductivity must be quantized.

Summarizing up to this point, we have presented how the anomalous Hall conductivity for noncollinear coplanar magnetic textures can be related to the breaking of M and TM symmetries, which is where the limit of the existing literature is reached. In the following, we will unravel the underlying microscopic mechanism.

C. Out-of-plane spin tilting of the conduction electrons

First, we consider a quantity that allows us to explain the emergence of the anomalous Hall effect in coplanar systems

microscopically: a tilted spin texture formed by the conduction electrons.

As mentioned, without spin-orbit interaction, the conduction electrons’ spins remain in the plane, partially aligned with the fixed magnetic texture [cf. completely gray bands in Fig. 2(a)]. When the spin-orbit interaction is taken into account in the toroidal phase, this is unchanged and the Hall conductivity stays zero (cf. Fig. 3 of the Supplemental Material [27]). However, in the radial phase, the spins start to cant out of the plane [red and blue in Fig. 2(b)]. This canting is k and band dependent, and general trends can be observed: For the first (energetically lowest) and fourth band, the tilting is along the $-z$ direction, while for the third and sixth (energetically highest) band it is along the $+z$ direction. This relates quite well to the anomalous Hall signal shown in Fig. 2(c): Within the first and fourth band, the conductivity is negative (or close to zero if positive) and within the third and sixth band it is positive. For energies within the second or fifth band, where the out-of-plane spin component is positive and negative, the anomalous conductivity changes sign.

Even though we have not yet explained what causes the tilting, one can register that the spin moment of the conduction electrons is nonzero in this model, even though the fixed magnetic texture is coplanar. For this reason, one may argue

that it is clear that a finite Hall conductivity is calculated by conventional means: the total texture has a net magnetization and even a net scalar spin chirality $\chi_s = \mathbf{s}_i \cdot (\mathbf{s}_j \times \mathbf{s}_k)$ which give rise to an anomalous and topological Hall effect, respectively.

While this explanation seems reasonable a first glance, in the following, we vary the azimuthal angle of the fixed magnetic texture and find that there exist cases for which this explanation does not hold: Even for a combined texture with a net moment and a net scalar spin chirality the Hall effect can be absent and for a completely compensated system the Hall effect can be finite. Therefore, next we analyze the system on the Hamiltonian level to unravel the microscopic mechanism and to show how the TM symmetry is broken precisely and how it can even be restored for certain noncoplanar magnetic textures.

D. Out-of-plane rotation of the magnetic texture

In the following, we tilt the fixed texture out of the kagome plane (azimuthal angle θ) which, in the end, allows us to establish the actual microscopic explanation for the emergence of the anomalous Hall effect in kagome magnets: the existence of a virtual texture $\{\tilde{\mathbf{m}}_i\}$ that is tilted with respect to the actual magnetic texture $\{\mathbf{m}_i\}$ due to the spin-orbit coupling.

First we present and discuss the results upon changing θ without taking spin-orbit interaction into account [Fig. 3(b)]. This reference system exhibits a pure topological Hall effect since the anomalous Hall effect is absent by definition. For $\theta = 0^\circ$ and 180° , the localized moments are parallel and point out of the kagome plane. For $\theta = 90^\circ$ the moments are coplanar as described above. In both cases the scalar spin chirality vanishes and a topological Hall effect does not emerge. For all other angles the scalar spin chirality

$$\chi_s = \mathbf{m}_i \cdot (\mathbf{m}_j \times \mathbf{m}_k) = \frac{3\sqrt{3}}{2} \cos\theta \sin^2\theta \quad (5)$$

(i, j , and k are the lattice sites of a kagome plaquette) is finite and so is the calculated Hall conductivity (except for single angles where contributions from different bands compensate). For all energies, the angular-dependent curves are antisymmetric with respect to $\theta = 90^\circ$, due to the antisymmetry of the scalar spin chirality. While continuously changing the azimuthal angle θ , the band structure changes considerably. For this reason, a fixed energy may even shift through band gaps into other bands as is seen in the blue curve for $E_F = 1.8t$. When the Fermi energy is located in the gap, the Hall conductivity is quantized. We repeated these calculations also for fixed occupation numbers (see Fig. 4 of the Supplemental Material [27]). The curves remained antisymmetric.

When we consider the spin-orbit interaction [cf. Fig. 3(g)], the curves change and the configurations $\theta = 0^\circ, 90^\circ$, and 180° now yield a finite signal in agreement with the above presented findings that the radial type of the coplanar configuration ($\theta = 90^\circ$) exhibits an anomalous Hall effect and compatible with the typical observation that a collinear ferromagnet ($\theta = 0^\circ, 180^\circ$) exhibits an anomalous Hall effect when spin-orbit interaction is present. Generally, the shape of this angular-dependent curve looks similar to the case without spin-orbit coupling. However, besides minor changes near the

ferromagnetic configurations, it is mainly shifted. The curve is still antisymmetric, not with respect to $\theta = 90^\circ$, but shifted by about $\Delta\theta_c = 13^\circ$ to an azimuthal angle $\theta_c = 103^\circ$. This critical angle is parameter dependent, and we will precisely derive it later in this paper.

The systems for the two angles $\theta = 13^\circ$ and $\theta = 103^\circ$ are special in several regards: the Hall conductivity vanishes, the Dirac points are reestablished, and the reciprocal-space spin texture is homogeneous, (anti)parallel to the fixed texture [homogeneous light colors in Fig. 3(h) and homogeneous bright colors in Fig. 3(i)]. For all other configurations, even for the coplanar texture ($\theta = 90^\circ$) or the ferromagnetic configuration ($\theta = 0^\circ, 180^\circ$) [Fig. 3(j)], none of these three features are fulfilled.

E. Microscopic mechanism: Tilted virtual texture hidden in the Hamiltonian

These findings point toward a higher symmetry for the two special configurations characterized by $\theta = \Delta\theta_c$ and $\theta = \theta_c = \Delta\theta_c + 90^\circ$, even though the texture itself does not have a higher symmetry than the other textures (they have an even lower symmetry compared to the coplanar or ferromagnetic configuration).

As we show, this stems from the fact that the electronic properties of the system are not determined by the fixed texture, the conduction electrons' spin texture, or a combined texture, but by a virtual texture characterized by the Hamiltonian. This virtual texture $\{\tilde{\mathbf{m}}_i\}$ arises, since the spin-orbit coupling in this system is equivalent to a canting of the fixed magnetic texture $\{\mathbf{m}_i\}$ out of the kagome plane [cf. red and black arrows in Figs. 3(a) and 3(f)], as we summarize in the following. The transformation is shown in the Appendix in detail.

The full Hamiltonian (1) used throughout this paper can be transformed to

$$H = \sum_{(i,j)} t_{ij}^{\text{eff}} d_i^\dagger d_j + m \sum_i d_i^\dagger (\tilde{\mathbf{m}}_i \cdot \boldsymbol{\sigma}) d_i + i\tilde{\lambda} \sum_{(i,j)} d_i^\dagger (\mathbf{n}_{ij} \cdot \boldsymbol{\sigma}) d_j, \quad (6)$$

by applying a unitary transformation U_i (new electron operators are d_i), that rotates the coordinate system at each lattice site. The new z axis of the coordinate system at lattice site i has an angle α with respect to the initial z axis and has been tilted along the direction of the magnetic moment \mathbf{m}_i . A sketch of this rotation is shown in Fig. 6 as part of the Appendix.

This transformation, of course, leaves the physical properties unchanged but the spin and the magnetic moments are measured differently. In this lattice-site dependent coordinate system, the azimuthal angle of the fixed magnetic texture is effectively decreased by α ,

$$\tilde{\mathbf{m}}_i = \begin{pmatrix} \cos(\Phi_i) \sin(\theta - \alpha) \\ \sin(\Phi_i) \sin(\theta - \alpha) \\ \cos(\theta - \alpha) \end{pmatrix}. \quad (7)$$

When the transformation is applied to the hopping term and the spin-orbit coupling, the (now spin-dependent) hopping amplitude is modified as given in the Appendix but most

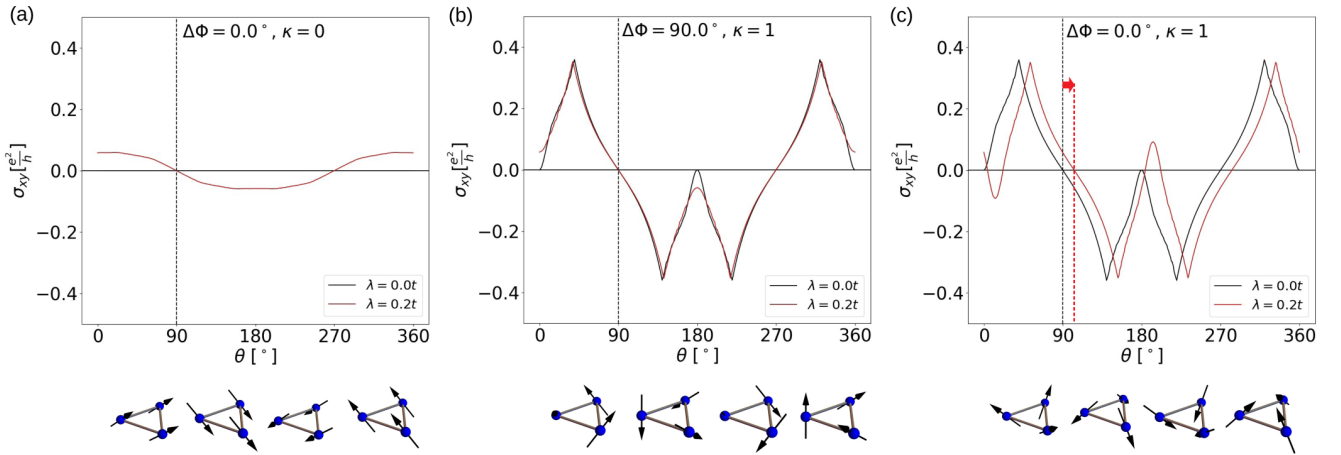


FIG. 4. Different contributions to the Hall effect for different magnetic textures. (a) The Hall conductivity for a collinear magnetic texture is shown under variation of the azimuthal angle θ . Only a conventional anomalous Hall effect proportional to m_z of the fixed magnetic texture is present when spin-orbit interaction is considered. (b) The toroidal texture is considered. Upon variation of θ the scalar spin chirality χ_s is finite and an additional topological Hall effect arises that is much larger than the anomalous Hall effect. (c) The radial texture is considered, as discussed above. The curve from the toroidal texture is mainly shifted by $\Delta\theta_c = 13^\circ$ which characterizes the nature of the “new” anomalous Hall effect in this material class. All calculations were performed at a constant occupation number of $n_{\text{occ}} = 3.4$.

importantly both terms now contribute with off-diagonal elements that can be identified as an effective spin-orbit coupling. For the radial phase it is quantified by

$$\tilde{\lambda} = -\frac{\sqrt{3}}{2}\sin(\alpha)t + \cos(\alpha)\lambda. \quad (8)$$

This transformation shows that the spin-orbit interaction and a texture that is tilted out of the kagome plane have the same effect in this system. Especially, a critical angle α_c exists, for which the effective spin-orbit coupling is compensated, $\tilde{\lambda} = 0$. This angle determines the effective tilting angle $-\Delta\theta_c$ of the virtual texture $\{\tilde{\mathbf{m}}_i\}$ compared to the fixed texture $\{\mathbf{m}_i\}$ [cf. Fig. 3(f)] that arises due to spin-orbit coupling. For the phase with positive vector spin chirality, $\kappa = +1$, the critical compensation angle of the magnetic texture for which the virtually tilted texture is coplanar is

$$\Delta\theta_c = \alpha_c = \arctan\left[\frac{\lambda}{t\sqrt{3}/2}\cos(\Delta\Phi)\right]; \quad (9)$$

see the Appendix. The λ and $\Delta\Phi$ dependencies have been confirmed numerically in Fig. 5 of the Supplemental Material [27]. The numerically determined data points have been determined by looking at the avoided crossings that form Dirac points at the critical angle. Furthermore, the Hall conductivity vanishes for all energies at these angles.

In summary, we have shown that the spin-orbit coupling term can be totally compensated by tilting the texture by $\Delta\theta_c$ along the azimuthal direction (and also modifying the hopping). This means that the consequences of the spin-orbit coupling and a tilted texture are equivalent in this system: A fixed texture $\{\mathbf{m}_i\}$ that is coplanar, $\theta = 90^\circ$, under the influence of spin-orbit coupling, $\lambda \neq 0$, behaves like a tilted texture $\{\tilde{\mathbf{m}}_i\}$ in a system without spin-orbit coupling, $\tilde{\lambda} = 0$, thereby explaining the emergence of the anomalous Hall effect in the coplanar system. Likewise, a texture $\{\mathbf{m}_i\}$ with a critical azimuthal angle $\theta_c = 90^\circ + \Delta\theta_c$ with spin-orbit coupling, $\lambda \neq 0$, behaves like a texture $\{\tilde{\mathbf{m}}_i\}$ that is coplanar, $\theta = 90^\circ$, in

a system without spin-orbit coupling, $\tilde{\lambda} = 0$, explaining why the Hall conductivity vanishes for $\theta = 103^\circ$ in Fig. 3(g). In a similar way, this explains why the configuration characterized by $\theta = 13^\circ$ in Fig. 3(i) behaves like a ferromagnetic configuration, while the actual ferromagnetic configuration does not: The azimuthal angle of the virtual textures is reduced by 13° .

The two special configurations for $\theta = \Delta\theta_c = 13^\circ$ and $\theta = \theta_c = \Delta\theta_c + 90^\circ = 103^\circ$ restore the TM symmetry of the Hamiltonian that we initially discussed in the coplanar system without spin-orbit coupling. This symmetry leads to the closing of Dirac points and to the absence of the Hall conductivity for these particular configurations since it renders the reciprocal-space Berry curvature antisymmetric $\Omega_n^{(z)}(-\mathbf{k}) = -\Omega_n^{(z)}(\mathbf{k})$. On the other hand, for a coplanar fixed magnetic texture ($\theta = 90^\circ$) the virtual texture is tilted by $-\Delta\theta_c$. This virtual texture has a net magnetization and a scalar spin chirality and therefore gives rise to anomalous and topological Hall effects which are allowed by the breaking of the TM symmetry.

F. Effective topological Hall effect

Next, we want to show which mechanism of the virtually tilted texture is more relevant: a virtual anomalous Hall effect caused by the net moment of the virtual texture or a virtual topological Hall effect caused by the scalar spin chirality of the virtual texture.

To differentiate the calculated signal into anomalous and topological Hall effects, in the following, we compare the θ dependence of the Hall conductivity of the radial-type magnetic texture with the toroidal phase and a collinear phase, as presented in Fig. 4. Without spin-orbit coupling, the toroidal spin texture behaves equally to the radial-type texture, since both exhibit a purely topological Hall effect, that is proportional to the scalar spin chirality, which is independent of $\Delta\Phi$ [given in Eq. (5)]. The collinear configuration does not

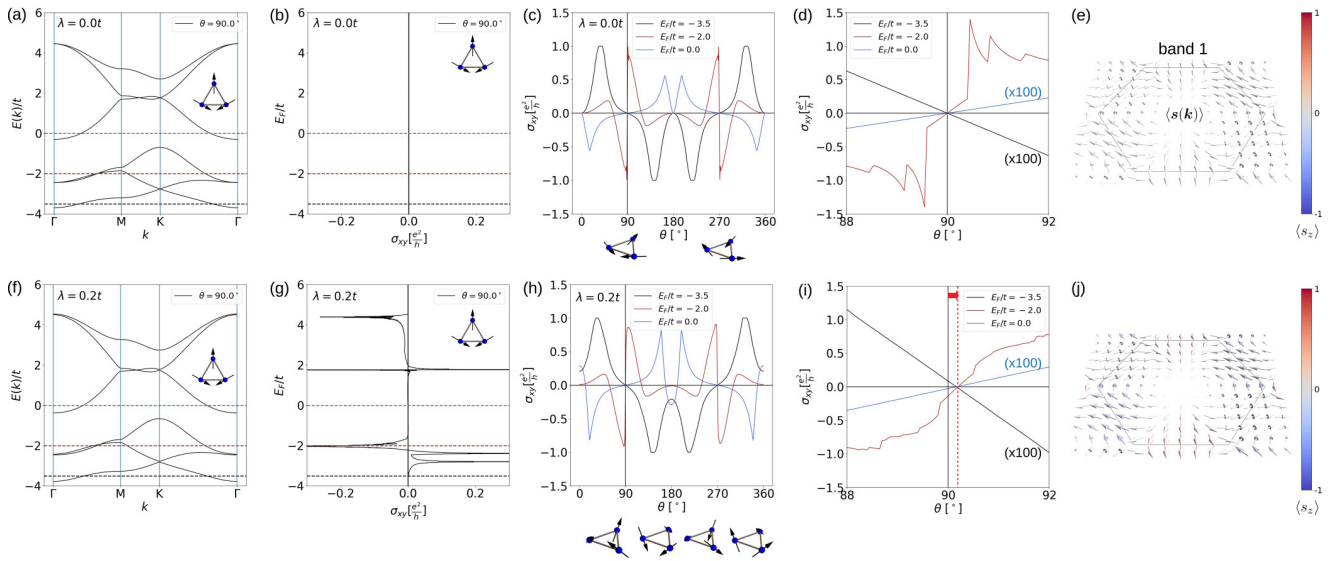


FIG. 5. Results for the phase of negative vector spin chirality, $\kappa = -1$ and $\Delta\Phi = 180^\circ$. This is the texture that has been experimentally investigated in Mn_3Ge [17]. (a)–(e) show the results without spin-orbit coupling. (a) The band structure, (b) the energy-resolved conductivity for the coplanar ($\theta = 90^\circ$) texture, (c) the Hall conductivity for different constant Fermi energies [colors as indicated in (a), (b)] in dependence on the azimuthal angle θ . (d) shows a magnification of (c) near $\theta = 90^\circ$. (e) The spin texture of the energetically lowest band for $\theta = 90^\circ$. (f)–(j) show the same quantities when the spin-orbit interaction $\lambda = 0.2t$ is taken into account. Similarly to the result of the radial phase (as extensively presented in the paper), the virtual texture $\{\tilde{m}_i\}$, determined by the Hamiltonian, is tilted due to the spin-orbit coupling. This also affects the reciprocal-space spin texture shown in (j).

exhibit a finite signal since the scalar spin chirality is always zero.

When spin-orbit coupling is taken into account, the anomalous Hall effect is also present. Conventionally, it is proportional to the out-of-plane magnetization $\cos\theta$ which is observable for the collinear configuration in panel (a), that exhibits a pure anomalous Hall effect. For the toroidal texture (b) the signal is symmetric with respect to $\theta = 90^\circ$. The topological Hall effect and the (considerably smaller) anomalous Hall effect are present. In panel (c) the radial configuration is shown as discussed above. In addition to these two effects, a shift in θ is observable which characterizes the nature of this “new” effect as explained above.

Since the topological Hall effect in these calculations is significantly larger than the anomalous Hall effect (largest for $\theta = 0^\circ, 180^\circ$), the “new” contribution to the Hall effect in kagome magnets can be understood mainly as a topological Hall effect caused by a virtually tilted texture.

G. Phase of negative vector spin chirality

Coming back to the experiments in Mn_3Sn [16] and Mn_3Ge [17] where this “new” anomalous Hall effect has been measured recently, we have also investigated the phase of negative vector spin chirality, $\kappa = -1$. The results are shown in Fig. 5. In these materials the calculated Hall conductivity is smaller compared to the phase of positive chirality but it is still considerable. The general statements from above hold also in this system: For a coplanar configuration, the spin expectation value is tilted out of the plane [cf. Fig. 5(j)] which can be related to the emergence of the Hall effect [cf. Fig. 5(g)]. Also, there exists a tilted virtual texture $\{\tilde{m}_i\}$ that determines the transport properties and a critical compensation angle θ_c

which is smaller here compared to the $\kappa = +1$ system [$\theta_c \approx 90.15^\circ$ for $\lambda = 0.2t$ as visible in Fig. 5(i)].

H. Comparison to the literature and validity of the model

Before we conclude, we want to discuss a few details that are important to realize in order to understand that our established mechanism is indeed the origin of the anomalous Hall effect in kagome magnets.

In the introduction we have mentioned several publications that report an anomalous Hall effect in kagome systems theoretically and experimentally. While these systems are mostly considered to be coplanar, actually, a small out-of-plane moment is calculated [14,30] or measured [16,17] (more than two orders of magnitude smaller than the actual magnetic moment of Mn). However, in these publications it is argued correctly that this moment is too small to explain the emergence of the calculated and measured anomalous Hall effect. In one of the first-principles calculations in Ref. [14] the system has even been artificially fixed in the perfectly coplanar configuration. As a consequence, the Hall conductivity only changed from $\sigma_{xy} = 218 \Omega^{-1} \text{cm}^{-1}$ to $\sigma_{xy} = 217 \Omega^{-1} \text{cm}^{-1}$ and not to zero which rules out the possibility to explain the Hall effect by means of an anomalous or topological Hall effect based on the actual magnetic texture. This means that an alternative mechanism must be present, which we have revealed in our paper.

In the study by Chen *et al.* [14] also a first investigation of the influence of an out-of-plane tilting of the texture on the Hall effect has been given by means of first-principles calculations. While they only calculated a few angles, it seems like the anomalous Hall effect is zero for several configurations. It would be interesting to have a more detailed curve and also the

energy dependence to compare it to our results. The existence of several zeros could be attributed to a (random) compensation of the electron and hole carrier densities but could also stem from the existence of carriers of different orbital character. In this case, the hopping amplitude t would differ between the carriers and electrons with different orbital character would experience different virtual tilting angles. This would imply that different locations of the Fermi energy (e.g., changed via doping or gating) would result in different virtual textures since the ratio of the carrier densities of electrons with different orbital characters changes. Furthermore, if the hopping amplitudes have different signs, even a compensation of the virtual tilting can occur resulting in additional zeros in the Hall conductivity. In the present model (as established in Refs. [14,18,26,28]) only a subspace of the total Hamiltonian is considered, which is why the virtual tilting angle is independent of the Fermi energy and only two zero transitions at $\Delta\theta_c$ and $\theta_c = 90^\circ + \Delta\theta_c$ occur.

Finally, we want to address an apparent invalidity of the model considered in Refs. [14,18,26,28]. This model (that we also consider in the present paper for $\theta = 90^\circ$) aims at discussing the anomalous Hall effect upon considering a coplanar magnetic texture. However, if we recall the results from the coplanar radial fixed magnetic texture (Fig. 2), we have found that while the fixed magnetic texture $\{m_i\}$ exhibits no net moment, the reciprocal-space spin texture $\langle s(\mathbf{k}) \rangle$ of the conduction electrons does. This would mean that the total magnetic moment is finite and that a magnetization would be measured. This puts the purpose of the considered model in these publications in question: The aim of these publications was to show that an anomalous Hall effect emerges in a compensated system. However, for $\theta = 90^\circ$, this tight-binding model does not actually consider a vanishing net magnetization (taking into account both the fixed magnetic texture and the k -dependent conduction electron spin texture) which is why the results of these publications do not actually serve their purpose, since one could argue that the finite Hall conductivity is not surprising even by conventional means.

However, as we show, for every tilted configuration, except for $\theta = \theta_c$, the Hall signal is nonzero which means that one can construct configurations for which the net moment of the fixed texture is compensated by the spin texture and still the Hall response is finite. In other words, a tweaked version of the model can sufficiently describe the completely compensated situation in which the net magnetization is absent. The fixed texture has to be considered with a small out-of-plane component $\theta \neq 90^\circ$ but different from the critical angle $\theta \neq \theta_c$.

IV. CONCLUSION

In summary, we have revealed microscopically how the anomalous Hall effect arises in kagome magnets like $Mn_3X(N)$. The Hamiltonian describes a virtual texture that determines the Hall conductivity instead of the actually measurable texture. For the coplanar radial-type arrangement, this texture is tilted out-of-plane due to the spin-orbit coupling. The virtual texture is characterized by a net moment and a net scalar spin chirality which give rise to a “virtual” anomalous and a “virtual” topological Hall effect, respectively. Our

explanation is in agreement with the recent experimental findings in Mn_3Sn [16] and Mn_3Ge [17].

Our results go beyond conventional symmetry analyses and show precisely if and how certain symmetries are broken by the texture and the spin-orbit coupling. Especially insightful is our result for a noncoplanar system characterized by the critical azimuthal angle $\theta = \theta_c$ [Fig. 3(f)]. The virtual tilting due to the spin-orbit coupling leads to a coplanar virtual texture. Consequently, the Hall signal is absent for this critical configuration. While a magnetic point group analysis would tell that the Hall signal is allowed, our established microscopic mechanism allows us to understand the absence due to a preserved TM symmetry of the virtual texture and the Hamiltonian of the here considered model.

As discussed, our model considers only a single orbital per lattice site, while the full system is characterized by electrons with different orbital character. In this case, due to the different hopping amplitudes [cf. Eq. (9)], different carriers cause different tilting angles of the (now orbital-dependent) virtual texture, which even allows for a compensation. This may explain why in kagome materials with a positive vector spin chirality (like Mn_3Rh , Mn_3Ir , Mn_3Pt) no such Hall effect has been measured yet, even though it is allowed by conventional symmetry analyses and was predicted more than 6 years ago. Tuning the Fermi energy by gating or doping can change the ratio of different carriers and may allow us to tune the Hall effect in these materials.

ACKNOWLEDGMENTS

This work is supported by CRC/TRR 227 of Deutsche Forschungsgemeinschaft (DFG). O.B. performed the tight-binding calculations with the help of B.G. B.G. established the transformation of the spin-orbit coupling and the virtually tilted texture. B.G. wrote the manuscript with significant inputs from all authors. O.B. prepared the figures. All authors discussed the results. B.G. and I.M. planned and supervised the project.

APPENDIX: TRANSFORMATION: EQUIVALENCE OF SPIN-ORBIT COUPLING AND A TILTED MAGNETIC TEXTURE

In the main text we have claimed that the spin-orbit coupling term behaves like a virtual tilting of the magnetic texture out of the kagome plane. In the following we derive this equivalence explicitly.

We start from the full Hamiltonian that includes hopping, Hund’s coupling, and spin-orbit coupling terms. Now we apply a transformation

$$U_i^\dagger = \begin{pmatrix} \cos(\frac{\alpha}{2}) & \sin(\frac{\alpha}{2})e^{-i\Phi_i} \\ -\sin(\frac{\alpha}{2})e^{i\Phi_i} & \cos(\frac{\alpha}{2}) \end{pmatrix} \quad (A1)$$

that is unitary,

$$U_i^\dagger U_i = 1. \quad (A2)$$

This transformation reorients the coordinate system for the magnetic moments of the fixed texture at every lattice site. Instead of aligning the z axis with the local moment, as has been done in Refs. [31–33], we tilt the z axis (now labeled

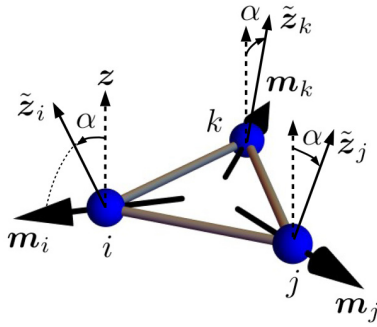


FIG. 6. Local rotation of the coordinate system as unitary transformation. The dashed coordinate system at each lattice cite i, j, k is rotated about the same angle α in the plane spanned by z and the local magnetic moment $\mathbf{m}_i, \mathbf{m}_j, \mathbf{m}_k$, respectively. The z axes of the reoriented, site-dependent coordinate systems are visualized by the solid arrows $\tilde{z}_i, \tilde{z}_j, \tilde{z}_k$. In these coordinate systems the magnetic moments are characterized by a different azimuthal angle $\theta - \alpha$; i.e., the texture is virtually tilted.

\tilde{z}) by an angle α toward the magnetic moment, as shown in Fig. 6,

$$\tilde{z}_i = (\cos \Phi_i \sin \alpha, \sin \Phi_i \sin \alpha, \cos \alpha)^T. \quad (\text{A3})$$

Here Φ_i is the polar angle of the fixed moment \mathbf{m}_i at site i .

The electron operator c_i is transformed to the new operator d_i as

$$c_i = U_i d_i. \quad (\text{A4})$$

$$t c_i^\dagger c_j = t d_i^\dagger U_i^\dagger U_j d_j = t U_i^\dagger U_j d_i^\dagger d_j, \quad (\text{A9})$$

$$U_i^\dagger U_j = \begin{pmatrix} \cos^2(\frac{\alpha}{2}) + \sin^2(\frac{\alpha}{2}) e^{-i(\Phi_i - \Phi_j)} & \frac{1}{2} \sin(\alpha) (e^{-i\Phi_i} - e^{-i\Phi_j}) \\ -\frac{1}{2} \sin(\alpha) (e^{i\Phi_i} - e^{i\Phi_j}) & \cos^2(\frac{\alpha}{2}) + \sin^2(\frac{\alpha}{2}) e^{i(\Phi_i - \Phi_j)} \end{pmatrix}. \quad (\text{A10})$$

The diagonal terms describe a hopping with a scaled hopping amplitude t_{ij}^{eff} . This hopping has a complex phase which is opposite for spin-up and spin-down (in this basis) electrons. For a small α , the effective hopping converges to t .

The off-diagonal terms have the shape of the spin-orbit coupling. For the radial texture they can be simplified to

$$-i \frac{\sqrt{3}}{2} \sin(\alpha) \mathbf{n}_{ij} \cdot \boldsymbol{\sigma}. \quad (\text{A11})$$

Lastly, we transform the original spin-orbit coupling term. Again, the result is a matrix with effective hopping terms on the diagonal and effective spin-orbit coupling terms on the off-diagonal:

$$c_i^\dagger (\tilde{\mathbf{n}}_{ij} \cdot \boldsymbol{\sigma}) c_j = d_i^\dagger U_i^\dagger (\tilde{\mathbf{n}}_{ij} \cdot \boldsymbol{\sigma}) U_j d_j \quad (\text{A12})$$

$$U_i^\dagger (\mathbf{n}_{ij} \cdot \boldsymbol{\sigma}) U_j = \cos(\alpha) \mathbf{n}_{ij} \cdot \boldsymbol{\sigma} + \sin(\alpha) \times \begin{pmatrix} e^{-i\frac{1}{2}(\Phi_i - \Phi_j)} & 0 \\ 0 & -e^{i\frac{1}{2}(\Phi_i - \Phi_j)} \end{pmatrix}. \quad (\text{A13})$$

First, we analyze how the Hund's coupling term transforms,

$$c_i^\dagger (\mathbf{m}_i \cdot \boldsymbol{\sigma}) c_i = d_i^\dagger U_i^\dagger (\mathbf{m}_i \cdot \boldsymbol{\sigma}) U_i d_i, \quad (\text{A5})$$

$$U_i^\dagger (\mathbf{m}_i \cdot \boldsymbol{\sigma}) U_i = \begin{pmatrix} \cos(\theta - \alpha) & \sin(\theta - \alpha) e^{-i\Phi_i} \\ \sin(\theta - \alpha) e^{i\Phi_i} & -\cos(\theta - \alpha) \end{pmatrix}. \quad (\text{A6})$$

As expected by geometric considerations, the azimuthal angle of the magnetic moment in this new coordinate system is decreased by α and the polar angle remains the same. Due to the application of the transformation, the spin is measured differently; the magnetic texture effectively acts as a new texture $\{\tilde{\mathbf{m}}_i\}$:

$$c_i^\dagger (\mathbf{m}_i \cdot \boldsymbol{\sigma}) c_i = d_i^\dagger (\tilde{\mathbf{m}}_i \cdot \boldsymbol{\sigma}) d_i, \quad (\text{A7})$$

$$\tilde{\mathbf{m}}_i = \begin{pmatrix} \cos(\Phi_i) \sin(\theta - \alpha) \\ \sin(\Phi_i) \sin(\theta - \alpha) \\ \cos(\theta - \alpha) \end{pmatrix}. \quad (\text{A8})$$

Of course, the unitary transformation has to be applied also to the other two terms to leave the physics of the system unchanged. Therefore, the effect of this new, tilted texture has to be compensated by the other terms in the Hamiltonian. Next, we transform the hopping term:

Summarizing the transformation, the Hamiltonian

$$H = t \sum_{\langle i,j \rangle} c_i^\dagger c_j + m \sum_i c_i^\dagger (\mathbf{m}_i \cdot \boldsymbol{\sigma}) c_i + i\lambda \sum_{\langle i,j \rangle} c_i^\dagger (\mathbf{n}_{ij} \cdot \boldsymbol{\sigma}) c_j \quad (\text{A14})$$

has been transformed to

$$H = \sum_{\langle i,j \rangle} t_{ij}^{\text{eff}} d_i^\dagger d_j + m \sum_i d_i^\dagger (\tilde{\mathbf{m}}_i \cdot \boldsymbol{\sigma}) d_i + i\tilde{\lambda} \sum_{\langle i,j \rangle} d_i^\dagger (\mathbf{n}_{ij} \cdot \boldsymbol{\sigma}) d_j, \quad (\text{A15})$$

with

$$t_{ij}^{\text{eff}\uparrow\downarrow} = t \left[\cos^2\left(\frac{\alpha}{2}\right) + \sin^2\left(\frac{\alpha}{2}\right) e^{\mp i(\Phi_i - \Phi_j)} \right] \pm i\tilde{\lambda} e^{\mp i\frac{1}{2}(\Phi_i - \Phi_j)} \sin(\alpha), \quad (\text{A16})$$

$$\tilde{\lambda} = -\frac{\sqrt{3}}{2} \sin(\alpha) t + \cos(\alpha) \lambda, \quad (\text{A17})$$

$$\tilde{m}_i = \begin{pmatrix} \cos(\Phi_i) \sin(\theta - \alpha) \\ \sin(\Phi_i) \sin(\theta - \alpha) \\ \cos(\theta - \alpha) \end{pmatrix}. \quad (\text{A18})$$

This means that a tilting of the texture is equivalent to the emergence of an effective spin-orbit coupling and a modified hopping amplitude, and vice versa. At a critical tilting angle α_c the spin-orbit coupling is compensated,

$$0 \stackrel{!}{=} \tilde{\lambda} = -\frac{\sqrt{3}}{2} \sin(\alpha_c)t + \cos(\alpha_c)\lambda. \quad (\text{A19})$$

This means that gauging away the spin-orbit coupling is equivalent to tilting the virtual texture by $-\alpha_c$. Therefore, a critical angle $\Delta\theta_c = +\alpha_c$ of the actual texture compensates this tilt and leads to a coplanar virtual texture that does not exhibit a Hall effect,

$$\Delta\theta_c = \alpha_c = \arctan \frac{\lambda}{t\sqrt{3}/2}. \quad (\text{A20})$$

For a general $\kappa = +1$ configuration, the angle is given by

$$\Delta\theta_c = \alpha_c = \arctan \left[\frac{\lambda}{t\sqrt{3}/2} \cos(\Delta\Phi) \right]. \quad (\text{A21})$$

-
- [1] E. H. Hall, On a new action of the magnet on electric currents, *Am. J. Math.* **2**, 287 (1879).
- [2] E. H. Hall, XVIII. On the “rotational coefficient” in nickel and cobalt, *The London, Edinburgh, and Dublin Philosophical Magazine and Journal of Science* **12**, 157 (1881).
- [3] N. Nagaosa, J. Sinova, S. Onoda, A. H. MacDonald, and N. P. Ong, Anomalous Hall effect, *Rev. Mod. Phys.* **82**, 1539 (2010).
- [4] J. Smit, The spontaneous Hall effect in ferromagnetics I, *Physica* **21**, 877 (1955).
- [5] J. Smit, The spontaneous Hall effect in ferromagnetics II, *Physica* **24**, 39 (1958).
- [6] L. Berger, Side-jump mechanism for the Hall effect of ferromagnets, *Phys. Rev. B* **2**, 4559 (1970).
- [7] R. Karplus and J. M. Luttinger, Hall effect in ferromagnetics, *Phys. Rev.* **95**, 1154 (1954).
- [8] M. V. Berry, Quantal phase factors accompanying adiabatic changes, *Proc. R. Soc. London A* **392**, 45 (1984).
- [9] J. Zak, Berry’s Phase for Energy Bands in Solids, *Phys. Rev. Lett.* **62**, 2747 (1989).
- [10] P. Bruno, V. K. Dugaev, and M. Taillefumier, Topological Hall Effect and Berry Phase in Magnetic Nanostructures, *Phys. Rev. Lett.* **93**, 096806 (2004).
- [11] S. Mühlbauer, B. Binz, F. Jonietz, C. Pfleiderer, A. Rosch, A. Neubauer, R. Georgii, and P. Böni, Skyrmion lattice in a chiral magnet, *Science* **323**, 915 (2009).
- [12] A. Neubauer, C. Pfleiderer, B. Binz, A. Rosch, R. Ritz, P. G. Niklowitz, and P. Böni, Topological Hall Effect in the A Phase of MnSi, *Phys. Rev. Lett.* **102**, 186602 (2009).
- [13] N. Nagaosa and Y. Tokura, Topological properties and dynamics of magnetic skyrmions, *Nat. Nanotechnol.* **8**, 899 (2013).
- [14] H. Chen, Q. Niu, and A. H. MacDonald, Anomalous Hall Effect Arising from Noncollinear Antiferromagnetism, *Phys. Rev. Lett.* **112**, 017205 (2014).
- [15] J. Kübler and C. Felser, Non-collinear antiferromagnets and the anomalous Hall effect, *Europhys. Lett.* **108**, 67001 (2014).
- [16] S. Nakatsuji, N. Kiyohara, and T. Higo, Large anomalous Hall effect in a non-collinear antiferromagnet at room temperature, *Nature (London)* **527**, 212 (2015).
- [17] A. K. Nayak, J. E. Fischer, Y. Sun, B. Yan, J. Karel, A. C. Komarek, C. Shekhar, N. Kumar, W. Schnelle, J. Kübler *et al.*, Large anomalous Hall effect driven by a nonvanishing Berry curvature in the noncollinear antiferromagnet Mn₃Ge, *Sci. Adv.* **2**, e1501870 (2016).
- [18] Y. Zhang, Y. Sun, H. Yang, J. Železný, S. P. P. Parkin, C. Felser, and B. Yan, Strong anisotropic anomalous Hall effect and spin Hall effect in the chiral antiferromagnetic compounds Mn₃X (X = Ge, Sn, Ga, Ir, Rh, and Pt), *Phys. Rev. B* **95**, 075128 (2017).
- [19] M. Seemann, D. Ködderitzsch, S. Wimmer, and H. Ebert, Symmetry-imposed shape of linear response tensors, *Phys. Rev. B* **92**, 155138 (2015).
- [20] Note that experiments [16,17] as well as first-principles calculations [14,30] find a very small net moment on the order of $10^{-2} \mu_B$ per unit cell for these systems. As stated in these publications, this moment is too small to explain the emergence of the anomalous Hall effect by conventional means. In Ref. [14] it has even been shown that the effect is only slightly reduced from $\sigma_{xy} = 218 \Omega^{-1} \text{cm}^{-1}$ to $\sigma_{xy} = 217 \Omega^{-1} \text{cm}^{-1}$ when the magnetic texture is artificially fixed in the plane in first-principles calculations, so that the moment is completely compensated. Therefore, an unconventional mechanism must be present.
- [21] C. L. Kane and E. J. Mele, Quantum Spin Hall Effect in Graphene, *Phys. Rev. Lett.* **95**, 226801 (2005).
- [22] E. F. Bertaut, D. Fruchart, J. P. Bouchaud, and R. Fruchart, Diffraction neutronique de Mn₃GaN, *Solid State Commun.* **6**, 251 (1968).
- [23] D. Fruchart and E. F. Bertaut, Magnetic studies of the metallic perovskite-type compounds of manganese, *J. Phys. Soc. Jpn.* **44**, 781 (1978).
- [24] W. Feng, G.-Y. Guo, J. Zhou, Y. Yao, and Q. Niu, Large magneto-optical Kerr effect in noncollinear antiferromagnets Mn₃X (X = Rh, Ir, Pt), *Phys. Rev. B* **92**, 144426 (2015).
- [25] G.-Y. Guo and T.-C. Wang, Large anomalous Nernst and spin Nernst effects in the noncollinear antiferromagnets Mn₃X (X = Sn, Ge, Ga), *Phys. Rev. B* **96**, 224415 (2017).
- [26] X. Zhou, J.-P. Hanke, W. Feng, F. Li, G.-Y. Guo, Y. Yao, S. Blügel, and Y. Mokrousov, Spin-order dependent anomalous Hall effect and magneto-optical effect in the noncollinear antiferromagnets Mn₃XN with X = Ga, Zn, Ag, or Ni, *Phys. Rev. B* **99**, 104428 (2019).
- [27] See Supplemental Material at <http://link.aps.org/supplemental/10.1103/PhysRevResearch.2.033112> for five supplementary figures. In Fig. S1 we present the band structure and the density of states of the structural kagome lattice. In Fig. S2 we compare the k-resolved spin expectation values for various configurations, and in Fig. S3 we show that the system with the

- toroidal texture is not affected by the spin-orbit coupling and does not exhibit an anomalous Hall effect. Furthermore, in Fig. S4 we analyze the tilted radial texture for a constant occupation number, and in Fig. S5 we confirm Eq. (9) numerically.
- [28] Y. Zhang, J. Železný, Y. Sun, J. van den Brink, and B. Yan, Spin Hall effect emerging from a noncollinear magnetic lattice without spin-orbit coupling, *New J. Phys.* **20**, 073028 (2018).
- [29] D. J. Thouless, M. Kohmoto, M. P. Nightingale, and M. Den Nijs, Quantized Hall Conductance in a Two-Dimensional Periodic Potential, *Phys. Rev. Lett.* **49**, 405 (1982).
- [30] D. Zhang, B. Yan, S.-C. Wu, J. Kübler, G. Kreiner, S. S. P. Parkin, and C. Felser, First-principles study of the structural stability of cubic, tetragonal and hexagonal phases in Mn_3Z ($Z = Ga, Sn$ and Ge) Heusler compounds, *J. Phys.: Condens. Matter* **25**, 206006 (2013).
- [31] K. Hamamoto, M. Ezawa, and N. Nagaosa, Quantized topological Hall effect in skyrmion crystal, *Phys. Rev. B* **92**, 115417 (2015).
- [32] B. Göbel, A. Mook, J. Henk, and I. Mertig, Unconventional topological Hall effect in skyrmion crystals caused by the topology of the lattice, *Phys. Rev. B* **95**, 094413 (2017).
- [33] B. Göbel, A. Mook, J. Henk, and I. Mertig, The family of topological Hall effects for electrons in skyrmion crystals, *Eur. Phys. J. B* **91**, 179 (2018).

4.2 Sources of the spin Hall effect in noncollinear kagome magnets

Spin Hall effect in systems without spin-orbit coupling. The generation of transverse spin currents as response to an applied electric field is called spin Hall effect (SHE). For a long time, it has been believed that the effect relies on spin-orbit coupling (SOC) which deflects spin \uparrow and \downarrow electrons in opposite directions. Consequently, in a nonmagnetic material, an equal number of \uparrow and \downarrow electrons results in a vanishing charge current, and a pure spin current (two-current model). In contrast, an imbalance of \uparrow and \downarrow electrons leads to spin-polarized currents, where spin and charge is transported. This scenario is present in a ferromagnet (FM) which exhibits an AHE and a SHE.

Recently, it has been shown that the SHE can be generated in systems with a noncoplanar magnetic texture even *without* SOC [134, 135]. And shortly after, the SHE has been predicted in the *coplanar* noncollinear kagome antiferromagnets [15] that also show a large AHE [cf. Sec. 4.1]. However, in contrast to the AHE, which requires SOC in these kagome magnets, the SHE may still emerge even in the absence of SOC [17] due to a non-vanishing spin Berry curvature [cf. Eq. (2.75)].

The SHE without SOC in the coplanar noncollinear magnetic texture has been predicted mainly based on symmetry arguments: a combination of time-reversal symmetry with a spin rotation by 180° renders the AHE zero while the SHE is allowed. However, a symmetry analysis does not allow to predict the magnitude of spin Hall signal, quantitatively. The later is the spin Hall conductivity σ_{xy}^z which relates the spin current $j_{S,x}^k$ with the applied electric field E_y .

This publication. In the following publication “Spin Hall effect in noncollinear kagome antiferromagnets” [OB2], two sources of the intrinsic spin Hall signal for various noncollinear kagome magnets are revealed.

We go beyond a conventional symmetry analysis and relate the results to findings reported in the previous publication [OB1], in which the origin of the AHE in these materials was established. In doing so, it is demonstrated that the noncollinear magnetic texture gives rise to the main contribution to the SHE. This mechanism is not affected if all magnetic moments are rotated within the kagome plane by the same angle, and exists without SOC. Thus, a pure spin current (without charge transport) is generated since the SHE is nonzero, while the AHE is absent without SOC.

The second contribution mainly *reduces* the spin Hall signal and originates from SOC or tilting of the magnetic moments out of the kagome plane, which are equivalent in this model [OB1]. In this scenario, the kagome magnets exhibit an AHE, that we identified as an effective THE, in addition to the SHE. Consequently, spin and charge are transported in form of spin-polarized currents, which effectively reduces the spin Hall signal. We show in detail that the reduction of the spin Hall conductivity is roughly proportional to the product of the anomalous Hall conductivity and an out-of-plane magnetization density; this product vanishes without SOC.

The findings allow to find analogies between noncollinear kagome magnets and collinear antiferromagnets and ferromagnets, which are relevant for spintronic applications. Pure spin currents can be generated in noncollinear kagome magnets without SOC similar to the situation in a collinear antiferromagnet, whereas spin-polarized currents flow like in collinear ferromagnets if SOC is not negligible (cf. Fig. 1 in [OB2]).

The following publication: Reprinted (whole article) with permission from O. Busch, B. Göbel and I. Mertig, *Physical Review B* **104**, 184423 (2021); Ref. [OB2]; Spin Hall effect in noncollinear kagome antiferromagnets. Copyright (2021) by the American Physical Society.

Spin Hall effect in noncollinear kagome antiferromagnetsOliver Busch ,* B3rge G3bel , and Ingrid Mertig*Institut f3ur Physik, Martin-Luther-Universit3at Halle-Wittenberg, D-06099 Halle (Saale), Germany*

(Received 30 August 2021; accepted 9 November 2021; published 18 November 2021)

The spin Hall effect is commonly considered to be related to spin-orbit interaction that causes a deflection of charge carriers according to their spin orientation into opposite directions. Thus, this effect creates spin currents in nonmagnetic materials with spin-orbit coupling. However, recently large spin Hall effects were predicted in coplanar kagome antiferromagnets Mn_3X even when spin-orbit interaction is not considered. Therefore, these materials are interesting candidates for spintronic applications. In our theoretical study we reveal two sources that determine the intrinsic spin Hall signal of two-dimensional kagome antiferromagnets. The main contribution to the spin Hall signal is originating from the noncollinear magnetic texture localized on the Mn sites and it is maximal for coplanar systems. In addition to that, spin-orbit coupling or an out-of-plane tilting of the magnetic moments, which are equivalent within the framework of this model, reduce the spin Hall effect effectively.

DOI: [10.1103/PhysRevB.104.184423](https://doi.org/10.1103/PhysRevB.104.184423)**I. INTRODUCTION**

Conventionally only the charge of electrons is used in electronic devices like transistors, displays, or solar panels [1]. However, in the emerging field of spintronics [2,3] the spin degree of freedom of the electrons is as well exploited [4,5]. Therefore, the investigation of materials, with regard to manipulation and control of spin and generation of spin currents, is mandatory for the development of new low-power consumption applications [6,7]. Besides, spin-based electronics can build on a wide range of different materials like metals [8], semiconductors [9–12], or superconductors [13] that have all been taken into account for application in spintronics devices for the last decades.

Spin currents are generated in metals by the spin Hall effect as a transverse response to a longitudinal electrical field [8,14,15]. In experiments, this effect can be quantified by a transverse accumulation of spin density with opposite sign at the edges that can be measured directly via the magneto-optical Kerr effect (MOKE) [16]. Alternatively, the spin Hall effect can be quantified by a spin Hall conductivity which is measured indirectly by exploiting the inverse spin Hall effect where the spin current is converted back into a transverse charge current [17]. A propagation of such spin currents across a metal/ferromagnet interface allows for magnetization switching via spin-orbit torque [18]. The same scenario holds for collinear antiferromagnets [cf. Fig. 1(a)]. Spin-polarized currents typically occur in ferromagnetic materials. Longitudinal spin-polarized currents are for example responsible for effects like the giant magnetoresistance and spin-transfer torque [19,20] which are utilized in magnetic RAMs [21]. Transversal spin-polarized currents are related to the anomalous Hall effect [cf. Fig. 1(b)].

Recently, materials with antiferromagnetic order gained attention. Although the observation and manipulation of antiferromagnetic textures and domains is much more challenging in experiments and applications [22,23], they show interesting properties like a strong robustness against external magnetic fields and the absence of magnetic stray fields [5]. Moreover, they allow for ultrafast spin dynamics and magnetotransport phenomena [24,25].

A special type of antiferromagnets is considered in this work: noncollinear magnetic textures on a two-dimensional kagome lattice. This structure can be found in some manganese compounds Mn_3X ($X = Rh, Ir, Pt, Ga, Ge, Sn$) that are constituted by layered kagome planes [26] where the magnetic moments of the Mn atoms form a noncollinear antiferromagnetic texture. These materials have been the subject of many recent theoretical and experimental studies about the anomalous and the spin Hall effect, where spin-orbit interaction plays an important role.

The anomalous Hall effect has been predicted [26–28] in these noncollinear kagome magnets and confirmed in experiments with Mn_3Sn [29] and Mn_3Ge [30,31]. Besides, Zhang *et al.* showed that in such compensated systems large spin Hall effects may occur as well [26], and most interestingly, even when spin-orbit coupling is not considered. Time-reversal symmetry \mathcal{T} is broken in magnetic systems, whereas a combination of \mathcal{T} with a spin rotation \mathcal{S} by 180° around the axis perpendicular to the kagome plane can still be a symmetry. This \mathcal{TS} symmetry forbids the existence of the anomalous Hall effect in a noncollinear coplanar magnetic texture but the spin Hall effect can exist, even without spin-orbit interaction [32].

The symmetry analysis is a powerful tool, however, it does not allow for a quantitative prediction of the size of the effect. There are cases where the magnetic space group of a crystalline material would allow for the existence of an anomalous Hall effect [32,33], but the effect can be absent, as was shown before in Ref. [34]. There we established a

*Corresponding author: oliver.busch@physik.uni-halle.de

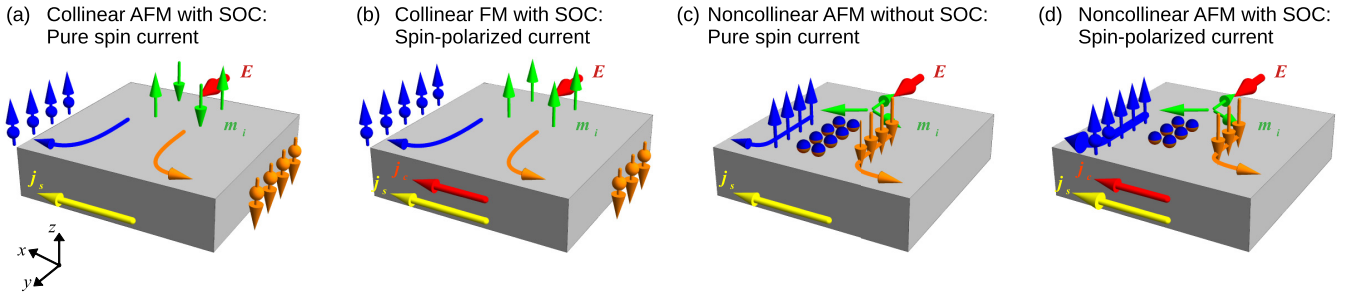


FIG. 1. Overview of spin currents and spin-polarized currents in different magnetic systems. Green arrows represent the magnetic texture $\{m_i\}$ [of the Mn atoms in (c) and (d)]. The thick red arrows indicate the electric field E along y . The electrons participating in transport are distinguished according to their spin orientation in z direction (blue: \uparrow , orange: \downarrow). The small spheres represent the charge of the electrons. (a) Collinear antiferromagnet (AFM) with spin-orbit coupling (SOC): pure transverse spin current j_s (yellow arrow) since electrons with different spin accumulate at opposite sites of the sample and no charge current j_c can be measured. (b) Collinear ferromagnet (FM) with SOC where not only spin but also charge is transported (thin red arrow), resulting in a spin-polarized charge current. (c) Noncollinear AFM without SOC: In contrast to the situation in (a), spin currents (yellow arrow) may exist even without spin-orbit interaction. (d) Same as (c) but with SOC that gives rise to an anomalous Hall effect in addition. Therefore, charge currents may flow in addition in analogy to the situation in (b).

microscopic picture that allows us to interpret the anomalous Hall effect in Mn_3X systems as an effective topological Hall effect: spin-orbit interaction induces a virtual tilting of the magnetic moments out of the kagome plane. Thus, the opening angle of this virtual noncoplanar texture generates an effective topological Hall effect due to a net scalar spin chirality, whereas the magnetic background texture formed by the magnetic moments of the Mn atoms remains coplanar.

In this work we are investigating the spin Hall effect [8,14,15] in the same model system and relate the findings to our previous results of the anomalous Hall effect and the virtual magnetic texture. We find that the spin Hall signal is determined by two different mechanisms. First, a large spin Hall effect emerges from the coplanar magnetic background texture itself that is independent of the in-plane rotation of the magnetic moments. In addition to that, spin-orbit coupling or an out-of-plane tilting of the magnetic moments, which is equivalent within this model, is related to a spin-polarized current that reduces the spin Hall signal of the background texture effectively. This allows us to distinguish pure spin currents, where only spin is transported by the electrons, and spin-polarized currents, where spin and charge are transported, as a transverse response to an applied electric field in those systems.

Hence, we find analogies between noncollinear kagome magnets and collinear (anti-)ferromagnets as illustrated in Fig. 1. Without spin-orbit interaction a pure spin current is flowing in coplanar kagome magnets [cf. Fig. 1(c)] like in a collinear antiferromagnet [cf. Fig. 1(a)]. Taking spin-orbit coupling into account causes additionally a spin-polarized current that is related to an anomalous Hall effect which reduces the spin Hall conductivity [cf. Fig. 1(d)]. The spin-polarized current is similar to the situation in a collinear ferromagnet [cf. Fig. 1(b)].

Although we stress the analogy of collinear antiferromagnets and noncollinear kagome antiferromagnets with respect to the generation of spin currents, there is a pronounced difference. Collinear bipartite antiferromagnets [35] show an analogy of Kramer's theorem since the time-reversal operation \mathcal{T} in combination with a translation between the sublattices T_d are a symmetry in the system. Consequently, the

bands are doubly degenerate and the corresponding eigenvectors can be classified into “spin-up” and “spin-down” states [cf. blue and orange small spheres in Fig. 1(a)]. There is no symmetry in kagome antiferromagnets that fulfills Kramer's theorem: the bands are not doubly degenerate [27]. However, the corresponding eigenvectors consist of equal contributions of spin-up and spin-down with respect to the quantization axis perpendicular to the kagome plane, which is illustrated by the two-colored small spheres in Fig. 1(c). Hence, each eigenstate generates a pure spin current on its own. Spin-orbit coupling is changing the equal distribution of spin-up and spin-down character. As a result an individual state still contributes to the spin current, however somewhat reduced, and delivers an appropriate amount of spin-polarized current as well [cf. Fig. 1(d)].

II. MODEL AND METHODS

The model Hamiltonian that we use was first introduced in Ref. [27] where the anomalous Hall effect has been predicted in the compensated kagome magnet Mn_3Ir . It is also known as an sd model that describes the interaction of itinerant s electrons with d magnetic moments that are localized on the Mn sites and form a noncollinear magnetic texture. In second quantization, the tight-binding Hamiltonian reads

$$H = H_{\text{kin}} + H_Z + H_{\text{SOC}}, \quad (1)$$

$$H_{\text{kin}} = t \sum_{\langle i,j \rangle} \sum_{\sigma} a_{i,\sigma}^{\dagger} a_{j,\sigma}, \quad (2)$$

$$H_Z = m \sum_i \sum_{\sigma,\sigma'} a_{i,\sigma}^{\dagger} (\mathbf{m}_i \cdot \boldsymbol{\sigma})_{\sigma\sigma'} a_{i,\sigma'}, \quad (3)$$

$$H_{\text{SOC}} = i\lambda \sum_{\langle i,j \rangle} \sum_{\sigma,\sigma'} a_{i,\sigma}^{\dagger} (\mathbf{n}_{ij} \cdot \boldsymbol{\sigma})_{\sigma\sigma'} a_{j,\sigma'}, \quad (4)$$

where $a_{i,\sigma}^{\dagger}$ and $a_{i,\sigma}$ are the creation and annihilation operators of an electron at site i with spin σ . Here we restrict ourselves to nearest-neighbor hopping between atomic sites i and j which is implied by the sum limits $\langle i,j \rangle$. The three parameters t , m , and λ denote the hopping energy, the strength of the Hund's coupling between the spin moment of the conduction

electron with the magnetic texture $\mathbf{m} = \{\mathbf{m}_i\}$, and the strength of spin-orbit interaction, respectively. Here

$$\mathbf{m}_i = \begin{pmatrix} \cos(\Phi_i) \sin(\theta_i) \\ \sin(\Phi_i) \sin(\theta_i) \\ \cos(\theta_i) \end{pmatrix} \quad (5)$$

is the magnetic moment at site i characterized by the polar and azimuthal angles Φ_i and θ_i and the vectors \mathbf{n}_{ij} are defined in Ref. [34] [cf. Fig. 1(a)]. These in-plane vectors \mathbf{n}_{ij} form a set of vectors that are anticlockwise orthogonal to the hopping vectors \mathbf{R}_{ij} which consider the different environments (left or right hand) of nearest-neighbor hoppings on a kagome lattice [27].

In our study the kagome lattice, which is a two-dimensional hexagonal lattice with a triangular unit cell (formed by Mn atoms), is located in the xy plane and is assumed to be periodic. The considered tight-binding model allows for a continuous rotation of the magnetic moments \mathbf{m}_i , that are carried by Mn atoms, within and out of the kagome plane. Following the notation from Ref. [34], the different magnetic textures can be characterized as follows. First of all, only magnetic textures with a positive vector spin chirality [36]

$$\kappa \equiv \frac{2\sqrt{3}}{9} \sum_{\langle i,j \rangle} (\mathbf{m}_i \times \mathbf{m}_j) \cdot \mathbf{e}_z = +1 \quad (6)$$

are considered. Rotating each magnetic moment by the same in-plane offset angle $\Delta\Phi$ within the xy plane, as visualized in the small cartoons in Fig. 4, does not change the vector spin chirality since the magnetic moments of neighboring atoms always differ by a polar angle of 120° .

Two configurations are special since they have different symmetries (time reversal \mathcal{T} , mirror reflection \mathcal{M}): “radial” ($\Delta\Phi = 0^\circ$, three $\mathcal{T}\mathcal{M}$ planes) and “toroidal” ($\Delta\Phi = 90^\circ$, three \mathcal{M} planes). We always assume that all three magnetic moments have the same azimuthal angle $\theta \equiv \theta_i$ for a certain magnetic texture. Thus, coplanar and noncoplanar configurations are classified by an azimuthal angle of $\theta = 90^\circ$ and $\theta \neq 90^\circ$, respectively, in this work.

We investigate the influence of the spin configuration on the spin Hall effect. Within linear response theory, the corresponding spin Hall conductivity σ_{ij}^k is a tensor of rank three and relates an electric field E_j (applied in j direction) to the spin current $j_{s,i}^k = \sigma_{ij}^k E_j$ that is generated as a response flowing in i direction with spin polarization in k direction ($i, j, k = x, y, z$). We focus on the intrinsic contribution which can be described by the Berry curvature formalism analog to the intrinsic anomalous Hall conductivity [37]. For a two-dimensional system at zero temperature, as considered here, the intrinsic spin Hall conductivity is defined as follows [26]:

$$\sigma_{xy}^z(E_F) = \frac{e}{\hbar} \sum_v \frac{1}{(2\pi)^2} \int_{\varepsilon(\mathbf{k}) \leq E_F} \Omega_{xy,v}^z(\mathbf{k}) d^2k, \quad (7)$$

where the Fermi energy E_F enters as a parameter that can be varied in practice by doping or by applying a gate voltage. In this equation, the Brillouin zone integration is performed over all occupied states for a quantity that is sometimes denoted as

“spin Berry curvature” [26,32]

$$\Omega_{xy,v}^z(\mathbf{k}) = -2\hbar^2 \text{Im} \sum_{\mu \neq \nu} \frac{\langle \nu, \mathbf{k} | \Sigma_x^z | \mu, \mathbf{k} \rangle \langle \mu, \mathbf{k} | v_y | \nu, \mathbf{k} \rangle}{[\varepsilon_\nu(\mathbf{k}) - \varepsilon_\mu(\mathbf{k})]^2} \quad (8)$$

of band ν that is calculated from the eigenvalues $\varepsilon_\nu(\mathbf{k})$ and the corresponding eigenvectors $|\nu, \mathbf{k}\rangle \equiv \varphi_\nu(\mathbf{k})$ of the tight-binding Hamiltonian. In contrast to the conventional Berry curvature, here one has to take into account the spin-current operator that can be defined by $\Sigma_i^k \equiv \frac{1}{2}\{v_i, s^k\}$ as the anticommutator of the velocity operator v_i and the spin operator s^k .

III. RESULTS AND DISCUSSION

The results section of our paper is organized as follows: we investigate the influence of the in-plane and out-of-plane orientation of the magnetic moments on the intrinsic spin Hall effect by systematically varying the parameters $\Delta\Phi$ and θ , respectively. Thereby we observe pure spin currents without spin-orbit coupling that cause the spin Hall signal. Spin-orbit interaction brings about spin-polarized currents, as well, that reduce the spin Hall signal effectively.

A. Spin Hall effect for the radial and toroidal coplanar configurations

Throughout this subsection the fixed magnetic texture is assumed to be coplanar ($\theta = 90^\circ$) and the parameter describing the Hund’s coupling is set to $m = 1.7t$.

First, the radial configuration ($\Delta\Phi = 0^\circ$) is investigated without taking spin-orbit interaction into account ($\lambda = 0.0t$). Figures 2(a) and 2(b) show the corresponding band structure where one obtains six individual bands and Dirac points at K due to the $\mathcal{T}\mathcal{M}$ symmetry of the magnetic texture [27]. The color of the energy bands represents the spin Berry curvature $\Omega_{xy,v}^z$ in units of a^2 , where a is the lattice constant. A detailed \mathbf{k} - and band-resolved plot of the spin Berry curvature in Fig. 2(c) illustrates that $\Omega_{xy,v}^z$ has finite values (green positive, yellow zero, and red negative) allowing for the occurrence of the spin Hall effect even though spin-orbit coupling is not considered, as predicted by Zhang *et al.* [32]. The corresponding spin Hall conductivity σ_{xy}^z according to Eq. (7) is plotted in units of $(\frac{e^2}{h})(\frac{\hbar}{e})$ as a function of energy simulated by a change of the Fermi energy E_F [black curve in Fig. 3(b)] which is in agreement with Ref. [32]. Note that this result corresponds to the situation illustrated for the sample in Fig. 1(c).

Now we take spin-orbit interaction into account ($\lambda = 0.2t$). Therefore, we briefly summarize the main results of our former work about the virtual magnetic texture that explains the anomalous Hall effect in this scenario [34].

We demonstrated via a transformation of the model Hamiltonian (1) that spin-orbit coupling and a tilting of the magnetic texture out of the kagome plane are equivalent.

The application of a set of unitary transformations that tilt the local z axis at each lattice site i by the same angle α towards the magnetic moment \mathbf{m}_i implies that one can change the reference system to a lattice-site dependent coordinate

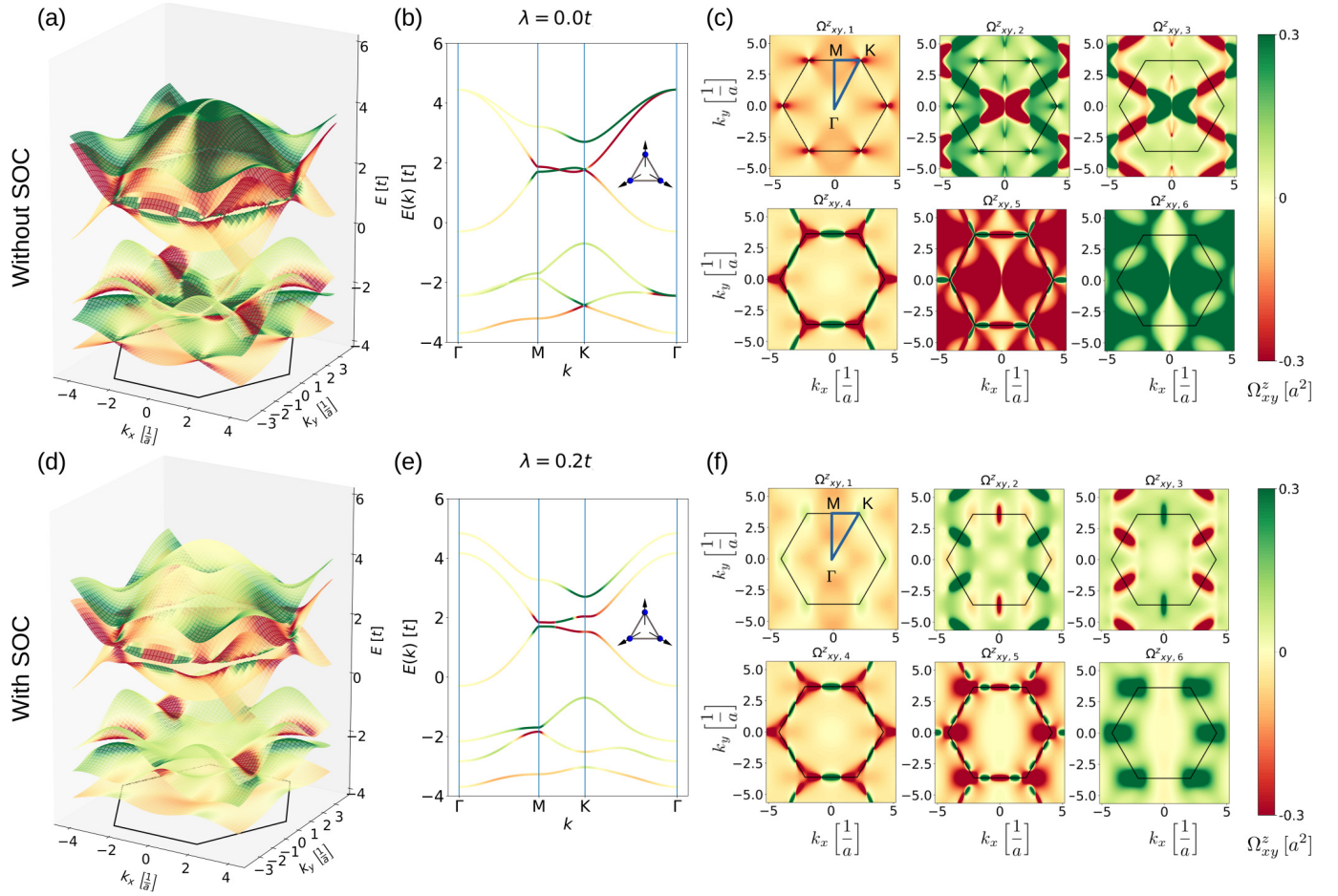


FIG. 2. Band structure and spin Berry curvature of the radial magnetic texture. In (a)–(c) spin-orbit coupling (SOC) is neglected, whereas in (d)–(f) it is considered. (a) Three-dimensional band structure $E(k_x, k_y)$ for all bands over the Brillouin zone (indicated by the black hexagon in the k_x - k_y plane). The color of the energy surfaces shows the value of the spin Berry curvature Ω_{xy}^z (green positive, red negative, and yellow zero as indicated by the legend on the right). (b) Same as in (a) but represented in the reduced zone scheme where the band structure is only plotted along the high-symmetry points (Γ -M-K- Γ). (c) Visualization of the spin Berry curvature of all bands resolved in the two-dimensional k space. The blue triangle in the upper left panel in (c) shows the reduced Brillouin zone. (d)–(f) Analog to (a)–(c), but spin-orbit interaction is taken into account ($\lambda = 0.2t$).

system where the magnetic texture is effectively tilted by α :

$$\tilde{\mathbf{m}}_i = \begin{pmatrix} \cos(\Phi_i) \sin(\theta - \alpha) \\ \sin(\Phi_i) \sin(\theta - \alpha) \\ \cos(\theta - \alpha) \end{pmatrix}. \quad (9)$$

Besides, the unitary transformation of the complete Hamiltonian (1) yields effective hopping and spin-orbit coupling amplitudes \tilde{t} and $\tilde{\lambda}$. For the radial configurations, the latter reads

$$\tilde{\lambda} = -\frac{\sqrt{3}}{2} \sin(\alpha)t + \cos(\alpha)\lambda. \quad (10)$$

This equation implies that the effective spin-orbit coupling can be compensated ($\tilde{\lambda} = 0$) by a critical tilting angle α_c . In this case, we call the effectively tilted magnetic texture $\{\tilde{\mathbf{m}}_i\}$ “virtual” and it is tilted with respect to the fixed magnetic texture $\mathbf{m} = \{\mathbf{m}_i\}$ by an azimuthal angle $\alpha_c = \Delta\theta_c$. In particular, Eq. (10) yields a critical angle $\alpha_c \approx 13^\circ$ for $\lambda = 0.2t$.

The virtual texture is hidden in the model Hamiltonian (1) and is thereby determined by the symmetry of the system. Consequently, the virtual texture is responsible for the

electronic properties and thus, the equivalence of spin-orbit interaction and an out-of-plane tilting allows for an interpretation of the anomalous Hall effect in the coplanar kagome magnet ($\theta = 90^\circ$) as an effective topological Hall effect due to a nonvanishing scalar spin chirality of the virtual noncoplanar magnetic texture ($\tilde{\theta} = 90^\circ - \alpha_c$).

Moreover, a noncoplanar background texture $\{\mathbf{m}_i\}$ that is characterized by a critical azimuthal angle $\theta_c = 90^\circ + \Delta\theta_c$ with spin-orbit coupling ($\lambda \neq 0$) is equivalent to a virtual coplanar texture, since $\{\tilde{\mathbf{m}}_i\}$ is tilted by $\alpha_c = \Delta\theta_c$ with respect to $\{\mathbf{m}_i\}$. Hence, spin-orbit coupling is effectively compensated ($\tilde{\lambda} = 0$) and the Hall effect vanishes again since the already mentioned \mathcal{TM} symmetry of the radial configuration, and thus of the Hamiltonian, is restored.

The out-of-plane tilting mechanism that arises from spin-orbit interaction is parameter dependent and the influence on the in-plane orientation of the magnetic moments is given by a cosine function [34]. Hence, it is maximal for the radial configuration and zero for the toroidal configuration which implies that the virtual texture is not tilted with respect to the original toroidal texture. The reason for this is that spin-orbit

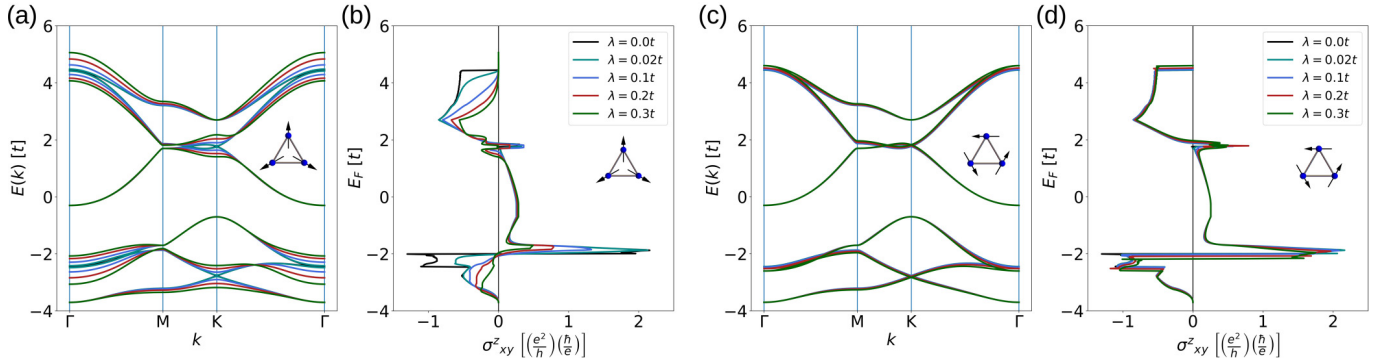


FIG. 3. Band structure and spin Hall conductivity σ_{xy}^z plotted against the Fermi level E_F for different spin-orbit coupling strengths λ as indicated. (a) and (b) show the results for the radial configuration ($\Delta\Phi = 0^\circ$), where band gaps occur due to spin-orbit coupling and broaden with increasing λ , whereas the spin Hall signal is reduced for most energies. (c) and (d) show the results of analog calculations for the toroidal texture ($\Delta\Phi = 90^\circ$) which is obtained by an in-plane rotation of each magnetic moment by 90° within the kagome plane.

coupling breaks the \mathcal{TM} symmetry of the radial configuration ($\Delta\Phi = 0^\circ$), whereas \mathcal{M} in the toroidal arrangement ($\Delta\Phi = 90^\circ$) is still conserved [27,36]. Note that the magnetic moments of textures with different in-plane orientations as discussed in Sec. III B can be interpreted as a superposition of a radial and a toroidal part. The tilting increases with the spin-orbit interaction strength λ .

Now we discuss the consequences of the virtual texture on the band structure and the spin Hall signal for the radial texture. Since spin-orbit coupling is considered, the \mathcal{TM} symmetry of the magnetic texture is broken and therefore degeneracies are lifted and global band gaps open [cf. Fig. 2(e)]. In Fig. 3(a) the dependence of the electronic band structure on the spin-orbit interaction strength λ is presented. Figure 3(b) shows the corresponding spin Hall signals, where we find that the magnitude of the spin Hall conductivity is decreasing for most energies with increasing λ . For the red curve in Fig. 3(b) we set $\lambda = 0.2t$ in correspondence to Ref. [32].

According to Ref. [38], a phase transition from the radial phase ($\Delta\Phi = 0^\circ$) to the toroidal phase ($\Delta\Phi = 90^\circ$) has been found experimentally at a critical temperature $T_C = 163$ K in the antiperovskite Mn_3NiN . Repeating the calculations for the toroidal texture reveals that both the electronic structure and the spin Hall signal are hardly affected by spin-orbit coupling [cf. Figs. 3(c) and 3(d)]: the Dirac points do not open as band gaps but the bandwidth is slightly broadened with increasing λ .

B. Spin Hall effect under in-plane rotation of the magnetic moments

The electronic properties (i.e., the band structure and the spin Hall conductivity) without spin-orbit coupling (black curves in Fig. 3) are identical for the two special configurations, but the effect of spin-orbit interaction is quite strong for the radial phase and almost negligible for the toroidal one. Motivated by this, we investigate the spin Hall effect for configurations between those two arrangements. Since the band structures of the radial and the toroidal configurations can differ significantly, if spin-orbit coupling is taken into account [cf. Fig. 3(a)], it is helpful to calculate the conductivity as a function of the occupation number n_{occ} instead of the

Fermi energy E_F to compare different systems with each other. Therefore, we calculate σ_{xy}^z upon a continuous variation of the in-plane offset angle $\Delta\Phi$ while n_{occ} is fixed.

As visible in Fig. 4(a), we find for each fixed occupation number that the spin Hall conductivity as a function of $\Delta\Phi$ is constant if spin-orbit interaction is not taken into account. This is in agreement with the above discussion of the spin transport in the radial and the toroidal configurations without spin-orbit coupling. The signal is independent of the in-plane orientation of the magnetic texture (illustrated by the small cartoons below the panel in Fig. 4). If spin-orbit interaction is taken into account ($\lambda = 0.2t$), we observe an extra contribution to the spin Hall signal that is oscillating with a period of 180° [cf. Fig. 4(b)]. This periodic behavior is in agreement with symmetry arguments since the (intrinsic) spin Hall conductivity, which is considered in this work, is even under time reversal \mathcal{T} which is equivalent to a rotation of each magnetic moment by 180° in the kagome plane. Consequently, the spin Hall signal fulfills $\sigma_{xy}^z(\Delta\Phi + 180^\circ) = \sigma_{xy}^z(\Delta\Phi)$.

The spin Hall conductivity for a fixed occupation can be strongly diminished depending on the in-plane orientation. The difference is maximal for the radial configuration and minimal for the toroidal one. To illustrate this more clearly, the spin Hall conductivity for those two magnetic textures and configurations in between are shown as a function of the occupation number in one diagram in Fig. 4(c) where the horizontal lines indicate the number of the occupied states that have been chosen for the in-plane rotation in Figs. 4(a) and 4(b).

C. Relation of spin Hall effect to anomalous Hall effect and magnetization density

Now we would like to interpret our results and relate them to the findings in Ref. [34] where the anomalous Hall effect has been investigated.

Without spin-orbit coupling, our calculations revealed that the anomalous Hall effect is absent and there is only a constant contribution to the spin Hall signal originating from the magnetic background texture. In this case there is only a pure spin current [cf. Fig. 1(c)]. As we will show in the following, the contribution which is arising from spin-orbit coupling and

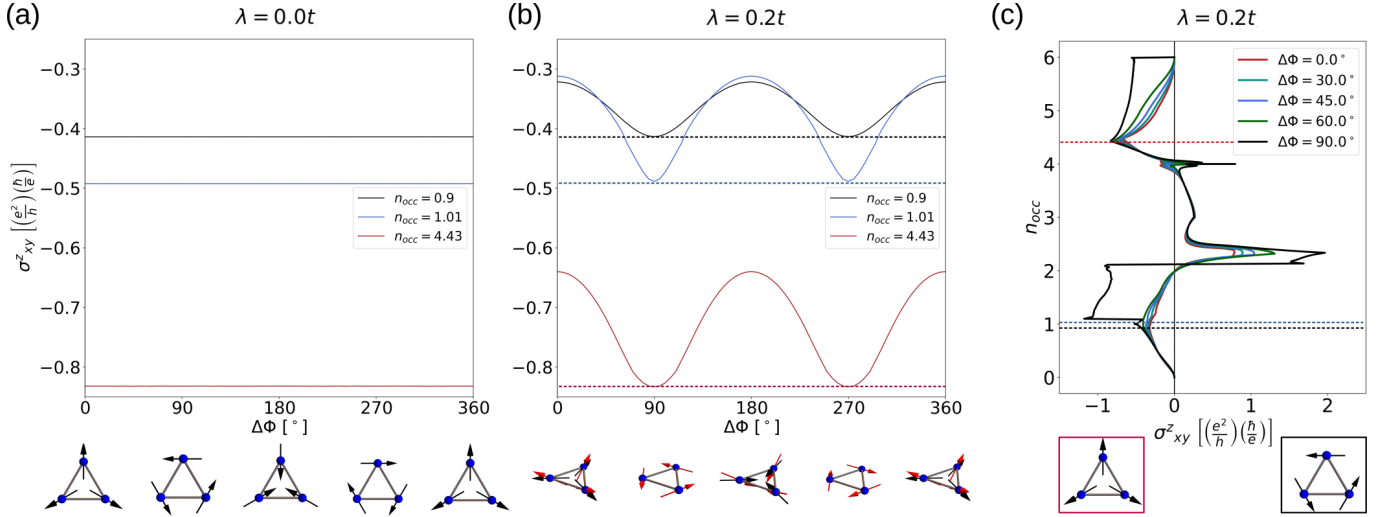


FIG. 4. Spin Hall conductivity for different fixed occupation numbers n_{occ} upon a continuous rotation of the magnetic moments within the kagome plane as indicated by the small cartoons below the panel. (a) Spin-orbit coupling is not taken into account and in this case the spin Hall signal is nonzero, but constant and thus independent of the in-plane orientation of the magnetic moments. (b) Same as (a) but spin-orbit interaction is considered ($\lambda = 0.2t$). Here the spin Hall conductivity is oscillating with a period of 180° and so does the out-of-plane component of the magnetic moments of the virtual texture (red arrows in the small cartoons). (c) σ_{xy}^z plotted against n_{occ} for the radial (red) and toroidal phase (black) and configurations in between the two with spin-orbit interaction taken into account [$\lambda = 0.2t$ as in (b)]. The horizontal lines indicate the values of the fixed occupation numbers in (a) and (b).

which is reducing the spin Hall signal is roughly proportional to the anomalous Hall conductivity σ_{xy} multiplied with the magnetization density μ_z^s ,

$$\Delta\sigma_{xy}^z(\text{SOC}) \propto \sigma_{xy} \mu_z^s. \quad (11)$$

We will demonstrate this now by examining the behavior of the systems while varying the parameter m that describes the Hund's coupling strength between the spin moment of the conduction electron and the magnetic texture $\{\mathbf{m}_i\}$. Therefore, we are calculating not only the spin Hall conductivity σ_{xy}^z but also the anomalous Hall conductivity σ_{xy} and the out-of-plane component of the magnetization density μ_z^s upon rotating the magnetic moments within the kagome plane, as before.

The calculation of σ_{xy} is performed via Kubo formalism [37]:

$$\sigma_{xy}(E_F) = -\frac{e^2}{h} \sum_v \frac{1}{2\pi} \int_{\varepsilon(\mathbf{k}) \leq E_F} \Omega_{xy,v}(\mathbf{k}) d^2k, \quad (12)$$

where one has to integrate over the conventional Berry curvature

$$\Omega_{xy,v}(\mathbf{k}) = -2\hbar^2 \text{Im} \sum_{\mu \neq v} \frac{\langle v, \mathbf{k} | v_x | \mu, \mathbf{k} \rangle \langle \mu, \mathbf{k} | v_y | v, \mathbf{k} \rangle}{[\varepsilon_v(\mathbf{k}) - \varepsilon_\mu(\mathbf{k})]^2}. \quad (13)$$

The magnetization density can be calculated from the spin texture of the itinerant magnetic moments of the conduction electrons' spins in reciprocal space. The z component of the spin texture of band v is obtained by the calculation of the spin expectation value

$$\langle s_v^z(\mathbf{k}) \rangle = \langle v, \mathbf{k} | \sigma^z | v, \mathbf{k} \rangle, \quad (14)$$

where σ^z is the Pauli matrix. Integrating over all occupied states in the Brillouin zone and summing over all bands yields

the out-of-plane component of the magnetization density

$$\mu_z^s = \mu_B \sum_v \frac{1}{(2\pi)^2} \int_{\varepsilon(\mathbf{k}) \leq E_F} \langle s_v^z(\mathbf{k}) \rangle d^2k. \quad (15)$$

The results for σ_{xy} (in units of $\frac{e^2}{h}$) and μ_z^s (in units of μ_B) are presented together with σ_{xy}^z in Fig. 5 where we set the occupation number $n_{\text{occ}} = 0.9$.

Without spin-orbit interaction (cf. dashed lines), the anomalous Hall effect is prohibited and the spin texture is coplanar, whereas the spin Hall effect is constant. σ_{xy} and μ_z^s vanish identically, independent of m and the in-plane rotation. The amount of σ_{xy}^z is decreased with increasing m [39].

Taking spin-orbit interaction into account ($\lambda = 0.2t$, solid lines in Fig. 5), yields a cosinusoidal behavior [40] of both the anomalous Hall conductivity and the z component of the magnetization density as a function of $\Delta\Phi$, whereas the spin Hall conductivity oscillates with the half-period, as before in Fig. 4. Now, enlarging the strength of the Hund's coupling m causes not only a reduction of the amount of the spin Hall signal, but also of the out-of-plane magnetization density, i.e., the spin texture aligns more and more with the coplanar texture. The amplitude of σ_{xy} is hardly affected by m .

For the toroidal configurations ($\Delta\Phi = 90^\circ, 270^\circ$), the anomalous Hall effect is absent and the spin texture remains coplanar, protected by the \mathcal{M} symmetry. Consequently, there is no reduction of the spin Hall signal [cf. Eq. (11)] and we would observe a pure spin current even upon considering spin-orbit coupling. For all other configurations, the product of the finite and cosinusoidal signals σ_{xy} and μ_z^s explains the reduction of the spin Hall signal which is oscillating with a period of 180° .

We interpret the nonvanishing out-of-plane magnetization and charge current emerging due to spin-orbit interaction as

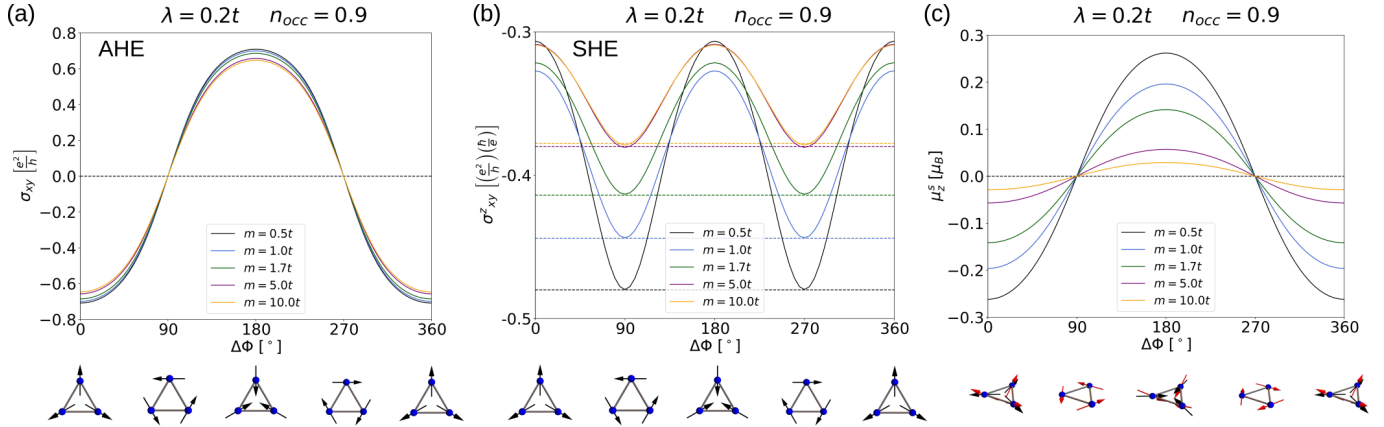


FIG. 5. Dependence of anomalous and spin Hall conductivity and the magnetization density on the Hund's coupling parameter m calculated for a fixed occupation number ($n_{\text{occ}} = 0.9$) as a function of $\Delta\Phi$, analog to Fig. 4. For calculations with spin-orbit interaction (solid lines), we set $\lambda = 0.2t$. The dashed lines indicate the results of analog calculations without spin-orbit coupling. (a) The anomalous Hall conductivity σ_{xy} is only finite (and cosinusoidal) if spin-orbit coupling is taken into account. The anomalous Hall signal is only weakly reduced with increasing m and remains zero for the toroidal arrangements ($\Delta\Phi = 90^\circ, 270^\circ$). (b) Spin Hall conductivity σ_{xy}^z analog to Fig. 4(b). The amplitude of the contribution originating from the magnetic texture is reduced by spin-orbit coupling for all configurations except for the toroidal one. This additional contribution is shrinking with growing m . (c) Like σ_{xy} , the z component of the spin texture and thus the magnetization density μ_z^z is only nonzero if spin-orbit coupling is taken into account. As visible, the spin texture is continuously aligning with the real coplanar magnetic texture upon increasing Hund's coupling strength m . Note that μ_z^z remains zero for the toroidal configurations independent of λ and m .

a spin-polarized current. The latter is reducing the pure spin current of the magnetic background texture that causes the spin Hall effect, which is illustrated in Fig. 1(d).

D. Spin Hall effect under out-of-plane rotation of the magnetic moments

Summing up to this point, two different mechanisms contribute to the intrinsic spin Hall effect in noncollinear kagome antiferromagnets. One source is the Hund's coupling of the spin of the conduction electron to the chiral antiferromagnetic texture $\{\mathbf{m}_i\}$ itself where spin-orbit interaction is not required. The second contribution to the signal is mainly reducing the spin conductivity and it is originating from spin-orbit coupling that gives rise to a virtual magnetic texture $\{\tilde{\mathbf{m}}_i\}$. As explained before, the virtual texture determines the electronic properties and can be interpreted as tilting with respect to the real texture depending on the in-plane orientation $\Delta\Phi$ and on the spin-orbit coupling strength λ .

Motivated by these findings, magnetic textures that are already tilted out-of the kagome plane [$\theta \neq 90^\circ$; cf. Eq. (5)] are investigated, in order to analyze the two contributions to the spin Hall signal. This could be achieved by applying an external magnetic field along z . However, we assume that the magnetic moments are only rotated and their magnitude does not change.

We calculate σ_{xy}^z for a fixed Fermi energy upon varying θ while $\Delta\Phi$ is constant [cf. small cartoons in Figs. 6(a) and 6(b)]. Since the tilting mechanism of the virtual magnetic texture is strongest for the radial arrangement, we set $\Delta\Phi = 0^\circ$.

First of all, we discuss the results if we neglect spin-orbit interaction [cf. Fig. 6(a)]. For the collinear configurations ($\theta = 0^\circ, 180^\circ$), the spin Hall signal is zero since the spin Hall effect is absent in ferromagnets without spin-orbit coupling

that would deflect electrons with different spin in opposite directions [41]. For all other configurations we get finite values and the spin Hall signal is completely symmetric with respect to $\theta = 90^\circ$. In this case, the virtual magnetic texture is not tilted with respect to the real texture but the noncoplanar texture has an opening angle that gives rise to a pure topological Hall effect which implies that charge is transported as a response to an applied electric field. Since the spin Hall signal without spin-orbit interaction is independent of the in-plane rotation $\Delta\Phi$, it is worth noting that analog calculations for arbitrary $\Delta\Phi$ yield the same results, as shown exemplarily for $\Delta\Phi = 0^\circ$ in Fig. 6(a).

With spin-orbit coupling ($\lambda = 0.2t$), the collinear ferromagnets exhibit a spin Hall effect [cf. Fig. 6(b)] which is equal for both collinear phases ($\theta = 0^\circ, 180^\circ$) since the spin Hall effect in ferromagnets is not affected by reversal of the magnetic moments [42]. Besides, the shape of the signal is only slightly deformed and the curves are mainly shifted by $\Delta\theta \approx 13^\circ$. This can be seen by comparing the positions of the local extrema in Figs. 6(a) and 6(b). This angle is the same critical angle $\Delta\theta_c$ that we revealed for $\lambda = 0.2t$ in Ref. [34].

As explained before, the anomalous Hall effect is absent for this noncoplanar (radial-type) texture characterized by $\theta_c = 90^\circ + \Delta\theta_c$. In this case, the virtual texture is coplanar and the effective spin-orbit coupling according to Eq. (10) is compensated. Therefore, the noncoplanar system behaves as if it was effectively coplanar due to the equivalence of spin-orbit interaction and out-of-plane tilting of the magnetic texture that compensate each other, here.

To corroborate this, we compare the spin Hall signal as a function of E_F for this critical angle [black curve in Fig. 6(c)] with the one of the coplanar configuration [red curve in Fig. 6(c)] that we have already shown before. As visible, the spin Hall signal characterized by this critical angle with spin-orbit coupling is the same as the one of the coplanar

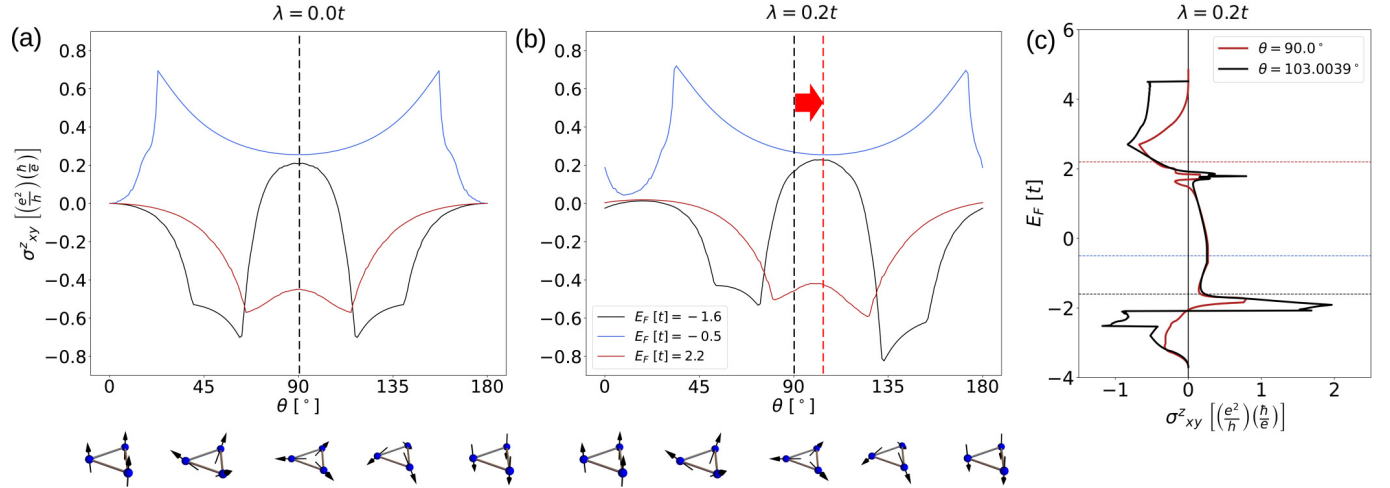


FIG. 6. Spin Hall conductivity under out-of-plane rotation of the radial-type magnetic texture ($\Delta\Phi = 0^\circ$). (a) The spin Hall signal is symmetric with respect to $\theta = 90^\circ$ if spin-orbit coupling is not considered. (b) If spin-orbit interaction is taken into account, the curves of (a) are slightly deformed and mainly shifted by the critical angle $\Delta\theta_c \approx 13^\circ$, as well. (c) The spin Hall conductivity as a function of E_F for the radial-type arrangement (with spin-orbit coupling) that is characterized by the critical out-of-plane orientation (black curve) is identical to the signal of the coplanar configuration without spin-orbit coupling [cf. black curve from Fig. 3(b)]. The red curve is the same as the red curve in Fig. 3(b) for the coplanar texture with spin-orbit coupling. The horizontal lines indicate the values of the Fermi level chosen in (a) and (b).

configuration where spin-orbit interaction is neglected [black curve in Fig. 3(b)].

This explicitly proves that tilting the texture has the same effect as spin-orbit coupling in this model.

IV. CONCLUSION

In summary, we have identified two mechanisms determining the spin Hall signal. We showed via tight-binding calculations that the main contribution is a pure spin current that originates from the coplanar magnetic background texture. Besides, spin-orbit coupling is equivalent to an out-of-plane tilting of the magnetic moments and thereby generates an asymmetry in the spin polarization with respect to the quantization axis perpendicular to the kagome plane. Thus, with spin-orbit interaction a spin-polarized current is flowing as well that reduces the spin Hall signal of the pure spin current effectively.

Therefore, noncollinear kagome antiferromagnets have the potential for applications in spintronic devices where they might be utilizable as alternative generators for spin currents and spin-polarized currents in analogy to collinear antiferromagnets and ferromagnets, respectively (cf. Fig. 1).

Besides, our results might be insightful for the experimental observation of the spin Hall effect in manganese compounds with a positive vector spin chirality like Mn_3Ir . In this material, the anomalous Hall effect was predicted theoretically seven years ago [27,28], but it has not been measured up to now. The reason is that domains with different phases that we characterize by $\Delta\Phi = 0^\circ$ and 180° occur in that material [43]. The anomalous Hall effect is allowed in both phases but both signals compensate each other due to their opposite sign [27,34]. However, our findings show that the spin Hall signal would be the same for both phases and therefore there could be the possibility to measure the spin Hall effect without the need to prepare single-domain samples.

ACKNOWLEDGMENTS

This work is supported by CRC/TRR 227 of Deutsche Forschungsgemeinschaft (DFG).

O.B. performed the tight-binding calculations with the help of B.G. O.B. wrote the manuscript with significant input from all authors. O.B. prepared the figures. All authors discussed the results. B.G. and I.M. planned and supervised the project.

- [1] K. Sadasivuni, A. Y. Al Haddad, H. Javed, W. Yoon, and J.-J. Cabibihan, Strain, pressure, temperature, proximity, and tactile sensors from biopolymer composites, in *Biopolymer Composites in Electronics* (Elsevier, Amsterdam, 2017), pp. 437–457.
- [2] M. I. D'yakonov and V. I. Perel, Current-induced spin orientation of electrons in semiconductors, *Phys. Lett. A* **35**, 459 (1971).
- [3] M. I. D'yakonov and V. I. Perel, Spin orientation of electrons associated with the interband absorption of light in semiconductors, *Soviet J. Exper. Theor. Phys.* **33**, 1053 (1971).

- [4] I. Žutić, J. Fabian, and S. D. Sarma, Spintronics: Fundamentals and applications, *Rev. Mod. Phys.* **76**, 323 (2004).
- [5] V. Baltz, A. Manchon, M. Tsoi, T. Moriyama, T. Ono, and Y. Tserkovnyak, Antiferromagnetic spintronics, *Rev. Mod. Phys.* **90**, 015005 (2018).
- [6] R. Duine, An alternating alternative, *Nat. Mater.* **10**, 344 (2011).
- [7] J. Sinova and I. Žutić, New moves of the spintronics tango, *Nat. Mater.* **11**, 368 (2012).
- [8] J. E. Hirsch, Spin Hall Effect, *Phys. Rev. Lett.* **83**, 1834 (1999).

- [9] H. Ohno, Making nonmagnetic semiconductors ferromagnetic, *Science* **281**, 951 (1998).
- [10] S. Pearton, C. Abernathy, M. Overberg, G. Thaler, D. Norton, N. Theodoropoulou, A. Hebard, Y. Park, F. Ren, J. Kim *et al.*, Wide band gap ferromagnetic semiconductors and oxides, *J. Appl. Phys.* **93**, 1 (2003).
- [11] V. Dediu, M. Murgia, F. Maticcotta, C. Taliani, and S. Barbanera, Room temperature spin polarized injection in organic semiconductor, *Solid State Commun.* **122**, 181 (2002).
- [12] D. A. Pejaković, C. Kitamura, J. S. Miller, and A. J. Epstein, Photoinduced Magnetization in the Organic-Based Magnet $\text{Mn}(\text{TCNE})_x \cdot y(\text{CH}_2\text{Cl}_2)$, *Phys. Rev. Lett.* **88**, 057202 (2002).
- [13] A. Goldman, V. Vas'ko, P. Kraus, K. Nikolaev, and V. Larkin, Cuprate/manganite heterostructures, *J. Magn. Magn. Mater.* **200**, 69 (1999).
- [14] J. Schliemann, Spin Hall effect, *Int. J. Mod. Phys. B* **20**, 1015 (2006).
- [15] J. Sinova, S. O. Valenzuela, J. Wunderlich, C. H. Back, and T. Jungwirth, Spin Hall effects, *Rev. Mod. Phys.* **87**, 1213 (2015).
- [16] Y. K. Kato, R. C. Myers, A. C. Gossard, and D. D. Awschalom, Observation of the spin Hall effect in semiconductors, *Science* **306**, 1910 (2004).
- [17] T. Kimura, Y. Otani, T. Sato, S. Takahashi, and S. Maekawa, Room-Temperature Reversible Spin Hall Effect, *Phys. Rev. Lett.* **98**, 156601 (2007).
- [18] L. Liu, C.-F. Pai, Y. Li, H. Tseng, D. Ralph, and R. Buhrman, Spin-torque switching with the giant spin Hall effect of tantalum, *Science* **336**, 555 (2012).
- [19] J. C. Slonczewski, Current-driven excitation of magnetic multilayers, *J. Magn. Magn. Mater.* **159**, L1 (1996).
- [20] L. Berger, Emission of spin waves by a magnetic multilayer traversed by a current, *Phys. Rev. B* **54**, 9353 (1996).
- [21] A. Khvalkovskiy, D. Apalkov, S. Watts, R. Chepulskii, R. Beach, A. Ong, X. Tang, A. Driskill-Smith, W. Butler, P. Visscher *et al.*, Basic principles of STT-MRAM cell operation in memory arrays, *J. Phys. D* **46**, 074001 (2013).
- [22] H. Reichlova, T. Janda, J. Godinho, A. Markou, D. Kriegner, R. Schlitz, J. Zelezny, Z. Soban, M. Bejarano, H. Schultheiss *et al.*, Imaging and writing magnetic domains in the non-collinear antiferromagnet Mn_3Sn , *Nat. Commun.* **10**, 5459 (2019).
- [23] S. A. Siddiqui, J. Sklenar, K. Kang, M. J. Gilbert, A. Schleife, N. Mason, and A. Hoffmann, Metallic antiferromagnets, *J. Appl. Phys.* **128**, 040904 (2020).
- [24] R. Cheng, M. W. Daniels, J.-G. Zhu, and D. Xiao, Ultrafast switching of antiferromagnets via spin-transfer torque, *Phys. Rev. B* **91**, 064423 (2015).
- [25] L. Šmejkal, Y. Mokrousov, B. Yan, and A. H. MacDonald, Topological antiferromagnetic spintronics, *Nat. Phys.* **14**, 242 (2018).
- [26] Y. Zhang, Y. Sun, H. Yang, J. Železny, S. P. P. Parkin, C. Felser, and B. Yan, Strong anisotropic anomalous Hall effect and spin Hall effect in the chiral antiferromagnetic compounds Mn_3X ($\text{X} = \text{Ge}, \text{Sn}, \text{Ga}, \text{Ir}, \text{Rh}, \text{and Pt}$), *Phys. Rev. B* **95**, 075128 (2017).
- [27] H. Chen, Q. Niu, and A. H. MacDonald, Anomalous Hall Effect Arising from Noncollinear Antiferromagnetism, *Phys. Rev. Lett.* **112**, 017205 (2014).
- [28] J. Kübler and C. Felser, Non-collinear antiferromagnets and the anomalous Hall effect, *Europhys. Lett.* **108**, 67001 (2014).
- [29] S. Nakatsuji, N. Kiyohara, and T. Higo, Large anomalous Hall effect in a non-collinear antiferromagnet at room temperature, *Nature (London)* **527**, 212 (2015).
- [30] A. K. Nayak, J. E. Fischer, Y. Sun, B. Yan, J. Karel, A. C. Komarek, C. Shekhar, N. Kumar, W. Schnelle, J. Kübler *et al.*, Large anomalous Hall effect driven by a nonvanishing Berry curvature in the noncolinear antiferromagnet Mn_3Ge , *Sci. Adv.* **2**, e1501870 (2016).
- [31] N. Kiyohara, T. Tomita, and S. Nakatsuji, Giant Anomalous Hall Effect in the Chiral Antiferromagnet Mn_3Ge , *Phys. Rev. Appl.* **5**, 064009 (2016).
- [32] Y. Zhang, J. Železny, Y. Sun, J. Van Den Brink, and B. Yan, Spin Hall effect emerging from a noncollinear magnetic lattice without spin-orbit coupling, *New J. Phys.* **20**, 073028 (2018).
- [33] M. Seemann, D. Ködderitzsch, S. Wimmer, and H. Ebert, Symmetry-imposed shape of linear response tensors, *Phys. Rev. B* **92**, 155138 (2015).
- [34] O. Busch, B. Göbel, and I. Mertig, Microscopic origin of the anomalous Hall effect in noncollinear kagome magnets, *Phys. Rev. Research* **2**, 033112 (2020).
- [35] C. Herring, *Magnetism: A Treatise on Modern Theory and Materials. 4. Exchange Interactions among Itinerant Electrons* (Academic, New York, 1966).
- [36] X. Zhou, J.-P. Hanke, W. Feng, F. Li, G.-Y. Guo, Y. Yao, S. Blügel, and Y. Mokrousov, Spin-order dependent anomalous Hall effect and magneto-optical effect in the noncollinear antiferromagnets Mn_3XN with $\text{X} = \text{Ga}, \text{Zn}, \text{Ag}, \text{or Ni}$, *Phys. Rev. B* **99**, 104428 (2019).
- [37] N. Nagaosa, J. Sinova, S. Onoda, A. H. MacDonald, and N. P. Ong, Anomalous Hall effect, *Rev. Mod. Phys.* **82**, 1539 (2010).
- [38] D. Fruchart and E. F. Bertaut, Magnetic studies of the metallic perovskite-type compounds of manganese, *J. Phys. Soc. Jpn.* **44**, 781 (1978).
- [39] Note that σ_{xy}^z is negative for the chosen fixed occupation number.
- [40] Note that their dependence can also be more complicated.
- [41] B. F. Miao, S. Y. Huang, D. Qu, and C. L. Chien, Inverse Spin Hall Effect in a Ferromagnetic Metal, *Phys. Rev. Lett.* **111**, 066602 (2013).
- [42] D. Tian, Y. Li, D. Qu, S. Y. Huang, X. Jin, and C. L. Chien, Manipulation of pure spin current in ferromagnetic metals independent of magnetization, *Phys. Rev. B* **94**, 020403(R) (2016).
- [43] C. Ulloa and A. S. Nunez, Solitonlike magnetization textures in noncollinear antiferromagnets, *Phys. Rev. B* **93**, 134429 (2016).

4.3 Unconventional orbital Hall effect arising in s -orbital systems

Hybridization of atomic orbitals as origin of the orbital Hall effect. The orbital degree of freedom has been investigated to a smaller extent than the spin companion, since orbital angular momentum (OAM) is often suppressed in the ground state; a phenomenon denoted as ‘orbital quenching’ [22]. However, it has been demonstrated that the situation is different in a *non-equilibrium* state: the application of an electric field may generate nonzero OAM which can be transported through the solid [23]. In analogy to the SHE, the creation of such orbital currents flowing transverse to the electric field is called ‘orbital Hall effect’ (OHE) [25]. SHE and OHE are closely related to each other, and they are both allowed in nonmagnetic and centrosymmetric materials, in which the AHE is forbidden, since the latter requires broken time-reversal symmetry. In contrast to the SHE, which is absent in such materials *without* SOC, the OHE is still allowed and predicted to be large. In fact, it has been shown that orbital currents are partially converted to spin currents *by* SOC, which makes the OHE more fundamental than the SHE.

The origin of the OHE is still debated, but early works claimed that the effect arises from hybridization of specific atomic orbitals at a particular lattice site: the superposition of cubic harmonic orbitals (s, p_x, p_y, \dots) forms spherical harmonic orbitals with an OAM transported by an orbital current [21]. This explanation considers only *intra*-atomic contributions and is known as the atomic center approximation (ACA). In order to account for *inter*-atomic contributions to the OHE as well, one has to apply the modern formulation of orbital magnetization [28].

This publication. In the following publication “Orbital Hall effect and orbital edge states caused by s electrons” [OB3], an alternative mechanism to generate orbital currents is established. By comparing results for the OHE computed with both methods – ACA and modern formulation of orbital magnetization – we show that the OHE may exist for pure states without hybridization of specific orbitals. As a minimal model for the generation of orbital currents, the *nonmagnetic* kagome lattice with only s orbitals and without SOC is introduced. Although s electrons in a single atom (intra-site contributions in ACA) do not carry OAM, a propagation over multiple atomic sites (inter-site contributions in modern formulation of orbital magnetization) allows for accumulation of OAM.

Furthermore, deeper insight into the microscopic mechanism of the OHE is achieved by investigating various kagome-lattice slab geometries. In doing so, we reveal the existence of ‘geometrical’ edge states in a nanoribbon with two different edges (‘straight’ and ‘triangular’; cf. Fig. 3(b) in [OB3]). These are ‘orbital edge states’ moving on cycloid trajectories, which gives rise to the generation of an orbital current as visualized in Fig. 1 in the publication. This situation is in analogy to the classical scenario of a rolling wheel where a simultaneous translation and rotation results in a transport of OAM, i.e. in an orbital current.

The following publication: Reprinted (whole article) with permission from O. Busch, I. Mertig and B. Göbel, *Physical Review Research* **5**, 043052 (2023); Ref. [OB3]; Orbital Hall effect and orbital edge states caused by s electrons. Published by the American Physical Society under the terms of the Creative Commons Attribution 4.0 International license.

Orbital Hall effect and orbital edge states caused by s electronsOliver Busch ^{*}, Ingrid Mertig , and B3rge G3bel [†]*Institut f3ur Physik, Martin-Luther-Universit3at Halle-Wittenberg, D-06099 Halle (Saale), Germany*

(Received 5 July 2023; revised 22 September 2023; accepted 25 September 2023; published 17 October 2023)

An orbital current can be generated whenever an object has a translational degree of freedom and a rotational degree of freedom. In condensed matter physics, intra-atomic contributions to the transverse orbital transport, labeled the orbital Hall effect, rely on propagating wave packets that must consist of hybridized atomic orbitals. However, interatomic contributions have to be considered as well because they give rise to an alternative mechanism for generating orbital currents. As we show, even wave packets consisting purely of s electrons can transport orbital angular momentum if they move on a cycloid trajectory. We introduce the kagome lattice with a single s orbital per atom as the minimal model for the orbital Hall effect and observe the cycloid motion of the electrons in the surface states.

DOI: [10.1103/PhysRevResearch.5.043052](https://doi.org/10.1103/PhysRevResearch.5.043052)

I. INTRODUCTION

The field of orbitronics is concerned with the orbital degree of freedom of electrons instead of their spin and charge [1]. Despite the fact that orbital quenching [2] leads to a suppressed orbital magnetization in most solids, orbital currents often surpass spin currents in magnitude, as the latter require considerable spin-orbit coupling to be generated. This makes orbital currents highly attractive for dissipationless orbitronic applications [3].

Charge, spin, and orbital currents can be generated by the charge [4], spin [5–8], and orbital Hall effects [9–13]: The application of an electric field leads to the generation of the different types of currents as a transverse response. While the conventional (charge) Hall effect requires a broken inversion and time-reversal symmetry, the spin and orbital Hall effects can exist even in nonmagnetic and centrosymmetric solids. The orbital Hall effect (OHE) has been predicted to exist even in systems without spin-orbit coupling, but a hybridization of different atomic orbitals has been strictly required in the models up to now [14,15].

The need for mixing of orbitals stems from the fact that earlier studies on the OHE were based on the atomic center approximation (ACA) for calculating the orbital angular momentum (OAM) [11–14]: An OAM, which is supposed to be transported as an orbital current, can only be generated at a particular lattice site. However, since the building blocks of every solid are cubic harmonic orbitals ($s, p_x, p_y, p_z, d_{xy}, d_{yz}, d_{zx}, \dots$), the OAM of a pure Bloch state

always vanishes. The cubic harmonic orbitals need to hybridize (e.g., form the superpositions $p_x \pm i p_y$ or $d_{yz} \pm i d_{xz}$) in order to generate an OAM $L_z = m\hbar$. However, the ACA neglects interatomic contributions to the effect: A wave packet propagating across several lattice sites can carry an OAM irrespective of its orbital composition [16].

In this paper, we take into account the interatomic contributions to the OHE by using the modern formulation of orbital magnetization [17–23]. We show that the generation of an OHE does not require a specific orbital hybridization but can exist even for pure states. We propose a kagome lattice with only s orbitals as the minimal model for the generation of an orbital Hall effect. We demonstrate that the OHE arises from a cycloid motion of a wave packet that is best observed in “geometrical” [24] edge states in a finite slab geometry. These states give rise to the same orbital current irrespective of their propagation direction [red and blue in Fig. 1(a)].

II. ORBITAL CURRENTS IN MACROSCOPIC SYSTEMS

The ACA requires an often complicated hybridization of specific atomic orbitals for the generation of an OAM and an orbital magnetization [11–14]. However, these quantities may emerge irrespective of the orbital contribution if the modern formulation of orbital magnetization is considered.

In the following, we want to point out that this is not surprising. Orbital currents are not “exotic” but appear whenever objects “translate” and “circulate” simultaneously. Even for macroscopic objects in classical mechanics, orbital currents are ubiquitous, as long as there is a translational and a rotational degree of freedom. For example, the rotors of a flying airplane can be identified with an orbital current. In the local coordinate system (moving with the center of mass) there is only a finite OAM $L = \rho \int \mathbf{r} \times \mathbf{v} d^3r$ since each point of the rotor follows a circular trajectory. In a global (stationary) coordinate system that lies on the path of the center of mass, the OAM is the same, but it is transported by the translational motion of the airplane. The result is an orbital current.

^{*}oliver.busch@physik.uni-halle.de[†]boerge.goebel@physik.uni-halle.de

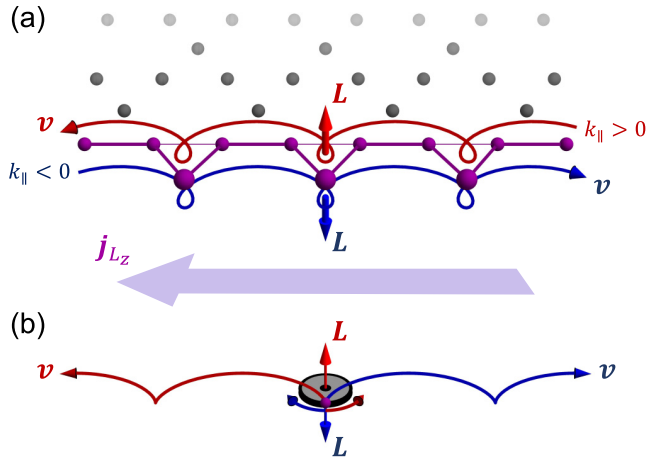


FIG. 1. Schematic representation of orbital currents. (a) Orbital current arising from edge states in a kagome lattice. Left- ($k_{\parallel} < 0$) and right-propagating states ($k_{\parallel} > 0$) carry an opposite orbital angular momentum L causing identical orbital currents j_{Lz} and a compensated charge current. (b) Orbital current of a tire rolling forward ($v > 0$) and backward ($v < 0$). Both states carry an opposite orbital angular momentum causing identical orbital currents.

As we will see later, most similar to the orbital current generated by the OHE in an s -orbital kagome model is the example of a rolling wheel (e.g., the tire of a car) [cf. Fig. 1(b)]. Without wheel slip, the friction force is strong enough to impose a constraint which couples the translational velocity (of the center of mass) v to the angular frequency ω via the radius R : $v = R\omega$. Likewise, the angular momentum $L \parallel \omega$ is coupled to v via the moment of inertia I : $v = RL/I$. In particular, if v changes sign, L has to change as well. Since the orbital current j_L is proportional to $v \times L$, it is identical for forward and backward motion even though L reverses.

Consequently, if one considers two wheels moving in opposite directions [red and blue in Fig. 1(b)], the total OAM L is compensated, but a net orbital current j_L arises. The trajectory of each point on the wheels is a cycloid in the global coordinate systems and a circle in the local coordinate system (origin is in the center of mass). As we demonstrate next, we observe an analogous scenario for j_L and the same type of trajectory for a wave packet propagating at the edge of a kagome lattice [cf. Fig. 1(a)]. Here, the OAM L is coupled to the group velocity $v = \nabla_k \varepsilon / \hbar$.

III. ORBITAL HALL EFFECT

In the existing literature, the hybridization of different cubic orbitals was claimed to be the origin of the OHE [11,13,14]. It was argued that they need to form the spherical harmonic orbitals with a net magnetic quantum number m that gives rise to a finite OAM [14,15]. As discussed in the Introduction, this is indeed the only possibility to generate an OHE when using the ACA. For example, a spherical atomic orbital with angular momentum quantum number $l = 1$ and magnetic quantum number $m = +1$ is formed by the superposition of the cubic orbitals p_x and p_y as $|l = 1, m = 1\rangle = (|p_x\rangle - i|p_y\rangle)/\sqrt{2}$ and gives rise to $L_z = m\hbar = +\hbar$.

In order to be able to account for the transported OAM via a cycloid trajectory, it is not sufficient to use the ACA for calculating the OHE. Instead, we take into account intersite contributions via the modern formulation of orbital magnetization [17–20] and use it to calculate the OHE regardless of the orbital composition. The calculation is not based on the on-site OAM operator that accounts for the hybridization of the cubic atomic orbitals, but it is calculated from the eigenvectors $|\nu\mathbf{k}\rangle \equiv |\varphi_\nu(\mathbf{k})\rangle$ and the eigenenergies $\varepsilon_{\nu\mathbf{k}} \equiv \varepsilon_\nu(\mathbf{k})$ of the tight-binding Hamiltonian that are \mathbf{k} dependent.

The orbital Hall conductivity (OHC) σ_{xy}^{Lz} quantifies the OHE by relating the generated orbital current to the applied electric field $j_x^{Lz} = \sigma_{xy}^{Lz} E_y$. The OHC of a two-dimensional system at zero temperature located in the xy plane, as considered in this paper, can be computed as [13,14,21]

$$\sigma_{xy}^{Lz}(E_F) = \frac{e}{\hbar} \sum_{\nu} \frac{1}{(2\pi)^2} \int_{\varepsilon_{\nu\mathbf{k}} \leq E_F} \Omega_{\nu,xy}^{Lz}(\mathbf{k}) d^2k \quad (1)$$

for a specific Fermi level E_F . By analogy with the spin Hall conductivity, the OHC is given as the Brillouin zone integral of a “mixed Berry curvature” that is labeled the “orbital Berry curvature” [21]

$$\Omega_{\nu,xy}^{Lz}(\mathbf{k}) = -2\hbar^2 \text{Im} \sum_{\mu \neq \nu} \frac{\langle \nu\mathbf{k} | \Lambda_x^z | \mu\mathbf{k} \rangle \langle \mu\mathbf{k} | v_y | \nu\mathbf{k} \rangle}{(\varepsilon_{\nu\mathbf{k}} - \varepsilon_{\mu\mathbf{k}})^2}. \quad (2)$$

Herein, $v_i = \frac{1}{\hbar} \frac{\partial H}{\partial k_i}$ is the velocity operator that is calculated from the Hamiltonian H . The orbital current operator is given by $\Lambda_x^z \equiv \frac{1}{2} \{v_x, L^z\}$ and can be evaluated according to the modern formulation of orbital magnetization via

$$\begin{aligned} \langle \nu\mathbf{k} | \Lambda_x^z | \mu\mathbf{k} \rangle &= \frac{1}{2} \sum_{\alpha} [\langle \nu\mathbf{k} | v_x | \alpha\mathbf{k} \rangle \langle \alpha\mathbf{k} | L_z | \mu\mathbf{k} \rangle \\ &\quad + \langle \nu\mathbf{k} | L_z | \alpha\mathbf{k} \rangle \langle \alpha\mathbf{k} | v_x | \mu\mathbf{k} \rangle]. \end{aligned}$$

The matrix elements of the OAM comprise both diagonal elements and off-diagonal elements

$$\begin{aligned} \langle \nu\mathbf{k} | L_z | \alpha\mathbf{k} \rangle &= -i \frac{e\hbar^2}{4g_L \mu_B} \sum_{\beta \neq \nu, \alpha} \left(\frac{1}{\varepsilon_{\beta\mathbf{k}} - \varepsilon_{\nu\mathbf{k}}} + \frac{1}{\varepsilon_{\beta\mathbf{k}} - \varepsilon_{\alpha\mathbf{k}}} \right) \\ &\quad \times (\langle \nu\mathbf{k} | v_x | \beta\mathbf{k} \rangle \langle \beta\mathbf{k} | v_y | \alpha\mathbf{k} \rangle - \langle \nu\mathbf{k} | v_y | \beta\mathbf{k} \rangle \langle \beta\mathbf{k} | v_x | \alpha\mathbf{k} \rangle), \quad (3) \end{aligned}$$

which is different compared with the ACA, where $\langle \nu\mathbf{k} | L_z | \alpha\mathbf{k} \rangle$ are constant matrix elements that mix different orbitals that are located at the same lattice site. The above equations were derived by Pezo *et al.* [21,23] based on the modern formulation of the orbital magnetization in the language of wave packet dynamics [18]. The full derivation can be found in the main text and Supplemental Material of Ref. [21], but we have corrected a mistake in Eq. (3) [25]. Note that in a finite sample the derivation differs slightly: As presented in Ref. [26], the velocity matrix elements can be calculated from the commutator between the position and the Hamiltonian operator.

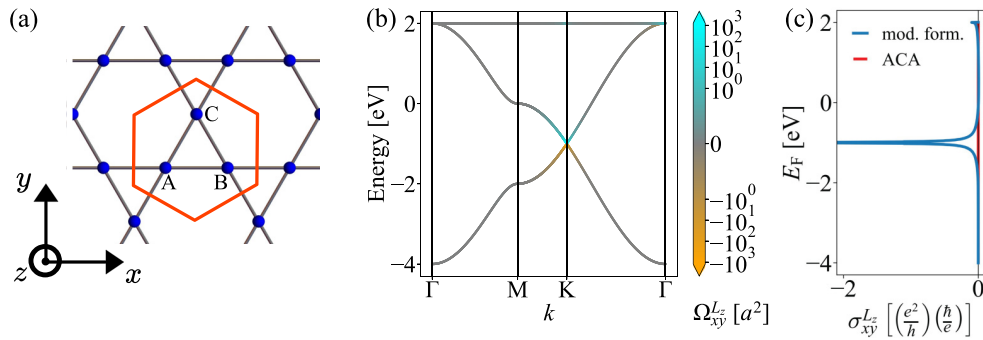


FIG. 2. Orbital Hall effect in an s -orbital kagome lattice. (a) Kagome lattice with three basis atoms (atoms A, B, and C) per unit cell (red hexagon). (b) Band structure of the bulk system, where the color of the bands indicates the orbital Berry curvature $\Omega_{xy}^{L_z}$ using the modern formulation (mod. form.; cyan, positive; orange, negative). (c) Orbital Hall conductivity as a function of the Fermi level E_F . Blue and red (zero) correspond to the modern formulation and ACA, respectively.

IV. MINIMAL MODEL: KAGOME LATTICE WITH s ORBITALS

As a minimal model that illustrates the crucial importance of using the modern formulations for computing the OHE, we have chosen a planar kagome lattice. This two-dimensional hexagonal lattice with a three-atom unit cell [cf. Fig. 2(a)] can be found in several materials including the ferromagnetic “kagome magnets” Fe_3Sn_2 [27,28] or $\text{Co}_3\text{Sn}_2\text{S}_2$ [29,30] and the famous chiral antiferromagnets Mn_3X ($X = \text{Ir, Rh, Pt, Ge, Sn, and Ga}$) [31–34].

Since the main goal of this paper is to show that considering the ACA is not sufficient to calculate the OHE, we completely avoid any hybridization of orbitals by using one s orbital per lattice site. Note that this orbital does not exhibit an on-site OAM (quantum number $l = 0$ and so $m = 0$). This means that only the modern formulation of the orbital magnetization contributes to the OHE via interatomic contributions. The ACA would always return a vanishing OHE, which is why this formalism is inappropriate to quantify the effect.

Since s orbitals do not exhibit spin-orbit coupling, our minimal model Hamiltonian includes only hopping terms $H = t \sum_{\langle i,j \rangle} c_i^\dagger c_j$ with the creation operator c_i^\dagger and the annihilation operator c_i of an electron at atom i . For simplicity, we consider only nearest-neighbor hopping and use $t = -1$ eV. In matrix form, the Hamiltonian reads

$$H = \begin{pmatrix} 0 & h_{AB} & h_{AC} \\ h_{BA} & 0 & h_{BC} \\ h_{CA} & h_{CB} & 0 \end{pmatrix} \quad (4)$$

with k -dependent entries $h_{AB} = h_{BA} = 2t \cos(k_x a)$, $h_{AC} = h_{CA} = 2t \cos(\frac{1}{2}k_x a + \frac{\sqrt{3}}{2}k_y a)$, and $h_{BC} = h_{CB} = 2t \cos(-\frac{1}{2}k_x a + \frac{\sqrt{3}}{2}k_y a)$ and the lattice constant a . We consider spin; so the matrix becomes 6×6 . The electronic band structure $\varepsilon_v(\mathbf{k})$ [cf. Fig. 2(b)] exhibits Dirac points similar to the ones found in honeycomb lattices, such as graphene [cf. Figs. 5(a) and 5(b) in Appendix A]. Additionally, a flat band arises from the three-atom basis that allows for closed loops and is not present in honeycomb lattices. All bands are spin degenerate due to inversion symmetry \mathcal{I} and time-reversal symmetry \mathcal{T} of the system in the absence of spin-orbit coupling.

As expected, the OHC vanishes in ACA because s electrons do not carry an on-site OAM. However, in the modern formulation, the OHC is finite and depends on the location of the Fermi level [cf. Fig. 2(c)]. The curve is almost constant within the bands but changes strongly at the band edges near the Dirac point and close to the flat band. For an occupation of two electrons per unit cell, the Fermi level is located at the Dirac point where the OHC is diverging.

Still, the effect cannot be attributed to the Dirac points alone, since a honeycomb lattice returns the same band structure (minus the flat band) but exhibits a vanishing OHC even in the modern formulation [cf. Fig. 5(c) in Appendix A]. The reason why two almost identical band structures result in drastically different orbital Hall effects is that the OHC [Eq. (1)] is determined by the eigenvectors as well.

The on-site (diagonal) elements of the OAM L_z , calculated by Eq. (3), vanish identically for all bands in the whole Brillouin zone (not shown here). However, the off-diagonal elements $\langle \nu \mathbf{k} | L_z | \alpha \mathbf{k} \rangle$ are finite in the kagome system, and they enter the matrix elements of the orbital current operator Λ_x^z and result in a finite orbital Berry curvature, which is encoded as a color code (cyan, positive; orange, negative) in the electronic structure [cf. Fig. 2(b)]. This means that no net OAM can be measured, even though the OHC is finite, and that the transported OAM is not generated at an individual lattice site but intersite contributions (off-diagonal elements) arise which correspond to a Bloch state that is spread out over all atoms in the unit cell. Thus the situation is comparable to the spin Hall effect, which can be finite despite a compensated spin magnetization S .

Unfortunately, a trajectory of electron wave packets cannot be analyzed for the bulk system, as the tight-binding formalism only allows us to access the probability density. However, investigating a slab geometry (nanoribbon) allows for a deeper insight into the origin of the orbital Hall effect.

V. EDGE STATES GENERATING CYCLOID TRAJECTORIES

A slab of the considered kagome system is only periodic along one direction giving rise to a single wave vector k_{\parallel} . Edges are introduced along the perpendicular direction. This

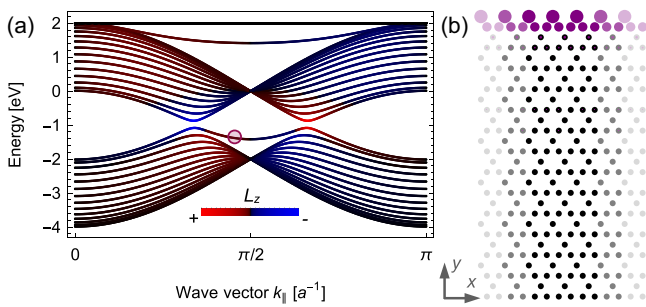


FIG. 3. Edge states in an asymmetric kagome-lattice slab that is periodic along the x direction. (a) Surface band structure along k_{\parallel} . The color indicates positive (red) and negative (blue) values of L_z . (b) Considered slab with probability density (area of purple circles) of the surface state indicated in (a) for $k_{\parallel} = 0.95\pi/2a$.

gives rise to a large unit cell and many bands in the slab band structure. The vast majority of these bands represent a projection of the bulk band structure, which is why signatures such as the Dirac points and the flat band appear in the slab band structure as well. Note that small supercell gaps occur due to the finite width of the system and that they converge to zero in the limit of an infinitely wide nanoribbon. However, caused by the edges, we observe features that were absent in the bulk band structure: the so-called surface states.

These states depend strongly on the specific shape of the edge: Most famously, a zigzag edge in a honeycomb lattice, such as graphene, exhibits an edge state, while an armchair edge does not [35–37]. For the kagome lattice, we observe several edge states for multiple edge geometries and want to focus on the geometry presented in Fig. 3, which has one “straight” edge and one “triangular” edge [cf. bottom and top edges of the sketch in Fig. 3(b)].

An edge state occurs close to the flat band, and another occurs between the two Dirac points [cf. Fig. 3(a)]. Their Chern numbers C are zero due to the time-reversal symmetry of the system. In Ref. [24] they have been labeled “geometrical edge states.” In contrast to the edge state in zigzag graphene, these states have a finite group velocity $v_v(k_{\parallel}) = \frac{1}{\hbar} \frac{\partial \epsilon_v(k_{\parallel})}{\partial k_{\parallel}} \neq 0$ allowing electron wave packets to propagate along the edges.

The edge states are symmetric with respect to k_{\parallel} ; for each right-propagating state at $+k_0$ there is a left-propagating state at $-k_0$. Due to the vanishing Chern numbers, the edges do not cause a quantum Hall effect. The Z_2 invariant and the spin Hall effect vanish as well because all the bands are spin degenerate due to the absence of spin-orbit coupling.

However, the OAM L_z is nonzero and has an opposite sign comparing states at $+k_0$ and $-k_0$. Note that L_z has been zero in the bulk because due to the periodic repetition of the three-atom unit cell, each upward-facing triangle automatically forms a neighboring downward-facing triangle with the same occupation. Therefore each circular orbit in the bulk automatically generates an orbit with opposite circumferential direction resulting in a compensated L_z . At the triangular edge, this balance of upward- and downward-facing triangles is impaired, and so a finite L_z can be generated [color in Fig. 3(a)].

In Fig. 3(b) we show the probability density of electrons for the surface state between the Dirac points at $k_{\parallel} = 0.95\frac{\pi}{2a}$.

Typical for an edge state, the probability density is largest for lattice sites close to the edge and decays exponentially going further into the bulk. In particular, the probability density is largest for the corners of the triangles at the very edge. Even though we can still only calculate the probability density and no currents, this distribution of electrons is in agreement with a cycloid trajectory as presented in Fig. 1(a). If a wave packet consists of $+k_0$ and $-k_0$ states, the scenario is in analogy with the forward and backward rolling wheel [cf. Fig. 1(b)], as discussed in the beginning of this paper: Edge states propagating along the right carry an opposite OAM compared with edge states propagating along the left, resulting in the same orbital current.

Our understanding of the behavior at the edge can be further condensed by considering a quasi-one-dimensional chain resembling the triangles at the very edges. Such a simplistic three-atom model allows us to calculate similar k_{\parallel} -resolved OAM and orbital currents as long as the chain does not have a glide-mirror symmetry with a symmetry axis along the periodic direction. In Appendix B, we demonstrate that the asymmetric chain, as we find at the edge of the considered kagome lattice, leads to an orbital current [Figs. 6(b) and 6(c)]. The cycloid trajectory with a curvature of constant sign can be understood as a superposition of a translation and a rotation as discussed before [cf. Fig. 1(a)]. On the other hand, a symmetric zigzag chain cannot exhibit an orbital current since the probability density corresponds to a sinelike trajectory with alternating curvatures that compensate each other [Figs. 6(e) and 6(g)] resulting in $L = 0$. Note that in a honeycomb lattice, a symmetric zigzag-shaped edge leads to a dispersionless surface state [38] and therefore no orbital current can be generated. This also agrees with the finding that the OHE vanishes for a honeycomb lattice, such as graphene, even in the modern theory.

So far, we have only taken into account s orbitals (which are equivalent to p_z orbitals for two-dimensional systems located in the xy plane). Taking into account all three p orbitals causes hybridization of p_x and p_y , which results in a finite OHE even within the ACA approach, similar to the findings in Ref. [14]. OAM-polarized edge states arise in this case as well, as shown for a related material, PtS₂, in Ref. [39]. If spin-orbit coupling is considered, one observes a partial conversion of the OHE into the spin Hall effect as shown by Go *et al.* using the ACA [14]. Spin-orbit coupling lifts the spin degeneracy and the edge state splits up as shown by Sun *et al.* [40].

A categorization of the quantum Hall effect, the quantum spin Hall effect, and the edge signature of the orbital Hall effect can be found in Fig. 4. Even though their origins are fundamentally different, the spin Hall effect (SHE) and OHE exhibit similar transport of (spin or orbital) angular momentum not only in the bulk but also along the edge. The SHE caused by an edge state is quantized due to the complete spin polarization of the surface states. This is not the case for the OHE because L is not quantized. In contrast to the quantized versions of the charge and SHE, the orbital edge current is not protected. In the considered kagome system, the edge contribution to the OHE appears in its pure form and is carried by a geometrical edge state that does not bridge the gap between two bulk bands [cf. Fig. 4(c)]. However,

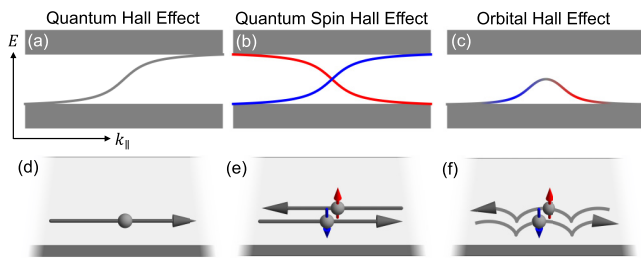


FIG. 4. Comparison of edge states and corresponding edge transport. (a) Schematic band structure of a slab giving rise to the quantum Hall effect. The bulk conduction and valence bands (gray rectangles) are connected by a chiral edge state that is not spin polarized (gray). (b) Quantum spin Hall effect. The two edge states are spin polarized (red, up; blue, down). (c) Orbital Hall effect. The geometric edge state does not bridge the gap and is partially polarized with respect to the orbital angular momentum (red, positive; blue, negative). (d)–(f) Corresponding edge currents in real space. The colored arrows in (e) correspond to the spin, and those in (f) correspond to the orbital angular momentum.

especially when spin-orbit coupling is considered, the SHE and OHE may arise at the same time, and the edge states can disperse differently. The gap may be bridged, and the topological invariants C and Z_2 may become nonzero integers giving rise to a quantum Hall effect and quantum SHE that may be superimposed with the edge contribution to the OHE.

VI. CONCLUSION

In conclusion, we used the method derived in Ref. [21] to account for intersite contributions to the OHE. While it has been known that these contributions can drastically differ from the ACA, our study demonstrates the emergence of a net OHE in a kagome lattice composed solely of s orbitals in which the OHE based on the ACA is strictly zero. Importantly, we find that the OHE is a more prevalent phenomenon compared with the spin Hall effect and can appear without a specific orbital composition. The emergence of orbital currents occurs more easily and is more omnipresent than anticipated by the ACA. Furthermore, we identify edge contributions to the OHE. The existence of edge states in this lattice gives rise to wave packets following a cycloid trajectory, akin to the trajectory of a particle on a rolling wheel. These observations highlight the significance of the OHE in various materials and its relevance for dissipationless orbitronic applications.

The magnitude of the calculated effect is considerable. At $1/3$ filling, the OHC is diverging in an ideal sample. In a realistic material, in which the Dirac point opens slightly, we expect values up to several $\frac{e}{2\pi}$. Therefore they are of the same order of magnitude as typical spin Hall conductivities and the orbital Hall conductivities that have been calculated before using the ACA for other materials such as $4d$ and $5d$ transition metals [12,13] and later $3d$ materials [41] and Pt [14]. Recently, the OHE has been observed experimentally in Ti using the magneto-optical Kerr effect, in which intersite contributions are already included [42]. Furthermore, orbital

currents have recently been detected on ultrafast time scales by terahertz emission spectroscopy measurements [43].

Moreover, we note that our findings bear relevance to the valley Hall effect [44,45], which has garnered significant attention in graphene research. In the context of the kagome lattice, the presence of distinct Dirac points at K and K' , which differ in a physical quantity, gives rise to a Hall effect in that quantity. This unique characteristic is exemplified in this paper, where the opposite orbital angular momentum associated with k and $-k$ states [extrema of L_z at the Dirac points in Fig. 3(a)] leads to the observed OHE.

Importantly, the OHE is not limited to a specific material. Rather, it is expected to manifest in kagome materials, as well as materials that allow for loops in the unit cell. This generality expands the potential avenues for exploring and harnessing the OHE in diverse systems. We have carried out additional calculations and find that it is present also in a square-octagon lattice (cf. Fig. 5 in Appendix A) which has four basis atoms forming a square in the unit cell.

ACKNOWLEDGMENT

This work is funded by the Deutsche Forschungsgemeinschaft (DFG, German Research Foundation) – Project No. 328545488 – TRR 227, Project No. B04.

O.B. and B.G. contributed equally to this work. O.B. performed the tight-binding and transport calculations for the bulk system; B.G. performed the edge state calculations. All authors discussed the results.

APPENDIX A: COMPARISON OF DIFFERENT TWO-DIMENSIONAL MODEL LATTICES

In this Appendix, we compare the orbital Hall conductivity (OHC) $\sigma_{xy}^{L_z}$ in four different model lattices. The results are presented in Fig. 5. In the atomic center approximation (ACA), the OHC vanishes in all cases because we consider only s electrons that are characterized by the orbital angular momentum quantum number $l = 0$. For simplicity, only nearest-neighbor hoppings with amplitudes $t = -1$ eV are considered. In the following, we want to discuss the orbital Berry curvature and the OHC in the modern formulation.

Figure 5(a) shows a honeycomb lattice such as that in graphene. The band structure in Fig. 5(b) shows the typical features such as the Dirac cone at K . The orbital Berry curvature based on the modern formulation [Eq. (2)] is zero everywhere, which is the reason why the OHC is zero for every energy [Fig. 5(c)]. The second row [Figs. 5(d)–5(f)] shows the same results for the kagome lattice. This time the orbital Berry curvature is nonzero as discussed in the main text. This leads to an energy-dependent OHC that exhibits a sharp peak close to the energy of the Dirac point.

The third [Figs. 5(g)–5(i)] and fourth rows [Figs. 5(j)–5(l)] show the results for a square lattice and a square-octagon lattice, respectively. The results are similar to the comparison of the honeycomb and kagome lattices: Like the honeycomb lattice, the square lattice [Fig. 5(g)] has no closed loops in the unit cell. The orbital Berry curvature [Fig. 5(h)] vanishes everywhere, and the OHC [Fig. 5(i)] is zero for every energy. However, the square-octagon lattice [Fig. 5(j)] has four atoms

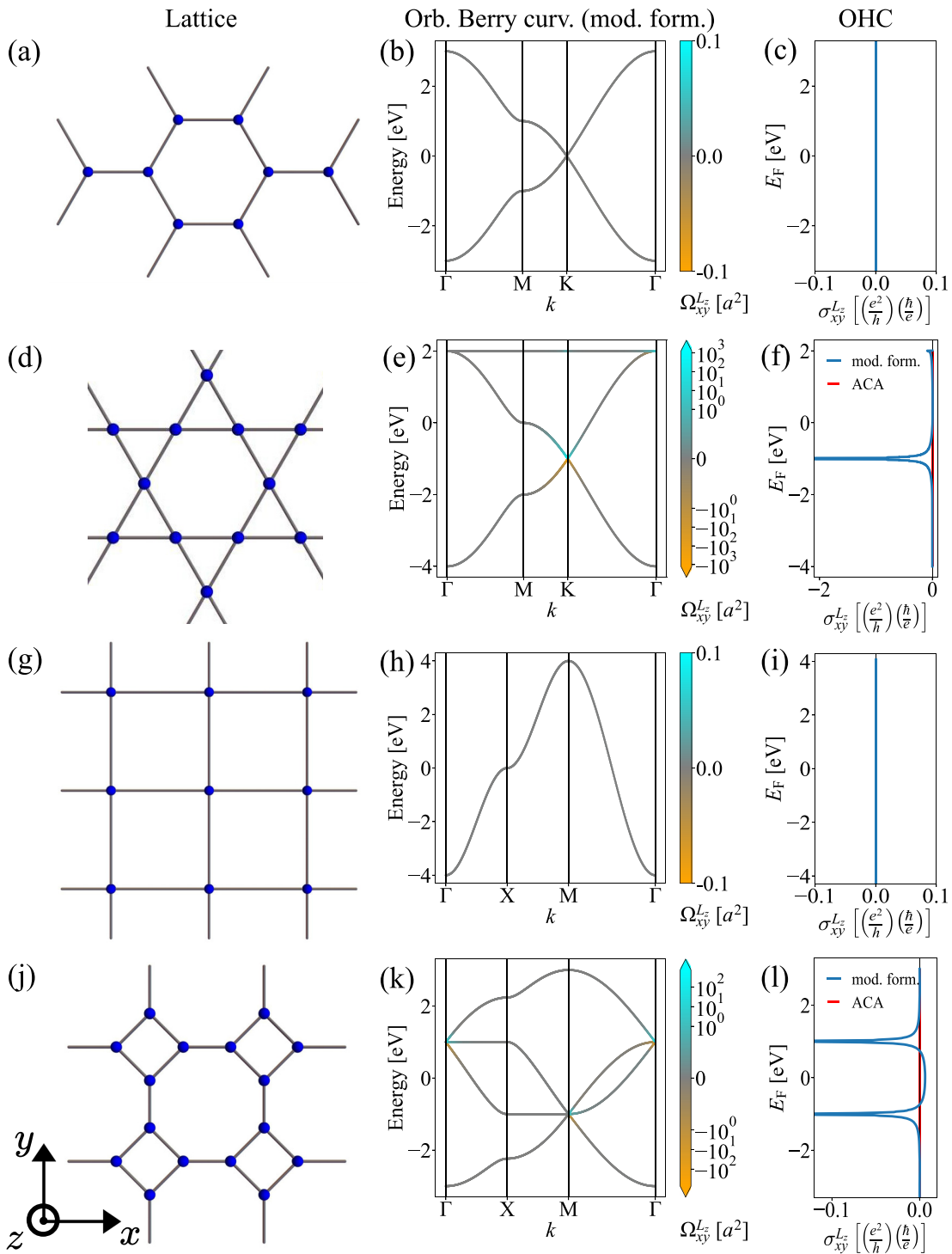


FIG. 5. Comparison of different two-dimensional model lattices with s orbitals located at the atomic sites (from the top row to the bottom row: honeycomb, kagome, square, and square-octagon lattices). (a) Honeycomb lattice as found in graphene. (b) Electronic structure with (vanishing) orbital Berry curvature (orb. Berry curv.) Ω_{xy}^{Lz} using the modern formulation (cyan, positive; orange, negative; gray, zero). (c) OHC σ_{xy}^{Lz} as a function of the Fermi energy E_F ; the OHC vanishes for both methods: ACA and modern theory. (d)–(f) Analog results for the kagome lattice, which exhibits a finite OHE, however, only if the modern formulation is used [cf. Fig. 2]. (g)–(i) Analog results for a square lattice, which does not exhibit an OHE. (j)–(l) Analog results for the square-octagon lattice, which allows for a finite OHE using the modern formulation.

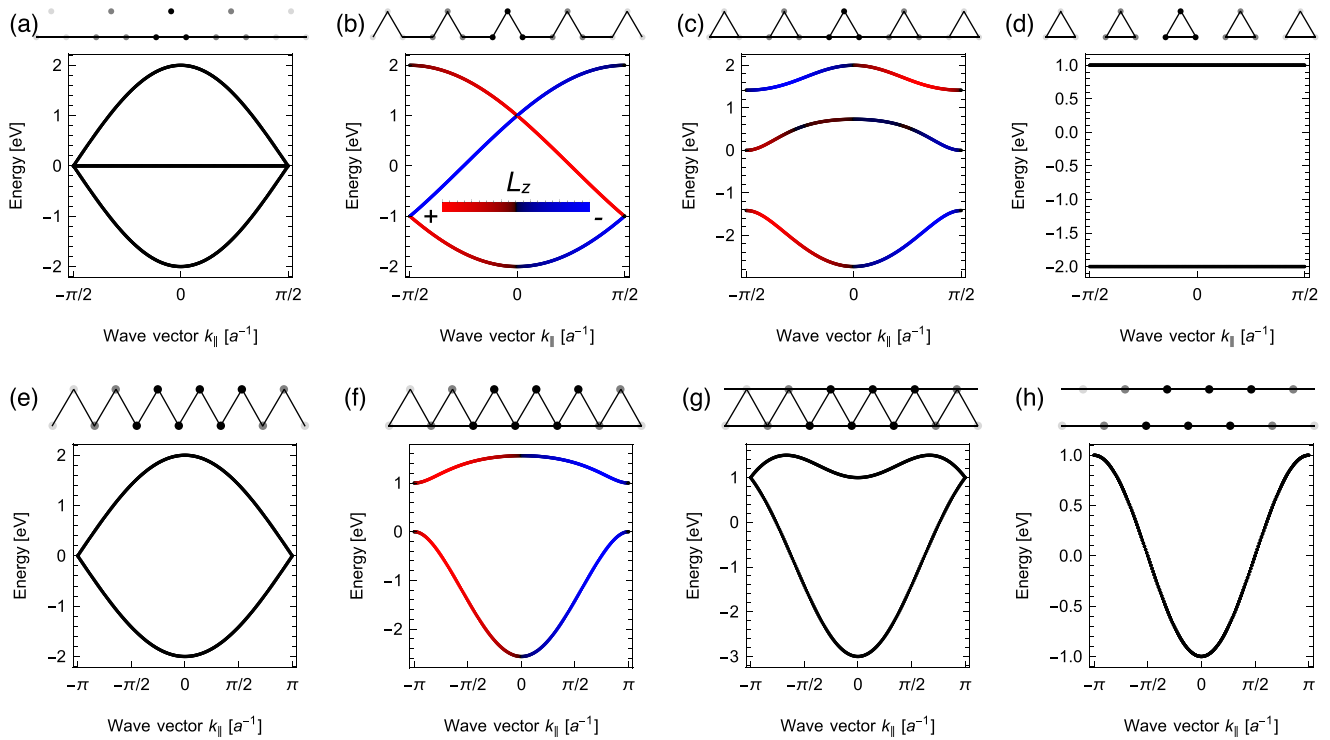


FIG. 6. Band structure and orbital angular momentum L_z (color is the same as in Fig. 3) for various quasi-one-dimensional chains. (a)–(d) Quasi-one-dimensional chain resembling the edge of the kagome slab with three atoms in the unit cell. (a) No L_z is generated (gray) when the edge is a straight line. (b) L_z is finite (red and blue) and antisymmetric with respect to k_{\parallel} once the additional atom is taken into account and the edge becomes asymmetric. (c) The same is true if all nearest-neighbor hoppings are considered. (d) Closed, unconnected loops are not sufficient to generate L_z . Since the individual triangles are not connected by hopping paths, the bands have no dispersion. (e)–(h) Simplified versions of the systems, consisting of a zigzag chain with two atoms in the unit cell. (e) A symmetric zigzag edge does not generate a finite L_z . (f) Once we artificially make the edge asymmetric by considering additional hoppings, L_z is generated. (g) and (h) In these scenarios the edge becomes symmetric again, giving rise to $L_z = 0$.

in the unit cell that allow for closed loops of the electron wave packets. The orbital Berry curvature according to the modern formulation [Fig. 5(k)] is nonzero, and the corresponding OHC [Fig. 5(l)] exhibits sharp peaks at the two Dirac points.

APPENDIX B: ORBITAL CURRENTS IN VARIOUS QUASI-ONE-DIMENSIONAL CHAINS

In the main text, we have discussed that an orbital current can arise when an object “translates” and “circulates” at the same time. At the triangular edge of the kagome nanoribbon, such a trajectory is present, which can give rise to a contribution to the OHC. In Fig. 6 we compare different quasi-one-dimensional chains, corresponding to possible edges of nanoribbons, and calculate their band structure and k -resolved orbital angular momentum. The graphs above the band structures resemble the considered system. The circles are the lattice sites, and the lines are the considered hoppings with strength $t_i = -1$ eV. All systems are periodic along the chain direction.

In Figs. 6(a)–6(d) the chain is like the edge of the kagome nanoribbon and consists of three atoms. However, we manipulate the hopping to figure out in which scenario translation (characterized by dispersion in the band structure, $v = \frac{1}{\hbar} \frac{\partial H}{\partial k_{\parallel}}$) and rotation (characterized by an orbital angular momentum

L_z) are present. In that case, an orbital current arises which contributes to the OHC.

In Fig. 6(a) an electron can propagate along the edge, so the band structure shows dispersion. However, since there are no closed loops of the hopping paths, the orbital angular momentum vanishes for every k point. For this reason, no orbital current arises. Note that the additional “unconnected” atom results in a dispersionless band because the hopping to this atom is disregarded here. In Figs. 6(b) and 6(c) the band structure exhibits dispersion, and the orbital angular momentum is nonzero for most k points, which is why an orbital current can arise in that case. Both scenarios resemble the edge of the kagome nanoribbon from the main text quite accurately and explain how the L_z and orbital Hall conductivity arise at the edge of a kagome slab. The only difference between the two chains is that in Fig. 6(c) closed loops are present, while in Fig. 6(b) this is not the case. Still, since the edge is asymmetric, the corresponding cycloid trajectory transports an orbital angular momentum, as explained in the main text. In Fig. 6(d), the individual triangular unit cells are not connected by hoppings. The band structure exhibits no dispersion, and no orbital currents can arise.

In the second row [Figs. 6(e)–6(h)], we present results for simplified systems. These systems, consisting of a zigzag chain with two atoms in the unit cell, allow for the

generation of orbital currents as well if the hoppings are chosen as in Fig. 6(f). The top and the bottom edges must be inequivalent; otherwise the orbital angular momentum is compensated due to the glide-mirror symmetry that is present

in Fig. 6(g). The same is true for the systems presented in Figs. 6(e) and 6(h), which is why the band structure shows dispersion but no k -resolved orbital angular momentum is generated.

- [1] D. Go, D. Jo, H.-W. Lee, M. Kläui, and Y. Mokrousov, Orbitoronics: Orbital currents in solids, *Europhys. Lett.* **135**, 37001 (2021).
- [2] C. Kittel, Surface and interface physics, in *Introduction to Solid State Physics* (Wiley, New York, 2004), Chap. 17, pp. 487–514.
- [3] Y. Cao, G. Xing, H. Lin, N. Zhang, H. Zheng, and K. Wang, Prospect of spin-orbitronic devices and their applications, *iScience* **23**, 101614 (2020).
- [4] N. Nagaosa, J. Sinova, S. Onoda, A. H. MacDonald, and N. P. Ong, Anomalous Hall effect, *Rev. Mod. Phys.* **82**, 1539 (2010).
- [5] M. I. D'yakonov and V. I. Perel, Current-induced spin orientation of electrons in semiconductors, *Phys. Lett. A* **35**, 459 (1971).
- [6] J. E. Hirsch, Spin Hall effect, *Phys. Rev. Lett.* **83**, 1834 (1999).
- [7] Y. K. Kato, R. C. Myers, A. C. Gossard, and D. D. Awschalom, Observation of the spin Hall effect in semiconductors, *Science* **306**, 1910 (2004).
- [8] J. Sinova, S. O. Valenzuela, J. Wunderlich, C. H. Back, and T. Jungwirth, Spin Hall effects, *Rev. Mod. Phys.* **87**, 1213 (2015).
- [9] S. Zhang and Z. Yang, Intrinsic spin and orbital angular momentum Hall effect, *Phys. Rev. Lett.* **94**, 066602 (2005).
- [10] B. A. Bernevig, T. L. Hughes, and S.-C. Zhang, Orbitronics: The intrinsic orbital current in p -doped silicon, *Phys. Rev. Lett.* **95**, 066601 (2005).
- [11] H. Kontani, T. Tanaka, D. S. Hirashima, K. Yamada, and J. Inoue, Giant intrinsic spin and orbital Hall effects in Sr_2MO_4 ($M = \text{Ru, Rh, Mo}$), *Phys. Rev. Lett.* **100**, 096601 (2008).
- [12] T. Tanaka, H. Kontani, M. Naito, T. Naito, D. S. Hirashima, K. Yamada, and J. Inoue, Intrinsic spin Hall effect and orbital Hall effect in $4d$ and $5d$ transition metals, *Phys. Rev. B* **77**, 165117 (2008).
- [13] H. Kontani, T. Tanaka, D. S. Hirashima, K. Yamada, and J. Inoue, Giant orbital Hall effect in transition metals: Origin of large spin and anomalous Hall effects, *Phys. Rev. Lett.* **102**, 016601 (2009).
- [14] D. Go, D. Jo, C. Kim, and H.-W. Lee, Intrinsic spin and orbital Hall effects from orbital texture, *Phys. Rev. Lett.* **121**, 086602 (2018).
- [15] D. Go and H.-W. Lee, Orbital torque: Torque generation by orbital current injection, *Phys. Rev. Res.* **2**, 013177 (2020).
- [16] M.-C. Chang and Q. Niu, Berry phase, hyperorbits, and the Hofstadter spectrum: Semiclassical dynamics in magnetic Bloch bands, *Phys. Rev. B* **53**, 7010 (1996).
- [17] T. Thonhauser, D. Ceresoli, D. Vanderbilt, and R. Resta, Orbital magnetization in periodic insulators, *Phys. Rev. Lett.* **95**, 137205 (2005).
- [18] D. Xiao, J. Shi, and Q. Niu, Berry phase correction to electron density of states in solids, *Phys. Rev. Lett.* **95**, 137204 (2005).
- [19] J. Shi, G. Vignale, D. Xiao, and Q. Niu, Quantum theory of orbital magnetization and its generalization to interacting systems, *Phys. Rev. Lett.* **99**, 197202 (2007).
- [20] T. Yoda, T. Yokoyama, and S. Murakami, Orbital Edelstein effect as a condensed-matter analog of solenoids, *Nano Lett.* **18**, 916 (2018).
- [21] A. Pezo, D. Garcia Ovalle, and A. Manchon, Orbital Hall effect in crystals: Interatomic versus intra-atomic contributions, *Phys. Rev. B* **106**, 104414 (2022).
- [22] T. P. Cysne, S. Bhowal, G. Vignale, and T. G. Rappoport, Orbital Hall effect in bilayer transition metal dichalcogenides: From the intra-atomic approximation to the Bloch states orbital magnetic moment approach, *Phys. Rev. B* **105**, 195421 (2022).
- [23] A. Pezo, D. G. Ovalle, and A. Manchon, Orbital Hall physics in two-dimensional Dirac materials, *Phys. Rev. B* **108**, 075427 (2023).
- [24] B.-J. Yang and N. Nagaosa, Emergent topological phenomena in thin films of pyrochlore iridates, *Phys. Rev. Lett.* **112**, 246402 (2014).
- [25] We replaced “Im” (determining the imaginary part of the following expression) by the negative of the imaginary unit “ $-i$ ”.
- [26] D. Go, J.-P. Hanke, P. M. Buhl, F. Freimuth, G. Bihlmayer, H.-W. Lee, Y. Mokrousov, and S. Blügel, Toward surface orbitronics: giant orbital magnetism from the orbital Rashba effect at the surface of sp -metals, *Sci. Rep.* **7**, 46742 (2017).
- [27] J.-X. Yin, S. S. Zhang, H. Li, K. Jiang, G. Chang, B. Zhang, B. Lian, C. Xiang, I. Belopolski, H. Zheng, T. A. Cochran, S.-Y. Xu, G. Bian, K. Liu, T.-R. Chang, H. Lin, Z.-Y. Lu, Z. Wang, S. Jia, W. Wang *et al.*, Giant and anisotropic many-body spin-orbit tunability in a strongly correlated kagome magnet, *Nature (London)* **562**, 91 (2018).
- [28] D. Khadka, T. R. Thapaliya, S. Hurtado Parra, J. Wen, R. Need, J. M. Kikkawa, and S. X. Huang, Anomalous Hall and Nernst effects in epitaxial films of topological kagome magnet Fe_3Sn_2 , *Phys. Rev. Mater.* **4**, 084203 (2020).
- [29] E. Liu, Y. Sun, N. Kumar, L. Muechler, A. Sun, L. Jiao, S.-Y. Yang, D. Liu, A. Liang, Q. Xu, J. Kroder, V. Stüb, H. Borrmann, C. Shekhar, Z. Wang, C. Xi, W. Wang, W. Schnelle, S. Wirth, Y. Chen *et al.*, Giant anomalous Hall effect in a ferromagnetic kagome-lattice semimetal, *Nat. Phys.* **14**, 1125 (2018).
- [30] O. V. Yazyev, An upside-down magnet, *Nat. Phys.* **15**, 424 (2019).
- [31] H. Chen, Q. Niu, and A. H. MacDonald, Anomalous Hall effect arising from noncollinear antiferromagnetism, *Phys. Rev. Lett.* **112**, 017205 (2014).
- [32] S. Nakatsuji, N. Kiyohara, and T. Higo, Large anomalous Hall effect in a non-collinear antiferromagnet at room temperature, *Nature (London)* **527**, 212 (2015).
- [33] A. K. Nayak, J. E. Fischer, Y. Sun, B. Yan, J. Karel, A. C. Komarek, C. Shekhar, N. Kumar, W. Schnelle, J. Kübler, C. Felser, and S. S. P. Parkin, Large anomalous Hall effect driven by a nonvanishing Berry curvature in the noncollinear antiferromagnet Mn_3Ge , *Sci. Adv.* **2**, e1501870 (2016).
- [34] Y. Zhang, Y. Sun, H. Yang, J. Železný, S. P. P. Parkin, C. Felser, and B. Yan, Strong anisotropic anomalous Hall effect and spin Hall effect in the chiral antiferromagnetic compounds Mn_3X

- ($X = \text{Ge, Sn, Ga, Ir, Rh, and Pt}$), [Phys. Rev. B **95**, 075128 \(2017\)](#).
- [35] Y. Niimi, T. Matsui, H. Kambara, K. Tagami, M. Tsukada, and H. Fukuyama, Scanning tunneling microscopy and spectroscopy studies of graphite edges, [Appl. Surf. Sci. **241**, 43 \(2005\)](#).
- [36] Y. Kobayashi, K.-I. Fukui, T. Enoki, K. Kusakabe, and Y. Kaburagi, Observation of zigzag and armchair edges of graphite using scanning tunneling microscopy and spectroscopy, [Phys. Rev. B **71**, 193406 \(2005\)](#).
- [37] K. Sasaki, S. Murakami, and R. Saito, Stabilization mechanism of edge states in graphene, [Appl. Phys. Lett. **88**, 113110 \(2006\)](#).
- [38] W. Yao, S. A. Yang, and Q. Niu, Edge states in graphene: From gapped flat-band to gapless chiral modes, [Phys. Rev. Lett. **102**, 096801 \(2009\)](#).
- [39] M. Costa, B. Focassio, L. M. Canonico, T. P. Cysne, G. R. Schleder, R. B. Muniz, A. Fazzio, and T. G. Rappoport, Connecting higher-order topology with the orbital Hall effect in monolayers of transition metal dichalcogenides, [Phys. Rev. Lett. **130**, 116204 \(2023\)](#).
- [40] Y.-L. Sun, G.-H. Chen, S.-C. Du, Z.-B. Chen, Y.-W. Zhou, and E.-J. Ye, Spin-valley polarized edge states in quasi-one-dimensional asymmetric kagome lattice, [Front. Phys. **10**, 33836 \(2022\)](#).
- [41] D. Jo, D. Go, and H.-W. Lee, Gigantic intrinsic orbital Hall effects in weakly spin-orbit coupled metals, [Phys. Rev. B **98**, 214405 \(2018\)](#).
- [42] Y.-G. Choi, D. Jo, K.-H. Ko, D. Go, K.-H. Kim, H. G. Park, C. Kim, B.-C. Min, G.-M. Choi, and H.-W. Lee, Observation of the orbital Hall effect in a light metal Ti, [Nature \(London\) **619**, 52 \(2023\)](#).
- [43] T. S. Seifert, D. Go, H. Hayashi, R. Rouzegar, F. Freimuth, K. Ando, Y. Mokrousov, and T. Kampfrath, Time-domain observation of ballistic orbital-angular-momentum currents with giant relaxation length in tungsten, [Nat. Nanotechnol. **18**, 1132 \(2023\)](#).
- [44] S. Bhowal and G. Vignale, Orbital Hall effect as an alternative to valley Hall effect in gapped graphene, [Phys. Rev. B **103**, 195309 \(2021\)](#).
- [45] T. P. Cysne, M. Costa, L. M. Canonico, M. B. Nardelli, R. B. Muniz, and T. G. Rappoport, Disentangling orbital and valley Hall effects in bilayers of transition metal dichalcogenides, [Phys. Rev. Lett. **126**, 056601 \(2021\)](#).

5 Publications: Laser-induced ultrafast electron dynamics

In the following section, I investigate how spin and orbital angular momenta are generated, manipulated and transferred in thin films, induced by excitation with femtosecond laser pulses (goal number two of the introduction). The photo-induced electron dynamics is discussed during the laser excitation, i.e. for timescales of a few 10 fs before and after the pulse. Two publications are presented which discuss the impact of light polarization, sample composition and inhomogeneities, in particular surfaces and magnetic/nonmagnetic interfaces, on the electron dynamics. The investigated systems are homogeneous samples of Cu(100) or Co(100) and a Co/Cu(100) heterostructure illuminated with either a linearly or a circularly polarized laser pulse.

The results have been simulated with `EVOLVE`, a computer code which is being developed in our group. As presented in Sec. 3, an effective one-electron density matrix is applied to describe the time evolution during the laser excitation. The latter enters the Hamiltonian via minimal coupling in dipole approximation. Access to spatio-temporal distributions of observables is gained by the real-space tight-binding approach.

Photo-induced spin angular momentum (SAM) and (spin-polarized) currents. In the first publication [OB4], the dynamics of photo-induced SAM and corresponding currents is studied giving detailed insight into tailoring electron dynamics with ultrafast laser pulses. A symmetry analysis tells that the laser-induced components of the SAM strongly depends on the polarization of the laser pulse and on the sample composition, which is fully confirmed by the simulations. Besides, we observe a transition from coherence to incoherence in the spatio-temporal distributions of the observables, which is attributed to increasing interference after the laser pulse. Moreover, surfaces and magnetic/nonmagnetic interfaces play a crucial role in ultrafast spin-polarization effects and facilitate the generation of (spin-polarized) currents.

Ultrafast dynamics of laser-induced orbital angular momentum (OAM). The second publication [OB5] deals with the laser-induced dynamics of the OAM which plays an increasingly important role in ultrafast electron and magnetization dynamics. By focusing on excitation with a circularly polarized laser pulse, we find that a long-lasting OAM component of sizable magnitude can be induced in a normal metal, such as Cu. Furthermore, an interface between a ferromagnet and a normal metal significantly facilitates the demagnetization of the magnet by the OAM contribution to the total magnetization. Finally, to transfer OAM from a ferromagnet into a normal metal, it is advantageous to choose a laser setup that induces the desired OAM component in the ferromagnet, but not in the normal metal.

5.1 Photo-induced spin angular momentum and (spin-polarized) currents

Spin-polarized free photo electrons in photoemission spectroscopy As explained in Sec. 2.5, angle-resolved photoemission spectroscopy (ARPES) is a widely used tool to map the electronic structure of materials. With some experimental setups it is also possible to access the spin polarization of the excited electrons and currents. This technique is called spin- and angle-resolved photoemission spectroscopy (SARPES). The spin polarization is dictated by the symmetry of the setup which is determined by the geometry of the sample and the details of the impinging laser pulse. In particular, the laser polarization plays a crucial role which results in dichroism in magnetic samples (cf. XMCD, XMLD in Sec. 2.5). Furthermore, the spin polarization of the *free photoelectrons* must not be aligned with the ground state magnetization of a laser-excited ferromagnetic (FM) material [39]. Moreover, spin-polarized photoelectrons and -currents can also be generated by laser excitation of nonmagnetic (NM) materials with spin-orbit coupling [38].

However, in the field of ultrafast magnetization dynamics one is not only interested in the spin polarization of the photoelectrons measured at a detector, but also of the conduction electrons *within* the laser-excited sample. Many works address the photo-induced demagnetization [34] and all-optical switching of magnetic materials [37]. Hence, the focus is often on the laser-induced change of the spin-polarization associated with the ground state magnetization, and the other components are disregarded.

This publication. In the following publication “Ultrafast dynamics of electrons excited by femtosecond laser pulses: Spin polarization and spin-polarized currents” [OB4], the photo-induced electron dynamics during and shortly after the pulse is systematically investigated. Herein, spin angular momentum (SAM), that is the angular momentum associated with the spin polarization, and (spin-polarized) currents are examined with femtosecond and atomic resolution [cf. Sec. 3.4].

First, NM Cu is discussed, since it has a vanishing SAM in equilibrium. Thus, the dependence of the laser-induced SAM components on the chosen light polarization (p, s and circularly polarized) is observed most clearly. The simulations demonstrate that SAM and ultrafast (spin-polarized) currents of sizable magnitudes are induced in a NM material, where the surface acts as a “source” for the currents.




The focus in magnetic samples is on excitation with a p-polarized laser pulse, first for a homogeneous Co sample. However, instead of aiming at demagnetization of the FM, the laser-induced SAM components which are *not* associated with the magnetization direction are investigated. In doing so, we observe a precession of the SAM vector which is driven by the laser pulse. Besides, striking differences between the SAM induced in FM and NM samples are found: a superposition of fast and long-period oscillations in Co, whereas Cu exhibits mainly long-period ones that are slightly modulated with rapid oscillations.


Finally, the Co/Cu heterostructure is investigated to address the impact of a FM/NM interface. The main finding is that photo-induced (spin-polarized) currents are initiated at the interface and propagate into both regions towards the surfaces, which is attributed to a (spin-dependent) imbalance of occupation. The simulations confirm the results of a symmetry analysis that predicts which components of the SAM are allowed or forbidden, dependent on the laser polarization [cf. Tab. II in the publication]. However, a general trend is observed in all simulations, namely unison oscillations before and reduced coherence after the pulse, which can be attributed to increasing interference.

Note that animations of the dynamics are provided in the supplemental material of the publication.

The following publication: Reprinted (whole article) with permission from O. Busch, F. Ziolkowski, I. Mertig and J. Henk, Physical Review B **108**, 184401 (2023); Ref. [OB4]; Ultrafast dynamics of electrons excited by femtosecond laser pulses: Spin polarization and spin-polarized currents. Copyright (2023) by the American Physical Society.

Ultrafast dynamics of electrons excited by femtosecond laser pulses: Spin polarization and spin-polarized currents

Oliver Busch ^{*}, Franziska Ziolkowski , Ingrid Mertig , and Jürgen Henk 
Institut für Physik, Martin Luther University Halle-Wittenberg, 06099 Halle, Germany

 (Received 26 April 2023; accepted 16 October 2023; published 2 November 2023)

Laser radiation incident on a ferromagnetic sample produces excited electrons and currents whose spin polarization must not be aligned with the magnetization—an effect due to spin-orbit coupling that is ubiquitous in spin- and angle-resolved photoemission. In this paper, we report on a systematic investigation of the dynamics of spin polarization and spin-polarized currents produced by femtosecond laser pulses, modeled within our theoretical framework *EVOLVE*. The spin polarization depends strongly on the properties of the laser pulse and on the sample composition, as shown by comparing results for Cu(100), Co(100), and a Co/Cu heterostructure. We find a transition from coherence before the laser pulse’s maximum to incoherence thereafter. Moreover, the time dependence of the spin-polarization components induced by spin-orbit coupling differ significantly in Cu and Co: in Cu, we find long-period oscillations with tiny rapid modulations, whereas in Co prominent rapid oscillations with long-period ones are superimposed. The pronounced spatial dependences of the signals underline the importance of inhomogeneities; in particular, magnetic/nonmagnetic interfaces act as a source for ultrafast spin-polarization effects. Our investigation provides detailed insight into electron dynamics during and shortly after a femtosecond laser excitation.

DOI: [10.1103/PhysRevB.108.184401](https://doi.org/10.1103/PhysRevB.108.184401)

I. INTRODUCTION

Spin-polarized photocurrents are ubiquitous in spin- and angle-resolved photoelectron spectroscopy (SARPES) [1,2]. In nonmagnetic samples, the spin polarization of the detected photocurrents—brought about by spin-orbit coupling—depends on details of the setup, in particular on those of the incident electromagnetic radiation (e.g., on photon energy, polarization, and incidence direction; see, for example, Ref. [3]) and on the symmetry of the surface [4–7]. In magnetic samples, the same effect results in magnetic dichroism [8,9], and as theoretical and experimental studies have shown, the spin-orbit-induced spin polarization of *photoelectrons* must not be aligned with the magnetization direction (see, for example, Ref. [8] and references therein).

In ultrafast spin dynamics, electrons are excited by electromagnetic radiation as well, for example, by a femtosecond laser pulse. Focusing on the demagnetization of a magnetic sample [10–12], one investigates mainly the reduction in the magnetization and disregards its change in direction. The latter could be brought about by photoinduced spin-polarization components that are not aligned with the ground state’s magnetization. In SARPES these “oblique” components are those of electrons measured *at a detector*, whereas in ultrafast spin dynamics they are those of electrons *within a sample*; thus, one is concerned with different boundary conditions [13]. This idea immediately calls for a systematic investigation of photoinduced spin polarization and spin-polarized currents caused by femtosecond laser pulses.

Ultrafast spin currents have been studied for more than a decade, for example, in terms of superdiffusive spin currents. Battiato and coworkers focused on the density of hot majority carriers [14–16]. The dynamics of the spin currents is calculated using spin-dependent scattering rates and spin-dependent transmission of the interface, while the excitation is treated as a source term. Other semiclassical approaches are based on the Boltzmann transport equation, as in the work by Nenno *et al.* [17], or on a wave-diffusion equation, as in the work by Kaltenborn *et al.* [18].

In the theoretical study reported in this paper, we concentrate on the spin-orbit-induced spin-polarization effects during and shortly after a laser excitation. In order to determine the main features we begin with a nonmagnetic sample, Cu(100), and then turn to a magnetic sample, fcc Co(100). Since real samples often contain interfaces, we investigate the role of the latter by means of a Co/Cu(100) heterostructure.

Questions worth considering are, among others, which components of the spin polarization are forbidden by symmetry? How large are the allowed components, and are their magnitudes comparable to those observed in SARPES? What are their temporal and spatial distributions? Does magnetism reduce the oblique spin-orbit-induced components (here in samples containing Co)? What are the detailed properties of the photoinduced currents? We respond to these questions in this work.

The simulations were performed using our computational framework *EVOLVE* [19,20]. In contrast to the established approaches mentioned above, *EVOLVE* goes beyond the two-current model. Moreover, details of the laser radiation are taken into account, with excitations included in the electric dipole approximation. On the other hand, scattering processes

^{*}Corresponding author: oliver.busch@physik.uni-halle.de

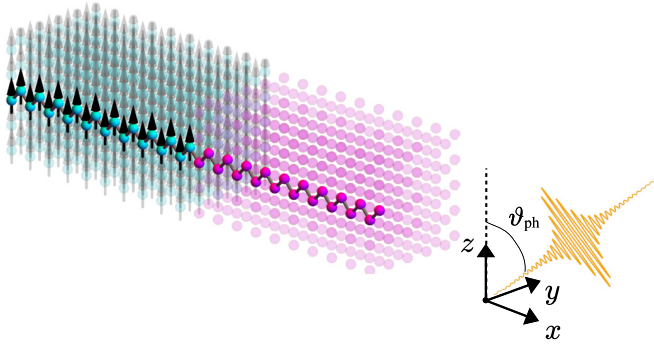


FIG. 1. Geometry of a Co/Cu heterostructure. The fcc film consists of 40 layers stacked in the x direction, with 20 layers of Co atoms (cyan spheres) and 20 layers of Cu atoms (magenta spheres). The Co magnetic moments point along the z direction (black arrows). The film is infinite in the y and z directions but finite in the x direction. Sites with intense color forming a zigzag chain belong to one unit cell of the slab. A laser pulse impinges with a polar angle ϑ_{ph} of 45° within the xz plane onto the sample.

are not considered on the microscopic level, but coupling to a bosonic heat bath allows for relaxation of the excited state toward the thermal ground state.

This paper is organized as follows. In Sec. II we sketch our approach to ultrafast electron dynamics (Sec. II A), discuss spin polarization as well as currents (Sec. II B), and perform a symmetry analysis (Sec. II C). Results are discussed in Sec. III: beginning with Cu(100) (Sec. III A), we turn then to magnetic systems, namely, fcc Co(100) (Sec. III B) and a Co/Cu(100) heterostructure (Sec. III C). We conclude in Sec. IV.

II. THEORETICAL ASPECTS

A. Ultrafast electron dynamics

The samples are freestanding fcc(100) films 40 layers thick. We consider Cu(100), Co(100), and Co/Cu(100) (with 20 layers each) films. The Cartesian x axis is perpendicular to the film, and we apply periodic boundary conditions within the film, i.e., in the y and z directions. In the case of Co(100) and Co/Cu(100), the magnetic moments are collinear and point along the z direction (Fig. 1) [21].

Co grows epitaxially on Cu(100), so that Co films adopt the in-plane lattice of Cu(100) but are tetragonally distorted (face-centered tetragonal lattice). However, the EVOLVE computer code requires a single lattice constant, so Co regions are taken as fcc with the lattice constant of Cu (0.36 nm [22] instead of 0.34 nm found for fcc Co [23]).

The electronic structure of the samples is described by a tight-binding Hamiltonian \hat{H}_0 of Slater-Koster type [24], with parameters for the s , p , and d orbitals taken from Ref. [25]. Collinear magnetism and spin-orbit coupling are taken into account as described in Ref. [26].

The electron system is excited by a femtosecond laser pulse with photon energy $E_{\text{ph}} = \omega$ (in atomic units, $\hbar = 1$). The laser's electric field

$$\mathbf{E}(t) = l(t) \sum_{l=s,p} \mathbf{E}_l \cos(\omega t + \varphi_l) \quad (1)$$

is a coherent superposition of s - and p -polarized partial waves modulated with a Lorentzian envelope $l(t)$. \mathbf{E}_l and φ_l are the amplitudes and the phase shifts of the partial waves, respectively.

The electromagnetic radiation impinges within the xz plane onto the films, with a polar angle $\vartheta_{\text{ph}} = 45^\circ$ of incidence. For s -polarized light ($\mathbf{E}_p = 0$), $\mathbf{E}(t)$ points along the y axis, which is perpendicular to the plane of incidence, the latter spanned by the incidence direction of the light and the surface normal. For p -polarized light ($\mathbf{E}_s = 0$), $\mathbf{E}(t)$ lies within the xz incidence plane. Circularly polarized radiation with helicity σ^\pm is obtained with $\varphi_s - \varphi_p = \pm 90^\circ$ and equal amplitudes ($E_s = E_p$).

Excitation with a circularly polarized laser pulse may induce a spin polarization [8], which is discussed in this work, or a magnetization, i.e., the inverse Faraday effect [27–29]. An induced magnetization creates a magnetic field that could dynamically affect the electrons and the magnetic texture of magnetic samples, thereby coupling the electron dynamics with magnetization dynamics. In the present stage of the EVOLVE framework, this feature is not incorporated.

The electron dynamics is described by the von Neumann equation

$$-i \frac{d\hat{\rho}(t)}{dt} = [\hat{\rho}(t), \hat{H}(t)] \quad (2)$$

for the one-particle density matrix

$$\hat{\rho}(t) = \sum_{n,m} |n\rangle p_{nm}(t) \langle m|. \quad (3)$$

$\{|n\rangle\}$ is the set of eigenstates of \hat{H}_0 , with $\hat{H}_0|n\rangle = \epsilon_n|n\rangle$. The time-dependent Hamiltonian $\hat{H}(t)$ comprises the electric field of the laser via minimal coupling [30]. The equation of motion (2) for $\hat{\rho}(t)$ is solved within our theoretical framework EVOLVE; for details see Refs. [19,20].

B. Spin polarization and spin-polarized currents

Site-, orbital-, and spin-resolved properties of an observable O are obtained by taking partial traces in the expectation values $\langle O \rangle(t) = \text{Tr}[\hat{\rho}(t)\hat{O}]$, with the density matrix in an appropriate basis.

In matrix form an expectation value reads $\langle O \rangle(t) = \text{tr}[\mathbf{P}(t)\mathbf{O}]$. We define matrices $\mathbf{p}_{kl}^{\sigma\sigma'}$ and $\mathbf{h}_{kl}^{\sigma\sigma'}$ for the density matrix and the Hamiltonian, respectively, with elements

$$(\mathbf{p}_{kl}^{\sigma\sigma'})_{\alpha\beta} = p_{k\alpha\sigma,l\beta\sigma'}, \quad (4a)$$

$$(\mathbf{h}_{kl}^{\sigma\sigma'})_{\alpha\beta} = h_{k\alpha\sigma,l\beta\sigma'}. \quad (4b)$$

k and l are site indices, σ and σ' specify the spin orientation (\uparrow and \downarrow with respect to the z direction), and α and β are orbital indices. These matrices are combined into site-resolved block matrices

$$\mathbf{P}_{kl} = \begin{pmatrix} \mathbf{p}_{kl}^{\uparrow\uparrow} & \mathbf{p}_{kl}^{\uparrow\downarrow} \\ \mathbf{p}_{kl}^{\downarrow\uparrow} & \mathbf{p}_{kl}^{\downarrow\downarrow} \end{pmatrix}, \quad (5a)$$

$$\mathbf{H}_{kl} = \begin{pmatrix} \mathbf{h}_{kl}^{\uparrow\uparrow} & \mathbf{h}_{kl}^{\uparrow\downarrow} \\ \mathbf{h}_{kl}^{\downarrow\uparrow} & \mathbf{h}_{kl}^{\downarrow\downarrow} \end{pmatrix}. \quad (5b)$$

The spin polarization at site l is given by

$$s_l^\mu = \text{tr}(\mathbf{P}_{ll}\Sigma^\mu), \quad \mu = x, y, z,$$

in which Σ^μ is a block Pauli matrix. Explicitly,

$$s_l^x = 2 \text{Re tr}(\mathbf{p}_{ll}^{\uparrow\downarrow}), \quad (6a)$$

$$s_l^y = -2 \text{Im tr}(\mathbf{p}_{ll}^{\uparrow\downarrow}), \quad (6b)$$

$$s_l^z = \text{tr}(\mathbf{p}_{ll}^{\uparrow\uparrow} - \mathbf{p}_{ll}^{\downarrow\downarrow}), \quad (6c)$$

with normalization $\text{tr}(\mathbf{P}_{ll}) = 1$. The site-averaged spin polarization

$$S^\mu = \frac{1}{N_{\text{site}}} \sum_l s_l^\mu, \quad \mu = x, y, z, \quad (7)$$

is obtained by summation over all N_{site} sites in a film's unit cell. Assuming a slab geometry, a unit cell consists of $N_{\text{site}} = 40$ sites forming a zigzag chain in the x direction (see the color-saturated sites belonging to one unit cell in Fig. 1).

The current

$$j_{kl} = -\frac{i}{2} \text{tr}(\mathbf{P}_{lk}\mathbf{H}_{kl}) - \langle l \leftrightarrow k \rangle \quad (8)$$

from site l to site k and the respective spin-polarized currents

$$j_{kl}^\mu = -\frac{i}{4} \text{tr}(\mathbf{P}_{lk}[\Sigma^\mu, \mathbf{H}_{kl}]_+) - \langle l \leftrightarrow k \rangle, \quad \mu = x, y, z, \quad (9)$$

are derived from Mahan's equation for the current operator in spin-symmetrized form [31] (see also Refs. [32,33]; $[\cdot, \cdot]_+$ is the anticommutator). For collinear magnetic textures, as discussed in this paper, intersite hopping with spin flip does not occur in \hat{H}_0 , i.e., $\mathbf{h}_{kl}^{\uparrow\downarrow} = 0$ and $\mathbf{h}_{kl}^{\downarrow\uparrow} = 0$. With this information, the above equations become

$$j_{kl} = -\frac{i}{2} \text{tr}(\mathbf{p}_{lk}^{\uparrow\uparrow}\mathbf{h}_{kl}^{\uparrow\uparrow} + \mathbf{p}_{lk}^{\downarrow\downarrow}\mathbf{h}_{kl}^{\downarrow\downarrow}) - \langle l \leftrightarrow k \rangle, \quad (10a)$$

$$j_{kl}^x = -\frac{i}{4} \text{tr}(\mathbf{p}_{lk}^{\uparrow\downarrow} + \mathbf{p}_{lk}^{\downarrow\uparrow})(\mathbf{h}_{kl}^{\uparrow\uparrow} + \mathbf{h}_{kl}^{\downarrow\downarrow}) - \langle l \leftrightarrow k \rangle, \quad (10b)$$

$$j_{kl}^y = \frac{1}{4} \text{tr}(\mathbf{p}_{lk}^{\uparrow\downarrow} - \mathbf{p}_{lk}^{\downarrow\uparrow})(\mathbf{h}_{kl}^{\uparrow\uparrow} + \mathbf{h}_{kl}^{\downarrow\downarrow}) - \langle l \leftrightarrow k \rangle, \quad (10c)$$

$$j_{kl}^z = -\frac{i}{2} \text{tr}(\mathbf{p}_{lk}^{\uparrow\uparrow}\mathbf{h}_{kl}^{\uparrow\uparrow} - \mathbf{p}_{lk}^{\downarrow\downarrow}\mathbf{h}_{kl}^{\downarrow\downarrow}) - \langle l \leftrightarrow k \rangle. \quad (10d)$$

Interchanging the site and the spin indices yields $j_{kl} = -j_{lk}$ and $j_{kl}^\mu = -j_{lk}^\mu = j_{lk}^{-\mu}$.

C. Symmetry analysis

Instead of a full group-theoretical analysis [8], we perform a symmetry analysis which reveals which components of the spin polarization are forbidden for a given setup. The important symmetry is the reflection \hat{m}_y , at the xz plane: $(x, y, z) \rightarrow (x, -y, z)$ since the xz plane is a symmetry plane of the lattice and is also the laser's plane of incidence (spanned by the light incidence direction and the surface normal).

For p -polarized light, \hat{m}_y is a symmetry operation for a nonmagnetic sample ($\mathbf{M} = 0$; here Cu) which indicates that only S^y is allowed to be nonzero (Table I). A z magnetization breaks this symmetry [$\mathbf{M} \neq 0$; here Co(100) and Co/Cu(100)], and all three components of \mathbf{S} are allowed to be nonzero.

TABLE I. Effect of symmetry operations on the laser's electric field \mathbf{E} decomposed into its s - and p -polarization components \mathbf{E}_s and \mathbf{E}_p , the magnetization \mathbf{M} in the z direction, and the electron spin polarization $\mathbf{S} = (S^x, S^y, S^z)$. $\hat{1}$ is the identity operation, and \hat{m}_y is the reflection at the xz plane.

Operation	Electric field		Magnetization	Spin polarization		
	\mathbf{E}_s	\mathbf{E}_p		S^x	S^y	S^z
$\hat{1}$	\mathbf{E}_s	\mathbf{E}_p	\mathbf{M}	S^x	S^y	S^z
\hat{m}_y	$-\mathbf{E}_s$	\mathbf{E}_p	$-\mathbf{M}$	$-S^x$	S^y	$-S^z$

For s -polarized light, the electric field of the laser is along the y direction. Since for homogeneous nonmagnetic samples (Cu) the z rotation by 180° leaves the setup invariant, $S^y = 0$ and $S^z = 0$. For S^y this symmetry holds for the spin polarization at each site ($s_l^y = 0$). For S^z , however, it holds only for the site-averaged spin polarization, that is, s_l^z at equivalent sites l may be nonzero but compensate each other (equivalent sites have the same distance from the two surfaces of a film).

Considering circularly polarized light, \hat{m}_y reverses the helicity $\sigma^\pm \rightarrow \sigma^\mp$ [$(\mathbf{E}_s, \mathbf{E}_p) \rightarrow (-\mathbf{E}_s, \mathbf{E}_p)$], which indicates that S^x and S^z change sign under helicity reversal for a nonmagnetic sample but S^y does not. For magnetic samples this strict relation is broken, which may be regarded as a magnetic spin dichroism (magnetic dichroism is an intensity change upon magnetization reversal [34]; here we are concerned with a change in the spin polarization). The symmetry-allowed and -forbidden spin-polarization components are summarized in Table II.

III. RESULTS AND DISCUSSION

To discuss our results, we increase the order of complexity step by step. We begin with a nonmagnetic Cu(100) film since it exhibits the phenomena most clearly. The effect of magnetism is addressed by fcc Co(100), and eventually, the combination of both systems into a Co/Cu(100) heterostructure allows an examination of the effect of a magnetic/nonmagnetic interface. For selected cases, animations of the spin dynamics are provided in the Supplemental Material [35].

In all simulations discussed below, the laser has a photon energy of 1.55 eV and a fluence of about 3.3 mJ cm^{-2} and is modulated with a Lorentzian $l(t)$ 10 fs wide. All samples comprise 40 layers, with sites 0 and 39 defining the bottom

TABLE II. Components of the site-averaged electron spin polarization $\mathbf{S} = (S^x, S^y, S^z)$ allowed (+) or forbidden (-) by symmetry, with the magnetic case given in rectangular brackets. For details see the text.

Polarization	S^x	S^y	S^z
p	- [+]	+ [+]	- [+]
s	- [-]	- [+]	- [+]
Circular	+ [+]	+ [+]	+ [+]

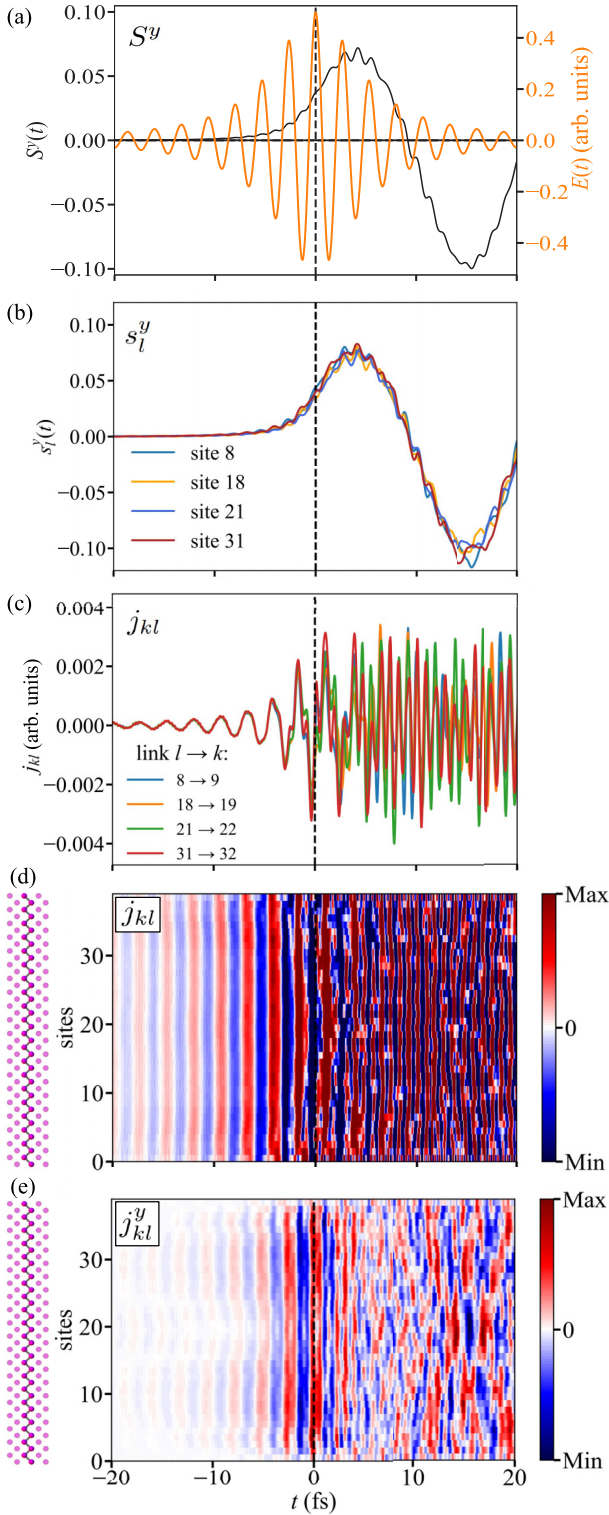


FIG. 2. Photoinduced spin polarization and currents for a Cu(100) sample excited by p -polarized light. (a) Site-averaged spin polarization $S^y(t)$ (black) and electric field of the laser pulse (orange; schematic). (b) Local spin polarization $s_l^y(t)$ for selected sites, as indicated. (c) Currents $j_{kl}(t)$ between neighboring sites $l \rightarrow k = l + 1$ for selected site pairs as indicated. (d) Currents $j_{kl}(t)$ and (e) spin-resolved currents $j_{kl}^y(t)$; their magnitude is indicated by color bars with the same range (red is positive; blue is negative). Data in [(c)–(e)] are in arbitrary units. Vertical dashed lines at $t = 0$ fs mark the maximum of the laser pulse.

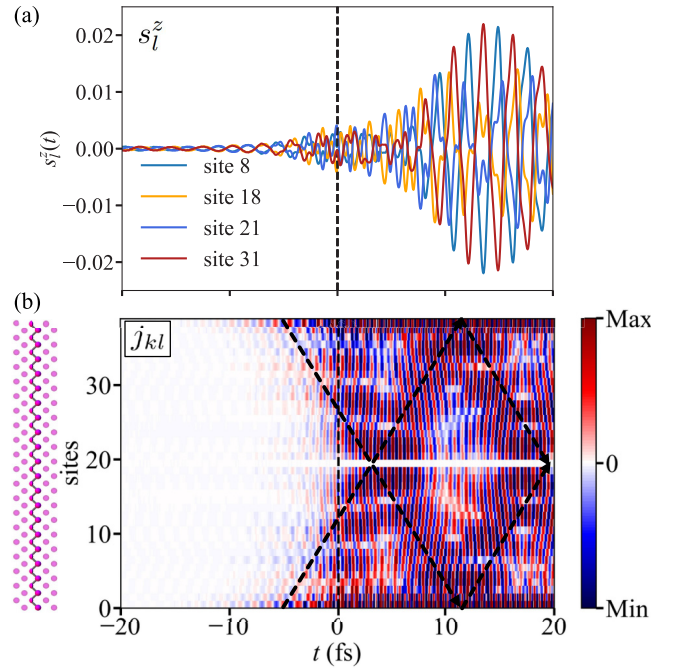


FIG. 3. Photoinduced spin polarization and current of a Cu(100) film excited by s -polarized light. (a) $s_l^z(t)$ for selected sites as indicated. Sites 8 (18) and 31 (21) are equivalent. (b) Currents $j_{kl}(t)$ displayed as a color scale (red is positive, and blue is negative; in arbitrary units). Dashed arrows serve as guides to the eye. Vertical dashed lines at $t = 0$ fs indicate the maximum of the laser pulse.

and top surfaces, respectively. We focus on currents across the samples, that is, along the zigzag path displayed in Fig. 1.

A. Cu(100)

In accordance with the symmetry analysis (Table II), the calculations for p -polarized light yield only a nonzero S^y that is slightly modulated with the doubled laser frequency [Fig. 2(a)]. The sizable magnitude is explained by the local contributions $s_l^y(t)$, which oscillate in phase with almost identical amplitudes [constructive interference; Fig. 2(b)]. After the laser pulse, deviations among the site-resolved spectra increase marginally (see $t > 12$ fs).

The above “unison” oscillations found for $s_l^y(t)$ show up as well in the currents $j_{kl}(t)$ before the laser pulse’s maximum [Figs. 2(c) and 2(d)], but with a much smaller period. The laser’s photon energy of 1.55 eV corresponds to a period of 2.7 fs, or about 3.7 oscillations within 10 fs, which is also seen in Figs. 2(c) and 2(d). This suggests that the electron system follows the electric field of the laser, which is a collective motion across the film (in the x direction). At about $t = -3$ fs, increasing interference, starting at the surfaces, reduces the coherence in the oscillations, thereby obliterating the pattern at later times.

The oscillations of the currents are accompanied by those of the spin-resolved currents $j_{kl}^y(t)$ in opposite directions [Fig. 2(e); the x and z components are zero]. A current in the positive x direction [red in Fig. 2(d)] appears simultaneously with a spin-polarized current in the opposite direction [blue in Fig. 2(e)], which implies a flow of $-y$ -polarized electrons in

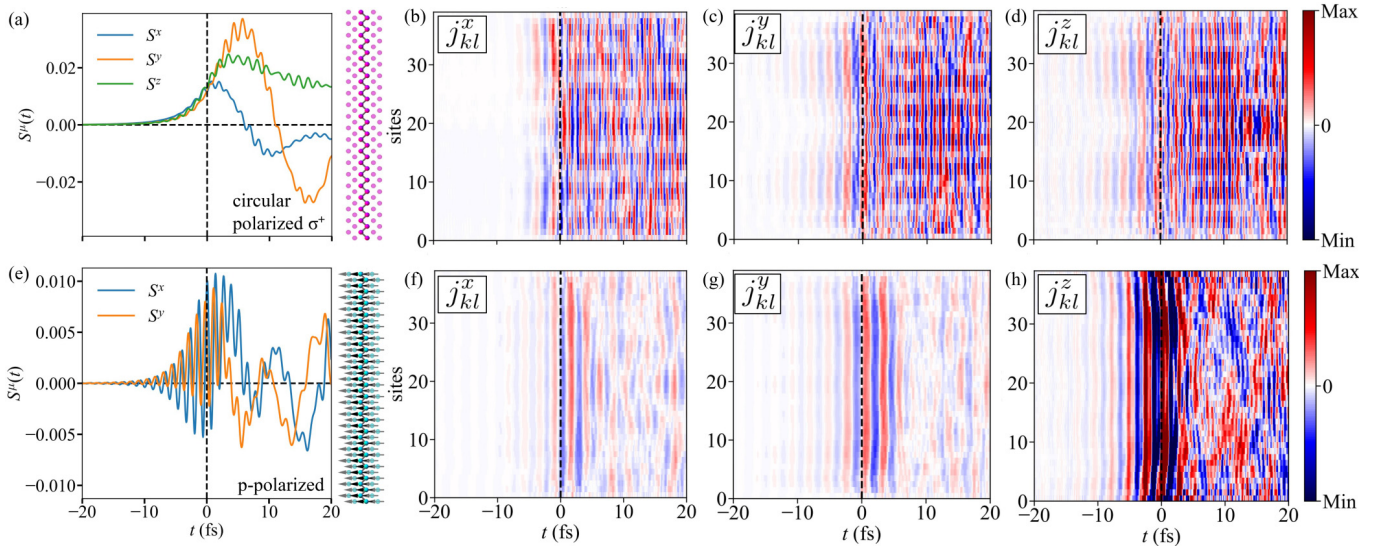


FIG. 4. Photoinduced spin polarization $S^\mu(t)$ and spin-resolved currents $j_{kl}^\mu(t)$ for a Cu(100) film excited by circularly polarized light with helicity σ^+ (top row) and for fcc Co(100) excited by p -polarized light (bottom row). (a) Site-averaged spin polarization $S^\mu(t)$ for Cu(100) ($\mu = x, y, z$). [(b)–(d)] Spin-resolved currents $j_{kl}^\mu(t)$ displayed as a color scale, as in Fig. 2. (e) $S^x(t)$ and $S^y(t)$ for Co(100). [(f)–(h)] The same as [(b)–(d)] using the same color scale. Dashed vertical lines indicate the maximum of the laser pulse at $t = 0$ fs.

the x direction [36]. Again, the current pattern becomes complicated after the laser pulse due to the interference mentioned before.

For s -polarized light, the symmetry analysis yields $\mathcal{S} = 0$ but allows for $s_i^z \neq 0$. The photoinduced local spin polarizations at equivalent sites thus have to compensate each other. This is fully confirmed by the simulations: the spin polarization is spatially antisymmetric within the Cu film [Fig. 3(a)].

The antisymmetry of the spin polarization may be attributed to the surface normals of the freestanding Cu film being opposite to each other. This reasoning complies with spin polarization effects in spin- and angle-resolved photoemission [4–8] since they rely on the presence of a surface (they do not occur in bulk samples). Hence, one may regard the present result as an indication of the importance of surfaces and interfaces for ultrafast spin dynamics; see, for example, Ref. [19] (for reviews on polarized electrons at surfaces we refer to Refs. [37,38]).

The above argument is supported by the currents $j_{kl}(t)$ [Fig. 3(b)] which are initiated at the surfaces: compare, for example, the darker color scale at surface sites 0 and 39 in Fig. 3(b) with the lighter colors in the interior of the film at $t = -5$ fs. The currents enter the film’s interior slightly after the laser’s maximum (at $t \approx 4$ fs), as is schematically indicated by the dashed arrows (due to the antisymmetry, the current at the film’s center vanishes, giving rise to the white horizontal stripe), and are reflected at the surfaces at $t \approx 12$ fs, leading to a crisscross pattern [see the dashed arrows in Fig. 3(b)]. The spin-resolved currents $j_{kl}^z(t)$ exhibit a pattern (not shown here) reminiscent of that of $j_{kl}^y(t)$ for p -polarized light displayed in Fig. 2(e).

The antisymmetry of the observed pattern is apparently related to the symmetry of the sample, in particular to the presence of two identical surfaces. It is understood as a superposition of two patterns with opposite signs, one attributed to the bottom surface and one attributed to the top surface. In

experiments, this symmetry is usually broken, for example, by a substrate, thereby leading to disparate surfaces. For this reason, one would observe a superposition of dissimilar patterns or, in the case of thick samples, the pattern attributed to one of the surfaces.

With regard to circularly polarized light, it is sufficient to discuss one helicity (here σ^+ as defined in Sec. II A) since the x and z components of both spin polarization and spin-resolved currents change sign upon helicity reversal, whereas the y component does not, as confirmed by our simulations.

All components of the site-averaged spin polarization $S^\mu(t)$ and the spin-resolved currents $j_{kl}^\mu(t)$ are nonzero (Fig. 4, top row). In an admittedly simple picture $S^x(t)$ and $S^z(t)$ may be viewed as being due to the optical orientation in the photoemission [39]. Recall that the laser impinges within the xz plane onto the film; for a single atom optical orientation by circularly polarized light would then cause spin polarization within the xz plane. Likewise, $S^y(t)$ may be attributed to the effect predicted by Tamura *et al.* [4] for SARPES. Of course, this “decomposition of effects” ignores that the superposition of the laser’s s - and p -polarized partial waves is coherent and shifted in phase. Moreover, the electron dynamics mixes the components of the local spin polarization because of spin-orbit coupling; nevertheless, $S^y(t)$ is reminiscent of that for p -polarized light [Fig. 2(a)].

As shown in Ref. [40], the spin polarization depends on the angle of incidence and on the photon energy. Moreover, it is strongly energy dependent, with extreme values of up to 0.5 (Fig. 8 in that publication). Averaging over energy in Figs. 8 and 10 in Ref. [40] would yield roughly 0.1, which is larger than but comparable to the maximum values in Fig. 4(a).

B. fcc Co(100)

For fcc Co(100) we focus on excitation by p -polarized light as a representative case (bottom row in Fig. 4; since illumi-

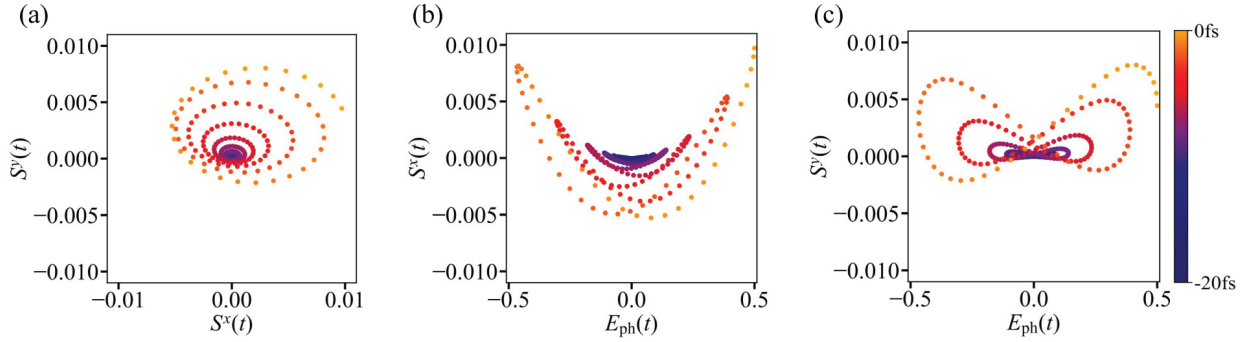


FIG. 5. Laser-driven precession of the spin polarization in Co(100) excited by p -polarized light. The color scale visualizes the time evolution from $t = -20$ fs (dark blue) to $t = 0$ fs (orange). (a) Correlation of $S^y(t)$ and $S^x(t)$ using data presented in Fig. 4(e). (b) and (c) show $S^x(t)$ and $S^y(t)$ versus the electric field $E_{ph}(t)$ of the laser pulse, respectively.

nation by circularly polarized light produced similar results, we refrain from discussing those results). As expected and often found in both experiment and theory, the site-averaged spin-polarization component $S^z(t)$ associated with magnetism is reduced by the laser pulse; that is, the sample becomes demagnetized (see Refs. [19,20] and references therein). This demagnetization is site dependent (not shown), similar to the induced spin polarization in Cu(100) discussed before.

In contrast to nonmagnetic Cu(100), the magnetization of Co(100) breaks the mirror symmetry at the xz plane and allows for nonzero $S^x(t)$ and $S^y(t)$ (see Table II). Both components are modulated with the doubled laser frequency but shifted in phase [Fig. 4(e)]. Their magnitudes are roughly 10 % of the S^y component in Cu(100) [Fig. 2(a)]. Moreover, both $S^x(t)$ and $S^y(t)$ of Co(100) exhibit a beating pattern (with maxima at about $t \approx 0, 10,$ and 20 fs), while $S^y(t)$ of Cu(100) displays a clear sinusoidal shape.

The spin-polarization components $S^x(t)$ and $S^y(t)$ exhibit a regular pattern before the maximum of the laser pulse [Fig. 4(e)], which hints at laser-driven precession of the spin polarization $\mathbf{S}(t)$. Indeed, $S^x(t)$ and $S^y(t)$ display a left-handed helix, starting at the origin, with increasing amplitude [Fig. 5(a)]. Moreover, the noticeable shift of the spiral center to positive values is explained by spin-orbit coupling: a minimal tight-binding model for the motion of $\mathbf{S}(t)$, including spin-orbit coupling, yields two features, a deformation of the precession cone and a shift of the cone axis off the magnetization direction (z axis). Without spin-orbit coupling, one finds the usual circular cone with its axis along the magnetization direction.

The time sequences of $S^x(t)$ and $S^y(t)$ versus the laser amplitude $E_{ph}(t)$ prove that the precession is driven by the laser [Figs. 5(b) and 5(c)]. The variations in the patterns are attributed to the phase shift between $S^x(t)$ and $S^y(t)$.

The striking differences in the spin polarization of Cu and Co could be due to the occupation of the electronic states, to spin-orbit coupling, or to exchange splitting. In order to shed light upon the origin we performed simulations for Cu and Co in which the number of initially occupied states, the strength of the spin-orbit coupling, and the exchange splitting were varied (not shown here). While the former two have a minute effect on the spin polarization in both Cu and Co, reducing the exchange splitting removes the rapid oscillations and preserves the long-period oscillations that are observed in

Co(100) [Fig. 4(e)]. These findings prompt exchange splitting as the main origin.

As for the spin polarization, all three components of the spin-resolved currents are nonzero [Figs. 4(f)–4(h)], with the z -component $j_{kl}^z(t)$ being the largest, as exhibited by darker colors in Fig. 4(h). All components oscillate in unison before the laser pulse maximum; complicated current patterns arise after the pulse.

Summarizing briefly for Cu and Co, we find that the simulations confirm the symmetry considerations. General trends are unison oscillations before the laser maximum and complicated patterns thereafter; the optically induced spin-polarization components are smaller in a magnetic sample but exhibit precession before the laser pulse maximum.

C. Co/Cu heterostructure

We now address a Co/Cu(100) heterostructure illuminated by p -polarized light. Decomposing $S^x(t)$ and $S^y(t)$ of the entire sample [black lines in Figs. 6(a) and 6(b)] into the respective parts in the Co (cyan) and Cu (magenta) regions indicates that $S^x(t)$ [Fig. 6(a)] is first induced by the laser pulse in the Co region and subsequently enters the Cu region [recall that $S^x(t)$ is symmetry forbidden in Cu(100); see Sec. III A]. This finding underlines the importance of an interface for ultrafast spin dynamics.

In contrast, $S^y(t)$ is by far the largest in the nonmagnetic Cu region [Fig. 6(b)], whereas it is strongly reduced in the Co region. This finding corroborates the above argument that magnetism may reduce photoinduced spin-polarization components. Both the magnitude and frequency of the site-averaged components in the two regions are reminiscent of those in the respective homogeneous samples.

The currents $j_{kl}(t)$ exhibit an oscillating collective motion across the sample before the pulse, similar to Cu(100) [Fig. 2(c)]. However, beginning slightly before the pulse maximum at $t = 0$ fs, the spatial homogeneity is lost; instead there are sizable currents initiated at the interface (visualized by the horizontal dashed line at site 19) and propagating toward the Co region [dark blue features in Fig. 6(c)]. This finding corroborates that the interface acts as a “source” of ultrafast spin currents. At the magnetic/nonmagnetic interface, the imbalance of occupation facilitates the production of currents. Moreover, since the imbalance is spin dependent,

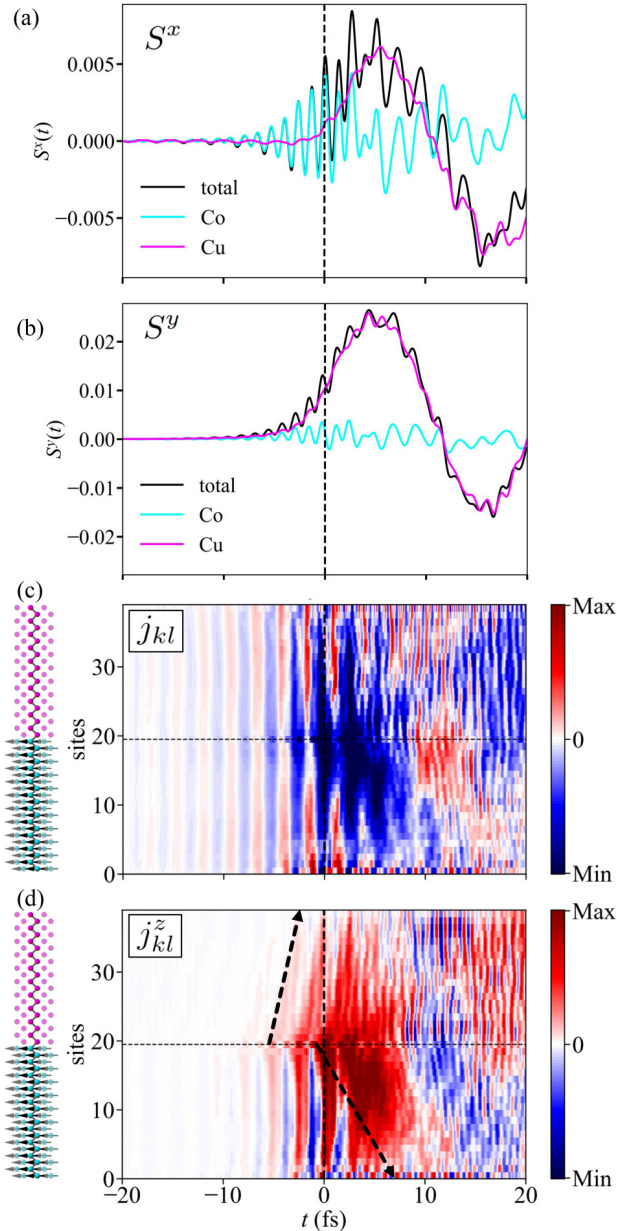


FIG. 6. Photoinduced spin polarization and currents of a Co/Cu(100) heterostructure excited by p -polarized light. (a) Component $S^x(t)$ of the site-averaged spin polarization (black) decomposed into that in the Co region (cyan) and that in the Cu region (magenta). The latter are normalized with respect to N_{site} [see Eq. (7)]. The maximum of the laser pulse at $t = 0$ fs is marked by the vertical dashed line. (b) The same as (a), but for $S^y(t)$. (c) Currents $j_{kl}(t)$ depicted as a color scale (red is positive; blue is negative). The Co/Cu interface is identified by the horizontal dashed line. (d) The same as (c), but for spin-resolved currents $j_{kl}^z(t)$. Arrows serve as a guide to the eye.

the spin-resolved currents $j_{kl}^z(t)$, that is, those with spin along the magnetization direction, should also be triggered at the interface. This is, indeed, verified by $j_{kl}^z(t)$ [Fig. 6(d)]. More precisely, these currents are homogeneous in the Co region before the pulse; they become enhanced at the interface at about $t = -5$ fs (dark red patches; also illustrated by the black arrows). The x - and y -spin-resolved currents (not shown here)

are not affected as much by the interface as the z component, which suggests that the imbalance of magnetization (spin-dependent occupation) at the interface is the most relevant origin.

The above argument concerning the importance of interfaces is further supported by the varying velocities of $j_{kl}^z(t)$ in the Cu and Co regions (approximately 2.8 nm/fs in Cu and 0.9 nm/fs in Co [see the inclinations of the arrows in Fig. 6(d)]; these velocities compare well with those computed for other materials, e.g., in Refs. [17,41]). In the latter, we find the homogeneous oscillating current pattern before the pulse maximum. In the Cu region, which is nonmagnetic, the same pattern appears oblique, as indicated by the black dashed arrows in Fig. 6(d). This means that these currents spill out from the Co region into the Cu region and propagate toward the Cu surface (site 39).

IV. CONCLUSION AND OUTLOOK

Our theoretical findings suggest that femtosecond laser pulses impinging on thin films may be used to generate ultrafast oscillating spin-polarized currents. Moreover, interfaces amplify the production of these currents, as is evidenced in our study. And the spin polarization can be tuned by details of the laser's electric field, in particular by the polarization of the radiation.

Inhomogeneities in the sample (surfaces, interfaces) yield intrinsic imbalances of occupation which facilitate the production of spin-polarized currents. This finding supports reasoning given in Ref. [42], in which it was argued that a spin-dependent imbalance of occupation, termed spin voltage in that paper, results in both demagnetization and spin currents.

Spin pumping is the transfer of spin from a ferromagnet into an attached normal metal due to precession of the local magnetic moments in the ferromagnet. Extending this picture, fluctuations of local magnetic moments may also cause the effect [43,44]. Assuming a fixed collinear magnetic structure, based on electron dynamics rather than on magnetization dynamics, the transfer of spin found in the presented simulations does not fall into this category of spin pumping but, nevertheless, may be termed “spin pumping” in a general sense. Hence, our study gives further details on the mechanisms for the transfer of spin polarization across a magnetic/normal metal interface generated by laser excitation, as reported, for example, in Refs. [14,17,45,46].

As shown in this paper, already the combination of 3d materials (here Co and Cu) produces sizable spin-polarization effects. The latter could be enhanced further by increasing the imbalance of spin-dependent occupation at interfaces. Material combinations worth investigating could comprise heavier elements with larger spin-orbit coupling (e.g., Pt [40]) and heavy magnetic materials (e.g., Gd).

A direct observation of the photoinduced spin polarization and the spin-polarized currents studied in this paper challenges experiments because of their as yet limited temporal resolution. However, it is conceivable to probe the currents via their emitted electromagnetic radiation (see, for example, Ref. [47]).

We conclude by discussing the advantages and disadvantages of the EVOLVE framework. The real-space approach gives access to spatiotemporal distributions of observables with atomic and femtosecond resolution. Being an effective one-electron approach, large samples and long time spans can be simulated; in contrast, *ab initio* approaches are limited in sample size and time interval but are more accurate (e.g., Ref. [48]). Moreover, EVOLVE is flexible: interactions (e.g., spin-orbit coupling and exchange splitting) can be varied deliberately, one can choose closed or open boundary conditions along individual directions, and samples may contain inhomogeneities (e.g., defects or interfaces, noncollinear magnetic textures). For thermalization (i.e., relaxation from an excited state toward the thermal ground state) that occurs on a timescale of a few hundred femtoseconds, coupling to a bosonic heat bath can be turned on [19,20].

Electron-electron scattering is currently not explicitly included in the simulations but may be added in the

Hartree-Fock approximation. The validity of the presented results is therefore somewhat limited, even when focusing on the period of a laser excitation. Since the electron-electron interaction is reflected partially in the tight-binding parameters (for the ground state), only deviations from the ground state's occupation profile need to be considered. We expect attraction and repulsion within the dynamic spatial charge distribution that is generated by the laser pulse. For example, the electron-electron interaction could reduce the propagation length of currents (attractive interaction) or spread regions with increased or decreased occupation (repulsive interaction), both of which could diminish the coherence in occupation and current profiles.

ACKNOWLEDGMENT

This work is funded by the Deutsche Forschungsgemeinschaft (DFG, German Research Foundation), Project ID No. 328545488–TRR 227, project B04.

-
- [1] S. Hüfner, *Photoelectron Spectroscopy: Principles and Applications*, 2nd ed. (Springer, Berlin, 1996).
- [2] *Solid-State Photoemission and Related Methods*, edited by W. Schattke and M. A. Van Hove (Wiley-VCH, Weinheim, 2003).
- [3] J. Henk, K. Miyamoto, and M. Donath, *Phys. Rev. B* **98**, 045124 (2018).
- [4] E. Tamura, W. Piepke, and R. Feder, *Phys. Rev. Lett.* **59**, 934 (1987).
- [5] E. Tamura and R. Feder, *Solid State Commun.* **79**, 989 (1991).
- [6] E. Tamura and R. Feder, *Europhys. Lett.* **16**, 695 (1991).
- [7] J. Henk and R. Feder, *Europhys. Lett.* **28**, 609 (1994).
- [8] J. Henk, T. Scheunemann, S. V. Halilov, and R. Feder, *J. Phys.: Condens. Matter* **8**, 47 (1996).
- [9] K. Starke, *Magnetic Dichroism in Core-Level Photoemission* (Springer, Berlin, 2007).
- [10] E. Beaupaire, J.-C. Merle, A. Daunois, and J.-Y. Bigot, *Phys. Rev. Lett.* **76**, 4250 (1996).
- [11] G. P. Zhang and W. Hübner, *Phys. Rev. Lett.* **85**, 3025 (2000).
- [12] G. Zhang, W. Hübner, E. Beaupaire, and J.-Y. Bigot, in *Spin Dynamics in Confined Magnetic Structures I*, edited by B. Hillebrands and K. Ounadjela (Springer, Berlin, 2003), p. 245.
- [13] J. Hermanson, *Solid State Commun.* **22**, 9 (1977).
- [14] M. Battiato, K. Carva, and P. M. Oppeneer, *Phys. Rev. Lett.* **105**, 027203 (2010).
- [15] M. Battiato, K. Carva, and P. M. Oppeneer, *Phys. Rev. B* **86**, 024404 (2012).
- [16] M. Battiato, P. Maldonado, and P. M. Oppeneer, *J. Appl. Phys.* **115**, 172611 (2014).
- [17] D. M. Nenzo, B. Rethfeld, and H. C. Schneider, *Phys. Rev. B* **98**, 224416 (2018).
- [18] S. Kaltenborn, Y.-H. Zhu, and H. C. Schneider, *Phys. Rev. B* **85**, 235101 (2012).
- [19] F. Töpler, J. Henk, and I. Mertig, *New J. Phys.* **23**, 033042 (2021).
- [20] F. Ziolkowski, O. Busch, I. Mertig, and J. Henk, *J. Phys.: Condens. Matter* **35**, 125501 (2023).
- [21] B. Heinrich, Z. Celinski, K. Myrtle, J. F. Cochran, M. Kowalewski, A. S. Arrott, and J. Kirschner, *J. Appl. Phys.* **69**, 5217 (1991).
- [22] M. J. Mehl and D. A. Papaconstantopoulos, *Phys. Rev. B* **54**, 4519 (1996).
- [23] C.-S. Yoo, P. Söderlind, and H. Cynn, *J. Phys.: Condens. Matter* **10**, L311 (1998).
- [24] J. C. Slater and G. F. Koster, *Phys. Rev.* **94**, 1498 (1954).
- [25] D. A. Papaconstantopoulos, *Handbook of the Band Structure of Elemental Solids* (Springer, Berlin, 2015).
- [26] S. Kunschuh, M. Gmitra, and J. Fabian, *Phys. Rev. B* **82**, 245412 (2010).
- [27] A. V. Kimel, A. Kirilyuk, P. A. Usachev, R. V. Pisarev, A. M. Balbashov, and T. Rasing, *Nature (London)* **435**, 655 (2005).
- [28] R. Hertel, *J. Magn. Magn. Mater.* **303**, L1 (2006).
- [29] S. B. Mishra and S. Coh, *Phys. Rev. B* **107**, 214432 (2023).
- [30] S. Savasta and R. Girlanda, *Solid State Commun.* **96**, 517 (1995).
- [31] G. D. Mahan, *Many-Particle Physics*, 3rd ed. (Springer, New York, 2000).
- [32] B. K. Nikolić, L. P. Zárbo, and S. Souma, *Phys. Rev. B* **73**, 075303 (2006).
- [33] M. D. Petrović, B. S. Popescu, U. Bajpai, P. Plecháč, and B. K. Nikolić, *Phys. Rev. Appl.* **10**, 054038 (2018).
- [34] *Spin-Orbit-Influenced Spectroscopies of Magnetic Solids*, edited by H. Ebert and G. Schütz (Springer, Berlin, 1996).
- [35] See Supplemental Material at <http://link.aps.org/supplemental/10.1103/PhysRevB.108.184401> for animations of the spin dynamics.
- [36] In the spirit of a two-current model one may write $j_x = j_x^{\uparrow y} + j_x^{\downarrow y}$ and $j_x^y = j_x^{\uparrow y} - j_x^{\downarrow y}$ for the spin-integrated current j_x and the y-spin-polarized current j_x^y , respectively. Denoting the spin orientation \uparrow_y (\downarrow_y) as the majority (minority) orientation with respect to the y direction, the finding is attributed to a flow of minority-spin electrons.
- [37] R. Feder, *Polarized Electrons in Surface Physics* (World Scientific, Singapore, 1986).

- [38] J. Kirschner, *Polarized Electrons at Surfaces* (Springer, Berlin, 1985).
- [39] J. Kessler, *Polarized Electrons*, 2nd ed. (Springer, Berlin, 1985).
- [40] C. M. Schneider and J. Kirschner, *Crit. Rev. Solid State Mater. Sci.* **20**, 179 (1995).
- [41] V. P. Zhukov, E. V. Chulkov, and P. M. Echenique, *Phys. Rev. B* **73**, 125105 (2006).
- [42] R. Rouzegar, L. Brandt, L. Nádvorník, D. A. Reiss, A. L. Chekhov, O. Gueckstock, C. In, M. Wolf, T. S. Seifert, P. W. Brouwer, G. Woltersdorf, and T. Kampfrath, *Phys. Rev. B* **106**, 144427 (2022).
- [43] Y. Tserkovnyak, A. Brataas, and G. E. W. Bauer, *Phys. Rev. Lett.* **88**, 117601 (2002).
- [44] Y. Tserkovnyak, A. Brataas, and G. E. W. Bauer, *Phys. Rev. B* **66**, 224403 (2002).
- [45] M. Battiato, Ph.D. thesis, Uppsala Universitet, 2013.
- [46] A. Alekhin, I. Razdolski, N. Ilin, J. P. Meyburg, D. Diesing, V. Roddatis, I. Rungger, M. Stamenova, S. Sanvito, U. Bovensiepen, and A. Melnikov, *Phys. Rev. Lett.* **119**, 017202 (2017).
- [47] T. Kampfrath, M. Battiato, P. Maldonado, P. G. Eilers, J. Nötzold, S. Mährlein, V. Zbarsky, F. Freimuth, Y. Mokrousov, S. Blügel, M. Wolf, I. Radu, P. M. Oppeneer, and M. Münzenberg, *Nat. Nanotechnol.* **8**, 256 (2013).
- [48] J. K. Dewhurst, P. Elliott, S. Shallcross, E. K. U. Gross, and S. Sharma, *Nano Lett.* **18**, 1842 (2018).

5.2 Ultrafast dynamics of laser-induced orbital angular momentum

Increasing role of orbital angular momentum in solid-state physics. In the field of ultrafast magnetization dynamics, many works examined how angular momentum can be generated, manipulated and transported, in particular induced by laser excitation (for a review, see e.g. Ref. [40]). After the photo-induced demagnetization of ferromagnets has been observed experimentally [34], it has been shown that the net magnetization of ferrimagnetic materials can be entirely reversed by all-optical switching [37]. Furthermore, multilayer systems, such as ferromagnetic/nonmagnetic heterostructures, gained interest in this field since angular momentum can be transported across the interface by ultrafast spin currents [45, 48].



However, the focus has been on the spin angular momentum (SAM) which lends its name to the field *spintronics*. An essential key element in the above effects is spin-orbit interaction which couples the SAM with its orbital companion, the orbital angular momentum (OAM). The latter has been given less consideration due to the aforementioned orbital quenching, the suppression of OAM in the ground state. Yet, in recent years, many groups started to investigate the dynamics of the OAM which led to the alternative field of *orbitronics* [21]. Since the detection of orbital currents and their distinction from spin currents in experiments remains challenging, the study of laser-induced generation and transport of OAM has great potential.


This publication. In the following publication “Ultrafast dynamics of orbital angular momentum of electrons induced by femtosecond laser pulses: Generation and transfer across interfaces” [OB5], the laser-induced orbital dynamics of electrons is examined. By investigating the same setups as in the previous publication [OB4], results for the OAM can be compared to the ones for the SAM. The components of the OAM, which are allowed or forbidden by the symmetry of the system, are the same as the ones of the SAM (cf. Tab. II in [OB4]). However, as a general trend, we observe faster oscillations and less decoherence after the laser pulse for the OAM dynamics than obtained for the SAM.

In publication [OB5], the focus is on excitation with circularly polarized light. We find that ultrafast orbital currents are generated in nonmagnetic [Cu(100)] and magnetic samples [Co(100) and Co/Cu(100)]. Furthermore, the induced OAM component is oriented along the propagation direction of the orbital current, and has a sizable magnitude which persists several 10 fs after the pulse. Akin to the (spin-polarized) currents, orbital currents are initiated at the surface or at the interface. For an efficient OAM transfer in the heterostructure, the simulations suggest to induce an OAM component, which is forbidden in the Cu region, in the Co region and transport the OAM by an orbital current across the Co/Cu interface. This can be tuned by the laser polarization.

The following publication: Reprinted (whole article) with permission from O. Busch, F. Ziolkowski, I. Mertig and J. Henk, *Physical Review B* **108**, 104408 (2023); Ref. [OB5]; Ultrafast dynamics of orbital angular momentum of electrons induced by femtosecond laser pulses: Generation and transfer across interfaces. Copyright (2023) by the American Physical Society.

Ultrafast dynamics of orbital angular momentum of electrons induced by femtosecond laser pulses: Generation and transfer across interfaces

Oliver Busch ^{*}, Franziska Ziolkowski, Ingrid Mertig, and Jürgen Henk 
Institut für Physik, Martin Luther University Halle-Wittenberg, 06099 Halle, Germany

 (Received 23 June 2023; revised 17 August 2023; accepted 28 August 2023; published 8 September 2023)

The orbital angular momenta (OAM) of electrons play an increasingly important role in ultrafast electron and magnetization dynamics. In this theoretical study, we investigate the electron dynamics induced by femtosecond laser pulses in a normal metal, a ferromagnet, and a ferromagnet/normal metal heterostructure. We analyze the spatiotemporal distributions of the laser-induced OAM and their respective currents. Our findings demonstrate that a circularly polarized laser pulse can induce a sizable and long-lasting OAM component in a normal metal. Furthermore, an interface between a ferromagnet and a normal metal facilitates the demagnetization of the magnet by the OAM contribution to the total magnetization. Finally, to transfer OAM from a ferromagnet into a normal metal, it is advantageous to use a laser setup that induces the desired OAM component in the ferromagnet, but not in the normal metal.

DOI: [10.1103/PhysRevB.108.104408](https://doi.org/10.1103/PhysRevB.108.104408)

I. INTRODUCTION

In recent years, there has been significant attention given to ultrafast phenomena in condensed matter physics. While much of the focus has been on the spin angular momentum (SAM) of electrons, which has led to the field of spintronics, the closely related orbital angular momentum (OAM) of electrons has also emerged as an important topic in its own right [1–3]. Orbitronic devices are seen as a potential alternative to electronic and spintronic devices [4–6].

A number of ultrafast phenomena are well described by means of SAM, for example, the optical manipulation of magnetic moments [7–9], the demagnetization of ferromagnets [10–12], and the transfer of magnetic moment between ferromagnetic layers [13–15] as well as across magnet/normal metal interfaces [16–18]. Moreover, femtosecond laser pulses induce SAM in nonmagnetic and magnetic samples [19,20].

Spin-orbit coupling is not only ubiquitous in solids but also indispensable for most of the phenomena mentioned above. Therefore, a question arises regarding the contributions of the OAM to these effects (recall that SAM and OAM add up to the total angular momentum). In this respect, we need to address several issues such as: what components of the OAM are induced by femtosecond laser pulses, what is their magnitude, and what is their spatiotemporal distribution? In this paper, we report on a theoretical study where we investigated photo-induced OAM and their currents in Cu(100), Co(100), and a Co/Cu(100) heterostructure excited with femtosecond laser pulses.

Our findings, based on investigations of a Cu(100) film, reveal a pronounced and persistent presence of laser-induced OAM in the direction of the OAM current which

propagates through the sample. Furthermore, in the context of a Co/Cu(100) heterostructure, we observe that the interaction at the interface between a ferromagnet and a normal metal facilitates the demagnetization of the magnet due to the OAM contribution to the overall magnetization. Notably, for efficient transfer of OAM from the ferromagnet to the normal metal, careful consideration should be given to the polarization configuration of the laser pulse. Specifically, inducing the desired OAM component exclusively within the ferromagnet, rather than in the normal metal, proves advantageous.

Our study offers valuable insights into the ultrafast dynamics of electron orbital angular momenta. These dynamics are determined by both the electronic and magnetic properties of the samples as well as by the laser pulse characteristics.

II. THEORETICAL ASPECTS

We briefly present the main ideas of our approach to ultrafast electron dynamics, EVOLVE, since it has been described elsewhere [20–22].

We consider free-standing films of Cu(100), face-centered cubic Co(100), and Co/Cu(100), each with a thickness of 40 layers (20 layers each for Co/Cu). The Cartesian x axis is perpendicular to the film, and periodic boundary conditions are applied in the y and z directions. The local magnetic moments in Co(100) and Co/Cu(100) are collinear and point along the z direction (Fig. 1) [23].

The electron dynamics is described by the von Neumann equation (in Hartree atomic units)

$$-i \frac{d\hat{\rho}(t)}{dt} = [\hat{\rho}(t), \hat{H}(t)] \quad (1)$$

for the one-particle density matrix

$$\hat{\rho}(t) = \sum_{n,m} |n\rangle p_{nm}(t) \langle m|. \quad (2)$$

^{*}Correspondence author: oliver.busch@physik.uni-halle.de

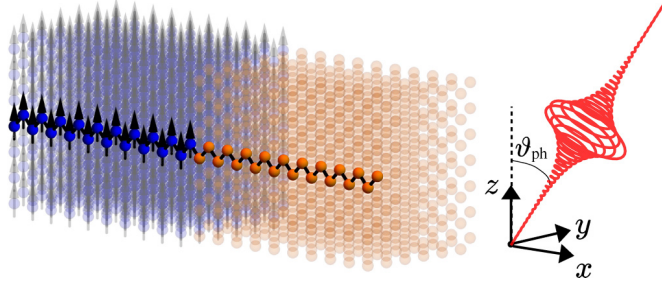


FIG. 1. Geometry of a fcc Co/Cu(100) heterostructure. The film is composed of 40 layers stacked in the x direction, with 20 layers of both Co atoms (blue spheres) and Cu atoms (orange spheres). It is infinite in both the y and the z direction. The Co magnetic moments point along the z direction (black arrows). A circularly polarized laser pulse is incident within the xz plane onto the sample.

$\{|n\rangle\}$ are the eigenstates of the Hamiltonian \hat{H}_0 which describes the electronic structure of the samples in tight-binding form [24,25]. Collinear magnetism and spin-orbit coupling are included [26].

The time-dependent Hamiltonian $\hat{H}(t)$ in Eq. (1) supplements \hat{H}_0 by the electric field of the femtosecond laser pulse [27]. This field is a coherent superposition of s - and p -polarized partial waves with energy ω and with a Lorentzian envelope. In this paper we focus on excitation by circularly polarized light with helicity σ_+ impinging within the xz plane onto the films with a polar angle $\vartheta_{ph} = 45^\circ$ of incidence (Fig. 1). All atomic sites are illuminated simultaneously and with the same laser intensity. Hence, we assume that the laser pulse's spatial extent is considerably larger than the sample's thickness. In an experiment for a thick sample, the laser intensity would vary across the slab, thereby introducing an additional occupation inhomogeneity, which complicates the interpretation of the results. Our assumption avoids this complication.

The geometry of the entire setup dictates what components of the orbital angular momentum $\langle L \rangle$ can be produced by the incident radiation [20,28]. As for the spin angular momentum (SAM) components $\langle S^\mu \rangle$, all three components $\langle L^\mu \rangle$ ($\mu = x, y, z$) of the OAM can be induced in both nonmagnetic and magnetic samples by circularly polarized light.

The spatiotemporal properties of an observable O are obtained by taking partial traces in the expectation value $\langle O \rangle(t) = \text{tr}[\hat{\rho}(t)\hat{O}]$, with the density matrix in an appropriate basis; partial trace means that the trace is restricted to the desired subspace, e.g., to a specific site, orbital, or OAM component. We address the OAM $\langle l_i \rangle(t)$ at site i and its site-averaged (global) companion

$$\langle L \rangle(t) \equiv \frac{1}{N} \sum_i \langle l_i \rangle(t), \quad (3)$$

in which the summation is over the N sites in a sample's unit cell. Similarly to the SAM currents in Ref. [20], OAM currents are computed from the symmetrized form

$$\langle j_{kl}^\mu \rangle(t) \equiv \frac{1}{2} (\langle L^\mu j_{kl} \rangle(t) + \langle j_{kl} L^\mu \rangle(t)), \quad \mu = x, y, z, \quad (4)$$

in which the operator \hat{j}_{kl} for the current from site l to site k is derived from Mahan's expression (cf. Ref. [29, page 25].

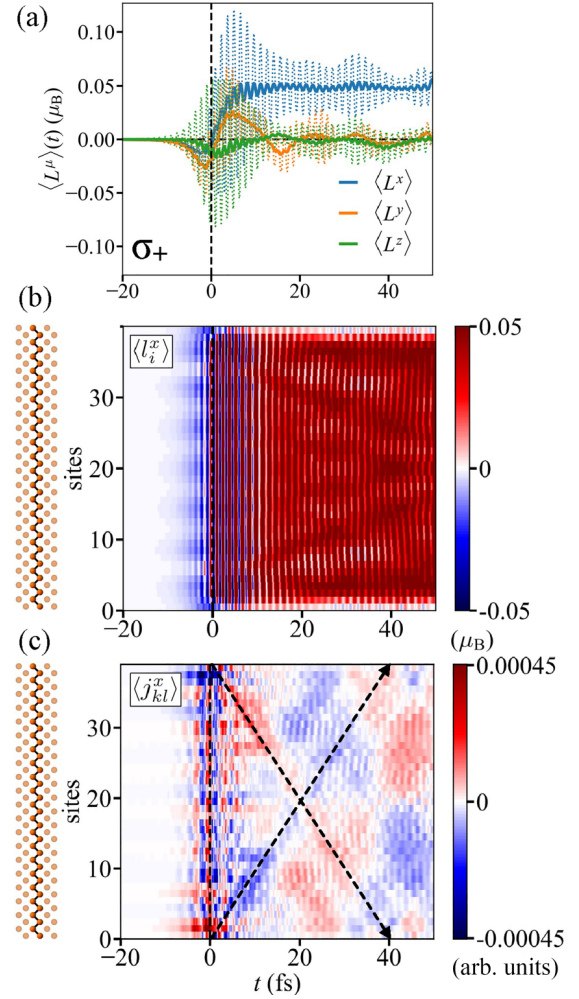


FIG. 2. Photo-induced orbital angular momentum (OAM) in Cu(100) is excited with a circularly polarized laser pulse with helicity σ_+ . (a) Site-averaged (global) OAM $\langle L^\mu \rangle(t)$, $\mu = x, y, z$. Thicker lines represent the data convoluted with a Gaussian with standard deviation $\sigma = 10$ to better visualize the main trends. (b) Spatiotemporal distribution of $\langle l_i^x \rangle(t)$ depicted as a color scale. (c) OAM current $\langle j_{kl}^x \rangle(t)$ across the sample. Arrows indicate the crisscross pattern. The color bars indicate positive (red) and negative values (blue) of $\langle l_i^x \rangle$ and $\langle j_{kl}^x \rangle$ in panels (b) and (c), respectively. Dashed vertical lines at $t = 0$ fs mark the laser-pulse maximum.

Here, we focus on nonequilibrium currents across the films (along the zigzag path in Fig. 1), since these are important for OAM transfer within stacked samples (as often used in experiments).

In all simulations discussed below, the laser has a photon energy of 1.55 eV, a fluence of about 3.3 mJ cm^{-2} , and is modulated with a Lorentzian with a width of 10 fs and centered at $t = 0$ fs. All samples comprise 40 layers, with sites 0 and 39 defining the bottom and top surfaces, respectively.

III. RESULTS AND DISCUSSION

A. Cu(100)

A circularly polarized laser pulse induces all three OAM components [panel (a) of Fig. 2]. As has been found for the

SAM [20], all components of $\langle \mathbf{L} \rangle$ exhibit rapid oscillations that are associated with the laser's frequency. Both $\langle L^y \rangle$ and $\langle L^z \rangle$ fluctuate slowly about 0 μ_B after the pulse. Strikingly, $\langle L^x \rangle$ is increased within 10 fs and oscillates about an almost constant value of 0.05 μ_B per site [thick blue spectrum in panel (a) of Fig. 2]. This finding implies that an OAM component of measurable magnitude persists considerably long after the femtosecond laser pulse in a nonmagnetic sample.

The spatial distribution of $\langle l_i^x \rangle$ is uniform across the sample, as evidenced by the negative (blue) onset before the laser-pulse maximum and the plateaulike positive (red) distribution after the laser pulse [panel (b) of Fig. 2]. Minor deviations from this uniformity result in an OAM current $\langle j_{kl}^x \rangle$, which is strongest at the surfaces [sites 0 and 39; panel (c) of Fig. 2] at $t \approx 0$ fs and moves toward the center of the sample. This creates an antisymmetric crisscross pattern [arrows in panel (c) of Fig. 2]; there is no net flow of OAM at any time t because of this antisymmetry. In a semi-infinite sample, an x -polarized OAM current $\langle j_{kl}^x \rangle$ would be observed starting at the surface, similar to the OAM of electron beams, which is also oriented in the propagation direction [30].

B. Co(100) and Co/Cu(100)

After successfully establishing sizable and long-lasting laser-induced OAM in copper, we now shift our attention towards magnetic systems.

For a Co(100) sample, one can observe a reduction of the SAM, well-known as demagnetization [10,20–22]. The z component of the OAM is strongly modulated during the pulse but remains constant thereafter [shown in green in panel (a) of Fig. 3] and has a magnitude similar to the intrinsic $\langle l^z \rangle$ (0.07 μ_B , which is in agreement with published data [31]). This result suggests that OAM does not significantly contribute to demagnetization in homogeneous magnetic samples, at least in fcc Co. It is worth noting that a laser pulse with opposite helicity σ_- also does not lead to orbital demagnetization (not shown here).

In the context of the Co/Cu(100) heterostructure, $\langle L^z \rangle$ is reduced to approximately 0.04 μ_B , representing a relative decrease of roughly 35% [green in panel (a) of Fig. 4]. This finding suggests that inhomogeneities play an important role in orbital demagnetization, a phenomenon that has already been established for the SAM [20,21]. In an inhomogeneous sample, the interface acts as a source for both SAM and OAM currents, which we attribute to the local imbalance of spin-dependent (SAM) or $\langle l_i^z \rangle$ occupation. Note that in a previous work a detailed microscopic mechanism has been revealed: the transfer of angular momentum across the interface arises from a “backflow mechanism” from the Cu into the Co region. Right after the laser pulse the occupation of spin-down d orbitals of Co sites is increased, whereas spin-down d orbitals of Cu sites near the interface are depopulated. For more details see Ref. [21] and references therein.

In contrast to Cu(100), $\langle L^x \rangle$ is relatively small in both Co(100) and Co/Cu(110) (about 0.01 μ_B) but persists, as well. Moreover, there is no precession of $\langle \mathbf{L} \rangle$ before the pulse maximum [32], which differs from the SAM [20].

Inspecting the spatiotemporal OAM-current distributions shows a crisscross pattern for Co, similar to that for Cu,

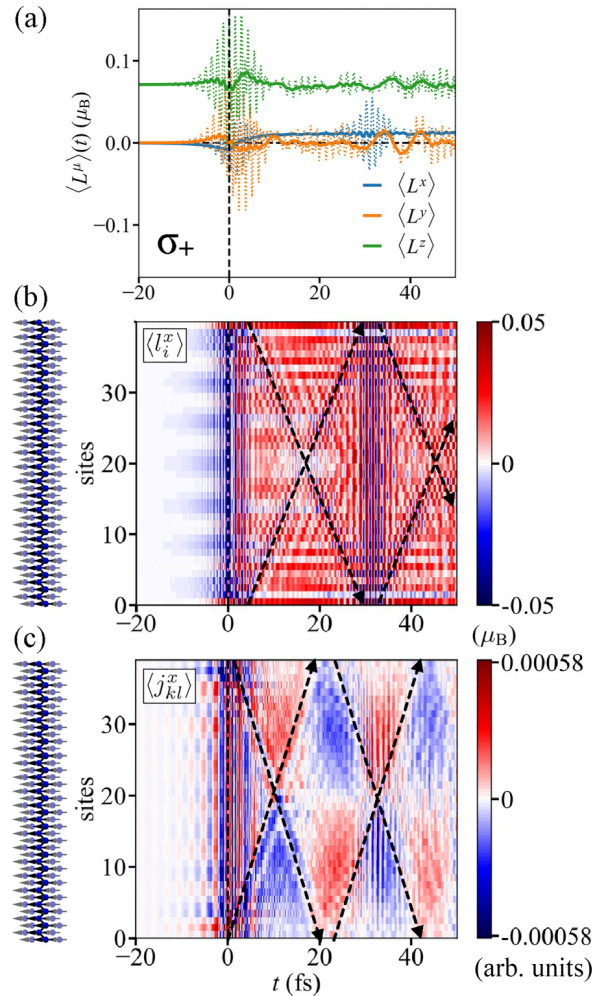


FIG. 3. Same as Fig. 2 but for face-centered-cubic Co(100). Recall that the OAM of Co has an intrinsic z component of 0.07 μ_B [green in panel (a)].

again without net flow of OAM currents. The pattern for Co/Cu(100) is slightly more complicated, but neither indicates a pronounced transfer of OAM across the interface, especially from Co into Cu.

For Co/Cu(100) we found a pronounced dependence of the SAM distribution on the laser's polarization [20], which suggests to replace circularly polarized light by p -polarized light (electric field oscillates in the xz plane; Fig. 1) in order to evoke transfer of OAM from Co into Cu. Recall that $\langle L^x \rangle$ is not induced by p -polarized light in Cu but in Co [33].

Indeed, the negative $\langle l_i^y \rangle(t)$ induced at about $t = 0$ fs in the Co region [dark blue region for sites 0 to 19; panel (e) of Fig. 4] is transferred into the Cu region (oblique blue stripe starting at the interface). In addition, the oscillations of $\langle l_i^x \rangle$ shortly after the laser pulse (red-blue from 10 fs to 20 fs) propagate into the Cu region, visible as oblique stripes. The pattern is perhaps better visible in the distribution of $\langle j_{kl}^x \rangle$ [panel (f) of Fig. 4]: the crisscross motif discussed before “spills over” from the Co region into the Cu region. This holds for the z -OAM as well (not shown here). Consequently, it is possible to transfer OAM from a ferromagnet into a normal metal using an appropriate laser pulse.

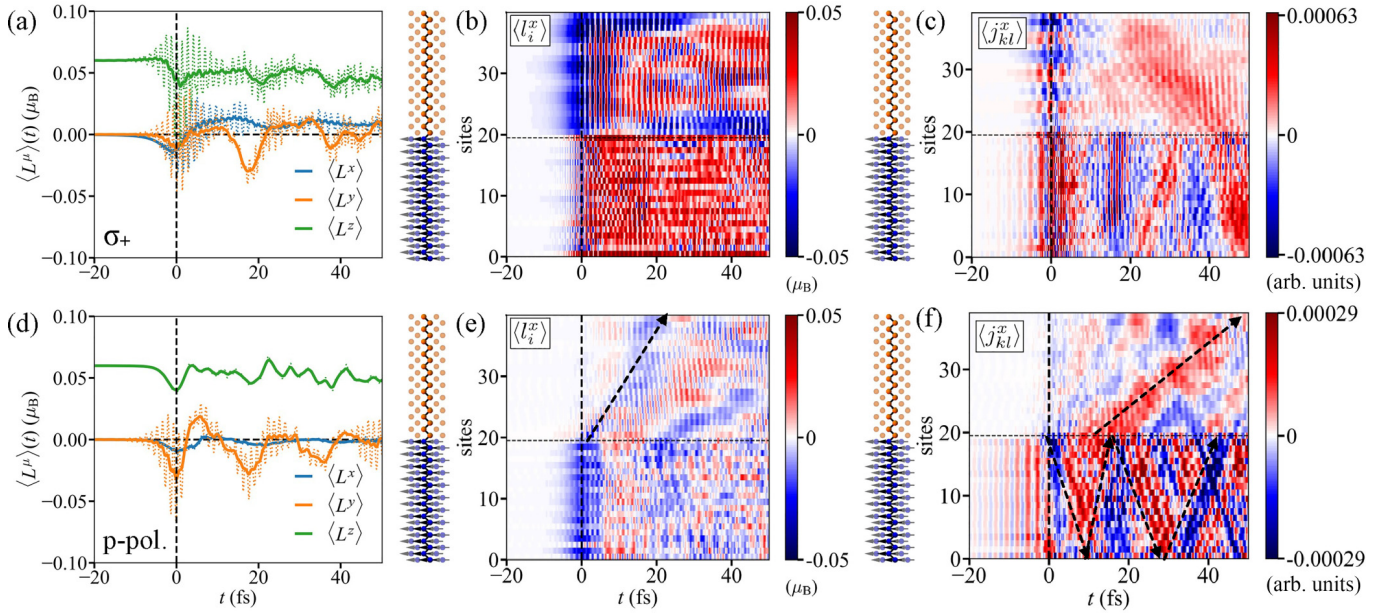


FIG. 4. Same as Fig. 2 but for a Co/Cu(100) heterostructure excited with circularly polarized [top row, panels (a)–(c)] and p-polarized laser pulse [bottom row, panels (d)–(f)].

IV. CONCLUDING REMARKS

Our theoretical investigation yields these results: a sizeable and persistent OAM component can be induced in Cu by a circularly polarized laser pulse; an interface between a ferromagnet and a normal metal facilitates the demagnetization of the magnet, not only for the SAM [20] but also for the OAM contribution to the total magnetization; in order to transfer OAM from a ferromagnet across an interface into a normal metal it appears advantageous to use a setup in which the respective OAM component is *not* induced in the normal metal; this concerns, in particular, the polarization of the femtosecond laser pulse.

Standing to reason, these findings call for experimental verification, which might be challenging. It is not just that experiments on ultrafast timescales are demanding, it may be intricate to disentangle the spin and orbital contributions to the total angular momentum. Nevertheless, OAM

currents have been measured in a recent experiment using THz emission spectroscopy [34]. In that work ferromagnet/normal metal heterostructures have been excited by femtosecond laser pulses. As suggested in Ref. [35], a suitable method for probing orbital currents could be similar to the indirect detection of spin currents via accumulated angular momentum at the edges of a sample via the magneto-optical Kerr effect (MOKE) [36–38]. In addition, x-ray magnetic circular dichroism (XMCD) measurements [39,40] allow to discriminate SAM and OAM; being element-specific they provide also details on the OAM in regions of heterostructures. Moreover, we consider it worthy to investigate other materials and material combinations.

ACKNOWLEDGMENT

This work is funded by the Deutsche Forschungsgemeinschaft (DFG, German Research Foundation), Project No. 328545488, TRR 227, Project No. B04.

- [1] C. Boeglin, E. Beaupaire, V. Halté, V. López-Flores, C. Stamm, N. Pontius, H. A. Dürr, and J.-Y. Bigot, *Nature (London)* **465**, 458 (2010).
- [2] C. Stamm, N. Pontius, T. Kachel, M. Wietstruk, and H. A. Dürr, *Phys. Rev. B* **81**, 104425 (2010).
- [3] M. Hennecke, I. Radu, R. Abrudan, T. Kachel, K. Holldack, R. Mitzner, A. Tsukamoto, and S. Eisebitt, *Phys. Rev. Lett.* **122**, 157202 (2019).
- [4] B. A. Bernevig, T. L. Hughes, and S.-C. Zhang, *Phys. Rev. Lett.* **95**, 066601 (2005).
- [5] D. Go, D. Jo, H.-W. Lee, M. Kläui, and Y. Mokrousov, *Europhys. Lett.* **135**, 37001 (2021).
- [6] D. Go and H.-W. Lee, *Phys. Rev. Res.* **2**, 013177 (2020).
- [7] N. P. Duong, T. Satoh, and M. Fiebig, *Phys. Rev. Lett.* **93**, 117402 (2004).
- [8] A. Kimel, A. Kirilyuk, and T. Rasing, *Laser Photonics Rev.* **1**, 275 (2007).
- [9] A. Kirilyuk, A. V. Kimel, and T. Rasing, *Rev. Mod. Phys.* **82**, 2731 (2010).
- [10] E. Beaupaire, J.-C. Merle, A. Daunois, and J.-Y. Bigot, *Phys. Rev. Lett.* **76**, 4250 (1996).
- [11] G. P. Zhang and W. Hübner, *Phys. Rev. Lett.* **85**, 3025 (2000).
- [12] G. Zhang, W. Hübner, E. Beaupaire, and J.-Y. Bigot, *Spin Dynamics in Confined Magnetic Structures I*, edited by B. Hillebrands and K. Ounadjela (Springer, Berlin, 2003), p. 245.
- [13] G. Malinowski, F. Dalla Longa, J. H. H. Rietjens, P. V. Paluskar, R. Huijink, H. J. M. Swagten, and B. Koopmans, *Nat. Phys.* **4**, 855 (2008).
- [14] A. J. Schellekens, K. C. Kuiper, R. R. J. C. de Wit, and B. Koopmans, *Nat. Commun.* **5**, 4333 (2014).

- [15] D. Rudolf, C. La-O-Vorakiat, M. Battiato, R. Adam, J. M. Shaw, E. Turgut, P. Maldonado, S. Mathias, P. Grychtol, H. T. Nembach *et al.*, *Nat. Commun.* **3**, 1037 (2012).
- [16] J. Chen, U. Bovensiepen, A. Eschenlohr, T. Müller, P. Elliott, E. K. U. Gross, J. K. Dewhurst, and S. Sharma, *Phys. Rev. Lett.* **122**, 067202 (2019).
- [17] A. Melnikov, I. Razdolski, T. O. Wehling, E. T. Papaioannou, V. Roddatis, P. Fumagalli, O. Aktsipetrov, A. I. Lichtenstein, and U. Bovensiepen, *Phys. Rev. Lett.* **107**, 076601 (2011).
- [18] A. Alekhin, I. Razdolski, N. Ilin, J. P. Meyburg, D. Diesing, V. Roddatis, I. Rungger, M. Stamenova, S. Sanvito, U. Bovensiepen *et al.*, *Phys. Rev. Lett.* **119**, 017202 (2017).
- [19] O. Neufeld, N. Tancogne-Dejean, U. De Giovannini, H. Hübener, and A. Rubio, *npj Comput. Mater.* **9**, 39 (2023).
- [20] O. Busch, F. Ziolkowski, I. Mertig, and J. Henk, [arXiv:2303.09291](https://arxiv.org/abs/2303.09291) [cond-mat.mtrl-sci].
- [21] F. Töpler, J. Henk, and I. Mertig, *New J. Phys.* **23**, 033042 (2021).
- [22] F. Ziolkowski, O. Busch, I. Mertig, and J. Henk, *J. Phys.: Condens. Matter* **35**, 125501 (2023).
- [23] B. Heinrich, Z. Celinski, K. Myrtle, J. F. Cochran, M. Kowalewski, A. S. Arrott, and J. Kirschner, *J. Appl. Phys.* **69**, 5217 (1991).
- [24] J. C. Slater and G. F. Koster, *Phys. Rev.* **94**, 1498 (1954).
- [25] D. A. Papaconstantopoulos, *Handbook of the Band Structure of Elemental Solids* (Springer, Berlin, 2015).
- [26] S. Kunschuh, M. Gmitra, and J. Fabian, *Phys. Rev. B* **82**, 245412 (2010).
- [27] S. Savasta and R. Girlanda, *Solid State Commun.* **96**, 517 (1995).
- [28] J. Henk, T. Scheunemann, S. V. Halilov, and R. Feder, *J. Phys.: Condens. Matter* **8**, 47 (1996).
- [29] G. D. Mahan, *Many-Particle Physics*, 3rd ed. (Springer, New York, 2000).
- [30] V. Grillo, A. H. Tavabi, F. Venturi, H. Larocque, R. Balboni, G. C. Gazzadi, S. Frabboni, P.-H. Lu, E. Mafakheri, F. Bouchard, R. E. Dunin-Borkowski, R. W. Boyd, M. P. J. Lavery, M. J. Padgett, and E. Karimi, *Nat. Commun.* **8**, 15536 (2017).
- [31] J.-i. Igarashi and K. Hirai, *Phys. Rev. B* **53**, 6442 (1996).
- [32] A simple explanation is that the Hamiltonian \hat{H}_0 does not contain OAM operators but SAM operators in order to account for exchange splitting (Zeeman term). The Heisenberg equations of motion for the angular-momenta components thus yield precession for the SAM but not for the OAM.
- [33] The symmetry analysis for the SAM, reported in Ref. [20], also holds for the OAM.
- [34] T. S. Seifert, D. Go, H. Hayashi, R. Rouzegar, F. Freimuth, K. Ando, Y. Mokrousov, and T. Kampfrath, *Nat. Nanotechnol.* (2023), doi:10.1038/s41565-023-01470-8.
- [35] D. Go, D. Jo, C. Kim, and H.-W. Lee, *Phys. Rev. Lett.* **121**, 086602 (2018).
- [36] Y. K. Kato, R. C. Myers, A. C. Gossard, and D. D. Awschalom, *Science* **306**, 1910 (2004).
- [37] J. Sinova, S. Murakami, S.-Q. Shen, and M.-S. Choi, *Solid State Commun.* **138**, 214 (2006).
- [38] C. Stamm, C. Murer, M. Berritta, J. Feng, M. Gabureac, P. M. Oppeneer, and P. Gambardella, *Phys. Rev. Lett.* **119**, 087203 (2017).
- [39] W. L. O'Brien and B. P. Tonner, *Phys. Rev. B* **50**, 12672 (1994).
- [40] S. Bonetti, *J. Phys.: Condens. Matter* **29**, 133004 (2017).

6 Conclusion and outlook

In this thesis, transport of the electron's charge, spin, and orbital angular momenta has been studied theoretically.

One part is concerned with the transport properties in various kagome systems in the steady state, where the response to an homogenous electric field has been investigated. The kagome lattice is a twodimensional hexagonal lattice with three basis atoms, on which a noncollinear magnetic texture can be localized. In particular, the transverse response, where resulting currents are not aligned with the applied electric field, has been studied in these systems. These transverse currents may carry charge, spin or orbital angular momenta and are phenomena denoted as 'Hall effects'. In this thesis, the intrinsic contributions to the Hall conductivities have been studied by utilizing a Berry curvature approach, based on tight-binding calculations in reciprocal space.

Another part of this thesis is attributed to ultrafast electron dynamics induced by excitation of thin films with femtosecond laser pulses. The investigated systems are homogeneous Cu or Co samples and a Co/Cu heterostructure illuminated with linearly or circularly polarized light. The simulation of finite systems is achieved by using a real-space tight-binding model. In order to govern the time evolution, an effective one-electron density matrix has been propagated in time by solving the von Neumann equation numerically. In this equation of motion, the perturbation due to the laser pulse has been considered in dipole approximation. The real-space approach allows access to observables, in particular spin and orbital angular momenta and respective currents, with atomic and femtosecond resolution.

Achievements/Accomplishments. In the introduction, two goals for this work have been formulated. Below, the main results, that have been presented in the cumulative part of the thesis, are listed.

1. Established understanding of Hall effects on the microscopic level in kagome systems.
 - In literature, the unconventional anomalous Hall effect (AHE) in the coplanar noncollinear kagome antiferromagnets has been predicted mainly based on symmetry arguments. In publication [OB1], it has been revealed that spin-orbit coupling (SOC) and a virtual tilting of the magnetic texture out of the kagome plane are equivalent within the framework of this model. Thus, a coplanar noncollinear kagome magnet with SOC can behave like a noncoplanar kagome magnet in which SOC is effectively compensated. Consequently, the AHE in several kagome magnets is interpreted as an effective topological Hall effect (THE) arising from a nonvanishing scalar spin chirality of the virtual noncoplanar texture. The aforementioned equivalence of SOC and tilting of the magnetic moments leads to another scenario, where a noncoplanar magnetic texture with SOC behaves as if it is coplanar and has no SOC. In this case, certain symmetries of the Hamiltonian are reestablished, which renders the Hall effect zero, although it is allowed by the magnetic point group of the system.
 - Recently, it has been predicted that the spin Hall effect (SHE) in coplanar noncollinear kagome magnets exists even in the absence of SOC, which is typically a key requirement for the SHE. In publication [OB2], two sources which determine the spin Hall signal in these systems are identified by combining the findings with the results of publication [OB1]. The first contribution to the SHE originates from the noncollinear coplanar magnetic texture and exists without SOC. In this case, pure spin currents flow, i.e. no charge is transported. The second contribution emerges from SOC or an out-of-plane tilting of the magnetic moments, which give rise to the effective THE in these systems. In this scenario, spin and charge are transported by spin-polarized currents that mainly reduce the spin Hall signal of the magnetic texture [OB2].

- Early works on the orbital Hall effect (OHE) consider intra-atomic contributions and claim hybridization of specific atomic orbitals as the origin of the effect. In publication [OB3], additional inter-atomic contributions are considered from which an alternative mechanism of the OHE is established. The s -orbital nonmagnetic kagome lattice (without SOC) is introduced as a minimal model for the generation of orbital currents. Hybridization of atomic orbitals is not necessary, since the orbital angular momentum is generated and transported by inter-site motion of pure s electrons on cycloid trajectories generated by ‘orbital edge states’. This scenario is in analogy with the trajectory of a point on a rolling wheel, where an orbital current is generated by simultaneous rotation and translation as well.

2. Analysis of how the laser-induced electron dynamics can be tuned, in particular in Co/Cu samples.

- In publications [OB4] and [OB5], the generation, manipulation and transfer of the spin angular momentum (SAM) and the orbital angular momentum (OAM) have been studied, respectively. A symmetry analysis predicts how the ultrafast dynamics depends on the laser polarization (s, p or circularly polarized) and the sample composition (nonmagnetic Cu, magnetic Co or a Co/Cu heterostructure). The symmetry-allowed or -forbidden components of the SAM and OAM are summarized in Tab. 1 and have been fully confirmed with the simulations. As a general trend, a transition from coherence before the laser pulse to an incoherent behaviour afterward is observed. This is attributed to increasing interference. Moreover, the simulations show less decoherence for the orbital dynamics than for the spin counterpart.

polarization of the laser pulse	$\langle J^x \rangle$	$\langle J^y \rangle$	$\langle J^z \rangle$
p polarized	– (+)	+ (+)	– (+)
s polarized	– (–)	– (+)	– (+)
circularly polarized	+ (+)	+ (+)	+ (+)

Table 1: Symmetry-allowed (+) or -forbidden (–) components of the site-averaged electron angular momentum $\langle \mathbf{J} \rangle = (\langle J^x \rangle, \langle J^y \rangle, \langle J^z \rangle)$ for the setups in publications [OB4] and [OB5]. Herein, $\langle \mathbf{J} \rangle$ is either the SAM $\langle \mathbf{S} \rangle$ or the OAM $\langle \mathbf{L} \rangle$ [cf. Eq. (3.66)]. The magnetic case is shown in brackets. This table is inspired by Tab. II in publication [OB4].

- Since the approach allows access to the spatio-temporal distribution of observables, a detailed insight into the dynamics of the SAM and OAM during the laser excitation is possible with femtosecond and atomic resolution. Thus, it is shown that inhomogeneities, in particular surfaces and Co/Cu interfaces, act as “sources” for currents that may transfer charge, SAM or OAM. For an efficient transfer of SAM or OAM across an interface, the results suggest to induce a component, which is forbidden in the nonmagnetic region, in the ferromagnetic region and transfer it to the nonmagnet.

Methods. Summarizing the results of my PhD thesis, I gained deeper understanding of the transport of charge, spin and orbital angular momenta in the steady state and on ultrafast time-scales. In the process, I learned and used different theoretical techniques. On the one hand, I worked analytically (e.g. unitary transformation of the model Hamiltonian and derivation of expressions for the expectation values of observables), and on the other hand I have used, modified, and developed computer codes to simulate the transport properties. I developed a simple tight-binding code (*python*) in which I implemented the computation of the (spin and orbital) Hall conductivities according to the Berry curvature formalism. For the simulation of ultrafast electron dynamics, I used the computational framework *EVOLVE* [54] (C++) which is being developed in our group. Therein, I contributed to the implementation of the spin and orbital currents. In order to analyze and visualize the computed data, I utilized *Mathematica* and self-written *python* codes. The latter have also been used to generate animations of the dynamics (see supplemental material of publication [OB4]).

Perspectives. In studies of the Hall effects in the kagome systems, only model calculations have been performed. For a more realistic model of the material class Mn_3X which are constituted of layered kagome sublattices, the tight-binding Hamiltonian can be fitted to band structures obtained by ab-initio calculations. This can be achieved, for example, by utilizing the *wannier90* community code [212] which calculates maximally-localised Wannier functions (MLWFs) in a very efficient way. Transport quantities such as AHE or SHE may be computed subsequently, for example with the high performance *WannierBerri* code [213]. The investigation of the laser-induced electron dynamics and manipulation of the noncollinear antiferromagnets Mn_3X with the framework *EVOLVE* would be a valuable future project. For example, linear spin polarization effects [39] suggest that the sublattices in these materials may be excited individually with an appropriate laser pulse. One may expect laser-induced spin currents with a spin-polarization component perpendicular to the kagome plane. Unfortunately, a tight-binding fit in the basis of MLWFs would not provide the necessary input in form of Slater-Koster parameters [cf. Sec. 2.1].

Nevertheless, the impact of noncollinearity may be studied with the *EVOLVE* approach. Although the publications presented in Sec. 5 considered collinear magnetism, we already started implementing noncollinear magnetic textures in *EVOLVE*. This would enable us to study the influence of thermally fluctuating spins on the electron dynamics in magnetic materials. Noncollinearity manifests itself in spin-mixing hopping terms, similar to spin-orbit coupling which opens additional transport channels. After a successful implementation, complex magnetic textures like skyrmions and related quasiparticles are worth investigating. The topology of the highly stable, noncollinear magnetic texture offers great potential for spintronic devices; for a recent review see [214].

Research on spintronics may be extended from materials with a noncollinear magnetic texture in *real* space to systems with a noncollinear spin texture in *reciprocal* space. For example, the two-dimensional electron gas (2DEG) $AlO/SrTiO_3$ with a Rashba spin texture at the interface is worth studying in the ultrafast regime, since significant spin and orbital Edelstein effects have been reported, recently [215]. For the investigation of an ‘ultrafast Edelstein effect’ induced by a laser pulse with *EVOLVE*, the theoretical description of the interface must be improved, e.g. by implementing Rashba spin-orbit coupling [81] in the real-space tight binding Hamiltonian. An extension of such established steady-state phenomena to the time domain would be of great interest for the ultrafast magnetization dynamics community. In a recent work [OB8], we studied laser-induced orbital currents in a Cu nanoribbon and found an ‘ultrafast OHE’. Being laser-driven, we found pronounced differences to the steady-state OHE. For example, similar to the scenario of a classical driven harmonic oscillator, our simulations revealed a phase shift between the laser’s driving electric field and the responding orbital current. This situation is different from the static OHE where the current is proportional to the field.

A general aspect on our agenda is to overcome limitations of the *EVOLVE* approach (cf. Sec. 3.5). In order to make the simulations more realistic, electron-phonon and electron-electron interaction should be included. The former is already taken into account partially by the feature of coupling the electron system to a bosonic heat bath via Lindbladians for so-called jump operators [54, OB7]. Thus, thermalization, relaxation towards thermal equilibrium and dephasing are simulated, since energy transfer between the two reservoirs is possible. However, the electron-phonon coupling constants may be improved by using results from ab-initio calculations.

Lastly, the electron-electron interaction is approximately accounted for by the exchange-correlation functional in density-functional theory, and is thus effectively included in the tight-binding description (recall that the parameters are chosen to reproduce ab-initio band structures). A full account of the electron-electron interaction requires a two-particle reduced density matrix approach whose implementation requires the development of a new computer code. Besides, this approach is computationally very demanding and thus is typically restricted to small systems and time spans, similar to time-dependent density functional theory [45]. However, the electron-electron interaction can be explicitly taken into account in *EVOLVE* by exploiting the Hartree-Fock approximation, which allows to stay within the one-particle reduced density matrix approach [57]. The implementation of this feature in our code is very challenging but on our agenda. We expect attraction and repulsion within the dynamic spatial charge distribution that is excited by the laser pulse. For example, the electron-electron interaction could reduce the propagation length of currents (attraction) and spread ‘occupation patches’ (spatial regions of increased or decreased occupation; repulsion). A general feature would be loss of coherence as often found in experiments.

List of own publications

- OB1. Busch, O., Göbel, B. & Mertig, I. Microscopic origin of the anomalous Hall effect in non-collinear kagome magnets. *Physical Review Research* **2**, 033112 (2020).
- OB2. Busch, O., Göbel, B. & Mertig, I. Spin Hall effect in noncollinear kagome antiferromagnets. *Physical Review B* **104**, 184423 (2021).
- OB3. Busch, O., Mertig, I. & Göbel, B. Orbital Hall effect and orbital edge states caused by s electrons. *Physical Review Research* **5**, 043052 (2023).
- OB4. Busch, O., Ziolkowski, F., Mertig, I. & Henk, J. Ultrafast dynamics of electrons excited by femtosecond laser pulses: Spin polarization and spin-polarized currents. *Physical Review B* **108**, 184401 (2023).
- OB5. Busch, O., Ziolkowski, F., Mertig, I. & Henk, J. Ultrafast dynamics of orbital angular momentum of electrons induced by femtosecond laser pulses: Generation and transfer across interfaces. *Physical Review B* **108**, 104408 (2023).

Other publications

- OB6. Pal, B. *et al.* Setting of the magnetic structure of chiral kagome antiferromagnets by a seeded spin-orbit torque. *Science Advances* **8**, eabo5930 (2022).
- OB7. Ziolkowski, F., Busch, O., Mertig, I. & Henk, J. Ultrafast spin dynamics: Complementing theoretical analyses by quantum state measures. *Journal of Physics: Condensed Matter* **35**, 125501 (2023).

Submitted manuscripts

- OB8. Busch, O., Ziolkowski, F., Göbel, B., Mertig, I. & Henk, J. *Ultrafast Orbital Hall Effect in Metallic Nanoribbons* 2023.

Copyright

Publication [OB1]: Published under the terms of the Creative Commons Attribution 4.0 International license.

Publication [OB2]: Reprinted (whole article) with permission from O. Busch, B. Göbel and I. Mertig, *Physical Review B* **104**, 184423 (2021); Spin Hall effect in noncollinear kagome antiferromagnets. Copyright (2021) by the American Physical Society.

Publication [OB3]: Published under the terms of the Creative Commons Attribution 4.0 International license.

Publication [OB4]: Reprinted (whole article) with permission from O. Busch, F. Ziolkowski, I. Mertig and J. Henk, *Physical Review B* **108**, 184401 (2023); Ultrafast dynamics of electrons excited by femtosecond laser pulses: Spin polarization and spin-polarized currents. Copyright (2023) by the American Physical Society.

Publication [OB5]: Reprinted (whole article) with permission from O. Busch, F. Ziolkowski, I. Mertig and J. Henk, *Physical Review B* **108**, 104408 (2023); Ultrafast dynamics of orbital angular momentum of electrons induced by femtosecond laser pulses: Generation and transfer across interfaces. Copyright (2023) by the American Physical Society.

References

1. Jungwirth, T., Wunderlich, J. & Olejník, K. Spin Hall effect devices. *Nature Materials* **11**, 382–390 (2012).
2. Baltz, V *et al.* Antiferromagnetic spintronics. *Reviews of Modern Physics* **90**, 015005 (2018).
3. Hirohata, A. *et al.* Review on spintronics: Principles and device applications. *Journal of Magnetism and Magnetic Materials* **509**, 166711 (2020).
4. Duine, R. An alternating alternative. *Nature Materials* **10**, 344–345 (2011).
5. Sinova, J. & Žutić, I. New moves of the spintronics tango. *Nature Materials* **11**, 368–371 (2012).
6. Gross, R. & Marx, A. *Festkörperphysik 3*. (De Gruyter, 2018).
7. Slonczewski, J. C. *et al.* Current-driven excitation of magnetic multilayers. *Journal of Magnetism and Magnetic Materials* **159**, L1 (1996).
8. Berger, L. Emission of spin waves by a magnetic multilayer traversed by a current. *Physical Review B* **54**, 9353 (1996).
9. Takei, S., Halperin, B. I., Yacoby, A. & Tserkovnyak, Y. Superfluid spin transport through antiferromagnetic insulators. *Physical Review B* **90**, 094408 (2014).
10. McGuire, T & Potter, R. Anisotropic magnetoresistance in ferromagnetic 3d alloys. *IEEE Transactions on Magnetics* **11**, 1018–1038 (1975).
11. Nagaosa, N., Sinova, J., Onoda, S., MacDonald, A. H. & Ong, N. P. Anomalous Hall effect. *Reviews of Modern Physics* **82**, 1539 (2010).
12. Sinova, J., Valenzuela, S. O., Wunderlich, J, Back, C. & Jungwirth, T. Spin Hall effects. *Reviews of Modern Physics* **87**, 1213 (2015).
13. Chen, H., Niu, Q. & MacDonald, A. H. Anomalous Hall effect arising from noncollinear antiferromagnetism. *Physical Review Letters* **112**, 017205 (2014).
14. Kübler, J. & Felser, C. Non-collinear antiferromagnets and the anomalous Hall effect. *Europhysics Letters* **108**, 67001 (2014).
15. Zhang, Y. *et al.* Strong anisotropic anomalous Hall effect and spin Hall effect in the chiral antiferromagnetic compounds Mn_3X ($X = Ge, Sn, Ga, Ir, Rh, \text{ and } Pt$). *Physical Review B* **95**, 075128 (2017).
16. Železný, J., Zhang, Y., Felser, C. & Yan, B. Spin-polarized current in noncollinear antiferromagnets. *Physical Review Letters* **119**, 187204 (2017).
17. Zhang, Y., Železný, J., Sun, Y., Van Den Brink, J. & Yan, B. Spin Hall effect emerging from a noncollinear magnetic lattice without spin–orbit coupling. *New Journal of Physics* **20**, 073028 (2018).
18. Nakatsuji, S., Kiyohara, N. & Higo, T. Large anomalous Hall effect in a non-collinear antiferromagnet at room temperature. *Nature* **527**, 212–215 (2015).
19. Nayak, A. K. *et al.* Large anomalous Hall effect driven by a nonvanishing Berry curvature in the noncolinear antiferromagnet Mn_3Ge . *Science Advances* **2**, e1501870 (2016).
20. Kimata, M. *et al.* Magnetic and magnetic inverse spin Hall effects in a non-collinear antiferromagnet. *Nature* **565**, 627–630 (2019).
21. Go, D., Jo, D., Lee, H.-W., Kläui, M. & Mokrousov, Y. Orbitronics: Orbital currents in solids. *Europhysics Letters* **135**, 37001 (2021).

22. Kittel, C. Surface and interface physics. *Introduction to Solid State Physics*; Wiley: New York, NY, USA, 487–514 (2004).
23. Go, D., Jo, D., Kim, C. & Lee, H.-W. Intrinsic spin and orbital Hall effects from orbital texture. *Physical Review Letters* **121**, 086602 (2018).
24. Go, D. & Lee, H.-W. Orbital torque: Torque generation by orbital current injection. *Physical Review Research* **2**, 013177 (2020).
25. Bernevig, B. A., Hughes, T. L. & Zhang, S.-C. Orbitronics: The intrinsic orbital current in *p*-doped silicon. *Physical Review Letters* **95**, 066601 (2005).
26. Go, D. *et al.* Toward surface orbitronics: giant orbital magnetism from the orbital Rashba effect at the surface of *sp*-metals. *Scientific Reports* **7**, 46742 (2017).
27. Cao, Y. *et al.* Prospect of Spin-Orbitronic Devices and Their Applications. *iScience* **23**, 101614 (2020).
28. Pezo, A., Ovalle, D. G. & Manchon, A. Orbital Hall effect in crystals: Interatomic versus intra-atomic contributions. *Physical Review B* **106**, 104414 (2022).
29. Bigot, J.-Y. & Vomir, M. Ultrafast magnetization dynamics of nanostructures. *Annalen der Physik* **525**, 2–30 (2013).
30. Kimel, A., Kirilyuk, A. & Rasing, T. Femtosecond opto-magnetism: ultrafast laser manipulation of magnetic materials. *Laser & Photonics Reviews* **1**, 275–287 (2007).
31. Phillips, K. C., Gandhi, H. H., Mazur, E. & Sundaram, S. K. Ultrafast laser processing of materials: a review. *Advances in Optics and Photonics* **7**, 684–712 (2015).
32. Shugaev, M. V. *et al.* Fundamentals of ultrafast laser–material interaction. *MRS Bulletin* **41**, 960–968 (2016).
33. Scheid, P., Remy, Q., Lebègue, S., Malinowski, G. & Mangin, S. Light induced ultrafast magnetization dynamics in metallic compounds. *Journal of Magnetism and Magnetic Materials* **560**, 169596 (2022).
34. Beaupaire, E., Merle, J.-C., Daunois, A. & Bigot, J.-Y. Ultrafast Spin Dynamics in Ferromagnetic Nickel. *Physical Review Letters* **76**, 4250–4253 (1996).
35. Kimel, A. V. *et al.* Ultrafast non-thermal control of magnetization by instantaneous photomagnetic pulses. *Nature* **435**, 655–657 (2005).
36. Stanciu, C. D. *et al.* All-Optical Magnetic Recording with Circularly Polarized Light. *Physical Review Letters* **99**, 047601 (2007).
37. Radu, I. *et al.* Transient ferromagnetic-like state mediating ultrafast reversal of antiferromagnetically coupled spins. *Nature* **472**, 205–208 (2011).
38. Henk, J. & Feder, R. Spin Polarization in Normal Photoemission by Linearly Polarized Light from Non-Magnetic (110) Surfaces. *Europhysics Letters* **28**, 609 (1994).
39. Henk, J., Scheunemann, T., Halilov, S. V. & Feder, R. Magnetic dichroism and electron spin polarization in photoemission: analytical results. *Journal of Physics: Condensed Matter* **8**, 47 (1996).
40. Kirilyuk, A., Kimel, A. V. & Rasing, T. Ultrafast optical manipulation of magnetic order. *Reviews of Modern Physics* **82**, 2731–2784 (2010).
41. Shin, D. *et al.* Phonon-driven spin-Floquet magneto-valleytronics in MoS₂. *Nature Communications* **9**, 638 (2018).
42. Okyay, M. S., Kulahlioglu, A. H., Kochan, D. & Park, N. Resonant amplification of the inverse Faraday effect magnetization dynamics of time reversal symmetric insulators. *Physical Review B* **102**, 104304 (2020).

43. Neufeld, O., Tancogne-Dejean, N., De Giovannini, U., Hübener, H. & Rubio, A. Attosecond magnetization dynamics in non-magnetic materials driven by intense femtosecond lasers. *npj Computational Materials* **9**, 39 (2023).
44. Zhang, G. P. & Hübner, W. Laser-Induced Ultrafast Demagnetization in Ferromagnetic Metals. *Physical Review Letters* **85**, 3025–3028 (2000).
45. Dewhurst, J. K., Elliott, P., Shallcross, S., Gross, E. K. U. & Sharma, S. Laser-Induced Intersite Spin Transfer. *Nano Letters* **18**, 1842 (2018).
46. Malinowski, G. *et al.* Control of speed and efficiency of ultrafast demagnetization by direct transfer of spin angular momentum. *Nature Physics* **4**, 855–858 (2008).
47. Schellekens, A. J., Kuiper, K. C., de Wit, R. R. J. C. & Koopmans, B. Ultrafast spin-transfer torque driven by femtosecond pulsed-laser excitation. *Nature Communications* **5**, 4333 (2014).
48. Melnikov, A. *et al.* Ultrafast Transport of Laser-Excited Spin-Polarized Carriers in Au/Fe/MgO(001). *Physical Review Letters* **107**, 076601 (2011).
49. Chen, J. *et al.* Competing Spin Transfer and Dissipation at Co/Cu(001) Interfaces on Femtosecond Timescales. *Physical Review Letters* **122**, 067202 (2019).
50. Boeglin, C. *et al.* Distinguishing the ultrafast dynamics of spin and orbital moments in solids. *Nature* **465**, 458–461 (2010).
51. Stamm, C., Pontius, N., Kachel, T., Wietstruk, M. & Dürr, H. A. Femtosecond x-ray absorption spectroscopy of spin and orbital angular momentum in photoexcited Ni films during ultrafast demagnetization. *Physical Review B* **81**, 104425 (2010).
52. Hennecke, M. *et al.* Angular Momentum Flow During Ultrafast Demagnetization of a Ferrimagnet. *Physical Review Letters* **122**, 157202 (2019).
53. Seifert, T. S. *et al.* Time-domain observation of ballistic orbital-angular-momentum currents with giant relaxation length in tungsten. *Nature Nanotechnology* (2023).
54. Töpler, F., Henk, J. & Mertig, I. Ultrafast spin dynamics in inhomogeneous systems: a density-matrix approach applied to Co/Cu interfaces. *New Journal of Physics* **23**, 033042 (2021).
55. Nolting, W. *Grundkurs Theoretische Physik 7: Viel-Teilchen-Theorie* (Springer-Verlag, 2014).
56. Born, M & Oppenheimer, R. Zur Quantentheorie der Molekeln. *Annalen der Physik* **389**, 457–484 (1927).
57. Runge, E, Gross, E. & Heinonen, O. *Many-particle theory* (1991).
58. Mahan, G. D. *Many-Particle Physics* 3. (Springer, New York, 2000).
59. Bloch, F. Über die Quantenmechanik der Elektronen in Kristallgittern. *Zeitschrift für Physik* **52**, 555–600 (1929).
60. Slater, J. C. & Koster, G. F. Simplified LCAO method for the periodic potential problem. *Physical Review* **94**, 1498 (1954).
61. Ashcroft, N., Mermin, N. & Mermin, N. *Solid State Physics* ISBN: 9780030839931 (Holt, Rinehart and Winston, 1976).
62. Papaconstantopoulos, D. A. & Mehl, M. J. The Slater–Koster tight-binding method: a computationally efficient and accurate approach. *Journal of Physics: Condensed Matter* **15**, R413 (2003).
63. Koskinen, P. & Mäkinen, V. Density-functional tight-binding for beginners. *Computational Materials Science* **47**, 237–253 (2009).

64. Harrison, W. A. *Electronic structure and the properties of solids: the physics of the chemical bond* (Courier Corporation, 2012).
65. Gradhand, M *et al.* First-principle calculations of the Berry curvature of Bloch states for charge and spin transport of electrons. *Journal of Physics: Condensed Matter* **24**, 213202 (2012).
66. Rauch, T. *Topological insulators and semimetals: theory for bulk and surface electronic properties* PhD thesis (Martin-Luther-Universität Halle-Wittenberg, 2016).
67. Papaconstantopoulos, D. A. *Handbook of the Band Structure of Elemental Solids* (Springer, Berlin, 2015).
68. Roothaan, C. J. A study of two-center integrals useful in calculations on molecular structure. I. *The Journal of Chemical Physics* **19**, 1445–1458 (1951).
69. Fry, J. L., Brener, N. E., Case, F. C. & Desai, N. L. Two-center approximation in the quantum theory of solids. *Physical Review B* **15**, 5811–5820 (1977).
70. Löwdin, P.-O. On the non-orthogonality problem connected with the use of atomic wave functions in the theory of molecules and crystals. *The Journal of Chemical Physics* **18**, 365–375 (1950).
71. Giannozzi, P. *et al.* Quantum ESPRESSO toward the exascale. *The Journal of Chemical Physics* **152**, 154105 (2020).
72. Damascelli, A. Probing the electronic structure of complex systems by ARPES. *Physica Scripta* **2004**, 61 (2004).
73. Cohen, M. L. & Chelikowsky, J. R. *Electronic structure and optical properties of semiconductors* (Springer Science & Business Media, 2012).
74. Stiles, M. D. Generalized Slater-Koster method for fitting band structures. *Physical Review B* **55**, 4168 (1997).
75. Pientka, F. *Geometrical Concepts in the Band Theory of Solids* PhD thesis (Martin-Luther-Universität Halle-Wittenberg, 2010).
76. Nolting, W. *Grundkurs Theoretische Physik 5/2: Quantenmechanik-Methoden und Anwendungen* 8. (Springer, 2011).
77. Pauli, W. Zur Quantenmechanik des magnetischen Elektrons. *Zeitschrift für Physik* **43**, 601–623 (1927).
78. Nolting, W. *Quantentheorie des Magnetismus: Teil 2: Modelle* (Springer-Verlag, 2013).
79. Hund, F. Zur Deutung verwickelter Spektren, insbesondere der Elemente Scandium bis Nickel. *Zeitschrift für Physik* **33**, 345–371 (1925).
80. Fließbach, T. *Quantenmechanik: Lehrbuch zur Theoretischen Physik III* (Springer-Verlag, 2018).
81. Rashba, E. Properties of semiconductors with an extremum loop. *Soviet Physics – Solid State* **2**, 1109 (1960).
82. Dzyaloshinsky, I. A thermodynamic theory of “weak” ferromagnetism of antiferromagnetics. *Journal of Physics and Chemistry of Solids* **4**, 241–255 (1958).
83. Moriya, T. Anisotropic superexchange interaction and weak ferromagnetism. *Physical Review* **120**, 91 (1960).
84. Jaffe, M. & Singh, J. Inclusion of spin-orbit coupling into tight binding bandstructure calculations for bulk and superlattice semiconductors. *Solid State Communications* **62**, 399–402 (1987).

85. Chisholm, C. D. H. *Group theoretical techniques in quantum chemistry*. (New York: Academic Press, 1976).
86. Varshalovich, D. A., Moskalev, A. N. & Khersonskii, V. K. *Quantum theory of angular momentum: irreducible tensors, spherical harmonics, vector coupling coefficients, 3nj symbols* (World Scientific, 1988).
87. Blanco, M. A., Flórez, M. & Bermejo, M. Evaluation of the rotation matrices in the basis of real spherical harmonics. *Journal of Molecular Structure: THEOCHEM* **419**, 19–27 (1997).
88. Petrucci, R. H., Herring, F. G. & Madura, J. D. *General chemistry: principles and modern applications* (Pearson Prentice Hall, 2010).
89. Jones, M. D. & Albers, R. C. Spin-orbit coupling in an *f*-electron tight-binding model: Electronic properties of Th, U, and Pu. *Physical Review B* **79**, 045107 (2009).
90. Konschuh, S., Gmitra, M. & Fabian, J. Tight-binding theory of the spin-orbit coupling in graphene. *Physical Review B* **82**, 245412 (2010).
91. Berry, M. V. Quantal phase factors accompanying adiabatic changes. *Proceedings of the Royal Society of London. A. Mathematical and Physical Sciences* **392**, 45–57 (1984).
92. Bruno, P. *Berry phase effects in magnetism* 2005.
93. Xiao, D., Chang, M.-C. & Niu, Q. Berry phase effects on electronic properties. *Review of Modern Physics* **82**, 1959–2007 (2010).
94. Bernevig, B. A. & Hughes, T. L. *Topological insulators and topological superconductors* (Princeton university press, 2013).
95. Haldane, F. D. M. Model for a Quantum Hall Effect without Landau Levels: Condensed-Matter Realization of the "Parity Anomaly". *Physical Review Letters* **61**, 2015–2018 (1988).
96. Kane, C. L. & Mele, E. J. Quantum spin Hall effect in graphene. *Physical Review Letters* **95**, 226801 (2005).
97. Fu, L. Topological Crystalline Insulators. *Physical Review Letters* **106**, 106802 (2011).
98. Zak, J. Berry's phase for energy bands in solids. *Physical Review Letters* **62**, 2747 (1989).
99. Zhou, X. *et al.* Spin-order dependent anomalous Hall effect and magneto-optical effect in the noncollinear antiferromagnets Mn_3XN with $X = Ga, Zn, Ag, \text{ or } Ni$. *Physical Review B* **99**, 104428 (2019).
100. Hall, E. H. On a new action of the magnet on electric currents. *American Journal of Mathematics* **2**, 287–292 (1879).
101. Ph.D., E. H. H. XVIII. On the "Rotational Coefficient" in nickel and cobalt. *The London, Edinburgh, and Dublin Philosophical Magazine and Journal of Science* **12**, 157–172 (1881).
102. Karplus, R. & Luttinger, J. M. Hall effect in ferromagnetics. *Physical Review* **95**, 1154–1160 (1954).
103. Ye, J. *et al.* Berry Phase Theory of the Anomalous Hall Effect: Application to Colossal Magnetoresistance Manganites. *Physical Review Letters* **83**, 3737–3740 (1999).
104. Taguchi, Y., Oohara, Y., Yoshizawa, H., Nagaosa, N. & Tokura, Y. Spin Chirality, Berry Phase, and Anomalous Hall Effect in a Frustrated Ferromagnet. *Science* **291**, 2573–2576 (2001).
105. Onoda, S. & Nagaosa, N. Spin chirality fluctuations and anomalous Hall effect in itinerant ferromagnets. *Physical Review Letters* **90**, 196602 (2003).
106. Bruno, P., Dugaev, V. K. & Taillefumier, M. Topological Hall Effect and Berry Phase in Magnetic Nanostructures. *Physical Review Letters* **93**, 096806 (2004).

107. Binz, B. & Vishwanath, A. Chirality induced anomalous-Hall effect in helical spin crystals. *Physica B: Condensed Matter* **403**, 1336–1340 (2008).
108. Neubauer, A. *et al.* Topological Hall Effect in the *A* Phase of MnSi. *Physical Review Letters* **102**, 186602 (2009).
109. Göbel, B. *Emergent electrodynamics in non-collinear spin textures* PhD thesis (Martin-Luther-Universität Halle-Wittenberg, 2020).
110. Smit, J. The spontaneous Hall effect in ferromagnetics I. *Physica* **21**, 877–887 (1955).
111. Berger, L. Side-Jump Mechanism for the Hall Effect of Ferromagnets. *Physical Review B* **2**, 4559–4566 (1970).
112. Chang, M.-C. & Niu, Q. Berry phase, hyperorbits, and the Hofstadter spectrum: Semiclassical dynamics in magnetic Bloch bands. *Physical Review B* **53**, 7010 (1996).
113. Kubo, R. Statistical-mechanical theory of irreversible processes. I. General theory and simple applications to magnetic and conduction problems. *Journal of the Physical Society of Japan* **12**, 570–586 (1957).
114. Chen, L.-Y. & Su, Z.-B. Equivalence of quantum Boltzmann equation and Kubo formula for dc conductivity. *International Journal of Modern Physics B* **4**, 293–315 (1990).
115. Wang, X., Yates, J. R., Souza, I. & Vanderbilt, D. Ab initio calculation of the anomalous Hall conductivity by Wannier interpolation. *Physical Review B* **74**, 195118 (2006).
116. Sundaram, G. & Niu, Q. Wave-packet dynamics in slowly perturbed crystals: Gradient corrections and Berry-phase effects. *Physical Review B* **59**, 14915 (1999).
117. Mook, A. *Topological Magnon Materials and Transverse Magnon Transport [kumulative Dissertation]* PhD thesis (Martin-Luther-Universität Halle-Wittenberg, 2017).
118. Cercignani, C. & Cercignani, C. *The Boltzmann equation* (Springer, 1988).
119. Callaway, J. *Quantum theory of the solid state* (Academic press, 2013).
120. Thouless, D. J., Kohmoto, M., Nightingale, M. P. & den Nijs, M. Quantized Hall conductance in a two-dimensional periodic potential. *Physical Review Letters* **49**, 405 (1982).
121. Sinova, J., Jungwirth, T., Kučera, J. & MacDonald, A. Infrared magneto-optical properties of (III, Mn) V ferromagnetic semiconductors. *Physical Review B* **67**, 235203 (2003).
122. Mott, N. F. Electrons in transition metals. *Advances in Physics* **13**, 325–422 (1964).
123. Shen, S., Ohodnicki, P., Kernion, S. & McHenry, M. E. Two-current model of the composition dependence of resistivity in amorphous $(\text{Fe}_{100-x}\text{Co}_x)_{89-y}\text{Zr}_7\text{B}_4\text{Cu}_y$ alloys using a rigid-band assumption. *Journal of Applied Physics* **112**, 103705 (2012).
124. Hirsch, J. Spin Hall effect. *Physical Review Letters* **83**, 1834 (1999).
125. Zhang, S. Spin Hall Effect in the Presence of Spin Diffusion. *Physical Review Letters* **85**, 393–396 (2000).
126. Murakami, S., Nagaosa, N. & Zhang, S.-C. Dissipationless Quantum Spin Current at Room Temperature. *Science* **301**, 1348–1351 (2003).
127. Sinova, J. *et al.* Universal intrinsic spin Hall effect. *Physical Review Letters* **92**, 126603 (2004).
128. Maekawa, S., Valenzuela, S. O., Kimura, T. & Saitoh, E. *Spin current* (Oxford University Press, 2017).
129. D’Yakonov, M. I. & Perel, V. Possibility of orienting electron spins with current. *Soviet Journal of Experimental and Theoretical Physics Letters* **13**, 467 (1971).
130. Dyakonov, M. I. & Perel, V. Current-induced spin orientation of electrons in semiconductors. *Physics Letters A* **35**, 459–460 (1971).

131. Culcer, D. *et al.* Semiclassical spin transport in spin-orbit-coupled bands. *Physical Review Letters* **93**, 046602 (2004).
132. Yao, Y & Fang, Z. Sign changes of intrinsic spin Hall effect in semiconductors and simple metals: First-principles calculations. *Physical Review Letters* **95**, 156601 (2005).
133. Hoffmann, A. Spin Hall Effects in Metals. *IEEE Transactions on Magnetics* **49**, 5172–5193 (2013).
134. Yin, G., Liu, Y., Barlas, Y., Zang, J. & Lake, R. K. Topological spin Hall effect resulting from magnetic skyrmions. *Physical Review B* **92**, 024411 (2015).
135. Buhl, P. M., Freimuth, F., Blügel, S. & Mokrousov, Y. Topological spin Hall effect in anti-ferromagnetic skyrmions. *Physica Status Solidi – Rapid Research Letters* **11**, 1700007 (2017).
136. Nan, T. *et al.* Controlling spin current polarization through non-collinear antiferromagnetism. *Nature Communications* **11**, 4671 (2020).
137. Parkin, S. & Yang, S.-H. Memory on the racetrack. *Nature Nanotechnology* **10**, 195–198 (2015).
138. Yang, S.-H., Ryu, K.-S. & Parkin, S. Domain-wall velocities of up to 750 m s^{-1} driven by exchange-coupling torque in synthetic antiferromagnets. *Nature Nanotechnology* **10**, 221–226 (2015).
139. Miron, I. M. *et al.* Perpendicular switching of a single ferromagnetic layer induced by in-plane current injection. *Nature* **476**, 189–193 (2011).
140. Liu, L. *et al.* Spin-Torque Switching with the Giant Spin Hall Effect of Tantalum. *Science* **336**, 555–558 (2012).
141. Zhang, S. & Yang, Z. Intrinsic Spin and Orbital Angular Momentum Hall Effect. *Physical Review Letters* **94**, 066602 (2005).
142. Kontani, H., Tanaka, T., Hirashima, D., Yamada, K & Inoue, J. Giant Intrinsic Spin and Orbital Hall Effects in Sr_2MO_4 ($M = \text{Ru, Rh, Mo}$). *Physical Review Letters* **100**, 096601 (2008).
143. Tanaka, T *et al.* Intrinsic spin Hall effect and orbital Hall effect in $4d$ and $5d$ transition metals. *Physical Review B* **77**, 165117 (2008).
144. Kontani, H., Tanaka, T., Hirashima, D., Yamada, K & Inoue, J. Giant orbital Hall effect in transition metals: Origin of large spin and anomalous Hall effects. *Physical Review Letters* **102**, 016601 (2009).
145. Pezo, A., Ovalle, D. G. & Manchon, A. *Orbital Hall physics in two-dimensional Dirac materials* 2023.
146. Go, D. *et al.* Theory of current-induced angular momentum transfer dynamics in spin-orbit coupled systems. *Physical Review Research* **2**, 033401 (2020).
147. Thonhauser, T., Ceresoli, D., Vanderbilt, D. & Resta, R. Orbital magnetization in periodic insulators. *Physical Review Letters* **95**, 137205 (2005).
148. Xiao, D., Shi, J. & Niu, Q. Berry phase correction to electron density of states in solids. *Physical Review Letters* **95**, 137204 (2005).
149. Shi, J., Vignale, G., Xiao, D. & Niu, Q. Quantum theory of orbital magnetization and its generalization to interacting systems. *Physical Review Letters* **99**, 197202 (2007).
150. Yoda, T., Yokoyama, T. & Murakami, S. Orbital Edelstein Effect as a Condensed-Matter Analog of Solenoids. *Nano Letters* **18**, 916–920 (2018).
151. Cysne, T. P., Bhowal, S., Vignale, G. & Rappoport, T. G. Orbital Hall effect in bilayer transition metal dichalcogenides: From the intra-atomic approximation to the Bloch states orbital magnetic moment approach. *Physical Review B* **105**, 195421 (2022).

152. Yin, J.-X. *et al.* Giant and anisotropic many-body spin–orbit tunability in a strongly correlated kagome magnet. *Nature* **562**, 91–95 (2018).
153. Khadka, D. *et al.* Anomalous Hall and Nernst effects in epitaxial films of topological kagome magnet Fe_3Sn_2 . *Physical Review Materials* **4**, 084203 (2020).
154. Liu, E. *et al.* Giant anomalous Hall effect in a ferromagnetic kagome-lattice semimetal. *Nature Physics* **14**, 1125–1131 (2018).
155. Yazyev, O. V. An upside-down magnet. *Nature Physics* **15**, 424–425 (2019).
156. Xiong, D. *et al.* Antiferromagnetic spintronics: An overview and outlook. *Fundamental Research* **2**, 522–534 (2022).
157. Bertaut, E., Fruchart, D, Bouchaud, J. & Fruchart, R. Diffraction neutronique de Mn_3GaN . *Solid State Communications* **6**, 251–256 (1968).
158. Fruchart, D & F. Bertaut, E. Magnetic studies of the metallic perovskite-type compounds of manganese. *Journal of the physical society of Japan* **44**, 781–791 (1978).
159. Feng, W., Guo, G.-Y., Zhou, J., Yao, Y. & Niu, Q. Large magneto-optical Kerr effect in non-collinear antiferromagnets Mn_3X ($X = \text{Rh}, \text{Ir}, \text{Pt}$). *Physical Review B* **92**, 144426 (2015).
160. Guo, G.-Y. & Wang, T.-C. Large anomalous Nernst and spin Nernst effects in the non-collinear antiferromagnets Mn_3X ($X = \text{Sn}, \text{Ge}, \text{Ga}$). *Physical Review B* **96**, 224415 (2017).
161. Spaldin, N. A., Fiebig, M. & Mostovoy, M. The toroidal moment in condensed-matter physics and its relation to the magnetoelectric effect. *Journal of Physics: Condensed Matter* **20**, 434203 (2008).
162. Taylor, J. M. *Epitaxial thin films of the noncollinear antiferromagnets Mn_3Ir and Mn_3Sn for topological spintronic applications* PhD thesis (Martin-Luther-Universität Halle-Wittenberg, 2020).
163. Yue, D. & Jin, X. Towards a Better Understanding of the Anomalous Hall Effect. *Journal of the Physical Society of Japan* **86**, 011006 (2017).
164. Taylor, J. M. *et al.* Anomalous and topological Hall effects in epitaxial thin films of the noncollinear antiferromagnet Mn_3Sn . *Physical Review B* **101**, 094404 (2020).
165. Brüne, C. *et al.* Evidence for the ballistic intrinsic spin Hall effect in HgTe nanostructures. *Nature Physics* **6**, 448–454 (2010).
166. Kimura, T., Otani, Y., Sato, T., Takahashi, S. & Maekawa, S. Room-Temperature Reversible Spin Hall Effect. *Physical Review Letters* **98**, 156601 (2007).
167. Kato, Y. K., Myers, R. C., Gossard, A. C. & Awschalom, D. D. Observation of the Spin Hall Effect in Semiconductors. *Science* **306**, 1910–1913 (2004).
168. Wunderlich, J., Kaestner, B., Sinova, J. & Jungwirth, T. Experimental Observation of the Spin-Hall Effect in a Two-Dimensional Spin-Orbit Coupled Semiconductor System. *Physical Review Letters* **94**, 047204 (2005).
169. Haider, T. A review of magneto-optic effects and its application. *International Journal of Electromagnetics and Applications* **7**, 17–24 (2017).
170. Choi, Y.-G. *et al.* Observation of the orbital Hall effect in a light metal Ti. *Nature* **619**, 52–56 (2023).
171. Chen, C. T. *et al.* Experimental Confirmation of the X-Ray Magnetic Circular Dichroism Sum Rules for Iron and Cobalt. *Physical Review Letters* **75**, 152–155 (1995).
172. Vernes, A. & Weinberger, P. Formally linear response theory of pump-probe experiments. *Physical Review B* **71**, 165108 (2005).

173. Zhang, G. P., Hübner, W., Lefkidis, G., Bai, Y. & George, T. F. Paradigm of the time-resolved magneto-optical Kerr effect for femtosecond magnetism. *Nature Physics* **5**, 499–502 (2009).
174. Huang, D., Lattery, D. & Wang, X. Materials Engineering Enabled by Time-Resolved Magneto-Optical Kerr Effect for Spintronic Applications. *ACS Applied Electronic Materials* **3**, 119–127 (2021).
175. Rohwer, T. *et al.* Collapse of long-range charge order tracked by time-resolved photoemission at high momenta. *Nature* **471**, 490–493 (2011).
176. Yaji, K. *et al.* High-resolution three-dimensional spin- and angle-resolved photoelectron spectrometer using vacuum ultraviolet laser light. *Review of Scientific Instruments* **87**, 053111 (2016).
177. Pizzini, S., Vogel, J., Bonfim, M. & Fontaine, A. in *Spin Dynamics in Confined Magnetic Structures II* (eds Hillebrands, B. & Ounadjela, K.) 157–187 (Springer Berlin Heidelberg, Berlin, Heidelberg, 2003).
178. Takubo, K. *et al.* Capturing ultrafast magnetic dynamics by time-resolved soft x-ray magnetic circular dichroism. *Applied Physics Letters* **110**, 162401 (2017).
179. Mehl, M. J. & Papaconstantopoulos, D. A. Applications of a tight-binding total-energy method for transition and noble metals: Elastic constants, vacancies, and surfaces of monatomic metals. *Physical Review B* **54**, 4519–4530 (1996).
180. Yoo, C.-S., Söderlind, P. & Cynn, H. The phase diagram of cobalt at high pressure and temperature: the stability of γ (fcc)-cobalt and new ϵ' (dhcp)-cobalt. *Journal of Physics: Condensed Matter* **10**, L311 (1998).
181. Wieczorek, J. *et al.* Separation of ultrafast spin currents and spin-flip scattering in Co/Cu(001) driven by femtosecond laser excitation employing the complex magneto-optical Kerr effect. *Physical Review B* **92**, 174410 (2015).
182. Heinrich, B. *et al.* Magnetic properties of MBE structures using fcc Co/Cu(001) and bcc Fe/Cu(001). *Journal of Applied Physics* **69**, 5217 (1991).
183. Igarashi, J.-i. & Hirai, K. Orbital moment and magnetic circular dichroism at the K edge in ferromagnetic cobalt. *Physical Review B* **53**, 6442–6450 (1996).
184. Nolting, W. *Grundkurs Theoretische Physik 6: Statistische Physik* (Springer-Verlag, 2013).
185. Schwabl, F. *Statistische Mechanik* (Springer Berlin Heidelberg, 2013).
186. Nolting, W. *Grundkurs Theoretische Physik 5/1: Quantenmechanik-Grundlagen 7.* (Springer, 2009).
187. Peierls, R. Zur Theorie des Diamagnetismus von Leitungselektronen. *Zeitschrift für Physik A Hadrons and Nuclei* **80**, 763–791 (1933).
188. Hojman, S., Rosenbaum, M., Ryan, M. P. & Shepley, L. C. Gauge invariance, minimal coupling, and torsion. *Physical Review D* **17**, 3141–3146 (1978).
189. Nolting, W. *Grundkurs Theoretische Physik 3: Elektrodynamik* (Springer, 2007).
190. Savasta, S. & Girlanda, R. The particle-photon interaction in systems described by model Hamiltonians in second quantization. *Solid State Communications* **96**, 517 (1995).
191. Starace, A. F. Length and Velocity Formulas in Approximate Oscillator-Strength Calculations. *Physical Review A* **3**, 1242–1245 (1971).
192. Louisell, W. H. *Quantum statistical properties of radiation* (John Wiley and Sons, Inc., New York, 1973).
193. Quattropani, A. & Girlanda, B. Two-photon absorption in atoms and solids. *La Rivista del Nuovo Cimento* (1978-1999) **6**, 1–37 (1983).

-
194. Weissbluth, M. *Photon-atom interactions* (Academic Press, 2012).
 195. Aucar, G. A., Saue, T., Visscher, L. & Jensen, H. J. A. On the origin and contribution of the diamagnetic term in four-component relativistic calculations of magnetic properties. *The Journal of Chemical Physics* **110**, 6208–6218 (1999).
 196. Cruzan, O. R. Translational addition theorems for spherical vector wave functions. *Quarterly of Applied Mathematics* **20**, 33–40 (1962).
 197. Harris, D. C. & Bertolucci, M. D. *Symmetry and spectroscopy: an introduction to vibrational and electronic spectroscopy* (Courier Corporation, 1989).
 198. Cotton, F. A. *Chemical applications of group theory* (John Wiley & Sons, 1991).
 199. Battiato, M., Carva, K. & Oppeneer, P. M. Superdiffusive Spin Transport as a Mechanism of Ultrafast Demagnetization. *Physical Review Letters* **105**, 027203 (2010).
 200. Battiato, M., Carva, K. & Oppeneer, P. M. Theory of laser-induced ultrafast superdiffusive spin transport in layered heterostructures. *Physical Review B* **86**, 024404 (2012).
 201. Battiato, M. *Superdiffusive Spin Transport and Ultrafast Magnetization Dynamics* PhD thesis (Uppsala Universitet, Uppsala, 2013).
 202. Battiato, M., Maldonado, P. & Oppeneer, P. M. Treating the effect of interface reflections on superdiffusive spin transport in multilayer samples (invited). en. *Journal of Applied Physics* **115**, 172611 (2014).
 203. Nenno, D. M., Rethfeld, B. & Schneider, H. C. Particle-in-cell simulation of ultrafast hot-carrier transport in Fe/Au heterostructures. *Physical Review B* **98**, 224416 (2018).
 204. Alekhin, A. *et al.* Femtosecond Spin Current Pulses Generated by the Nonthermal Spin-Dependent Seebeck Effect and Interacting with Ferromagnets in Spin Valves. *Physical Review Letters* **119**, 017202 (2017).
 205. Kaltenborn, S., Zhu, Y.-H. & Schneider, H. C. Wave-diffusion theory of spin transport in metals after ultrashort-pulse excitation. *Physical Review B* **85**, 235101 (2012).
 206. Knorren, R., Bennemann, K. H., Burgermeister, R. & Aeschlimann, M. Dynamics of excited electrons in copper and ferromagnetic transition metals: Theory and experiment. *Physical Review B* **61**, 9427–9440 (2000).
 207. Knezevic, I. & Ferry, D. K. Partial-trace-free time-convolutionless equation of motion for the reduced density matrix. *Physical Review E* **66**, 016131 (2002).
 208. Nathan, F. & Rudner, M. S. Universal Lindblad equation for open quantum systems. *Physical Review B* **102**, 115109 (2020).
 209. Pershin, Y. V., Dubi, Y. & Di Ventra, M. Effective single-particle order- N scheme for the dynamics of open noninteracting many-body systems. *Physical Review B* **78**, 054302 (2008).
 210. Ullrich, C. A. *Time-dependent density-functional theory: concepts and applications* (2011).
 211. Krieger, K., Dewhurst, J. K., Elliott, P., Sharma, S. & Gross, E. K. U. Laser-Induced Demagnetization at Ultrashort Time Scales: Predictions of TDDFT. *Journal of Chemical Theory and Computation* **11**, 4870–4874 (2015).
 212. Pizzi, G. *et al.* Wannier90 as a community code: new features and applications. *Journal of Physics: Condensed Matter* **32**, 165902 (2020).
 213. Tsirkin, S. S. High performance Wannier interpolation of Berry curvature and related quantities with WannierBerri code. *npj Computational Materials* **7**, 33 (2021).
 214. Göbel, B., Mertig, I. & Tretiakov, O. A. Beyond skyrmions: Review and perspectives of alternative magnetic quasiparticles. *Physics Reports* **895**, 1–28 (2021).
-

215. Johansson, A., Göbel, B., Henk, J., Bibes, M. & Mertig, I. Spin and orbital Edelstein effects in a two-dimensional electron gas: Theory and application to SrTiO₃ interfaces. *Physical Review Research* **3**, 013275 (2021).

Acknowledgments

I would like to thank everyone who supported and motivated me throughout my studies and the preparation of my PhD thesis.

First of all, I would like to sincerely thank Ingrid Mertig for accepting me in her working group and for providing me with versatile support for six years now. I am very grateful for the possibility to absolve my PhD thesis there and for the numerous discussions and meetings that helped me enormously with valuable tips and advice. I want to thank all members of the group for the nice time and for fruitful and interesting discussions related to our field or far away from it.

In particular, I would like to thank Børge Göbel and Jürgen Henk very much for being available as my mentors and direct contacts in the group from the beginning and that they always found time to help me besides all their projects. They never lost patience with me and my questions and were able to teach me a great deal, professionally. I would like to thank them in particular for their help in publishing my research results! I would be very happy to work with both of you in future projects.

Finally, of course, I would like to thank Theresa, my family and friends from near and far who have always supported me in nice and frustrating situations during the last few years. Thank everyone of you from the bottom of my heart!

Curriculum vitae

Personal Data

Name Busch Oliver

Nationality German

Gender Male

Education

since 03/2021 Member of the integrated Research Training Group (iRTG) of the transregional collaborative Center TRR 227 "Ultrafast Spin Dynamics"

since 10/2020 PhD studies at the Institute of Physics, Martin Luther University, Halle (Saale), Germany

Supervisor: Prof. Dr. Ingrid Mertig

10/2018 – 09/2020 Master of Science in Physics at the Martin Luther University
Master thesis: "Transversal transport coefficients in non-collinear magnetic systems"

10/2016 – 09/2018 Bachelor of Science in Physics at the Martin Luther University
Bachelor thesis: "Einfluss der toroidalen Ordnung auf die Leitfähigkeit und die magnetoelektrische Kopplung"

10/2014 – 09/2016 Study of Physics at the University of Regensburg, Regensburg, Germany

10/2011 – 09/2014 Bachelor of Engineering in Mechanical Engineering at the Duale Hochschule Baden-Württemberg, Heidenheim an der Brenz, Germany
Bachelor thesis: "Analyse der Ursachen für den Versatz und die Verbiegung von Steckerpins beim Herstellungsprozess der Gehäuse für Bremssteuergeräte"

2002 – 2011 Abitur at Simon-Marius-Gymnasium (grammar school), Gunzenhausen, Germany

Academic work experience

since 2020 Research assistant, Institute of Physics, Martin Luther University, Group of Prof. Dr. Ingrid Mertig

09/2017 – 09/2020 Student assistant, Institute of Physics, Martin Luther University, Group of Prof. Dr. Ingrid Mertig

09/2011 – 09/2014 Internship semesters, production and construction departments of Robert Bosch GmbH, Ansbach, Germany

Halle (Saale), 13.12.2023 Oliver Busch

Eidesstattliche Erklärung

Hiermit erkläre ich, Oliver Busch, dass ich die vorliegende Arbeit mit dem Titel *Simulation of steady-state and ultrafast transport of charge, spin, and orbital angular momenta* selbständig und ohne fremde Hilfe verfasst habe, keine anderen als die von mir angegebenen Quellen und Hilfsmittel benutzt habe, und die den benutzten Werken wörtlich oder inhaltlich entnommenen Stellen als solche kenntlich gemacht habe.

Ich erkläre, dass ich alle Angaben wahrheitsgemäß gemacht habe und bisher keine vergleichlichen Promotionsversuche unternommen habe, und dass ich die Dissertation weder in der gegenwärtigen noch in einer anderen Fassung bereits einer anderen Fakultät vorgelegt habe. Außerdem erkläre ich, dass ich mich noch bei keiner anderen Hochschule einem Promotionsverfahren unterzogen oder dieses begonnen habe.

Ich bin weder vorbestraft noch sind Ermittlungsverfahren gegen mich anhängig.

Halle (Saale), 13.12.2023 Oliver Busch